UNIVERSITÉ DE STRASBOURG

LABORATOIRE DE PHYSIQUE THÉORIQUE

# THÈSE

*présentée pour obtenir le grade de*

**DOCTEUR EN SCIENCES**
**SPÉCIALITÉ PHYSIQUE THÉORIQUE**

# Effects of lattice distortions on low-dimensional strongly correlated systems

par
Marion MOLINER

Soutenue le 3 février 2009 devant la commision d'examen:

| | | |
|---|---|---|
| M. Rodolfo JALABERT | IPCMS, Strasbourg | *Rapporteur* |
| M. Peter HOLDSWORTH | ENS, Lyon | *Rapporteur* |
| M. Didier POILBLANC | IRSAMC, Toulouse | *Rapporteur* |
| M. Andreas HONECKER | Georg-August Universität, Göttingen | *Examinateur* |
| M. Daniel C. CABRA | IPCMS, Strasbourg et UNLP, La Plata | *Directeur de thèse* |
| M. Pierre PUJOL | IRSAMC, Toulouse | *Co-directeur de thèse* |

« *So Long, and Thanks for All the Fish* »
Douglas N. Adams, “The Hitchhiker’s Guide to the Galaxy”.

# Acknowledgments

Mes premiers remerciements vont à Vincent qui m’a soutenue avec beaucoup de patience tout au long de cette thèse. Il m’aurait été bien plus difficile de terminer sans ses encouragements permanents.
Je remercie Daniel Cabra pour m’avoir permis de travailler sur les systèmes de basse dimensionalité fortement corrélés et pour les opportunités de collaboration qu’il m’a proposées.
Un immense merci à Pierre Pujol pour avoir accepté de co-diriger cette thèse en court de route. Sa gentillesse et sa disponibilité (téléphonique en particulier) m’ont été d’une grande aide. Merci aussi pour m’avoir montré la beauté de la physique des systèmes de spins classiques.
Je remercie chaleureusement Andreas Honecker pour ses précieux conseils et encouragements ainsi que pour sa grande disponibilité, autant lors de mes visites à Goettingen qu’en ligne.
Je suis très reconnaissante envers Rodolfo Jalabert, Peter Holdsworth et Didier Poilblanc pour avoir accepté le rôle de rapporteur et pour leurs remarques constructives.
Je remercie mon ancien camarade de bureau, Franck Stauffer, avec qui j’ai eu beaucoup de plaisir à travailler et à parler de physique (et pas que).
Je suis très reconnaissante envers Claudine Lacroix qui m’a plusieurs fois apporté un soutien matériel très précieux.
Je remercie les étudiants strasbourgeois, Raoul Dillenschneider pour ses conseils avisés et mes collègues étudiants Ala Siwek et Mathieu Planat ainsi que les non-étudiants, Véronique Bernard, Michel Rausch et Jean-Yves Fortin.
Je tiens à remercier les membres du Laboratoire de Physique Théorique de Toulouse et de l’Institut de Physique Théorique de Goettingen pour leur accueil chaleureux lors des mes visites que j’ai vraiment beaucoup appréciées.
Finalement, je remercie le soutien financier de l’*European Science Foundation* (ESF) qui a rendu matériellement possible mon travail à l’Institut de Physique Théorique de Goettingen.

*Ceci est le manuscrit de la dernière thèse soutenue au Laboratoire de Physique Théorique de Strasbourg.*

# Preamble and outline

The work carried out in this thesis lies within the general framework of condensed matter physics and, more precisely, it deals with strongly correlated systems whose spatial dimension is below three.
So-called strongly correlated systems are electronic systems in which the interaction cannot be neglected compared with other degrees of freedom. As a consequence those systems are true manybody systems and one often needs to call upon both analytical and numerical methods so as to tackle with their study. Moreover the effects of the interaction are dramatically enhanced as the dimension of a system is reduced, which makes the study of systems in one and two spatial dimensions particularly relevant.
Strongly correlated systems have been attracting much interest over the last decades since they are expected to bring understanding of "exotic" phenomena such as high critical temperature superconductivity.

In this thesis, we focus on the effects of phonons on low-dimensional strongly correlated systems. The phonons are considered only in the adiabatic limit in which their frequencies are much lower than the ones of other degrees of freedom. Consequently, they are treated as classical variables related to small displacements of the lattice sites. Previous works on the pyrochlore lattice with classical spins as well as various works on low-dimensional quantum systems showed that spin-lattice couplings can lead to the appearance of magnetization plateaux. Most of the work presented in the following is related to the effects of lattice distortions on the magnetic properties of low-dimensional strongly correlated systems.

In this thesis, both classical and quantum systems are considered. The first chapter is a summary of the whole thesis in French. In the second chapter, we lay the theoretical and experimental foundations for both classical and quantum systems. We first introduce models for strongly correlated electrons systems. In particular, we present the Hubbard model and some of its limits cases such as the Heisenberg Hamiltonian. A couple of experimental low-dimensional strongly correlated systems that exhibit exciting properties such as superconducting phases are then discussed. We also underline the particular interest of low dimension and review both the Fermi and Luttinger liquid models.
We then address frustrated classical spins systems and discuss the geometrical origin of frustration as well as competing magnetic couplings. We end this chapter by presenting briefly the Monte-Carlo algorithms that are widely used in the following studies on classical spin systems.

The third chapter is dedicated to the work performed on classical spin systems in one and two dimensions. We first discuss the origin of magnetization plateaux in classical systems. Then a section tackles the issue of thermal fluctuations and presents the *Order by Disorder* effect that selects particular spin configurations for entropic reasons.
The first work presented deals with the classical spin chain with nearest and next-to-nearest neighbors couplings and adiabatic phonons. Both analytical and numerical (Monte Carlo) treatments are used to show that the spin-lattice coupling stabilizes a magnetization plateau at one third of the saturated magnetization. We obtain a phase diagram as a function of the magnetic couplings ratio and spin-lattice coupling.
We then move to a two-dimensional frustrated lattice, the Shastry-Sutherland lattice, and study its magnetization process. We show, through classical spin-waves and Monte Carlo simulations, that thermal fluctuations stabilize a collinear phase by the *Order by Disorder* effect and hence allow a pseudo-magnetization plateau to appear at one third of the magnetization. By mean of Monte Carlo simulations, we obtain a phase diagram as a function of temperature and applied magnetic field.

Finally, the fourth chapter reviews the work done on the one-dimensional Hubbard chain at quarter filling. For this particular filling, the Hubbard chain in the presence of distortions is known to be a good model for organic compounds such as the Bechgaard and Fabre salts. Two kinds of lattice couplings are considered: the on-site Holstein distortions and the Peierls distortions that couple two nearest-neighbor sites. We perform the study in the low-energy limit through a field theory approach and bosonize the Hamiltonian before studying its ground-state. Both kinds of lattice distortions induce particular ground states with both charge density waves and bond order waves. By this method, we qualitatively recover tetramerized and dimerized phases that were previously obtained by numerical and analytical studies.

# Contents

# Chapter I

# Résumé en Français

*This chapter is a summary of the thesis, in French, as required by the university. I chose to introduce the concepts used in the thesis in a qualitative way rather than actually summarizing the work done. I left the precise description and the technical discussions for the forthcoming chapters. Moreover the references cited in this chapter are, in most cases, reviews and books, instead of precise articles.*

## 1 Systèmes de basses dimensionalité fortement corrélés

Les travaux effectués dans cette thèse s'inscrivent dans le très large cadre de la matière condensée, et plus particulièrement portent sur la physique des systèmes de basse dimensionalité (à une ou deux dimensions d'espace) fortement corrélés.
On parle de systèmes *fortement corrélés*, lorsque les corrélations ne peuvent pas être négligées. Dans ce cas, la matière ne peut plus être modélisée par un ensemble de particules libres ou quasi-libres (atomes, molécules, électrons ...) et on doit traiter des problèmes à $N$ corps.
L'étude des systèmes fortement corrélés a été grandement motivée par la découverte des supraconducteurs à haute température critique, notamment chez les oxydes cuivre, les cuprates [1, 2]. Cette vaste famille de composés présente des plans $CuO_2$ séparés par des plans d'autres atomes. Même s'il est aujourd'hui établi que la supraconductivité prend son origine dans des processus complexes d'appariement dans les plans $CuO_2$, les mécanismes ne sont pas encore complètement compris. Notamment, on sait que les plans d'autres atomes servent de réservoirs de porteurs de charges et que seulement une certaine densité de porteurs permet l'apparition d'une phase superconductrice, mais le lien entre la densité de porteurs et la température critique n'est pas encore bien établi.
La *basse dimensionalité* (dimension d'espace strictement inférieure à trois), augmente de façon spectaculaire les effets des interactions. Elle permet l'apparition d'états électroniques nouveaux qui n'apparaissent pas dans des systèmes à trois dimensions d'espace. Notamment, à une dimension le modèle du liquide de Fermi ne s'applique plus. En effet, un système unidimensionnel ne présente que des excitations collectives, ce qui requiert une description théorique particulière : le liquide de Luttinger [3, 4].
On peut trouver une justification expérimentale à l'étude de systèmes de basse dimensionalité dans le fait que chez certains composés chimiques, les couplages selon certaines directions sont suffisamment faibles pour que leurs propriétés physiques puissent être décrites en les

traitant comme des systèmes uni ou bidimensionnels.

Cette thèse aborde deux grandes thématiques relatives aux systèmes de basse dimensionalité fortement corrélés. Dans la première, on s'intéresse à des modèles de *spins classiques* sur réseaux. C'est à dire qu'à chaque site du réseau, au lieu de placer une particule, atome ou électron, sera placé seulement le degré de liberté de spin. De cette façon, l'étude est concentrée sur les propriétés magnétiques de la matière.
De plus, on se place dans la limite classique pour les spins (approximation grand $S$). Les spins classiques sont représentés par de simples vecteurs à trois composantes $\mathbf{S_j}$ (*spins de Heisenberg*), dont les normes sont fixées à 1. Cette partie se décompose en deux projets. Le premier traite le cas d'une chaîne de spins frustrés par deux couplages antiferromagnétiques et couplée à des phonons [5]. Dans le second, on considère un réseau bidimensionnel, le réseau de Shastry-Sutherland [6, 7].
La seconde partie de cette thèse est dédiée à l'étude d'une chaîne de fermions à un quart de remplissage et couplée à des phonons via deux types de couplages [8]. Dans ce cas on étudie un système quantique où non seulement le degré de liberté de spin joue un rôle mais aussi celui de charge, ce qui permet d'appréhender également les propriétés de conduction du système.

# 2 Systèmes de spins classiques

Cette première partie aborde des systèmes de spins classiques à une et deux dimensions d'espace. Tout d'abord, nous présentons brièvement la notion de frustration et l'effet, sur ces systèmes, de fluctuations thermiques qui peuvent se traduire par l'effet d'*Ordre par le Désordre*.

## 2.1 Systèmes de spins classiques frustrés

Les systèmes classiques étudiés dans cette thèse sont des systèmes antiferromagnétiques *frustrés*. La particularité d'un réseau frustré est que chaque interaction entre deux spins ne peut pas être minimisée indépendamment des autres interactions du réseau. La frustration peut induire une très grande dégénérescence de l'état fondamental, ce qui rend ces systèmes très sensibles à des perturbations (comme par exemple des fluctuations thermiques). La frustration peut avoir deux origines : une compétition entre des couplages magnétiques différents ou la géométrie du réseau [9].
La chaîne de spins classiques $J_1 - J_2$ avec des couplages antiferromagnétiques entre premiers en seconds voisins est un exemple très simple pour illustrer la frustration induite par des couplages magnétiques différents. Lorsque le couplage $J_2$ est nul, la chaîne s'ordonne selon un ordre de Néel, qui est maintenu jusqu'à $J_2/J_1 = 1/4$. Au-delà, les spins sont, d'un coté tentés de suivre un ordre de Néel entre premiers voisins (et donc un ordre ferromagnétique entre seconds voisins), mais d'un autre côté le couplage $J_2$ tend aussi à les aligner antiparallèlement. On parle alors de frustration et pour tenter de satisfaire aux deux couplages en même temps, les spins forment une spirale qui s'enroule tout au long de la chaîne et dont l'enroulement est fonction du rapport entre les deux couplages magnétiques.

La frustration géométrique peut être illustrée simplement en considérant un triangle dont chaque côté porte un couplage antiferromagnétique. On peut facilement placer deux spins ; en revanche le troisième sera forcément parallèle à un deux premiers, ce qui est extrêmement défavorable. Là encore, ce système frustré s'adapte en ne satisfaisant pleinement aucune des interactions et, dans la configuration résultante, chaque paire de spins formera un angle de 120°.
Dans les deux cas, on voit bien qu'un système frustré minimise son énergie en réalisant des configurations qui ne seraient pas idéales pour des paires spins isolées.

## 2.2 Fluctuations thermiques et phénomène d'Ordre par le Désordre

Généralement, on s'attend à ce que des fluctuations thermiques détruisent l'ordre présent à température nulle. Dans certains systèmes frustrés, les fluctuations thermiques peuvent au contraire, sélectionner une configuration ou un sous-ensemble de configurations parmi un large ensemble de configurations fondamentales dégénérées à température nulle. On parle alors d'*Ordre par le Désordre* [10].
Par exemple, le réseau de Kagomé s'est avéré être un systèmes dans lequel l'*Ordre par le Désordre* joue un rôle très important [11] (voir chapitre III). L'énergie fondamentale "classique" est extrêmement dégénérée, mais, parmi les configurations qui lui correspondent, on peut montrer qu'il en existe certaines qui peuvent supporter la présence de lignes de défauts sans que leur création ne coûte d'énergie *dans l'approximation quadratique*. On dit que ces configurations ont des modes mous et on peut montrer que ces modes contribuent moitié moins à l'énergie libre que les modes non-mous. En conséquence, en présence de fluctuations thermiques, ces configurations vont être favorisées pour des raisons entropiques.
Afin d'étudier la présence de modes mous, on applique, à une configuration donnée, des ondes de spins classiques. On développe le Hamiltonien jusqu'à l'ordre quadratique en ordres sur les déviations des positions des spins. Si la configuration étudiée a des modes mous, le spectre dans l'espace de Fourier de sa partie quadratique doit présenter autant de valeurs propres nulles que de modes mous. Nous avons utilisé cette méthode pour l'étude du réseau de Shastry-Sutherland.

## 2.3 Phonons dans la limite adiabatique

Dans cette thèse sont étudiés les effets de *distorsions du réseau* sur des systèmes de basse dimensionalité fortement corrélés.
Les modes normaux de vibration d'un réseau cristallin sont quantifiés et les quanta d'énergie associés sont les phonons. Dans le cadre de cette thèse, on se place dans la limite où la dynamique des phonons peut être négligée (limite adiabatique) et on ne traite plus directement les phonons mais les distorsions du réseau qui en résultent. Ces dernières sont des variables classiques qui traduisent les déplacements des sites du réseau. On se placera toujours dans l'hypothèse où les déplacements des sites sont petits devant les distances inter sites initiales.
Des travaux récents, portant en particulier sur le réseau pyrochlore avec des spins classiques [12] et sur la chaîne de spin $S = 1/2$ frustrée $J_1 - J_2$ [13], ont montrés que le couplage entre les

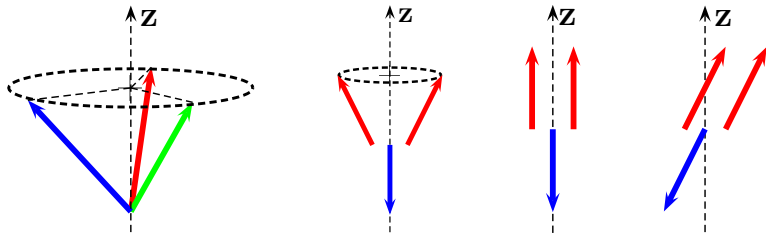


FIG. I.1: *De gauche à droite : représentation des configurations "parapluie", "Y", UUD et de "l'état plié".*

spins et le réseau peut être à l'origine de phases exotiques et notamment, en présence d'un champ magnétique, générer des plateaux dans la courbe d'aimantation.

## 2.4 Effets des distorsions du réseau sur une chaîne de spins classiques frustrés

Nous avons étudié une chaîne de spins classiques frustrée par deux couplages magnétiques $J_1$ et $J_2$, respectivement entre sites premiers et second voisins [5]. Pour une zone de l'espace des phase, paramétrée par le couplage spins-réseau et le rapport des couplages $J_1$ et $J_2$, des plateaux apparaissent à un tiers de l'aimantation de saturation.
Nous considérons un Hamiltonien effectif dont la dérivation est détaillée dans le Chapitre III. La chaîne $J_1 - J_2$ (avec $\alpha \equiv J_2/J_1$) est couplée à des déformations des liens $\delta_i$ par une constante de couplage spins-réseau $A_1$. La constante de raideur des phonons a été absorbée dans les autres constantes.

$$\mathscr{H}_{\text{eff}} = \sum_i \left( \mathbf{S_i} \cdot \mathbf{S_{i+1}} + \alpha \mathbf{S_i} \cdot \mathbf{S_{i+2}} - \frac{A_1^2}{2} (\mathbf{S_i} \cdot \mathbf{S_{i+1}})^2 \right) - h \sum_i S_i^z \tag{I.1}$$

Lorsque $A_1 < \sqrt{4\alpha - 1}$, la configuration de plus basse énergie est une spirale coplanaire. Sous un champ magnétique, avant d'atteindre l'état saturé, cette spirale passe par une succession de configurations avec deux spins sur trois au dessus du plan de la spirale et un en dessous : "$Y$", la configuration colinéaire "Up-Up-Down" ($UUD$) et l'état plié (voir Figure I.1). L'état $UUD$ est une condition nécessaire pour avoir un plateau à $1/3$ de l'aimantation de saturation.
Nous avons étudié ce système analytiquement et numériquement au moyen d'algorithmes Monte Carlo classiques (Métropolis). Cette étude est détaillée dans le chapitre III. En l'absence de couplage avec le réseau, lorsqu'on applique un champ magnétique, la chaîne de spins classiques frustrée présente des plateaux dans sa courbe d'aimantation à un tiers de l'aimantation de saturation, pour une gamme de valeurs du rapport $J_2/J_1$.
Nous avons montré que pour une plage de valeurs du couplage spins-réseau, les plateaux d'aimantation sont stabilisés (voir Figure I.2, à gauche). En étudiant l'énergie, nous avons également déterminé la nature de la configuration de plus basse énergie dans le plateau ($UUD$), en champ faible ("$Y$") et en champ fort (état plié avec le spin sous le plan remontant jusqu'à l'état saturé).
De plus on avons établi un diagramme de phase, en fonction du rapport des couplages ma-

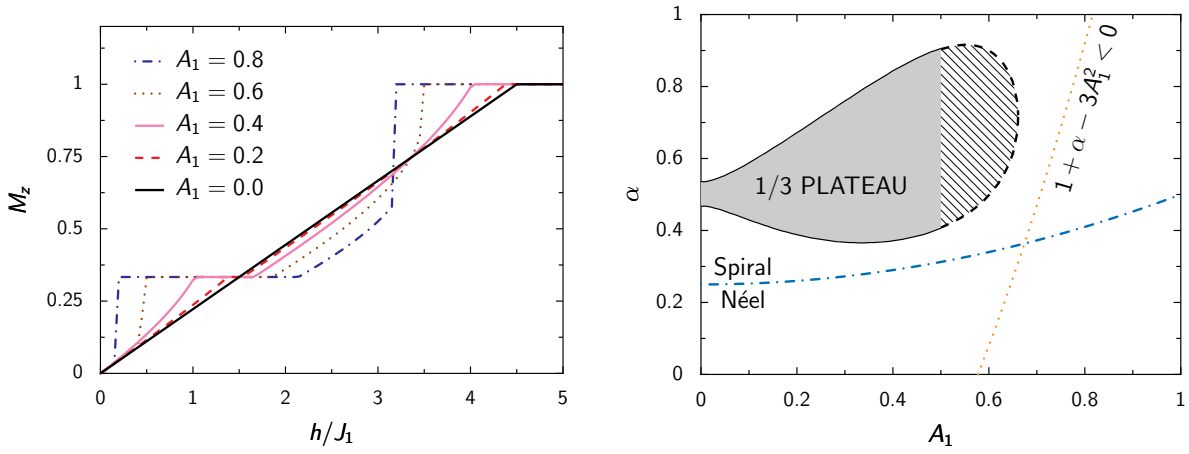


FIG. I.2: *À gauche : Plateau à* 1/3 *de l'aimantation de saturation dans la chaîne de spins classiques* $J_1 - J_2$ *pour différentes valeurs du couplage spins-réseau* ($\alpha = J_2/J_1 = 0.5$). *À droite : Diagramme de phase qualitatif en fonction de* $\alpha$ *et du couplage spins-réseau* $A_1$. *Le plateau* 1/3 *existe dans la région en gris. Dans la région hachurée, notre approche n'est plus valable.*

gnétiques $\alpha$ et du couplage spins-réseau $A_1$, montrant la zone d'existence de ces plateaux (voir Figure I.2, à droite). Par ailleurs, nous avons déterminé la nature de la transition de phase pour arriver à l'aimantation de saturation. En fonction des valeurs des différents couplages, elle peut être du premier ou du second ordre.

## 2.5 Étude de l'aimantation du réseau de Shastry-Sutherland classique

Une deuxième partie de cette thèse est consacrée à l'étude de spins classiques sur un réseau bidimensionnel, le réseau de Shastry-Sutherland [6, 7]. Il s'agit d'un réseau carré avec des couplages antiferromagnétiques $J'$ et des couplages diagonaux additionnels $J$ dans un carré sur deux (Figure I.3, à gauche). Nous avons montré que, à température non-nulle, le réseau de Shastry-Sutherland avec des spins classiques de Heisenberg présente des pseudo-plateaux à un tiers de l'aimantation de saturation.

Il est connu depuis quelques années que, dans certains plans atomiques du composé chimique $SrCu_2(BO_3)_2$, les atomes de cuivres sont placés selon un réseau topologiquement équivalent au réseau de Shastry-Sutherland (Figure I.3, à droite). Ce composé de spin $S = 1/2$ présente un diagramme de phase très riche, comme par exemple des phases à plateaux à différentes valeurs rationnelles de l'aimantation de saturation, et il a déjà fait l'objet de nombreux travaux, autant théoriques qu'expérimentaux [14].
Récemment, de nombreux travaux expérimentaux ont rapportés que des composés de la famille des tétraborides de terre rares $RB_4$ (où R représente l'atome de terre rare) présentent des plateaux dans leurs courbes d'aimantation. Dans ces composés, les atomes de terres rares sont placés selon un réseau topologiquement équivalent au réseau de Shastry-Sutherland. Une caractéristique importante de ces composés est également leurs grands moments angulaires to-

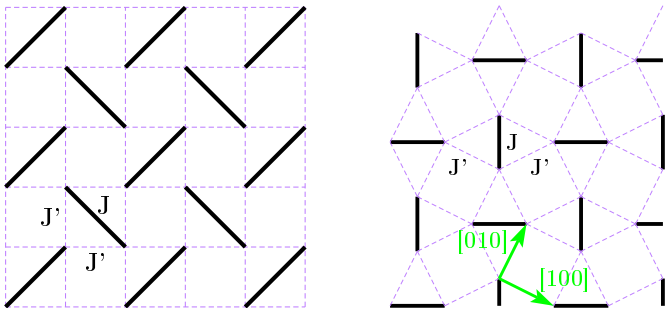


FIG. I.3: *Le réseau de Shastry-Sutherland (gauche) et le réseau topologiquement équivalent réalisé dans les plan* (001) *de* $SrCu_2(BO_3)_2$ *et des tétraborides de terres rares* $RB_4$. $J'$ *sont les couplages selon les côtés des carrés et* $J$ *les couplages des dimères orthogonaux.*

taux qui justifient une modélisation par un modèle de spins *classiques* [15–22].

### 2.5.1 Réseau de Shastry-Sutherland classique sous champ magnétique

Le Hamiltonien du réseau de Shastry-Sutherland avec des spins de Heisenberg classiques est donné par :

$$\mathscr{H} = \frac{J'}{J} \sum_{\text{côtés}}^{N} \mathbf{S_i} \cdot \mathbf{S_j} + \sum_{\text{diagonales}}^{N} \mathbf{S_i} \cdot \mathbf{S_j} - \frac{h}{J} \sum_{i}^{N} S_i^z . \tag{I.2}$$

Ce Hamiltonien peut être réécrit simplement comme une somme sur des triangles dans le cas particulier $J'/J = 1/2$. Les détails sont donnés dans le chapitre III. En minimisant l'énergie sur un triangle, on obtient que le champ magnétique à appliquer pour être à aimantation 1/3 est $h_{1/3} = 3J'$.
À température nulle et à aimantation 1/3, les configurations "parapluie" et $UUD$ (voir Figure I.1) ont la même énergie. La courbe d'aimantation ne présente aucune inflexion.
Cependant en présence de fluctuations thermiques nous avons montré que le réseau de Shastry-Sutherland avec des spins classiques de Heisenberg, présente le même type de comportement que le réseau triangulaire [23, 24] et les fluctuations thermiques vont favoriser l'état $UUD$ et donc permettre l'apparition d'un pseudo-plateau.

### 2.5.2 Fluctuations thermiques et pseudo-plateaux d'aimantation

Nous avons effectué un calcul d'ondes de spins classiques à partir de la configuration $UUD$. Le réseau de Shastry-Sutherland avec des spins classiques ne présente pas de branches de modes mous. Cependant, il est possible de trouver des lignes dans l'espace de Fourier pour lesquelles les fluctuations harmoniques ne coûtent pas d'énergie.
Cette sélection entropique permet à la configuration $UUD$ d'être favorisée par rapport à la configuration parapluie, ce qui permet ainsi l'apparition d'un plateau dans la courbe d'aimantation.
Nous avons effectué des simulations Monte Carlo (Métropolis) afin d'obtenir les courbes d'aimantation, de susceptibilité et de chaleur spécifique pour des systèmes dont la taille est

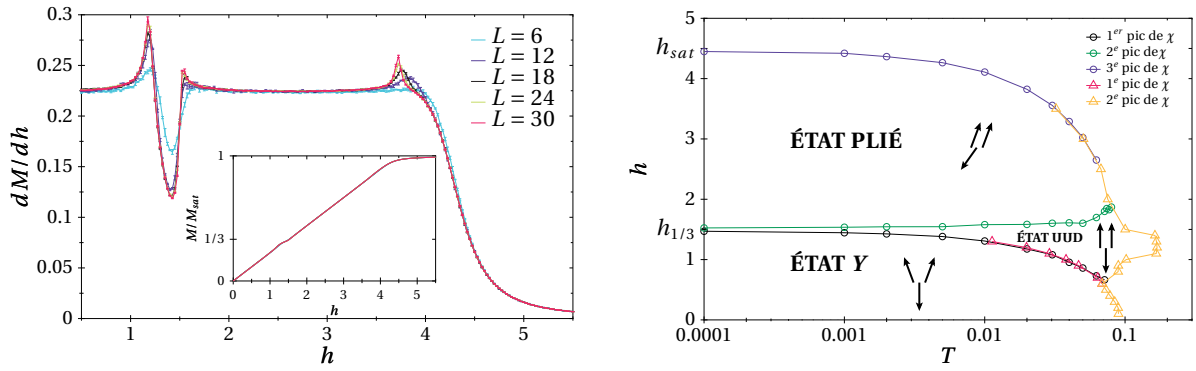


FIG. I.4: *Rapport de couplage $J'/J = 1/2$. À gauche : Susceptibilité en fonction du champ magnétique appliqué et courbe d'aimantation (cadre) à $T = 0.02$. À droite : Diagramme de phase (simulations sur des systèmes de taille $L = 12$). Les triangles correspondent aux balayages en température et les carrés aux balayages en champ magnétique.*

commensurable à la maille unitaire à 12 spins de la configuration $UUD$. La courbe d'aimantation présente un pseudo-plateau dont la taille augmente avec la taille du système (Figure I.4, à gauche). La susceptibilité et la chaleur spécifique présentent des pics indiquant des transitions de phases.
Nous avons effectué des balayages en champ magnétique et en température et utilisé ces pics afin de tracer un diagramme de phase qualitatif dans l'espace champ magnétique appliqué en fonction de la température (Figure I.4, à droite). Ce diagramme de phase est similaire à celui des réseaux triangulaire [24] et Kagomé [25] avec des spins de Heisenberg classiques. On obtient trois phases dans lesquelles la symétrie du réseau est brisée. Dans la région en bas champ, on obtient la configuration "$Y$", puis la configuration $UUD$ au-dessous et jusqu'à aimantation $1/3$ et finalement l'état plié entre l'aimantation $1/3$ et la saturation. Dans le chapitre III nous argumentons que la configuration $UUD$ est la seule à présenter un l'ordre à longue portée, car, de part sa colinéarité elle ne brise pas la symétrie $U(1)$. Dans les configurations "$Y$" et l'état plié, l'ordre à longue portée n'est possible que sous un seul sous-réseau.

Nous avons également effectué des simulations numériques en Monte Carlo qui ont montrées que pour d'autres valeurs du rapport de couplages magnétiques ces plateaux survivent (Figure I.5, à gauche). Le calcul des ondes de spins classiques indique que dans les gammes de températures accessibles par une approximation harmonique en déviation des positions des spins, la configuration qui minimise l'énergie n'est plus $UUD$. En effet, pour un rapport de couplages $J'/J \neq 1/2$, l'état fondamental classique n'est plus une spirale commensurée. Sous l'application d'un champ magnétique, cette spirale incommensurée remonte en configuration parapluie, qui est maintenue même pour une température non-nulle. En revanche il existe une gamme de température qui restaure la commensurabilité en position *moyenne* des spins. Dans cette gamme de température, on retrouve donc les même phases que pour le rapport $J'/J = 1/2$ : "$Y$" puis $UUD$ puis l'état plié (Figure I.5, droite). La présence d'une phase $UUD$ se traduit par des pseudo-plateaux à $1/3$ de l'aimantation de saturation.

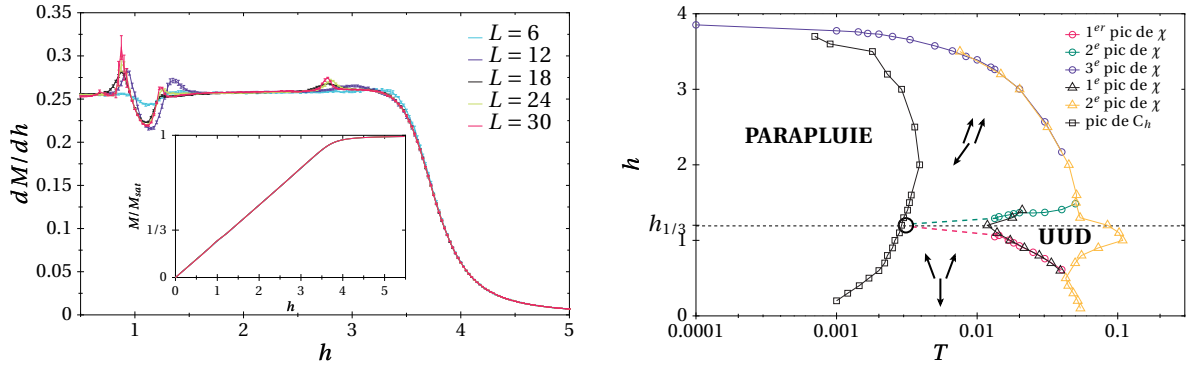


FIG. I.5: *Rapport de couplage $J'/J = 1/2 \pm \epsilon$, ici $J'/J = 0.4$. À gauche : Susceptibilité en fonction du champ magnétique appliqué et courbe d'aimantation (cadre) à $T = 0.02$. À droite : Diagramme de phase (simulations sur des systèmes de taille $L = 12$). Les triangles correspondent aux balayages en température et les carrés aux balayages en champ magnétique.*

# 3 Chaîne de Hubbard à quart-remplissage en présence de distorsions du réseau

La seconde partie de cette thèse est consacrée à l'étude d'une chaîne de fermions (de spin $S = 1/2$) couplée à des déformations du réseau [8]. On étudie un Hamiltonien de Hubbard quart-rempli que l'on couple à des phonons adiabatiques de Holstein (sur sites) et de Peierls.

## 3.1 La chaîne de Hubbard

Le Hamiltonien étendu de la chaîne de Hubbard prenant en compte la répulsion sur site $U$ et entre premiers voisins $V$ ($U > 0$ et $V > 0$) est donné par :

$$\mathscr{H} = -t\sum_{j,\sigma}(c^{+}_{\sigma,j+1}c_{\sigma,j} + h.c.) + U\sum_{j} n_{\uparrow,j}n_{\downarrow,j} + V\sum_{i} n_i n_{i+1} + \mu\sum_{\sigma,j} n_{\sigma,j} \tag{I.3}$$

L'intégrale de saut $t$ couple les sites avec leurs premiers voisins et le potentiel chimique $\mu$ permet de fixer le remplissage du système. Ce Hamiltonien est étudié dans la limite basse énergie dans laquelle on linéarise la relation de dispersion au voisinage des points de Fermi. Les champs fermioniques sont écrit comme des sommes d'opérateurs de vertex bosoniques par la méthode de bosonisation [26, 27]. Les degrés de liberté de charge et de spin des fermions sont, en l'absence de champ magnétique, découplés et on obtient un liquide de Luttinger avec des vitesses de Fermi et paramètres de Luttinger différents dans les deux secteurs.
Les produits de quatre opérateurs fermioniques qui apparaissent avec les interactions engendrent des perturbations à la théorie gaussienne qui peuvent ouvrir un gap. Le secteur de spin est représenté par un modèle de sine-Gordon qui peut présenter un gap ou pas, en fonction des valeurs relatives des répulsions $U$ et $V$ [1]. En revanche, le secteur de charge n'a de

[1] Si $V = 0$, le secteur de spin n'a pas de gap.

perturbation pertinente que lorsque le système est demi-rempli ($n = 1$). Nous allons voir que les distorsions du réseau ajoutent des termes dans le Hamiltonien qui ont un effet drastique sur ces résultats.

Nous nous concentrons sur le remplissage un quart ($n = 1/2$). En effet, une très vaste classe de composé chimiques présentant, à très basses températures, des phases exotiques, notamment une phase superconductrice, est décrite par ce modèle. Il s'agit des sels de Bechgaard $(TMTSF)_2X$ et leur analogues sulfurés, les sels de Fabre $(TMTTF)_2X$, où X est le contre-ion [28]. D'un point de vue théorique, ces composés ont déjà fait l'objet de nombreux travaux numériques [29–32] et analytiques par la méthode de g-ologie [33, 34]. On cherche à reproduire analytiquement par la méthode de bosonisation les diagrammes de phases obtenus numériquement par Poilblanc et Riera [29, 30].

## 3.2 Hamiltonien de Hubbard quart-rempli en présence de distorsions du réseau

Deux types de distorsions du réseau sont considérées séparément : des distorsions "sur site", qui se traduisent par une modulation du potentiel chimique du site (phonons de Holstein) et des distorsions des liens inter sites (phonons de Peierls). Dans les deux cas on reste dans la limite adiabatique.
Les phonons sur site de Holstein peuvent être interprétés comme des vibrations du cortège électronique autour de l'ion localisé sur le site. Le Hamiltonien est donné par :

$$\mathscr{H}_{\text{Holstein}} = -t\sum_{j,\sigma}\left(c^{+}_{\sigma,j+1}c_{\sigma,j}+h.c.\right)+\frac{K^H}{2}\sum_j(\delta^H_j)^2+tA^H\sum_{\sigma,j}\delta^H_j n_{\sigma,j}+U\sum_j n_{\uparrow,j}n_{\downarrow,j}+V\sum_j n_j n_{j+1} \tag{I.4}$$

Les phonons de Peierls correspondent à des vibrations des ions (c'est à dire des sites), et entraînent donc une modulation des liens inter sites :

$$\mathscr{H}_{\text{Peierls}} = -t\sum_{j,\sigma}(1-A^P\delta^P_j)\left(c^{+}_{\sigma,j+1}c_{\sigma,j}+h.c.\right)+\frac{K^P}{2}\sum_j(\delta^P_j)^2+U\sum_j n_{\uparrow,j}n_{\downarrow,j}+V\sum_j n_j n_{j+1} \tag{I.5}$$

Comme mentionné plus haut, à remplissage un quart et sans distorsion, le modèle de Hubbard est décrit par un modèle de Luttinger dans le secteur de charge, et par un modèle de sine-Gordon avec ou sans masse en fonction de la valeur de $V$ dans le secteur de spin. Le couplage avec les distorsions du réseau va rendre commensurables de nouveaux termes et en conséquence ouvrir des gaps. D'une part il faut ajouter des termes dans l'expression bosonisée des opérateurs fermioniques afin d'introduire les interactions et d'autre part il faut considérer une déformation générique avec suffisamment d'harmoniques pour que tous les termes *pertinents* du développement précédents survivent.
En ce qui concerne le premier point, nous utilisons les règles de bosonisation qui ont été développées précédemment par Cabra *et al.* [35, 36] à partir du calcul des fonctions de corrélation du modèle de Hubbard effectué par Frahm et Korepin [37, 38] en utilisant l'ansatz de Bethe.

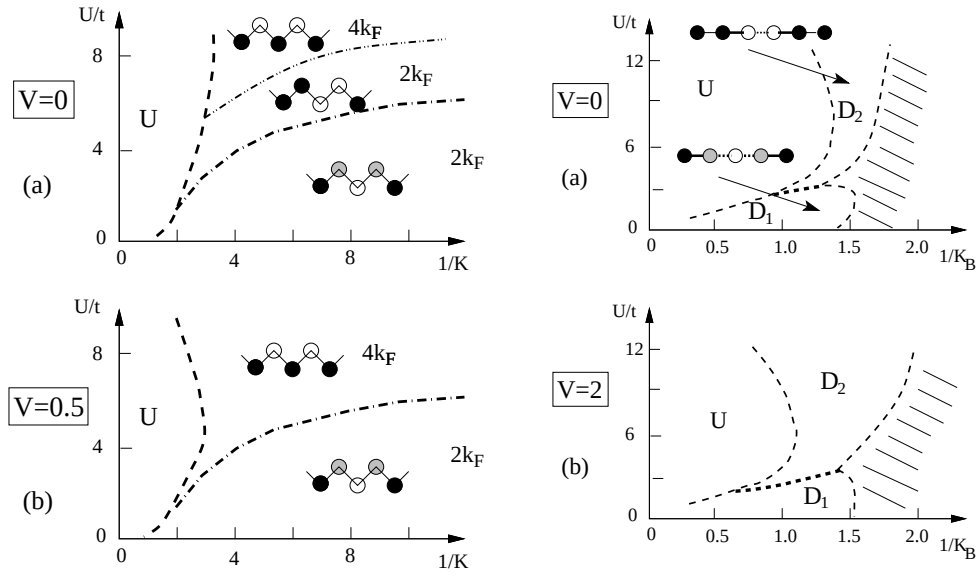


FIG. I.6: *Diagrammes de phase de la chaîne de Hubbard, pour différents types de couplages, en fonction de la répulsion sur site U et de la constante de raideur K. À gauche : Couplage avec des phonons de Holstein. Figure d'après Poilblanc et Riera [29]. À droite : Couplage avec des phonons de Peierls. Les régions hachurées ne sont pas physiques. Figure d'après Poilblanc et Riera [30].*

Ces règles de bosonisation prennent en compte le couplage entre les secteurs 'Up' et 'Down' (et donc spin et charge) due à l'interaction (voir annexe C). Elles donnent un développement des opérateurs fermioniques en somme de produits d'opérateurs de vertex qui couplent les deux secteurs avec des coefficients qui dépendent de l'interaction.
Par ailleurs, on montre qu'afin de garder dans le Hamiltonien bosonisé tous les termes pertinents obtenus à partir de ce développement, la déformation générique du réseau doit avoir deux harmoniques [2].

$$\delta(x) = \delta_2 \cos(2k_F x + \beta_2) + \tilde{\delta}_4 \cos(4k_F x + \beta_4) = \delta_2 \cos(\frac{\pi}{2} x + \beta) + \delta_4 (-1)^x \tag{I.6}$$

Le premier terme correspond à une modulation à $2k_F = \pi/2$ [3] et tend à tétramériser la densité électronique (ce qui induit une déformation du réseau en conséquence). Le deuxième terme est une modulation à $4k_F = \pi$ et crée une dimérisation.
Les détails de la bosonisation du Hamiltonien avec distorsions sont donnés dans le chapitre IV. La présence du couplage fermions-réseau couple les secteurs de charge et de spin et ajoute également une masse au secteur de charge qui n'en avait pas pour le remplissage un quart.

On étudie ensuite l'énergie semi-classique du fondamental du Hamiltonien bosonisé. On établit le diagramme de phase dans l'espace répulsion sur site $U$ en fonction du couplage avec le réseau, pour une répulsion inter-sites $V$ donnée. On étudie d'une part la modulation de la

[2] Il n'est pas utile d'en ajouter d'avantage car elles seraient couplées avec des opérateurs non-pertinents
[3] Au quart-remplissage et sans champ magnétique appliqué, le vecteur de Fermi, défini par $k_F = n\pi/2$, vaut $\pi/4$.

position des sites qui ont été déplacés par des déformations périodiques du réseau et d'autre part la densité électronique qui a également été modulée afin de s'adapter aux nouvelles positions des sites. Cette approche n'est rigoureusement valable que pour des faibles valeurs de la répulsion sur site $U$, mais elle permet néanmoins d'avoir une image qualitative des phases qui apparaissent. On obtient ainsi plusieurs phases caractérisées par des modulations de la positions des sites, ou *ondes de densité de lien*, et par des modulations de la densité de charge, ou *ondes de densité de charge* en complet accord avec les résultats numériques existants (voir Figures I.6).
Pour des phonons de Holstein (Figures I.6, à gauche), on trouve pour $U$ petit une phase présentant une onde de densité de charge tétramérisée et centrée sur les sites du réseau. Lorsque $U$ augmente, on continue à avoir un motif tétramérisé, mais cette fois-ci, l'onde de densité de charge présente une phase qui la délocalise hors des sites du réseau. Dans cette phase les deux harmoniques de la déformation générique Eq. I.6 cohabitent. Enfin, à forte répulsion, la seconde harmonique de la déformation générique ($4k_F$) prend le dessus et on obtient une dimérisation. L'ajout de la répulsion inter-sites $V$ supprime la phase tétramérisée avec maximum de densité délocalisée entre les sites.
Dans le cas de phonons de Peierls (Figures I.6, à droite), on obtient une onde de densité de lien similaire à celle obtenue numériquement. Lorsque la répulsion sur site est faible, une onde de densité de lien tétramérisée avec une phase coexiste avec une onde de densité de charge tétramérisée sans phase. À plus forte répulsion, les deux harmoniques de la déformation générique coexistent.
Dans le chapitre IV, nous détaillons davantage ces phases et effectuons une comparaison avec les résultats numériques.
Pour l'instant notre approche par la bosonisation a permis de reproduire qualitativement les résultats numériques. Nous obtenons un Hamiltonien similaire à celui donné par la g-ologie, qui est une méthode basée sur une décomposition en processus de différents types des excitations du liquide de Luttinger. Pour continuer cette étude, nous allons étudier l'effet de phonons de Holstein et Peierls combinés. L'ajout d'un champ magnétique à ce modèle devrait aussi s'avérer très intéressant.

# 4 Conclusion et perspectives

Dans ce chapitre de résumé, nous avons survolé l'ensemble des travaux présentés dans cette thèse de façon qualitative.
Nous avons tout d'abord passé en revue le travail effectué sur deux systèmes de spins de Heisenberg classiques. En premier, nous avons présenté le travail effectué sur la chaîne de spins classiques frustrée $J_1 - J_2$ en présence de phonons adiabatiques. Ces derniers stabilisent des plateaux à un tiers de l'aimantation de saturation dans une vaste région de l'espace des phases. Nous avons ensuite discuté la présence de pseudo-plateaux à un tiers de l'aimantation dans le réseau de Shastry-Sutherland avec des spins classique à température non-nulle. Au moyen de simulations Monte-Carlo, nous avons obtenu un diagramme des phases similaire à celui des réseaux triangulaire et Kagomé.

Nous avons ensuite abordé le travail effectué sur le Hamiltonien de Hubbard, dans lequel l'effet des distorsions de réseau permet l'apparition de nouvelles phases. Notre méthode retrouve correctement les résultats de la g-ologie et reproduit qualitativement les diagrammes de phases obtenus numériquement.
Le cadre théorique et expérimental, ainsi que les détails techniques des travaux mentionnés ci-dessus, sont présentés dans les chapitres suivants.

# Chapter II

# Theoretical and experimental background

This chapter lays the theoretical foundations for the work on low-dimensional strongly correlated systems coupled with lattice distortions that we present in the next chapters.
In a first part, we introduce the models that are used to describe strongly correlated systems. This will lead to the Hubbard Hamiltonian and some of its limits such as the Heisenberg Hamiltonian. We then address electronic liquids and discuss the effects of correlations as a function of the dimension of the system. On the one hand, we review the Fermi liquid model that describes two and three-dimensional systems and on the other hand, we present the Luttinger liquid for one-dimensional systems. Indeed, in one-dimension, the effects of correlation are extremely enhanced and all excitations become collective, which cannot be described by a Fermi liquid. We then justify the theoretical study of low-dimensional strongly correlated systems by presenting experimental results. We briefly present superconductors with high critical temperature and systems that can be treated as one-dimensional systems such as particular organic compounds and nanotubes. We introduce the concept of frustration that we widely use in the study of classical spin systems. We review the two possible origins of frustration that can be either the geometry of the lattice or competing interactions. Finally, the last section introduces the Monte Carlo algorithms. We focus on the Metropolis algorithm which is widely used for the study of classical spin systems.
All the notations are summarized in Appendix A.

## 1 Strongly correlated systems

This section introduces the Hubbard model and some of its limits that are the starting point of the work presented in the next chapters. We briefly review how this model arises from the description of interacting electrons in solids.

### 1.1 Models of strongly correlated systems

This section reviews how condensed matter is represented and how interactions are taken into account. We will start with uncorrelated electrons on a lattice, add the coulombian interaction

and finally obtain the one-band Hubbard model that will be widely discussed in Chapter IV. We briefly present what are the hypotheses that are stated in this model.

### 1.1.1 Uncorrelated electronic systems

We first start with the case in which correlations are switched off. We consider $N_e$ electrons in a $N$ sites periodic lattice of volume $V = L_x \cdot L_y \cdot L_z$ that represents the crystal structure of matter. The Schrödinger equation in a periodic potential $\mathcal{V}_{ion}(\mathbf{r})$, taking into account a chemical potential $\mu$, is given by:

$$\Big[ -\frac{\hbar^2}{2m}\nabla^2 + \mathcal{V}_{ion}(\mathbf{r}) - \mu \Big] \varphi_{\alpha,\mathbf{k}}(\mathbf{r}) = E_\alpha(\mathbf{k})\varphi_{\alpha,\mathbf{k}}(\mathbf{r}) \tag{II.1}$$

The solutions are the Bloch functions $\varphi_{\alpha,\mathbf{k}}$, where $\alpha$ stands for the energy band index and $\mathbf{k}$ is a wave vector belonging to the first Brillouin zone ($\mathcal{FBZ}$). The Fermi surface is defined by $E_\alpha(\mathbf{k}) = E_F$, where $E_F$ is the Fermi energy. A Bloch function is the product of the plane wave function describing a free electron times a function $u_{\alpha,\mathbf{k}}(\mathbf{r})$ that has the translational symmetry of the lattice [39–41]. The Bloch function reads:

$$\varphi_{\alpha,\mathbf{k}}(\mathbf{r}) = u_{\alpha,\mathbf{k}}(\mathbf{r}) \cdot e^{i\mathbf{k}\cdot\mathbf{r}} \tag{II.2}$$

Taking into account all the energy bands, the electron field operator with spin $\sigma$ can be expanded as a sum of Bloch functions multiplied by creation $c^+_{\alpha,\mathbf{k},\sigma}$ (or annihilation $c_{\alpha,\mathbf{k},\sigma}$) operators:

$$\psi^+_\sigma(\mathbf{r}) = \sum_{\alpha,\mathbf{k}} \varphi^*_{\alpha,\mathbf{k}}(\mathbf{r}) c^+_{\alpha,\mathbf{k},\sigma} \tag{II.3}$$

We can rewrite the Hamiltonian from Eq. II.1 in terms of creation and annihilation as:

$$\mathcal{H}_{\text{kinetic}} = \sum_{\alpha,\mathbf{k},\sigma} \big(E_\alpha(\mathbf{k}) - \mu\big) c^+_{\alpha,\mathbf{k},\sigma} c_{\alpha,\mathbf{k},\sigma} \tag{II.4}$$

This term corresponds to a kinetic energy term. The chemical potential fixes the filling of the system. In systems were electrons are highly mobile, such as metals, the Hamiltonian Eq. II.4 captures quite well the physics [1].

We will not continue with nearly free electron systems. On the contrary, we are interested in *strongly correlated systems* in which the interaction has the same order of magnitude with the kinetic term.

### 1.1.2 Correlated electronic systems

In this section we introduce correlated electronic systems in the framework of the *tight binding* approximation for the lattice of atoms. It is assumed that the wave functions solution of the Schrödinger equation Eq. II.1 can be described by the restricted Hilbert space spanned by

[1] Note that considering free electrons is equivalent with setting $u_{\alpha,\mathbf{k}}(\mathbf{r}) = 1\ ,\ \forall \mathbf{r}$ in Eq. II.2

atomic-like orbitals centred at each lattice site.

Let us add to the hopping kinetic Hamiltonian Eq. II.4 the coulombian interaction:

$$\mathscr{H}_{Coulomb} = \int d\mathbf{r} d\mathbf{r}' \psi^+_\sigma(\mathbf{r}) \psi^+_{\sigma'}(\mathbf{r}') \frac{e^2}{|\mathbf{r}-\mathbf{r}'|} \psi_{\sigma'}(\mathbf{r}') \psi_\sigma(\mathbf{r}) \tag{II.5}$$

The main problem lies in the fact that it is a long-range interaction and the Hamiltonian can no longer be treated as a sum of independent terms. Simplifications are possible without losing the most interesting properties of those systems. Describing those methods is beyond the scope of the chapter and more details can be found for example in Ref. [41].

The residual interaction $\mathscr{V}$ is obtained by a dynamical process called *screening* that is related to the mobility of the charge carriers (electrons) in the lattice. Starting now and in the Hubbard model, we consider electrons interacting through this screened interaction. One can rewrite Eq. II.5 as:

$$\mathscr{H}_{\mathscr{V}} = \int d\mathbf{r} d\mathbf{r}' \psi^+_\sigma(\mathbf{r}) \psi^+_{\sigma'}(\mathbf{r}') \mathscr{V}(\mathbf{r},\mathbf{r}') \psi_{\sigma'}(\mathbf{r}') \psi_\sigma(\mathbf{r}) \tag{II.6}$$

In the tight-binding approximation, the overlap between two nearest-neighbor lattice sites is very weak and instead of working with the Bloch functions that are widely spread in real space, one defines a new set of functions, the Wannier functions, that are localized around the lattice sites $j$ ($j = 1 \dots N$). They are defined in terms of the Bloch functions as [2]:

$$\varphi_{\mathbf{r}_j,\alpha}(\mathbf{r}) = \frac{1}{\sqrt{N}} \sum_{\mathbf{k} \in \mathscr{F}\mathscr{B}\mathscr{Z}} e^{-i\mathbf{k}\cdot\mathbf{r}_j} \varphi_{\mathbf{k},\alpha}(\mathbf{r}) \tag{II.7}$$

The electron field operator is given, in terms of the Wannier operators, by:

$$\psi^+_\sigma(\mathbf{r}) = \sum_{\alpha,j} \varphi^*_{\mathbf{r}_j,\alpha}(\mathbf{r}) c^+_{\alpha,j,\sigma} \tag{II.8}$$

We also make another assumption that consists in considering that only one band $\alpha$ contributes to the conduction. This approximation would not apply to systems such as $f-$orbitals where more sophisticated Hamiltonians are needed such as the Anderson [42] or the Kondo Hamiltonians.

From now, we stay in this approximation and the model obtained is called the *single-band Hubbard model*. Moreover we focus on the *one-dimensional Hubbard model* (i.e. each site has only two nearest-neighbors).
Under these approximations, we will no longer use the indices $\alpha$. Let us rewrite the full Hamiltonian (both kinetic and interaction terms) as a function of creation and annihilation Wannier

[2] For the sake of clear notation, we write $\varphi_\alpha(\mathbf{r}-\mathbf{r}_j) \equiv \varphi_{\mathbf{r}_j,\alpha}(\mathbf{r})$

operators:

$$\mathcal{H}_{Wannier} = -\sum t_{ij}\left(c^{+}_{i\sigma}c_{j\sigma} + h.c.\right) + \sum U_{ijkl}c^{+}_{i\sigma}c^{+}_{j\sigma'}c_{k\sigma'}c_{l\sigma} \quad \text{(II.9)}$$

$$t_{\alpha ij} = \frac{1}{N}\sum_{\mathbf{k}\in\mathcal{FBZ}} e^{-i(\mathbf{r}_j-\mathbf{r}_i)\cdot\mathbf{k}}E_\alpha(\mathbf{k}) \quad \text{(II.10)}$$

$$U_{ijkl} \approx \int d\mathbf{r}d\mathbf{r}'\varphi^{*}_{\mathbf{r}_i}(\mathbf{r})\varphi^{*}_{\mathbf{r}_j}(\mathbf{r}')\mathcal{V}(\mathbf{r},\mathbf{r}')\varphi_{\mathbf{r}_k}(\mathbf{r}')\varphi_{\mathbf{r}_l}(\mathbf{r}) \quad \text{(II.11)}$$

$t_{ij}$ are called *hopping* matrix elements and $U_{ijkl}$ are the interactions parameters. The screened potential interaction $\mathcal{V}(\mathbf{r},\mathbf{r}')$ is a short-range interaction and decreases rapidly as the separating distance $|\mathbf{r}-\mathbf{r}'|$ increases. Therefore it is reasonable to consider that the one-site repulsion $U_{iiii} \equiv U$ will be the strongest and the second largest, if taken into account, will take place between nearest-neighbors sites.

## 1.2 The Hubbard model

Let us study more carefully the one-band Hubbard model [43–45]. It is based on the Hamiltonian defined by Eq. II.9 in the tight-binding approximation. We consider that electrons can only hop from one site to its nearest neighbors. Therefore the hopping integral $t_{ij}$ (Eq. II.10) becomes: $t_{ij} = t$ if the sites $i$ and $j$ are nearest neighbors, otherwise $t_{ij} = 0$.
More details on the Hubbard Hamiltonian can be found in Ref. [41, 46] and in particular, Ref. [47] gives a state of the art description of the one-dimensional Hubbard model.

Using the second quantization language, the one-dimensional, one-band Hubbard Hamiltonian is given by:

$$\mathcal{H}_{\text{Hubbard}} = -t\sum_{j,\sigma}(c^{+}_{j,\sigma}c_{j+1,\sigma} + h.c.) + U\sum_{j} n_{j,\uparrow}n_{j,\downarrow} + \mu\sum_{j,\sigma} n_{j,\sigma} \quad \text{(II.12)}$$

We introduced the density operators:

$$n_{j,\sigma} = c^{+}_{j,\sigma}c_{j,\sigma} \quad \text{(II.13)}$$

The first term is a kinetic term that corresponds to the hopping of particles located on sites $j$ ($j = 1\ldots N$) and with spins $\sigma$. We will only consider electrons; hence $S = 1/2$ and $\sigma$ takes the values $\sigma = \uparrow, \downarrow$. The second term describes the on-site repulsion. In this thesis, we focus on the *repulsive* Hubbard model ($U > 0$). Finally, the last term gives the filling of the system $n$ which is adjusted by the chemical potential $\mu$. Let $N_e$ be the number of electrons, the filling is defined by $n = N_e/N$ ($0 \le n \le 2$). In Chapter IV we will discuss the particular case of half-filling ($n = 1$) and then study quarter-filled systems ($n = 1/2$) coupled with lattice distortions.

So far, the analytical methods to solve the Hubbard model in two and three dimensions are all approximate. On the other hand, the one-dimensional case was completely solved by Lieb and Wu [48] using an extension of the Bethe ansatz technique [49] to fermions. Integrable systems in one dimension are often solved by the Bethe ansatz technique. For example, this is also the

case of the $XXZ$ spin chain.
Moreover there exists ground states theorems for the Hubbard model and some of its limits that give information on the total magnetization in particular situations such as bipartite lattices or attractive models (for a summary see for example Ref. [41, 47]).

### 1.2.1 Symmetries of the Hubbard model

Apart of the translation invariance, the Hubbard model has various symmetries:

- The charge sector is invariant under a $U(1)$ transformation. This corresponds to applying an arbitrary phase $\theta$:

$$\tilde{c}_{j,\sigma} = e^{i\theta} c_{j,\sigma} \tag{II.14}$$

  The $U(1)$ symmetry is actually the expression of the charge conservation.

- The spin sector has a $SU(2)$ invariance that indicates that the Hubbard model should not change under a rotation of the spin quantization axis.

- In case of a bipartite lattice, the sign of the hopping can be changed and there is a particle-hole symmetry. Let us call $A$ and $B$ the two sublattices. The transformation:

$$\begin{aligned} c_{\sigma,i} &\rightarrow +c_{\sigma,i} \text{ if } i \in A \\ c_{\sigma,i} &\rightarrow -c_{\sigma,i} \text{ if } i \in B \end{aligned} \tag{II.15}$$

  does not affect the potential term, but changes the sign of the kinetic term:

$$t c^+_{\sigma,i} c_{\sigma,j} \rightarrow -t c^+_{\sigma,i} c_{\sigma,j} \ , \ i \in A \ , \ j \in B \tag{II.16}$$

  This transformation leaves the spectrum unchanged.

### 1.2.2 Particular limits of the Hubbard model

Let us review a couple of models that arise as particular limits of the Hubbard model:

- In the limit of strong repulsion ($U/t \gg 1$), doubly occupied sites are disfavored and sites will contain a hole, a $\uparrow$ or a $\downarrow$ spin [3]. The Pauli principle prevents an electron to hop on one of its neighboring sites unless the electron on the neighboring site has the opposite spin value. Therefore strong repulsion tends to order the system antiferromagnetically and we obtain a system in which electrons can still hop while the repulsion becomes an effective spin-spin antiferromagnetic interaction $J$. This is the $t-J$ model:

$$\mathscr{H}_{\text{t-J}} = t \sum_{\sigma,j} (c^+_j c_{j+1} + h.c.) + J \sum_j \hat{s}_j \hat{s}_{j+1} \tag{II.17}$$

$$J = \frac{4t^2}{U} \tag{II.18}$$

[3] The attractive Hubbard model would lead to the opposite: $U < 0$ favors local singlets $S = 0$ which are either empty or doubly occupied sites.

where the spin operator on site $j$ is:

$$\hat{s}_j = \frac{\hbar}{2}\sum_{ss'} c^+_{s,j}\sigma_{ss'}c_{s',j} \tag{II.19}$$

$$\sigma_1 = \begin{pmatrix} 0 & 1 \\ 1 & 0 \end{pmatrix}, \sigma_2 = \begin{pmatrix} 0 & -i \\ i & 0 \end{pmatrix}, \sigma_3 = \begin{pmatrix} 1 & 0 \\ 0 & -1 \end{pmatrix} \tag{II.20}$$

where $\sigma_i$ are the Pauli matrices.

- The $t-J$ model has a particular behavior at half-filling. Due to the strong repulsion, the system has exactly one electron per site. The model is reduced to a pure spin model known as the *Heisenberg model*:

$$\mathscr{H}_{\text{Heisenberg}} = J\sum_j \hat{s}_j\hat{s}_{j+1} = J\sum_j\left(\frac{1}{2}(\hat{s}^+_j\hat{s}^-_{j+1} + \hat{s}^-_j\hat{s}^+_{j+1}) + \hat{s}^z_j\hat{s}^z_{j+1}\right) \tag{II.21}$$

  At half-filling the system undergoes a transition from a conducting state to the *Mott insulator state*. The charge degree of freedom is frozen and a gap opens at the Fermi level while the spin degree of freedom remains gapless. We will recover this behavior in Chapter IV with the bosonization technique. We will use the Heisenberg model in Chapter III and study classical spin systems in one and two dimensions.

- For some systems, such as organic conductors, one also has to take into account repulsion with nearest-neighbors sites $V$ ($V > 0$). We obtain the so-called *extended Hubbard Hamiltonian*:

$$\mathscr{H}_{\text{extended}} = \mathscr{H}_{\text{Hubbard}} + \mathscr{H}_{\text{V}} \tag{II.22}$$

$$\mathscr{H}_{\text{V}} = V\sum_j n_j n_{j+1} \tag{II.23}$$

## 1.3 Phonons

One of the main ingredient that will be added in both the Hubbard model and the Heisenberg model in the forthcoming chapters is *adiabatic phonons*. In particular, we will see in Chapter III that phonons can act as a mechanism for the appearance of magnetization plateaux in classical spins systems. In Chapter IV, we show that phonons on a Hubbard chain lead to dimerization and/or tetramerization of the electronic density.
In this section let us do a short summary on phonons and introduce the adiabatic limit.

The phonon Hamiltonian reads:

$$\mathscr{H}_{\text{ph}} = \sum_j [\frac{1}{2m}p_j^2 + \frac{m}{2}w_0^2\delta_j^2] \tag{II.24}$$

$$\delta_j = u(r_{j+1}) - u(r_j)\text{ , Acoustic phonons} \tag{II.25}$$

$$\delta_j = u(r_j)\text{ , Optical phonons} \tag{II.26}$$

Here $u_i$ are the displacements of the magnetic ions from their equilibrium positions.
The dispersion relation of acoustic phonons is gapless. Acoustic phonons are the Goldstone bosons generated by the breaking of the translational symmetry due to the creation of the lattice.

The adiabatic limit consists in considering that the phonon degrees of liberty are frozen. Their pulsations tends towards zero and their masses towards infinity:

$$\{\omega_0 \to 0\ ,\ m \to \infty\} \Rightarrow K \equiv m\omega_0^2 = \text{constant} \tag{II.27}$$

Hence, the elastic energy term Eq. II.25 becomes:

$$\mathscr{H}_{\text{elas}} = \frac{K}{2}\sum_j \delta_i^2 \tag{II.28}$$

The fermion-phonon coupling is given by:

$$\mathscr{H}_{int} = -tA\sum_j \delta_j \left(c^+_{\sigma,i} c_{\sigma,i+1} + h.c.\right) \tag{II.29}$$

Phonons can lead to very interesting phenomena, such as the spin-Peierls transition. Peierls showed in the fifties that the electron-phonon coupling prevents the existence of one-dimensional metal [50]. A half-filled metal is unstable towards a lattice dimerization (Peierls instability). A gap opens and the system undergoes a metal-insulator transition. Similarly, the *spin-Peierls* transition takes place in one-dimensional antiferromagnet: the lattice sites dimerizes and the antiferromagnetic quasi-long-range order is replaced by a gapped singlet state.
A couple of experimental realization of the spin-Peierls transition were identified in organic charge transfer systems and later in the inorganic compound $CuGeO_3$ (see Chapter III). More recently a spin-Peierls transition was found in the TiOX (X = Cl, Br) compounds.

To conclude, in this section we have introduced the models that will be used for the study of low-dimensional strongly correlated systems. In particular, we described the Hubbard model on some of its limits, which will we studied in the next chapter.

# 2 Why are low dimensional systems so exciting?

The effects of interactions in two and three-dimensional systems were explained by Landau's theory on Fermi liquids. These systems have properties very similar with the ones of the gas of free fermions. They can be described in terms of free electrons dressed with density fluctuations. We briefly review this model in a first part.
In one dimension, the Fermi liquid model is no longer accurate. Instead, the system is described by spin and charge collective modes. This electronic state is called a Luttinger liquid.

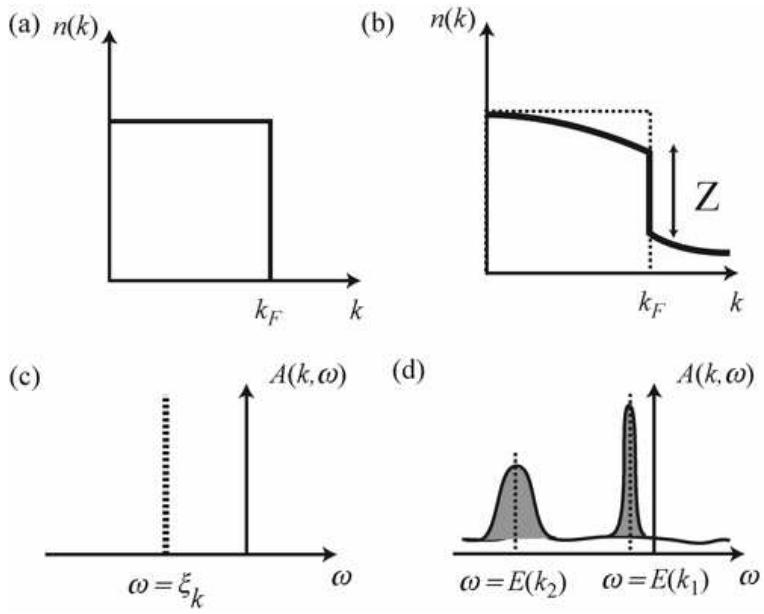


Figure II.1: *Particle distribution as a function of momenta* **k** *(upper panel) and spectral function (lower panel) of a free electron gas (left panel) and of a Fermi liquid (right panel). Figure from Giamarchi [52].*

## 2.1 The Fermi liquid

Before discussing the particular case of one-dimensional systems, let us briefly review the two and three dimensional cases. A detailed presentation of the Fermi liquid can be found in textbooks such as Ref. [3, 51–53].
Landau developed in the late fifties the *Fermi liquid theory* that describes the effects of interactions in two and three-dimensional solids [54–56]. In these systems, the interaction is neither dominant nor negligible compared to the kinetic energy. Thus perturbation theory cannot be used. Landau showed that the macroscopic properties of metals in two and three dimensions are very similar with the ones of a free electrons gas. In this model, the presence of interactions does not lead to drastic changes in the system's properties. Instead of considering electrons, that are still strongly interacting, the Fermi liquid deals with fermionic particles that corresponds to electrons dressed with density fluctuations. This particles are referred to as *quasi-particles* and part of the interaction is absorbed in the definition of their parameters (such as their effective mass $m^*$). A residual interaction still remains between the quasi-particles and it is described by the Landau parameters, which we do not detail here.

In a gas of free electrons at zero temperature, all the states within the Fermi surface (i.e. states with energies $\epsilon(\mathbf{k}) < \epsilon(k_F)$ [4]) are occupied while all the states outside it are unoccupied. The distribution $n(\mathbf{k})$ of free fermions with momenta $\mathbf{k}$ obeys a Fermi-Dirac statistics: at zero temperature it presents a discontinuity at the Fermi level $\mathbf{k} = k_F$ with $n(\mathbf{k}) = 1$ if $\mathbf{k} < k_F$ and $n(\mathbf{k}) = 0$

[4] We use Giamarchi's notation: $\epsilon(\mathbf{k})$ stand for the energy of a free particle, $\xi(\mathbf{k})$ is the energy relative to the chemical potential $\mu$ and interacting particles have energy $E(\mathbf{k})$.

otherwise (see left upper panel in Fig. II.1). An elementary low-energy excitation can create (resp. annihilate) a particle with a well-defined momentum **k** in a state just above (resp. below) the Fermi level. Such excitations are called particle (resp. hole) excitations. They are eigenstates of the Hamiltonian and their lifetime is infinite.
The spectral function is related to the Green function as:

$$A(\mathbf{k},\omega) = -\frac{1}{\pi}\mathrm{Im}G_0(\mathbf{k},\omega) \tag{II.30}$$

For free fermions the Green function is given by:

$$ImG_0(\mathbf{k},\omega) = \mathrm{Im}\frac{1}{\omega-\xi_k+i\eta} = -\pi\delta(\omega-\xi_k)\ ,\ \xi_K = \epsilon(\mathbf{k})-\mu \tag{II.31}$$

where $\mu$ is the chemical potential. Hence the spectral function for the free fermions is a Dirac distribution (see left lower panel in Fig. II.1) which indicates that free electrons have well-defined frequency-momentum relation $\omega = \xi(\mathbf{k})$.

In the interacting case, we can absorb a part of the interaction in the definition of the quasi-particles. They are treated like free elementary particles that interact through a residual interaction described by the Landau parameters.
The distribution still has a discontinuity at the Fermi surface. However, the amplitude of this discontinuity is no longer 1 but a number $Z$. The discontinuity becomes smaller as the interaction increases (see right upper panel in Fig. II.1). The excitations, in a Fermi liquid, are electrons dressed by density fluctuations. Since excitations will have wave-vectors close to $k_F$, one can linearize the dispersion and the energy of a quasi-particle is:

$$E(\mathbf{k}) \approx E(k_F) + \frac{k_F}{m^*}(\mathbf{k}-k_F) \tag{II.32}$$

The spectral functions for the quasi particles still exhibits peaks but no longer correspond to a Dirac distribution (see Fig. II.1). Instead, they obey a Lorentzian distribution centered on $\omega = E(\mathbf{k})$ and with a width $1/\tau$, where $\tau$ is the lifetime of the quasi particles. These peaks become sharper for particles whose momenta are closer to the Fermi level. The total weight in these quasi particles corresponds to the amplitude of the discontinuity $Z$ in the particle distribution.

The Green function for an interacting fermion is:

$$G(\mathbf{k},\omega) = \frac{1}{\epsilon(\mathbf{k})-\omega-\Sigma(\mathbf{k},\omega)} \tag{II.33}$$

where $\Sigma(\mathbf{k},\omega)$ is the self-energy containing the many-body effects. The existence of quasi-particles involves that the self-energy is smooth enough so as to be expanded in the vicinity of the Fermi surface. The Green function is then rewritten close to the Fermi surface, which allows to compute the exact value of $Z$. Giving qualitative details on the Fermi liquid is beyond the scope of this section and more details can be found, for example, in Ref. [57].

Let us go back to the systems we are interested in, fermions in $1+1$ dimension. Electrons in a one-dimensional motion will have to "push" their neighbors and hence any excitation becomes a collective one. The concept of quasi particle no longer applies and the Fermi liquid theory breaks. One-dimensional systems are described by a new electronic state: the *Luttinger liquid*.

## 2.2 The Luttinger liquid

In one dimension, since only collective excitations exist, the single fermionic excitations "break" into two collective excitations, carrying two different degrees of freedom: the charge and the spin. These excitations can have different velocities. The Luttinger was introduced by Tomonaga [58] and Luttinger [59] to describe the behavior of one-dimensional systems. The main idea of the Luttinger model is to linearize the dispersion relation in the vicinity of the Fermi points $\pm k_F$. This approximation is correct as long as the momenta considered stay within a cut-off. We will not give more details on the Luttinger liquid since it will be derived with the bosonization technique in Chapter IV and App. C.
For more detail on the Luttinger liquid one can refer to Ref. [3, 52, 57].

# 3 Experimental context

In this section we briefly present the major experimental motivations for the study of strongly correlated low dimensional systems.
The main field of application is understanding the high critical temperature superconductivity. Compounds of the cuprates family were found to exhibit a superconducting phase with critical temperature half way between zero and room temperature. Even though many theories were proposed to explain the complex pairing mechanisms leading to this behavior they still remain not fully understood. The possible technological applications for superconductivity at high temperature add supplementary motivation for understanding these systems.
In a second part we focus on quasi-one-dimensional organic conductors such as the Bechgaard salts. Those compounds have a very rich phase diagram that includes superconducting phases. The existence of Luttinger liquid phases justifies a description through a one-dimensional Hubbard model.
Finally the last part reviews other, more recent, experimental realizations of one dimensional systems such as nanowires and nanotubes.

## 3.1 High $T_c$ superconductivity

Bednorz and Müller reported in 1986 [1] superconductivity at about 30 K in the BaLaCuO ceramic copper oxides. This discovery marked the start of intensive research of new compounds with even higher critical temperature $T_c$. For example, the mercury based compounds HgBaCaCuO were found to have $T_c \sim 133$ K [60]. For a review on the high-$T_c$ superconductors, one can refer to Ref. [2].
High $T_c$ superconductors generally crystallize in the tetragonal system (see Fig. II.2, upper panel) and have in their structure at least one copper oxide ($CuO_2$) plane which make them

belong to the cuprate compounds family. In fact it was observed that the critical temperature increases with the number of $CuO_2$ layers. Those planes are separated by layers of atoms such as La, Ba and Hg (for example, see the upper panel of Fig. II.2).

Most works in the field of High-$T_c$ superconductors agree that superconductivity is related with processes such as pairing occurring in the $CuO_2$ layers. The planes of other atoms play the role of carrier reservoirs. However the strong anisotropy of the structure, as well as the presence of phonons and defects complicate the interpretation of the experimental results.

At very low temperature, these materials have the common feature to present antiferromagnetic order in the undoped regime (i.e. when the carriers from the layers of other atoms are not in the $CuO_2$ planes). They remain Mott insulators until a critical value of the hole/electron doping (see Fig. II.2, lower panel). The value of the doping that removes the long-range spin order depends on the cuprate considered. A "pseudo-gapped" phase exists between the antiferromagnetic and the superconducting phases. The dome-shaped superconducting phase shows that the highest critical temperature is obtained for a precise optimal value of the doping.

Particular behaviors of the cuprates suggest that the Fermi-liquid model is not accurate to describe those compounds. In particular, a non-Fermi liquid phase can appear at higher temperature above the superconducting phase. As for the pairing in the $CuO_2$ layers, the Bardeen-Cooper-Shieffer (BCS) pairing model is believed not to work in the cuprates [42, 61]. In the BCS theory the order parameter of the $s$ orbitals has an isotropic gap which is not in agreement with the superconducting gap of the cuprates. Shen *et al.* [62] measured a large gap anisotropy in the $a-b$ planes of $Bi_2Sr_2CaCu_2O_{8+\delta}$ and established that the order parameter should be $\Delta(\mathbf{k}) \sim \cos k_x a - \cos k_y a$ which is consistent with the order parameter of the $d_{x^2-y^2}$ orbitals of the copper atoms.

Various theories have been proposed to describe the cuprates, such as one and three band Hubbard models. Due to the very strong bonds in the $CuO_2$ planes, a first approximation consists in studying a two-dimensional Hubbard Hamiltonian on a square lattice in order to describe the electrons moving in the $CuO_2$ planes. The coupling with the other atom planes can eventually be added later.

A three-band Hubbard model with one $p$ band for the oxygen and two $d_{x^2-y^2}$ bands for the copper atoms was considered (see Ref. [2] and references therein). Using a hole notation, it takes into account the hybridization between the nearest-neighbor copper and oxygen atoms, a direct hopping between oxygen atoms, and three types of repulsions between the holes belonging to the same $d$ or $p$ band and between the adjacent copper and oxygen holes. In this model the first hole added by the doping energetically prefers the $d$ copper orbital while supplementary holes will prefer the oxygen orbitals (as long as the repulsion between holes of the same $d$ orbitals is strong enough).

Zhang and Rice [63] showed that from this three-band model it is possible to extract an effective simpler model through a one-band Hubbard model in the $t-J$ limit. Let us consider one copper ion surrounded by four oxygens (see pyramid in Fig. II.2). The hole of the oxygen can combine with the copper hole and create spin singlet or triplet states. Zhang and Rice used a perturbative approach to show that the spin singlet has lower energy and assumed that it is possible to work in this singlet subspace without losing the main features of the system. In their

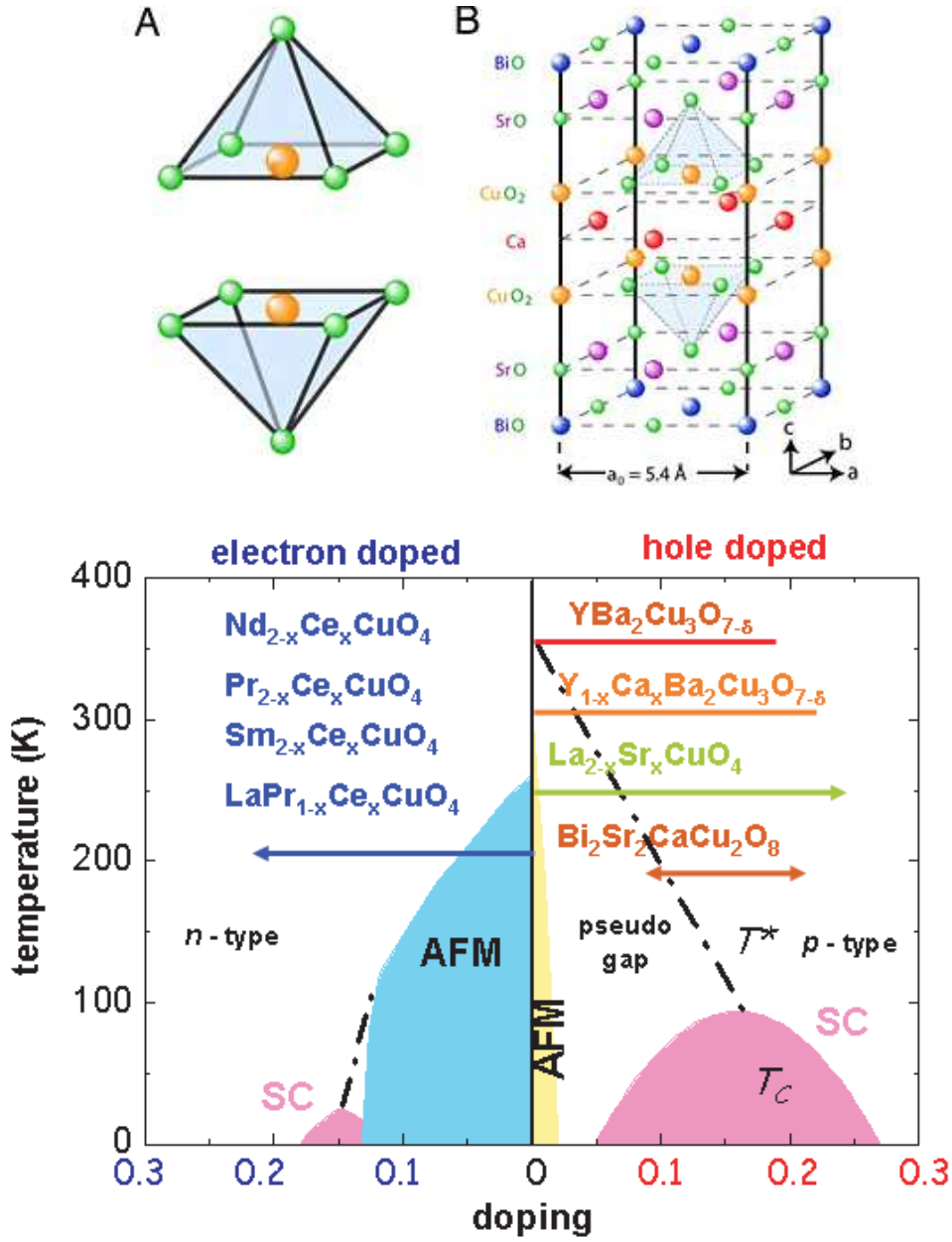


Figure II.2: *Upper panel: Left: Example of crystal structure of a cuprate. It consists of layers of copper oxide interleaved with layers of other atoms. Right: The oxygen atoms form a pyramid with a copper atom at the center of the base. Figure from Cornell Chronicle Online (http://www.news.cornell.edu/stories/May08/Davis.distances.ws.html). Lower panel: Schematic phase diagram of the cuprates as a function of electrons and hole dopings. In the low doping region antiferromagnetic order (AFM) is obtained. Both kinds of doping can lead to superconducting states (SC). Figure from the Research Unit FOR538, Doping Dependence of Phase Transitions and Ordering Phenomena in Copper-Oxygen Superconductors (http://www.wmi.badw-muenchen.de).*

model the hole of the oxygen is replaced by a spin singlet on the copper which is equivalent with removing one copper spin from a square lattice of copper spins. Hence they converted the three band model into a simpler spins and holes model.

On top of its fundamental interest, the discovery of compounds with superconducting temperature above liquid nitrogen temperature opened high-$T_c$ superconductor thin films technological applications. For example high-$T_c$ cuprates were used in superconducting quantum interference device (SQUID) magnometers and Josephson integrated circuits [64].

To conclude this part, it is widely believed that understanding the underlying mechanisms of superconductivity in high-$T_c$ cuprates should open a path toward even higher critical temperatures. Hence a tremendous experimental and theoretical effort was made in this field of investigation, and even though it has led to considerable progress much remains to be done. In particular, the pairing mechanism is still not understood, as well as the impurity scattering and some features of the phase diagram.

## 3.2 One dimensional organic systems

In this section, we introduce chemical compounds for which a one-dimensional Hubbard model is justified due to the strong anisotropy of magnetic couplings.
The first organic compounds to exhibit superconductivity are the Bechgaard salts [65]. Besides of a superconducting phase, their phase diagram presents many interesting phases such as non-Fermi liquid or spin-Peierls states [3, 28].
The Bechgaard salts are a series of organic salts $(TMTSF)_2X$ where X is the counter ion that insure the electronic neutrality and TMTSF a flat molecule that donates electrons easily. Bechgaard salts are isostructural with the sulfur series[5] $(TMTTF)_2X$, also called Fabre salts. Both $(TMTSF)_2X$ and $(TMTTF)_2X$ crystallize as stacks of TM molecules (TM = TMTSF or TMTTF) separated by the counter ions X. Fig. II.3, left panel shows the crystal structure of those compounds. Example of X are symmetric molecules such as $PF_6$ or $AsF_6$ or asymmetric such as $ClO_4$, $ReO_4$ and $NO_3$.
The TM molecules have double bonds between the carbon atoms and the $\pi$ orbital of the selenium/sulfur atoms. As one can see in Fig. II.3, there is only one ion for two TM molecule and the chain is quarter-filled. We will come back on that particular filling in Chapter IV and study in particular the influence of lattice distortions on such systems.

The stacking direction suggests that these compounds may be well described through a one or at least quasi-one-dimensional model. Moreover a high mobility of the electrons along the stacking direction is made possible thanks to the overlap of the $\pi$ orbitals of the selenium/sulfur atoms. However one has to compare the hopping integrals along the stacking direction with the one in the perpendicular directions. Roughly, the values of the integrals along the stacking directions are $t_{stack} \approx 1000$ K, while the ones along the axis pointing towards neighboring

[5] TMTSF stands for tetramethyltetraselenafulvalene and TMTTF stands for tretramethylthiafulvalene. The latter contains sulfur atoms instead of selenium.

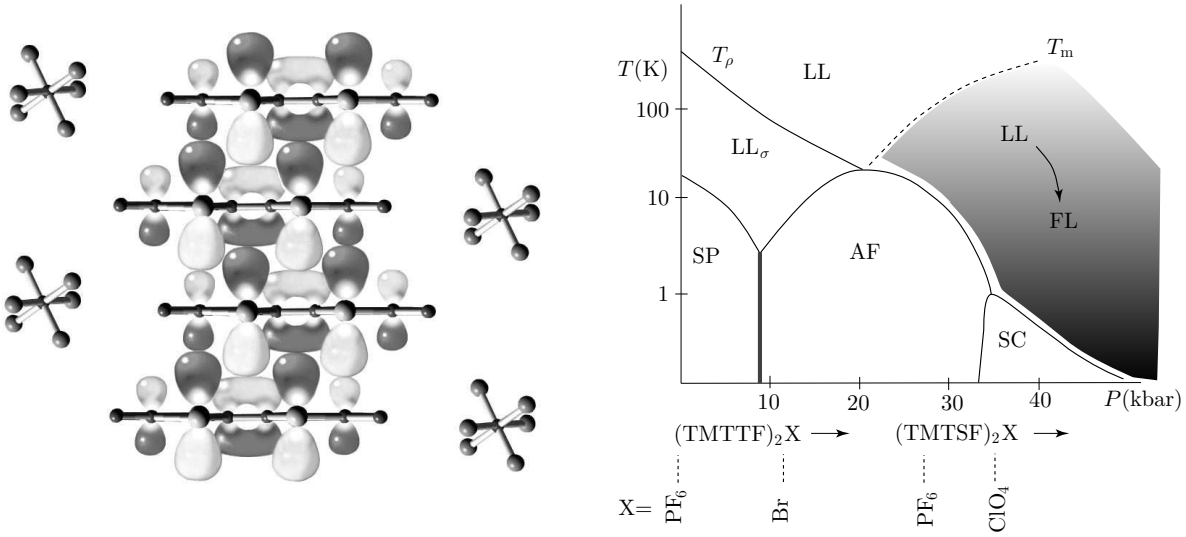


Figure II.3: *Left panel: Structure of the Bechgaard salt $(TMTSF)_2X$ and their sulfur analog, the Fabre salts $(TMTTF)_2X$. A stack of flat TM organic molecules with their orbitals is represented between the smaller counter ions. In this figure the stack axis is the $z-$axis. Right panel: Schematic phase diagram for the TM compounds as a function of temperature and pressure ($\sim 1/U$). Increasing the pressure is equivalent with going from the TMTTF to the TMTSF family and changing the counter ion X (see detail of the phases in the text). Figures from Bourbonnais and Jérôme [28].*

stacks are $t_{stack-stack} \approx 100$ K and finally the ones along the axis pointing towards the counter ions are $t_{ions} \approx 30$ K [3]. Therefore one can describe these materials as one-dimensional chains with hopping $t_{stack}$ eventually coupled by small inter chain couplings $t_{stack-stack}$.

It is quite easy to vary experimentally the parameters that govern the properties of the $(TM)_2X$ by changing the nature of the counter ion X, applying a magnetic field or varying the pressure. The nature of TM molecule (TMTSF or TMTTF) and of the counter ion X changes the hopping $t_{ions}$ which leads to a very rich phase diagram. A schematic phase diagram as a function of pressure or ion substitution and temperature for both $(TMTSF)_2X$ and $(TMTTF)_2X$ families is shown in Fig. II.3, left panel.
One notes that in the phase diagram the pressure and chemical changes (see $x-$axis in Fig. II.3) have similar effects. At low pressure, some compounds of the sulfur series can develop spin-Peierls (SP) or commensurate-localized antiferromagnetic long-range order (AF) while either itinerant antiferromagnetism or superconductivity (SC) are found in the selenide series. At very low temperature these systems exhibit various ordered phases as the pressure varies: spin-Peierls (SP), antiferromagnetic (AF), spin-density-wave and superconducting (SC).
At intermediate temperature the sulfur compounds $(TMTTF)_2X$ can be described as a Luttinger liquid (LL) that becomes gapped in the charge sector ($LL_\sigma$) below $T_\rho$. Under pressure, the properties of the sulfur family evolve toward those of the selenides (Bechgaard salts) which exhibit, at intermediate temperature, a progressive restoration of a Fermi liquid (FL, represented

in dark in the phase diagram).
At ambient pressure some of the $(TM)_2X$ compounds, such as the $(TMTTF)_2PF_6$, present an insulating behavior. As the pressure increases it undergoes a transition to a metallic phase and the properties of this $(TMTTF)_2X$ compound evolves towards those of Bechgaard salts family which are good conductors [66].

The scenario for the appearance of the superconducting phase in these systems has not been studied as much as for the two-dimensional high-$T_c$ discussed in the previous section. The superconducting transition was found to be more sensitive to impurities than it would be expected in a regular superconductor. Various scenarios are proposed such as a spin-triplet pairing with the possibility of reentrant superconductivity at very high magnetic fields applied along the axis pointing towards neighboring stacks. At the optimum pressure value, the critical temperature is $T_c \sim 1$ K. Even if theoretical predictions [67] support the existence of an "exotic" pairing via the inter chain exchange, experimental evidences are still missing.

## 3.3 Nanowires and nanotubes

Advances in technology over the past few decades, such as molecular beam epitaxy, made it possible to create and study experimentally low-dimensional systems in which electrons are strongly confined in one or two dimensions. Nanowires and nanotubes are examples of experimental realizations of one-dimensional systems.
Nanowires (see upper panel in Fig. II.4) seem to be the closest experimental realization of an atomic chain. However they are very sensitive to disorder and thus are not the best candidates for studying transport in one dimension.

On the other hand, nanotubes were recently found to be an experimental realization of the Tomonaga-Luttinger liquid. Let us briefly review what a nanotube is.
The first carbon nanotubes were observed by transmission electron microscopy in 1991 [68]. They were multi-walled carbon nanotubes with an outer diameter $\sim 2-20$ nm (see lower panel of Fig. II.4). The first single-walled nanotubes were realized two years after [69, 70] and present a much smaller diameter $\sim 1$ nm. A single-wall nanotube is basically a single layer of graphite (i.e. a graphene sheet) rolled into a tube. Individual carbon nanotubes are predicted to be either semi conducting or conducting, depending on the chirality and diameter of the nanotube. Detailed explanations on how to synthesize nanotubes and how to perform transport measurements on them can be found in Ref. [71].

Since these systems are very "one-dimensional-like", early experiments on one-dimensional semiconductor nanowires were interpreted using the Luttinger-liquid theory [72, 73] without real agreement with theoretical predictions.
Bockrath *et al.* [74] first reported measurements of the conductance of conducting "ropes" made with single-wall carbon nanotubes (see lower panel of Fig. II.4) that agreed with predictions for tunneling into a Luttinger liquid. The Luttinger parameter for single-wall carbon nanotubes was predicted to be smaller than unity [75, 76]. Using previous experimental results,

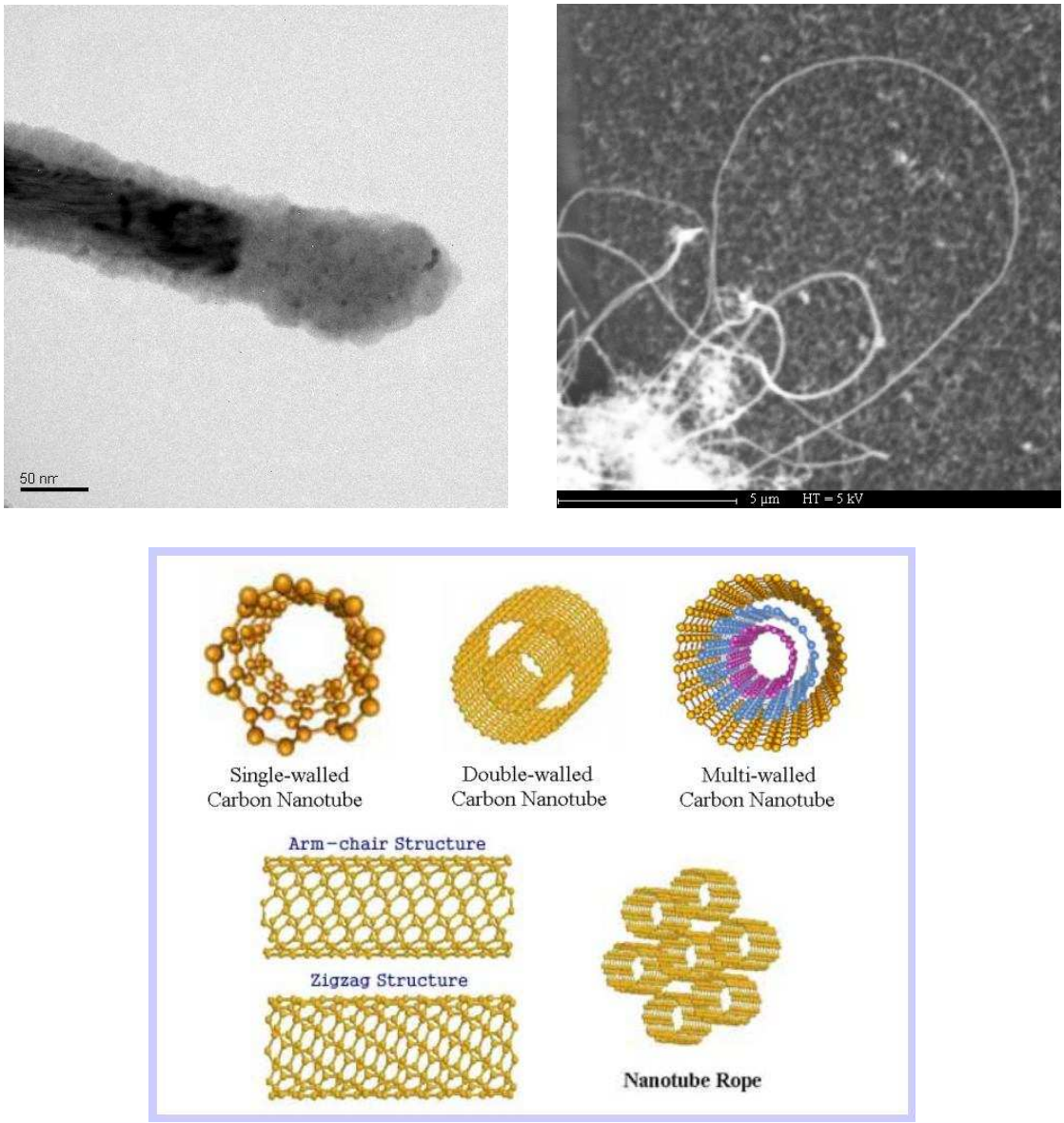


Figure II.4: *Upper panel, left: Transmission Electron Microscopy (TEM) picture of a cobalt nanowire (thickness 80 nm). The dark zone is cobalt, the clear sheath is cobalt oxide. Enlarging* = ×60000. *Picture from MSc lab work on a Philips CM300 TEM. Upper panel, right: Scanning Electron Microscopy (SEM) picture of a "ball" of carbon nanowires. Enlarging* = ×6500. *Picture from MSc lab work. Lower panel: Schematic pictures of carbon nanotube structures, including single-walled, multi-walled and "ropes" nanotubes. Figure from Korea University (http://nanotube.korea.ac.kr).*

the predicted Luttinger parameter for a "rope" should be ~ 0.28 [77, 78]. Bockrath *et al.* measured the conductance $G$ of single-wall carbon nanotubes as a function of temperature and voltage $V$ and compared these results with the theoretical power laws:

$$G(T) \propto T^{\alpha}\ , (Ev \ll k_B T) \tag{II.34}$$

$$dI/dV \propto V^{\alpha}\ , (Ev \gg k_B T) \tag{II.35}$$

The exponent $\alpha$ of these power laws depends on the number of one-dimensional channels in the "rope". The Luttinger parameter can be calculated from the exponent $\alpha$ [75, 76] and the experimental value was found to be in good agreement with the theoretical prediction.

The nature of the electronic liquid in carbon nanotubes still remains a very active field of research. Rauf *et al.* [79] recently reported a transition from a Tomonaga-Luttinger liquid to a Fermi liquid behavior in single-wall carbon nanotubes. They displaced the Fermi level by adding doping. For low dopant concentration, these nanotubes behave as a Tomonaga-Luttinger liquid while they become a Fermi liquid when the concentration is high enough so as to fill the conduction band.

To conclude this section, we have presented a couple of experimental realizations of low-dimensional systems. Due to technological progress in the field of nanotechnologies, the study of low-dimensional is becoming even more relevant. The quasi-one dimensional organic conductors are studied in Chapter IV through a quarter-filled Hubbard model.

# 4 Frustrated systems

Frustrated systems were first investigated at the beginning of the fifties after it was noticed that Ising spins on the triangular lattice exhibit very particular properties [80]. However, the concept of frustration was defined by Villian [81] and Toulouse [82] in the late seventies in the context of spin glasses, which marked the beginning of extensive investigation on frustrated systems.
A spin system is called *frustrated* when it cannot satisfy simultaneously all its interactions between every pair of spins. The resulting configurations minimize the energy of the whole system, but not all the energies of interaction between one spin and its neighbors.
Frustrated systems exhibit very rich behaviors such as a very large ground state degeneracy. Particular interest in those magnetic systems stems from the fact that they were found to present new phases such as Resonating Valence Bonds (RVB) spin liquids [83], super solids [84–87] and spin ices [88–92].
Frustration has two possible origins: it can arise either from competing magnetic interactions, such as in the $J_1 - J_2$ spin chain, or from geometry. Geometric frustration will be illustrated through a couple of example among the family of corner-sharing lattices [93].
The exploration of frustrated systems is a wide and expanding field of condensed matter physics. The purpose of this section is only to gives a brief overview on frustrated systems and we will focus on *classical* spin systems, which are the subject of Chapter III. Reviews on frustrated quantum magnets can be found in Ref. [94–96]. For more details on frustrated systems, one can refer Ref. [9] and Ref. [97, 98] for supplementary experimental details.

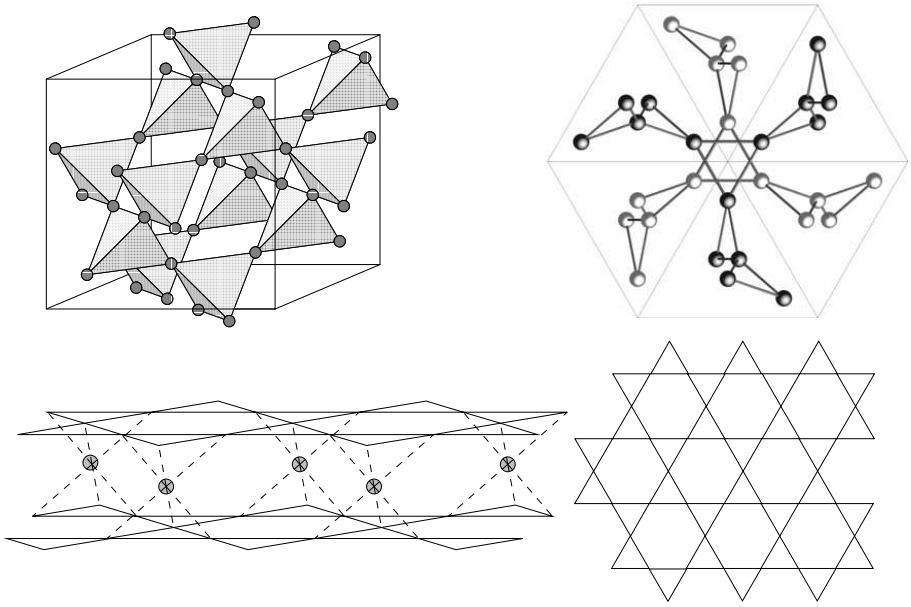

Figure II.5: *Examples of corner-sharing frustrated lattices. Upper panel, left: the pyrochlore lattice which consists in corner-sharing tetrahedra. Upper panel, right: the Gadolinium Gallium Garnet (GGG). Lower panel, right: the Kagomé lattice. Lower panel, left: the SCGO lattice, which consists in layers of Kagomé lattices separated by tetrahedra. Figure from Moessner [93].*

## 4.1 Frustration from competing interactions

Let us first discus the frustration that arises from competing interactions. The first non-collinear spin configurations due to competing interactions were studied by Kaplan [99], Villian [100] and Yoshimori [101] in 1959.

We consider a pair of two nearest-neighbor classical spins (i.e. vectors) interacting through an antiferromagnetic coupling $J_1$. The energy of this pair is minimized if the spins are anti parallel (Néel order). Let us add a next-nearest-neighbor antiferromagnetic interaction $J_2$ [6]. If $J_2$ is "low enough", each nearest-neighbor pair $(\mathbf{S_i}, \mathbf{S_{i+1}})$ still tends to align anti-parallel. However, above a certain value of $J_2$, the pairs of next-nearest-neighbors $(\mathbf{S_i}, \mathbf{S_{i+2}})$ will also try to lie anti-parallel, which is impossible due to the $J_1$ coupling. As a consequence, for a range of values of the ratio $J_1/J_2$, the interplay between the two antiferromagnetic couplings will lead to non-collinear configuration, a spiral state, that does not fully satisfy any of the interactions [7]. In such case the system is *frustrated by the competition* between the $J_1$ and $J_2$ couplings.

We will come back and give more quantitative details on the $J_1 - J_2$ classical spin chain in Chapter III. We will also consider the effects of lattice distortions on this system.

[6] Frustration can also arise if *one*, and only one, of the couplings is ferromagnetic (i.e. $J_i < 0$). Ferromagnetic systems cannot be frustrated by competing interactions.

[7] Of course, the pitch angle of this spiral depends on the ratio $J_1/J_2$ (see Chapter III).

## 4.2 Geometrical frustration

The simplest example to illustrate systems frustrated by the geometry of the lattice is to consider a triangle with antiferromagnetic couplings $J$ on all edges. In order to satisfy independently all interactions, spins should align anti-parallel along each edge, which is not possible. Instead, spins will realize a 120° coplanar configuration in order to minimize the energy of the *whole triangle*.
Let us generalize this to lattices containing elementary plaquettes (triangles, squares ...). Toulouse [82] proposed a criterion on the product of the bonds of a plaquette $\mathscr{P}$:

$$\mathscr{P} = \prod_{\langle i,j \rangle} \text{sign}(J_{ij}) \tag{II.36}$$

If $\mathscr{P} < 0$, the plaquette is geometrically frustrated. For example, if we consider only antiferromagnetic couplings, examples of geometrically frustrated two-dimensional systems are the triangular lattice, the Kagomé lattice (see Fig. II.5), the checkerboard lattice [8], the Shastry-Sutherland lattice. The square lattice, with an even number of antiferromagnetic couplings per plaquette, fails Toulouse's criterion. However, a square plaquette with three ferromagnetic bonds and one antiferromagnetic bond becomes frustrated.
Let us extend this discussion to a whole lattice of $N$ spins. Minimizing the energy on the whole lattice may be problematic, however, in some cases it is possible to rewrite the Hamiltonian as a sum on independent elementary plaquettes (e.g. triangles):

$$\sum_{\text{bonds}} \mathbf{S_i} \cdot \mathbf{S_j} = \frac{J}{2} \sum_{\text{plaquettes}} \mathbf{L}^2 + \text{constant} \tag{II.37}$$

$$\mathbf{L} = \sum_{i=1}^{q} \mathbf{S_i} \tag{II.38}$$

where $\mathbf{L}$ is the total spin of a plaquette. The number of degrees of freedom increases with the number of bonds $q$ in a single plaquette (for example, $q = 3$ if the plaquette is a triangle). The classical ground states satisfy $\mathbf{L} = 0$ in each plaquette. This condition leads to $n = 3$ constrains for Heisenberg spins. The dimension of ground state grows with $q$ and $n$. If we call $F$ the number of degrees of freedom and $K$ the number of constrains, the dimension of the ground state $D$ is [93, 102]:

$$D = F - K = \frac{N\big(n(q-2) - q\big)}{2} \tag{II.39}$$

Hence the ground state of geometrically frustrated systems is highly degenerated and its dimension increases with the number of bonds per plaquette and the number of spin components. Quantum or thermal fluctuations can partially lift this degeneracy, which is called the *Order by Disorder* effect. We will come back on that point in Chapter III, Section 2.
Let us give a couple of example of corner-sharing lattices whose Hamiltonians can be rewritten as a sum on elementary plaquettes (see Chapter III). This is the case of the Kagomé lattice (Fig. II.5) and, for a precise value of the diagonal couplings, of the checkerboard lattice, frustrated

[8] The checkerboard lattice is a square lattice with two diagonal couplings in one square out of two.

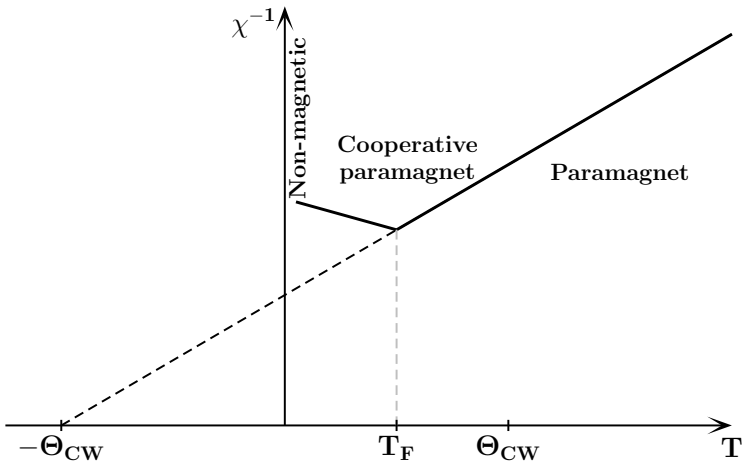


Figure II.6: *Schematic curve of the inverse of the susceptibility $\chi$ as a function of temperature showing the signature of geometrical frustration. $\Theta_{CW}$ is the Curie-Weiss temperature and $T_F$, the temperature of deviation (see text).*

square lattice and Shastry-Sutherland lattice (Chapter III, Section 4).
Example if three-dimensional geometrically frustrated lattices are shown in Fig. II.5. Geometrical frustration does not require antiferromagnetic couplings. Let us briefly discuss the case of the pyrochlore lattice (corner-sharing tetrahedra). Antiferromagnetic couplings do not frustrate the pyrochlore lattice. On the other hand, ferromagnetic couplings, which tend to maximize the total spin per tetrahedra, lead to a highly degenerated classical ground state. In this configuration, each tetrahedron has two spins pointing in and two pointing out. This configuration is called *spin ice*. This name is comes from the fact that this configuration is compared with the arrangement of the protons in the tetrahedra of the solid water structure [103]. Spin ice is the subject of expanding investigation, both theoretical [91, 92] and experimental. It is realized experimentally in $Ho_2Ti_2O_7$ [103] and $Dy_2Ti_2O_7$ [104] and in an increasing number of chemical compounds [105].

Experimentally, strong frustration can be identified from the behavior of the inverse of the susceptibility $\chi^{-1}$. Figure II.6 shows a schematic curve of a strongly frustrated magnet. The usual paramagnetic regime takes place above the Curie-Weiss temperature $\Theta_{CW}$. Between $\Theta_{CW}$ and $T_F$, strongly frustrated systems then present a phase in which correlations are weak (cooperative paramagnet region). A deviation takes place at a temperature $T_F \ll \Theta_{CW}$ indicating a transition to a non-generic state which varies from one compound to another [93, 102]. The ratio $T_F/\Theta_{CW} \ll 1$ is considered as a characteristic of strong frustration.

To conclude, this sections reviews the two types of frustration mechanism, from competing interactions and from the lattice geometry. In Chapter III we will consider first a one-dimensional system frustrated by competing interactions and then the Shastry-Sutherland lattice.

# 5 A short introduction to classical Monte-Carlo algorithms

Monte Carlo algorithms are powerful numerical tools used to study large systems. They can be applied to various systems, such as for example spin systems, and they are especially useful to study those with a large number of coupled degrees of freedom.
The term Monte Carlo encompasses a broad family of algorithms that can treat either classical or quantum systems. We are interested in classical spin systems and we only consider one of these algorithms: the *Metropolis algorithm* [106]. A detailed presentation of the Monte Carlo algorithms can be found for example in the textbooks Ref. [107–109].
The main idea of Monte Carlo is to perform stochastic moves (i.e. non deterministic) to reproduce the statistical distribution of the configurations of the system. However, one does not sample phase space randomly but rather use *importance sampling*. Indeed, these stochastic moves are based on a Markov chain which depends on the use of random numbers [9] that are generated during the simulation. As a consequence, if one runs a couple of simulations on the same system, the values of the physical quantities will not be exactly the same, but they should agree up to a statistical error.
We first discuss how a configuration is constructed from a Markov chain, then we explain how we move from one configuration to the next one, and finally we review how the physical quantities we are interested in are computed.

Let us consider a system that has a finite set of possible states $\{S_i\}$ $(i = 1 \dots N)$. So far we consider a discrete stochastic evolution of the system with time labeled $(t = 1 \dots N)$. At each moment $t$, we call $X_t$ the state of the system. We consider the conditional probabilities so that the system configuration at the time $t = j$, $X_{t=j}$, is the $j^{th}$ state $S_{i=j}$ $(j = 1 \dots N)$:

$$P(X_{t=j} = S_{i=j} | X_{t=j-1} = S_{i=j-1}, \dots, X_{t=1} = S_{i=1}) \tag{II.40}$$

If we were using a true random chain, the probability of occurrence of the $j^{th}$ state would be independent from the occurrence of the previous states:

$$P(X_{t=j} = S_{i=j} | X_{t=j-1} = S_{i=j-1}, \dots, X_{t=1} = S_{i=1}) = \prod_{k=1}^{k=j} P(X_{t=k} = S_{i=k}) \tag{II.41}$$

In Monte Carlo algorithms, the conditional probabilities Eq. II.40 are not independent: they are constructed through a *Markov chain* in which each configuration is generated with a probability that depends *only* on the previous configuration. The probability of occurrence of the $j^{th}$ state then becomes:

$$P(X_{t=j} = S_{i=j} | X_{t=j-1} = S_{i=j-1}, \dots, X_{t=1} = S_{i=1}) = P(X_{t=k} = S_{i=k}) \prod_{k=1}^{k=j} T_{k,k-1} P(X_{t=k-1} = S_{i=k-1}) \tag{II.42}$$

[9] Computer generated random numbers are not completely random. We will mention random numbers keeping in mind that they are actually *pseudo-random* numbers. We discuss later under what conditions we can safely consider them as true random numbers.

where $T_{k,k-1}$ is the transition probability between $X_{t=k} = S_{i=k}$ and $X_{t=k-1} = S_{i=k-1}$ :

$$T_{i,j} \equiv T(S_i \rightarrow S_j) = P(X_{t=n} = S_i | X_{t=n-1} = S_j) \tag{II.43}$$

The transition probabilities $T_{i,j}$ ($i = 1 \ldots N$ and $j = 1 \ldots N$) are positive and normalized:

$$T_{i,j} \leq 0 \tag{II.44}$$

$$\sum T_{i,j} = 1 \tag{II.45}$$

One can see in Eq. II.42 that in a Markov process, having the configuration $S_{j-1}$ at $t = j-1$ determines the probability to have $S_j$ at $t = j$, which is the future of the system. On the other hand, this probability does not depend on the history of the system (i.e. the configurations of the system before $t = j$) and a Markovian system can eventually come back, after a certain amount of time, to a configuration that it has already visited.

The transition probabilities $T_{i,j}$ are chosen so as to generate a Markov chain of system configurations with the Boltzmann distribution. This distribution has to be independent of the position in the chain and of the initial configuration. This conditions are fulfilled if:

- Every configuration among $\{S_i\}$ ($i = 1 \ldots N$) can be reached from every other configuration within a finite number of steps. This is the condition of connectedness.
- The Markov chain is not periodic: the system cannot come back in a given configuration except after a "long time".

If these conditions are fulfilled, the Markov chain becomes *ergodic*.

Let us rewrite the probability to obtain a given state as a function of time:

$$P(X_{t=n} = S_{i=j}) \equiv P(S_j, t) \tag{II.46}$$

We now consider the function $P$ which gives the probability to have the system in the state $S_j$ at the time $t$ [10]. Two processes govern the changes in the function $P$:

- $P(S_j, t)$ decreases if the systems moves from a configuration $S_i$ at time $t$ to $S_j$ at time $t+1$.
- $P(S_j, t)$ increases if the systems moves from a configuration $S_j$ at time $t$ to $S_i$ at time $t+1$.

These mechanisms are described by the *master equation*:

$$\frac{\partial P(S_j, t)}{\partial t} = -\sum_i T_{j,i} P(S_j, t) + \sum_i T_{i,j} P(S_i, t) \tag{II.47}$$

In order to reach the stationary state, one has to let the system *thermalize*. This is achieved by relaxation from an arbitrary configuration.

[10] We now consider a continuous time dependence. In an ergodic chain, the time dependence actually disappears after "a long time".

The Boltzmann distribution will arise from the stationary solutions which contains the Boltzmann weights of the configurations. The stationary solutions are given by:

$$\frac{\partial P(S_j,t)}{\partial t} = 0 \Leftrightarrow \sum_i T_{j,i} P_{eq}(S_j,t) = \sum_i T_{i,j} P_{eq}(S_i,t) \tag{II.48}$$

The particular solution for $T_{j,i}$, in which the terms of both sums and for all pairs of configuration $(S_j, S_i)$ are equal, is called the *detailed balance*:

$$T_{j,i} P_{eq}(S_j) = T_{i,j} P_{eq}(S_i) \tag{II.49}$$

The equilibrium probability is proportional to the Boltzmann distribution:

$$P_{eq}(S_j,t) = \frac{e^{-\beta E(S_j)}}{\mathcal{Z}} \tag{II.50}$$

where $\beta = 1/k_B T$, $\mathcal{Z}$ is the partition function and $E(S_i)$ is the energy associated to the $S_i$ configuration. In practice, one studies the ratio of the probability between two consecutive configurations $S_i$ and $S_j$ [11] in order to get rid of the partition function. Therefore the transition rate between these configurations depends on their energy difference:

$$\Delta E = E_i - E_j \tag{II.51}$$

As long as a transition rate from the state $S_i$ to the state $S_j$ satisfies the detailed balance Eq. II.49, it can be used [12]. However let us focus on Metropolis' choice [106]. At each step (i.e. at each discrete value of $t$), one spin is flipped, if we have Ising spins, or "tilted" if we have Heisenberg spins. For example, in the Monte Carlo codes used to study the Shastry-Sutherland lattice (see Section 4) we consider Heisenberg classical spins, with norms fixed to unity, that are parameterized with the spherical coordinates $\theta$ and $\phi$. These coordinates are updated independently with $\phi \in [0, 2\pi]$ and $\theta$ so that $\cos(\theta) \in [-1; 1]$.

The Metropolis' rate is independent of $\mathcal{Z}$ and satisfies the detailed balance Eq. II.49. It is defined as:

$$\begin{array}{lcll} T_{i,j} & = & \tau_0^{-1} e^{-\Delta E/k_B T} & \text{if} \quad \Delta E > 0 \\ T_{i,j} & = & \tau_0^{-1} & \text{if} \quad \Delta E < 0 \end{array}$$

where $\tau_0$ is the time required to perform the spin movement (spin-flip or other movement). In practice, $\tau = 1$.

We consider a lattice with $N$ sites. Then the Metropolis algorithm consists in performing the following steps:

1. Choose an initial state (for example $S_j$). Then $X_{t=0} = S_{i=j}$.

[11] Configurations that are reached consecutively in time.

[12] This choice depends on the system studied. For example, at high temperatures the Metropolis algorithm becomes non-ergodic, and instead one can use the Glauber dynamics [110].

2. Choose a site $k$, $k = 1 \dots N$ and perform a change on it (flipping or tilting).
3. Compute the energy change $\Delta E$ which results if the spin at site $k$ is flipped or tilted.
4. Generate a random number $r$ uniformly within $[0;1]$.
5. If $r < e^{-\beta \Delta E}$, flip (or tilt) the spin. The resulting configuration is kept so as to compute the physical quantities, such as magnetization or specific heat, *averaged* by a number $N_c$ of collects that is fixed as an input.
6. Go to the next site and restart from step 3, until the right number of accepted configurations is achieved.

Let us come back to the problem of random numbers. The number of tries to do so that every site of the system as been considered once is called a Monte Carlo step. Its value increases with the system size, and also, the lower the temperature is, the higher it is. It also depends on the value of $\Delta E$ and we come back on this point later. The fact that computers are actually using pseudo-random numbers will not be a problem as long as the periodicity of the random number generator is large enough, compared with the Monte Carlo step. One also has to make sure that random numbers are not correlated.

One can force the algorithm to accept more tries by taking into account, in the computation of $\Delta E$, a "local field" $\mathbf{h_i}$ that is generated by the spins surrounding the site $i$ that is considered:

$$\mathbf{h_i} = \sum_j J_{i,j} \mathbf{S_j} \tag{II.52}$$

$$E = \sum_{i,j} J_{i,j} \mathbf{S_i} \cdot \mathbf{S_j} = \sum_i \mathbf{h_i} \cdot \mathbf{S_i} \tag{II.53}$$

Then when we move to the next site $i'$ (step 3 in the algorithm), we simply have to compute:

$$\Delta E = \mathbf{h_i} \cdot (\mathbf{S_i}' - \mathbf{S_i}) \tag{II.54}$$

By keeping track of $\mathbf{h_i}$, the energy difference is computed much faster than a difference of total energies.

Let us now discuss what are the physical quantities we extract from the Monte Carlo simulations. In order to simplify the notation, let us define $\mathbf{x} = \{\mathbf{S_i}\}$. The thermal average of an observable $A(\mathbf{x})$ is defined as:

$$\langle A(\mathbf{x}) \rangle_T = \frac{1}{\mathcal{Z}} \int d\mathbf{x} e^{-\beta \mathcal{H}(\mathbf{x})} A(\mathbf{x}) \tag{II.55}$$

$$\mathcal{Z} = \int d\mathbf{x} e^{-\beta \mathcal{H}(\mathbf{x})} \tag{II.56}$$

In our case, it is estimated as:

$$\langle A(\mathbf{x}) \rangle_T = \frac{1}{N_c} \sum_{i=1}^{N_c} A(\mathbf{x}) \tag{II.57}$$

$$P(\mathbf{x}) \propto e^{-\beta \mathcal{H}(\mathbf{x})} \tag{II.58}$$

where $N_c$ is the number of collects (number of measurements).

For a $N$ spin system, the energy and the normalized magnetization are:

$$E = \frac{\langle \mathscr{H} \rangle_T}{N} \tag{II.59}$$

$$M_n = \frac{\langle \sum_i^N \mathbf{S_i} \rangle_T}{N} \tag{II.60}$$

In the above equations, the data are thermally averaged and spatially averaged by dividing by the number of spins $N$. We are interested in the magnetization (that is measured along the $z-$axis), the susceptibility and the specific heat. These physical quantities are then averaged by the number of collects $N_c$:

$$\text{Collect average magnetization:} \qquad M = \frac{M_n}{N_c} \tag{II.61}$$

$$\text{Susceptibility:} \qquad \chi = N\beta\Big[\frac{M_n^2}{N_c} - \big(\frac{M_n}{N_c}\big)^2\Big] \tag{II.62}$$

$$\text{Specific heat:} \qquad C_h = N\beta^2\Big[\frac{E^2}{N_c} - \big(\frac{E}{N_c}\big)^2\Big] \tag{II.63}$$

Finally, these physical values are collected for a couple of simulations ($\sim 5$ simulations) , which should tally up to some statistical errors. We compute their standard deviation $\sigma$ so as to add errors bars in the curves (see Chapter III):

$$\sigma = \sqrt{< X^2 > - < X >^2}\,, \ (X = M, \chi, C_h) \tag{II.64}$$

To conclude, in this section we briefly laid the foundations of the Metropolis algorithm that is used next for the study of classical spin systems. Results of Monte Carlo simulations are presented in Chapter III, for both the study of the frustrated $J_1 - J_2$ spin chain with lattice distortions (Sec. 3) and the Shastry-Sutherland lattice (Sec. 4).

# 6 Background: summary and outlook

For many years, the main experimental motivation for the study of low-dimensional systems was the existence of superconducting phases with high critical temperature in compounds whose anisotropic magnetic couplings allow a description trough one or two-dimensional models. The most famous are the cuprate family which are widely studied through various Hubbard models and organic compounds such as the Bechgaard salts which can be described by Hubbard chains or ladders. More recently, an experimental realization of the Luttinger model was found in carbon nanotubes. This opens a broader field of new applications for the study on one-dimensional systems.
In two and three dimensions, correlated systems can be described by the Fermi liquid model in which interaction can be included in the definition of quasi particles. In one dimension, the effect of interaction is extremely enhanced and all excitations become collective. This phenomenon is described by the Luttinger model.

In this chapter, we reviewed how correlated systems can be described and in particular we introduced the Hubbard and the Heisenberg models.
In the next chapter we are going to focus on the Heisenberg model with classical spins. We will study frustrated systems, first with frustration due to competing interactions and then with geometric frustration. Lattice distortions will be introduced as an ingredient capable of stabilizing magnetization plateaux in a frustrated lattice.
The Hubbard model will be used in the last chapter. We will see that the coupling with lattice distortions can lead to charge-density-waves.

# Chapter III

# Classical spins systems

This chapter reviews the work done on one and two-dimensional *classical* spin systems.
We first explain what is a classical configuration in a magnetization plateau in classical spin systems. Then we discuss the effect of non zero temperature on frustrated classical spin systems. Frustrated systems have the particularity to present large degeneracy in their ground states. Thermal fluctuations can lift, or at least partially, this degeneracy by selecting a state or a submanifold of states. This effect is known as *Order by Disorder* and we will illustrate it in the Kagomé lattice.
A third part is dedicated to the study of a frustrated $J_1 - J_2$ classical Heisenberg spins chain under an external magnetic field and in presence of lattice distortions. The classical $J_1 - J_2$ chain exhibits plateaux at 1/3 of the saturation magnetization $M_{sat}$. We show that in presence of adiabatic phonons those plateaux become broader and survive for a wider range of magnetic couplings ratios. We obtain a phase diagram as a function of the magnetic couplings ratios and spin-lattice coupling.
Finally the last section reviews the work done on the two-dimensional Shastry-Sutherland lattice with classical Heisenberg spins. Under a magnetic field this system exhibits magnetization pseudo-plateaux at $M/M_{sat} = 1/3$ at finite temperature. We show that thermal fluctuations select a collinear spin configuration and hence allow the appearance of a magnetization pseudo-plateau. We present a phase diagram as a function of temperature, magnetic field and and also discuss what happens for different magnetic coupling ratios.

## 1 Magnetization plateaux in classical spin systems

In the following work, we focus on Heisenberg spins (i.e. spins with three components). The quantum spin operators that were defined in Section 1.2.2 obey:

$$[\hat{s}^j, \hat{s}^k] = i\hbar\epsilon^{jkl}\hat{s}^l \text{ , where } \{j,k,l\} = \{x,y,z\} \tag{III.1}$$

$$\hat{s}^2 = S(S+1) \tag{III.2}$$

*Classical* spins correspond to the limit $S \to \infty$. The commutators $\mathcal{O}(S)$ can be neglected if compared with $\mathcal{O}(S^2)$ and hence classical spins commute. They are represented by vectors $\mathbf{S}$ of fixed norm, which is arbitrarily set to 1.

Let us briefly review what we call a magnetization plateau *classical* state and what types of configurations are possible in the plateaux phases of classical spin systems.

For classical spin systems, Misguish and Lhuillier [95] showed under the assumption that the classical energy is a continuous and differentiable function of the spins directions, that the spin configurations in the plateaux *must be collinear* with the magnetic field direction. Let us call $n$ the number of spins in the unit cell and $p$ is an integer. The possible configurations are:

$$U^{n-p}D^{p} \tag{III.3}$$

where $n-p$ is the number of spin 'Up' ($U$) and $p$ of spins 'Down' ($D$). The corresponding magnetization plateaux arise at:

$$\frac{M}{M_{sat}} = 1 - 2\frac{p}{n} \tag{III.4}$$

For example, the spin configuration in plateaux at 1/3 of the saturation magnetization $M_{sat}$ is the collinear "Up-Up-Down" state ($UUD$), in which two out of three spins are pointing up along the $z-$axis and the last one is pointing down.

Classical plateau states can sometimes survive in quantum spin systems. Affleck and Hida [111] studied the competition of two possible states in the 1/3 magnetization plateau of a $S = 1/2$ frustrated Heisenberg spin chain using bosonization, renormalization group and numerical diagonalization methods. Depending on the exchange modulation, the $M/M_{sat} = 1/3$ *classical* or *quantum* plateau state is favored.
The classical 1/3 plateau state, which appears in the conventional $S = 1/2$ frustrated Heisenberg chain

$$\mathscr{H}_{\delta} = J\sum_{i}^{L} \hat{s}_i \hat{s}_{i+1} + \delta\, \hat{s}_i \hat{s}_{i+2} \tag{III.5}$$

consists in a 3−fold degenerate $\uparrow\downarrow\uparrow$ structure (i.e. the quantum analog of the classical collinear $UUD$ configuration) accompanied by the spontaneous $Z_3$ translational symmetry breakdown. The quantum case corresponds to $\bullet\!\!-\!\!\bullet\uparrow$ (where $\bullet\!\!-\!\!\bullet$ is a singlet dimer). This state is favored by a period−3 exchange modulation:

$$\mathscr{H}_{\alpha} = J\sum_{i}^{L/3} \Big[ (1-\alpha)(\hat{s}_{3l-1}\hat{s}_{3l} + \hat{s}_{3l}\hat{s}_{3l+1}) + (1+\alpha)\hat{s}_{3l+1}\hat{s}_{3l+2} \Big] \tag{III.6}$$

This state is also the exact ground-state of the translationally invariant *Valence Bond Solid* model with 4−spin and third neighbor interactions:

$$\begin{aligned} \mathscr{H} &\propto \sum_{i}^{L} \hat{T}_i^2(\hat{T}_i^2 - 2) \\ \hat{T}_i &= \hat{s}_i + \hat{s}_{i+1} + \hat{s}_{i+2} + \hat{s}_{i+3}\ , \ \left(\hat{T}^2 = T(T+1)\right) \end{aligned} \tag{III.7}$$

However Affleck and Hida found that the classical 1/3 plateau state $\uparrow\downarrow\uparrow$ can also be the ground state of Hamiltonians Eq. III.6 and Eq. III.7. In particular they showed that two classical configurations ($|\downarrow\uparrow\uparrow\downarrow\uparrow\uparrow\ldots\rangle$ and $|\uparrow\downarrow\uparrow\uparrow\downarrow\uparrow\ldots\rangle$) survive up to a critical value of the period−3 exchange modulation $\alpha > 0$, while the last one ($|\uparrow\uparrow\downarrow\uparrow\uparrow\downarrow\ldots\rangle$) only survives for $\alpha < 0$.
They established the phase diagrams for the existence of the classical state in both cases and also analyzed the nature of the phase transitions.

To conclude, this section reviewed a very important result for the forthcoming discussions: in classical spin systems, the spin configurations in magnetization plateaux are collinear. Quantum systems can also exhibit classical configurations in the plateaux phases. As we will see later, these classical plateaux are the most likely to survive in the classical limit for spins.

# 2 Order by Disorder

One generally expects an ordered state to be destroyed by thermal (or quantum) fluctuations. In this section, let us review the *Order by Disorder* effect which consists precisely in the opposite: order is induced by fluctuations.
The *Order by Disorder* effect was first introduced by Villain *et al.* [112] and Shender [113]. Villain *et al.* considered the "domino model", which has the particularity to be disordered at zero temperature whereas low temperature allows the appearance of long range order. The "domino model" consists in Ising spins lying on a square lattice with frustration induced by ferromagnetic couplings in the $x-$direction and in the $y-$direction in one line over two. The remaining lines in the $y-$direction present antiferromagnetic couplings. This system is paramagnetic at zero temperature. Villain *et al.* showed that at finite temperature the $i^{th}$ antiferromagnetic line have lower excitations if the surrounding $i-1^{th}$ and $i+1^{th}$ ferromagnetic lines have parallel spins (in state of anti-parallel). The ferrimagnetic ordered states have a larger Boltzmann weight and as a consequence ferrimagnetic order is induced by low but finite temperature.

The *Order by Disorder* effect attracted much attention as it was found to explain the selection of particular coplanar ground states of the Kagomé antiferromagnets [11, 114, 115], which will be discussed later. The concept of *Order by Disorder* was later extended to quantum fluctuations. We focus the discussion on classical systems with thermal fluctuations. Thermal or quantum fluctuations can sometimes select a particular long range ordered state within a large manifold of states that have the same classical energy. The case of frustrated systems may therefore be particularly relevant due to the large degeneracy of their ground states (Section 4). The manifold of continuously degenerated states of classical Heisenberg spins systems is referred as the "ground state manifold" [10, 93]. Its topology is particularly interesting because it addresses the question whether the system can wander within the ground state manifold ("connected ground state") or whether it may encounter energy barriers. The answer to that question is known in particular cases, such as the pyrochlore lattice. For this three-dimensional lattice, Moessner and Chalker [116, 117] showed that any ground state can be transformed

into another ground state by a continuous deformation that costs no energy. Is this case the ground-state is connected.
At finite temperature the quantity that is minimized is the free energy. States belonging to the ground state manifold can have lower free energy thanks to thermal fluctuations which increase their entropic weight relatively to other states of the ground state manifold. A deformation that costs no energy is called a *zero mode*. If it cost no energy only in the harmonic approximation (but eventually costs energy at higher orders) it is called a *soft mode*. For convenience we will only refer to soft modes in the following discussion [1]. Hence a ground state with more soft modes accesses a larger region of the parameter space under thermal fluctuations than a state with no or less soft modes. If such a state exists then the system may spend more time fluctuating around it. In the extreme case in which the entropy of a state is higher than the sum of the entropies of the other states, the system can actually spend all its time fluctuating around this state.

In the next two sections let us detail more quantitatively the *Order by Disorder* . The next section presents the classical spin-wave approach and after that the *Order by Disorder* will be illustrated on the Kagomé lattice with classical Heisenberg spins. We briefly review what are the consequences of *Order by Disorder* on the thermodynamic quantities.

## 2.1 The spin-waves approach

The spin-wave theory applies to both quantum and classical systems. The main idea of spin-waves is that, in an ordered phase, the average positions of the spins operators are non-zero in at least one direction. In the spin-wave approach one describes quantum or thermal fluctuations with small deviations of the spins coordinates around their average value.

In the quantum case, the spin-waves approach consists in dealing with quantum effects as time dependent fluctuations around the classical ground-state. In systems with large degeneracy, such as frustrated systems, one can select a particular classical ground state within the ground state manifold and expand the partition function in a saddle point expansion controlled by the spins norm [41, 118]. In the harmonic approximation the spin-waves are non-interacting bosons. The spins operators are rewritten through the Holstein-Primakov transformations including bosonic operators on top of the classical ground state:

$$\mathscr{H} = \mathscr{H}_0 + \frac{S}{2}\left(\mathscr{H}_2 + \mathscr{O}(\frac{1}{\sqrt{S}})\right) \tag{III.8}$$

where $\mathscr{H}_2$ is a quadratic Hamiltonian of magnon creation and annihilation operators. The $\mathscr{O}(\frac{1}{\sqrt{S}})$ part contains higher order terms in these operators.

In the classical case, one starts from a particular classical ground-state and assume that at low-temperature the spin directions vary smoothly from site to site. We can approximate the spin coordinates at "very low temperature" by the two first term of a Taylor expansion on the

[1] What will be said for soft modes is also true for zero modes since zero modes are actually soft modes.

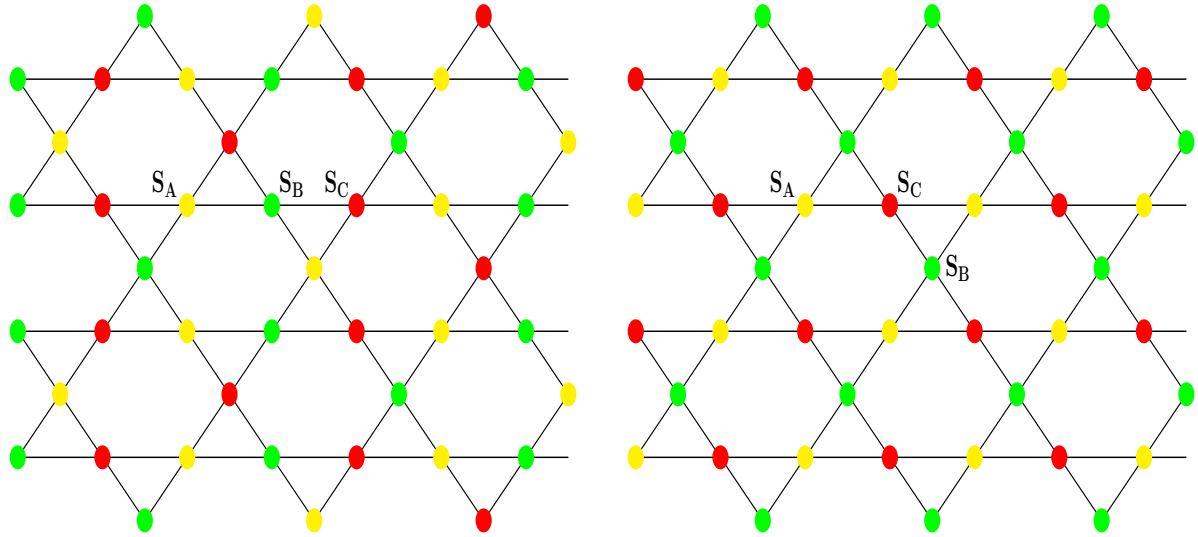


Figure III.1: *Two possible coplanar configurations for the Kagomé lattice with classical Heisenberg spins. The three types of spin orientations* $\mathbf{S_A}$, $\mathbf{S_B}$, *and* $\mathbf{S_C}$ *are represented with different colors. Left panel:* $\sqrt{3}\times\sqrt{3}$ *configuration. Right panel:* $q=0$ *configuration.*

spin deviations.
Let us have a more technical look on how to proceed. For a given spin configuration let us consider that each spin is aligned in one direction in its *own referential* as in Eq. III.9 (let us choose arbitrarily the $z-$axis). Under thermal fluctuations, the spin will deviate from this position by small deviations ($\epsilon^u$, $u=x,y$) and its new coordinates are given by Eq. III.10 and III.11:

$$T=0\text{: }\mathbf{S_i} = (0,0,1)\ ,\ \|\mathbf{S_i}\|=1 \tag{III.9}$$

$$T\neq 0\text{: }\mathbf{S_i} = \left(\epsilon^x,\epsilon^y,1-\alpha_i\right) \tag{III.10}$$

$$\alpha_i = \frac{1}{2}\left((\epsilon^x)^2+(\epsilon^y)^2\right) \tag{III.11}$$

$\alpha_i$ is chosen so as to conserve the norm of the spins up to quadratic order in thermal fluctuations. Of course, one may have to apply rotations on particular sublattices in order to bring all the spins in the same referential before calculating the Hamiltonian. Once this is done, the Hamiltonian is rewritten as an expansion on the spins deviations in a form that reminds Eq. III.8:

$$\mathscr{H} = E_0+\sum_n \mathscr{H}_n\ ,\ \mathscr{H}_n=\mathscr{O}(\epsilon^n) \tag{III.12}$$

In the next section we apply this on an example of classical spin-waves in a two-dimensional classical Heisenberg spin system.

## 2.2 Example of Order by Disorder in the Kagomé lattice

In this part we briefly review the *Order by Disorder* effect on the Kagomé lattice with classical Heisenberg spins as a well-known example of *Order by Disorder* [10, 11, 119, 120].

The Hamiltonian can be rewritten as a sum on triangles (up to a constant term):

$$\mathscr{H} = J \sum_{<i,j>} \mathbf{S_i}.\mathbf{S_j} = \frac{J}{2} \sum_{\Delta}^{N_\Delta} \mathbf{S}_\Delta^2 \tag{III.13}$$

Where $\mathbf{S}_\Delta = \sum_{i \in \Delta} \mathbf{S_i}$ is the total spin of one triangle and $N_\Delta$ is the number of triangles. The lowest energy configuration is reached when $\mathbf{S}_\Delta = 0$ in all triangles, which corresponds to coplanar 120° configurations with three sublattices $\mathbf{S_A}$, $\mathbf{S_B}$, and $\mathbf{S_C}$. Different coplanar ordered configurations (i.e. tilings) satisfy this conditions. The classical ground state of the Kagomé lattice has an infinite degeneracy. Among this infinite set one can cite the $\sqrt{3} \times \sqrt{3}$ and the $q = 0$ coplanar configurations with respectively nine and three sublattices (see Fig III.1). Both of those configurations present lines of defects. For example, in the $\sqrt{3} \times \sqrt{3}$, the rotation of the spin sequence inside an hexagon, let us say $\mathbf{S_A} - \mathbf{S_B} - \mathbf{S_A} - \mathbf{S_B} - \mathbf{S_A} - \mathbf{S_B}$, costs no energy. This is called the *weather vane defect.*

Chalker *et al.* [11] showed that in the Kagomé lattice thermal fluctuations select a subset of states in the ground state manifold via *Order by Disorder* . Using a classical spin-wave approach (Section 2.1), they computed the Hamiltonian up to second order in spin deviations:

$$\mathscr{H}_2 = \frac{J}{2}\left[(3\delta_{ij} - m_{ij})\epsilon_i^x \epsilon_j^x + 2m_{ij}\epsilon_i^y \epsilon_j^y\right] \tag{III.14}$$

A very important result is that the coefficients $m_{ij}$ of the matrix $\mathscr{M}$ are exactly the same for all coplanar configurations ($\sqrt{3} \times \sqrt{3}$, $q = 0$, ...) [114]. In fact, whatever the tilling is, one can always find a transformation so that Eq. III.14 is true *up to quadratic order.* The coefficients $m_{ij}$ are non zero only if $i$ and $j$ are nearest neighbors sites else they are defined by: $m_{ii} = 1$ and $m_{ij} = 1/2$. What changes is the dimension of the matrix: $\mathscr{M}$ is a $n \times n$ matrix where $n$ is the number of sublattices which varies with the tilling that is considered.
One of the eigenvalues of $\mathscr{M}$ is zero, meaning that the deviations up to second order in the $y-$direction presents a full branch of soft modes, *whatever the considered coplanar state is*[2].
Chalker *et al.* [11] suggested that non-coplanar states may have less soft modes and as a consequence are disfavored by thermal fluctuations.
They also estimated the statistical weight of different states in the phase space, which tells if the system actually spends more time in states favored by thermal fluctuations. As discussed in Section 2, soft modes cost no energy in the harmonic approximation and if one takes into account higher order correction, those modes are found to bring a quartic contribution to the partition function $(T/J)^{1/4}$. On this other hand, "Normal modes" contribute to $(T/J)^{1/2}$. More precisely, let us consider a state with classical energy $E_0$ that has $N_4$ soft modes and $N_2 = N - N_4$ "normal" modes. The free energy is given by:

$$F \sim E_0 - T\left(\frac{N_2}{2} + \frac{N_4}{4}\right)\ln\left(\frac{T}{J}\right) \tag{III.15}$$

[2] However this is no longer true at higher order in fluctuations: beyond the harmonic approximation, the spectra of the different tilings differ.

It is clear that the free energy is minimized if, in state of wandering in the whole phase space, the system stays in the region that has the largest number of soft modes. Chalker *et al.* [11] also confirmed this by Monte Carlo simulations. A signature of entropic selection also appears in the specific heat. In a system with no soft mode each degree of freedom brings a contribution of $k_B/2$ to the specific heat while the quartic contribution of each soft mode only adds $k_B/4$. As an example, the specific heat per spin of the Kagomé lattice presents as fall of 1/12 from unity which can be calculated as (in units of $k_B$):

$$C_v = \frac{1}{3}\Big(\underbrace{(6-1)}_{N_2}.\frac{1}{2} + \underbrace{1}_{N_4}.\frac{1}{4}\Big) = \frac{11}{12} \tag{III.16}$$

Hence thermal fluctuations favor the submanifold of coplanar configurations among the ground state manifold.
Those coplanar configurations do not have the same statistical weight and one can address the question whether another selection takes place within this submanifold. The $\sqrt{3}\times\sqrt{3}$ configuration appears to have the largest weight [119]. However a competition takes place between the temperature that favors the creation of $\sqrt{3}\times\sqrt{3}$ domains and the energy required to create domain walls. Monte Carlo simulations show that the spins texture, under thermal fluctuations, present domains in the $\sqrt{3}\times\sqrt{3}$ configuration [119]. Therefore one cannot talk of a rigorous selection of a particular state since the system fluctuates a lot within the subset of coplanar states. More details on *Order by Disorder* in the Kagomé lattice can be found in Ref. [10].

Other examples of *Order by Disorder* in classical spin systems will be presented in Section 4.4.1, such as the triangular lattice and the frustrated square lattice. In Section. 4.4.2 we perform in the Shastry-Sutherland lattice with classical Heisenberg spins the same kinds of calculations as detailed in this section on the Kagomé lattice.

# 3 Effects of lattice distortions on a $J_1 - J_2$ chain

This section reviews the work done on the $J_1 - J_2$ frustrated classical spin chain coupled to adiabatic phonons [5].
One-dimensional frustrated quantum spin systems are in general well under control, mainly thanks to the availability of powerful techniques like bosonization [26] and DMRG [121–123].
As briefly discuss in Section 2.1, a standard way to study quantum spin systems is to start from the analysis of the classical limit and then try to include the effects of quantum fluctuations with the spin-wave approach [41]. In certain cases, this procedure can lead to a reasonable description of an otherwise intractable problem.
Previously, the interplay between frustration and classical phonons has been shown to lead to interesting features even for classical spin systems. Penc *et al.* [12] studied the three-dimensional pyrochlore lattice and showed that spin-lattice coupling can stabilize a magnetization plateau at 1/2 of the saturation magnetization. Tchernyshyov *et al.* [124] studied the effects of magnetoelastic couplings in the pyrochlore lattice with classical spins

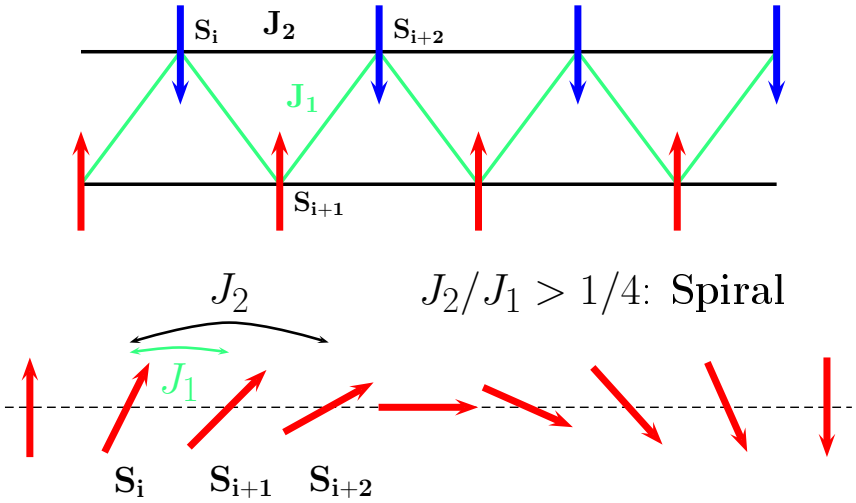


Figure III.2: *Frustrated $J_1 - J_2$ classical spin chain without lattice distortions. Upper panel: the $J_1 - J_2$ spin chain represented as the zig-zag chain for a ratio $J_2/J_1 < 1/4$: the classical spins are Néel ordered. Lower panel: for $J_2/J_1 > 1/4$, the classical ground-state is a spiral.*

as a mechanism to lift the ground state degeneracy. They showed that lattice distortions induce various types of spin ordering such as collinear, coplanar and mixed spin patterns and predicted that the collinear state should support large numbers of spin waves.

In this section we focus on a one-dimensional $J_1 - J_2$ model coupled to adiabatic phonons, where both the quantum and classical situations can be analyzed and compared.
The quantum version of this model has been studied by Vekua *et al.* [13], where it has been shown that the effects of lattice distortions coupled to a given frustrated quantum spin system can lead to new phases, in particular to plateaux and jumps in the magnetization curve. Although plateaux phases are also present in the pure spin system [125, 126], it has been shown that lattice effects can lead to the enhancement of these phases under certain circumstances. Then, a natural question that arises is whether the classical limit could be generally a good starting point to tackle the issue of the interplay between frustration and lattice deformations and its incidence on the appearance of magnetization plateaux.

The $J_1 - J_2$ model appears to be a good model to describe inorganic compounds such as $CuGeO_3$ [127] and $LiVi_2O_5$ [128, 129], rendering its study both theoretically and experimentally relevant. Values for the exchange integrals, such as $J_1 \approx 160K$ and the ratio $J_2/J_1 \approx 0.36$, have also been proposed for copper germanate [130].

## 3.1 Spin-lattice coupling in the $J_1 - J_2$ spin chain

We shall address the question of whether the effects of lattice deformations in the $J_1 - J_2$ Heisenberg spin chain can already lead to interesting magnetization properties at the classical level. The main motivation for the present study is to analyze the origin of such plateaux in

the particular case of a classical zig-zag chain (See Fig. III.2). Although this case is particularly simple and the quantum model can be treated using bosonization (for $S = 1/2$), understanding the role of lattice deformations for classical spins could lead to a way to study more involved situations, such as two dimensional frustrated systems, where analytical techniques are not as powerful as in one dimension.

Without lattice distortions, the lowest energy configuration of the is $J_1 - J_2$ classical spin chain is Néel ordered for $J_2/J_1 < 1/4$, else it is a spiral with a pitch angle:

$$\theta_0 = \arccos\Big(-\frac{1}{4.J_2/J_1}\Big)\,,\ \lim_{J_1\to 0}\theta_0 = \frac{\pi}{2} \tag{III.17}$$

Of course, in the limit $J_1 \to 0$, which corresponds to the limit of two separated chains, one recovers Néel order in each chain.
The effect of frustration on the $J_1 - J_2$ chain with classical spins have been studied long time ago [131–133], as well as its thermodynamic properties. Quantum phonons on the $J_1 - J_2$ classical spins chain without an applied magnetic field were considered by Oguchi and Tsuchida [134]. They obtained a phase diagram as a function of the magnetic couplings and phonon pulsations.

The Hamiltonian of the $J_1 - J_2$ classical spins frustrated chain coupled to adiabatic phonons is:

$$\mathscr{H} = \frac{\tilde{K}}{2}\sum_i \delta_i^2 + J_1\sum_i (1 - \tilde{A}_1\delta_i)\,\mathbf{S_i}\cdot\mathbf{S_{i+1}} + J_2\sum_i \mathbf{S_i}\cdot\mathbf{S_{i+2}} - H\sum_i S_i^z. \tag{III.18}$$

In the previous Hamiltonian, we chose to modulate only the nearest neighbor interaction term, and to consider there is no effect on the next nearest neighbor coupling. This minimizes the number of parameters in the Hamiltonian. We have however checked that the inclusion of such a modulation on the next nearest neighbor couplings does not belie our main conclusions.

In the classical system phonons can be integrated out [135], leading to an extra quartic interaction among the spins. In order to do so, let us define the following reduced quantities:

$$K = \frac{\tilde{K}}{J_1}\,,\ \alpha = \frac{J_2}{J_1}\,,\ A_1 = \frac{\tilde{A}_1}{\tilde{K}^{1/2}}\,,\ h = \frac{H}{J_1} \tag{III.19}$$

The Hamiltonian reads:

$$\mathscr{H} = \frac{K}{2}\sum_i (\delta_i - \frac{A_1}{\sqrt{K}}\mathbf{S_i}.\mathbf{S_{i+1}})^2 - \frac{A_1^2}{2}\sum_i (\mathbf{S_i}.\mathbf{S_{i+1}})^2 + \sum_i \mathbf{S_i}.\mathbf{S_{i+1}} + \alpha\sum_i \mathbf{S_i}.\mathbf{S_{i+2}} - h\sum_i S_i^z \tag{III.20}$$

The partition function is given by:

$$\begin{aligned}
\mathscr{Z}(h) &= \int d\mathbf{S_i}\, d\delta_i\, e^{-\beta\mathscr{H}(\delta_i,\mathbf{S_i},h)} \\
&= \int d\mathbf{S_i}\, d\delta_i\, e^{-\frac{\beta K}{2}\sum_i(\delta_i - \frac{A_1}{\sqrt{K}}\mathbf{S_i}.\mathbf{S_{i+1}})^2}\, e^{-\beta\mathscr{H}_{eff}(\mathbf{S_i},h)} \\
&= \int d\mathbf{S_i}\, d\delta_i\, e^{-\frac{\beta K}{2}\sum_i \tilde{\delta_i}^2}\, e^{-\beta\mathscr{H}_{eff}(\mathbf{S_i},h)} \\
&\sim \int d\mathbf{S_i}\, e^{-\beta\mathscr{H}_{eff}(\mathbf{S_i},h)}
\end{aligned} \tag{III.21}$$

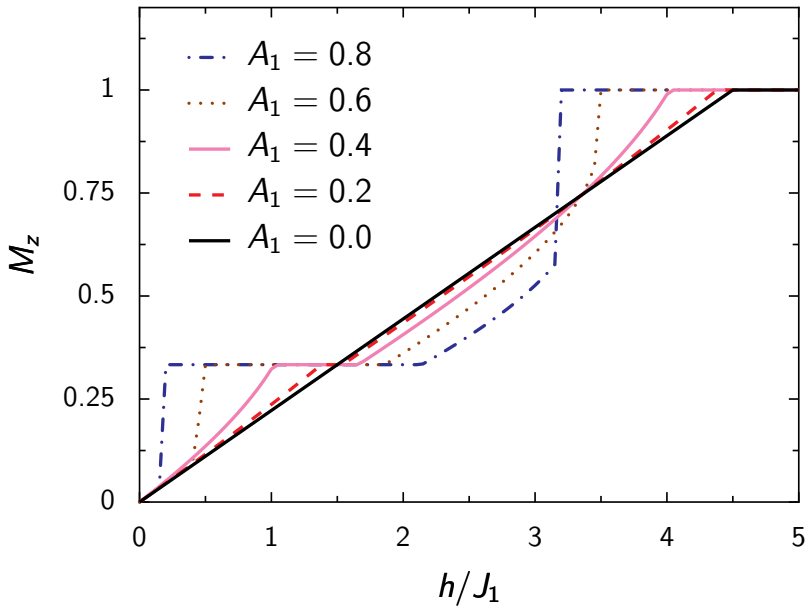


Figure III.3: *Magnetization curves $M(h)$ for $N = 30$ spins with $\alpha = 0.5$ and $A_1 = 0.0, \cdots, 0.8$ in steps of 0.2. Periodic boundary conditions are applied on the chain. The system is gradually cooled to $T \approx 0$ over $3 \times 10^6$ Monte Carlo sweeps.*

Where we defined $\widetilde{\delta_i} \equiv \delta_i - \frac{A_1}{\sqrt{K}} \mathbf{S_i}.\mathbf{S_{i+1}}$ (and $d\widetilde{\delta_i} = d\delta_i$). The effective Hamiltonian, written in units of $J_1$, reads:

$$\mathscr{H}_{\text{eff}} = \sum_i \left( \mathbf{S_i} \cdot \mathbf{S_{i+1}} + \alpha \mathbf{S_i} \cdot \mathbf{S_{i+2}} - \frac{A_1^2}{2} (\mathbf{S_i} \cdot \mathbf{S_{i+1}})^2 \right) - h \sum_i S_i^z \tag{III.22}$$

Even though one ought to study the effect of the elastic constant $K$ and $\tilde{A}_1$ separately, we will focus on the reduced coupling $A_1$ whenever possible, reducing the number of parameters to a manageable size.

In the next section, we study the magnetic phase diagram using analytical and numerical (Monte Carlo) techniques. We pinpoint a region in the parameter space where a plateau appears at $M_z = 1/3$ only. This should be contrasted with the quantum model, which shows in addition a clear $M_z = 0$ plateau in a wide region of the parameter space, and another at $M_z = 1/2$ in a narrower region. Looking into the detailed structure of the ground state at these plateaux, one can understand this discrepancy in the following way: the structure at $M_z = 1/3$ is of the "Up-Up-Down" ($UUD$) type, indicating a classical plateau [111], while in the $M_z = 0$ case the singlet structure can be identified with a quantum one.
In Section 3.3 we discuss the transition to saturation, which is found to be either of first or second order depending on the ratio between frustration and effective lattice coupling.

## 3.2 Study of the $1/3$ magnetization plateau

Let us analyze the magnetic phase diagram of the model Eq. III.22 in the absence of an external magnetic field.
When $A_1 < \sqrt{4\alpha - 1}$, the ground state is a spiral with a pitch angle $\theta$ given by $\cos\theta = 1/(A_1^2 - 4\alpha)$. Its energy is:

$$E_{\text{spiral}} = \frac{1}{2}\cos\theta - \alpha. \tag{III.23}$$

When $A_1 > \sqrt{4\alpha - 1}$ the ground state is Néel ordered.

Before embarking on a quantitative discussion, let us first take a look at a numerical results obtained by classical Monte Carlo (Metropolis algorithm, see Section 5 for details). The magnetization curves of this system show interesting features, which vary depending on the relation between $\alpha$ and $A_1$, as we discuss below.
In Figure III.3 we represent the magnetization $M$ for a fixed value of the frustration $\alpha = 1/2$ and different values of the spin-phonon coupling $A_1$. Starting at high-temperatures we perform several thousands of Monte Carlo sweeps, and then cool down the system to a fraction of the initial temperature. This procedure is then repeated, slowly annealing the system to zero temperature. We observe that a steady magnetization plateau at $1/3$ appears as soon as the coupling to the lattice is slightly turned on, whose length increases with $A_1$. One can notice that the way the system enters the plateau from the low-field side and eventually saturates differs depending on the effective lattice coupling $A_1$, which is detailed next. For $A_1 \gtrsim 0.6$ the two are first order transitions.
Another interesting characteristic seen in Fig. III.3, is that all curves represented (except one) cross at the same field $h_\times \approx 3.35$ for which $M_\times = M(h_\times) \approx 0.745$. We shall discuss this point at the end of Section 3.3. This brief overview suggests that the coupling with the phonons stabilizes the state at $M_z = 1/3$. Since the plateaux are observed at zero temperature, we can fairly assume that this effect is energy driven.

After this numerical preamble, let us now derive some analytical predictions on the characteristics of the magnetization plateau. For this purpose, we need to find out which states describe the system in the low and high-field regions around $M_z = 1/3$. We expect the plateau phase to correspond to "Up-Up-Down" ($UUD$) configuration (see Section 1). In this state, the spins are aligned along the $z$-axis, two up spins alternating with one down spin which is precisely the structure seen at the $1/3$ plateau in the quantum model [13].

In the next sections, we will explain how the critical fields at the entrance and exit of the plateau are calculated, which allows to determine the width of the plateau. We will also establish a phase diagram showing the domain of existence of the plateau and finally we study the nature of the lattice deformation in the plateau phase.

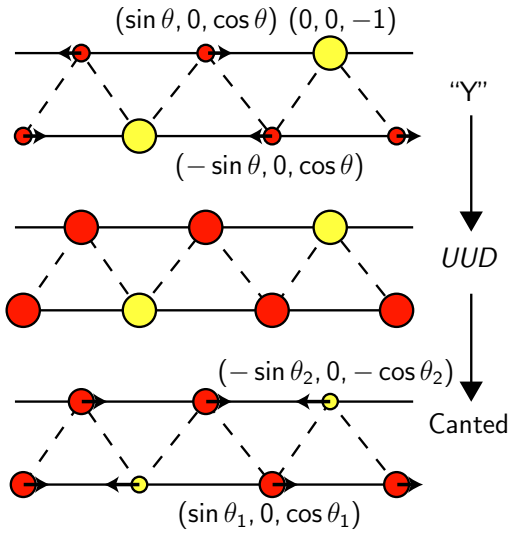


Figure III.4: *Configurations observed in the low-field ("Y " configuration), the 1/3 magnetization plateau (UUD) and high-field regions (canted state). The chain is viewed in the* $(x, y)$ *plane. The arrows denote the projection of the spins in this plane, whereas the circles represent the* $S^z$ *component (red for* $S^z > 0$*, yellow otherwise and radius proportional to* $|S^z|$*). The parameterization of the states is given for each configuration.*

### 3.2.1 Critical field $h_{c1}$ to enter the plateau phase

The classical Monte Carlo data indicates that the situation in the low-field region may present two different scenarios. On the one hand, the transition to the $UUD$ state can occur at a very low field, where the system is not far from its zero field classical ground state. Then, there is no small unit cell structure providing a good description of the system, since the zero field configuration is a spiral. On the other hand, when the transition is smooth in the low-field region, a plausible assumption is to consider that the system adopts a coplanar "Y" configuration parameterized by a single angular degree of freedom $\theta$ (see Fig. III.4). The unit cell energy for this state reads:

$$E_Y(\theta) = (1+\alpha)\,(2\cos\theta(\cos\theta - 1) - 1) - \frac{A_1^2}{2}\left(2\cos^2\theta + \left(2\cos^2\theta - 1\right)^2\right) - h(2\cos\theta - 1) \quad \text{(III.24)}$$

This expression can be minimized for any set of the parameters $h, \alpha$ and $A_1$. As the magnetic field increases, the solution will eventually yield $\theta = 0$ corresponding to the $UUD$ state. This configuration is always a solution of $\partial_\theta E_Y(\theta) = 0$, but it is only a minimum of the energy when:

$$h \geq h_Y = 1 + \alpha - 3{A_1}^2 \quad \text{(III.25)}$$

We should emphasize that this discussion only makes sense whenever $h_Y$ is positive. For a given value of the magnetic field, there can be other solutions satisfying:

$$h = (1+\alpha)\left(2\sqrt{1-X^2} - 1\right) - {A_1}^2\left(3 - 4X^2\right)\sqrt{1-X^2} \quad \text{(III.26)}$$

$$X = \sin\theta\,, \text{ assuming } \cos\theta > 0 \quad \text{(III.27)}$$

The study of Eq. III.27 boils down to finding the sign of a polynomial expression. Introducing $\Delta = 2(1+\alpha) - 11{A_1}^2$, we can show that when $\Delta \geq 0$ there is exactly one more extremum of the energy for $h \leq h_Y$ and that it is always a minimum. This solution becomes precisely the $UUD$ state at $h = h_Y$. Under these assumptions, we can conclude that the critical field for which we recover $M_z = 1/3$ from the low field regime is:

$$h_{c1} = 1 + \alpha - 3{A_1}^2, \quad \Delta \geq 0. \tag{III.28}$$

This can be compared to our Monte Carlo results. For instance, the data for $\alpha = 0.5$ and $A_1 = 0.4$ (solid pink curve in Fig. III.3 ) allows us to obtain a precise estimate for $h_{c1}$ at $T \approx 0$. We get $h_{c1} = 1.02 \pm 0.01$. For this set of parameters, $\Delta$ is positive so that we are ruled by the previous assumptions. The analytical expression Eq. III.28 yields $h_{c1} = 1.02$, which is in excellent agreement with the simulations. This is also the case for all the other curves in Fig. III.3 corresponding to smaller values of $A_1$.

For $\Delta < 0$ there can be up to two extra solutions when $h \geq h_Y$. As there is always one solution that never turns out to become $UUD$ for a certain value of the magnetic field, we ought to perform a detailed comparison of the two solutions' energies in order to conclude. We shall not step further into this discussion, which can nevertheless be conducted numerically using the previous analytical expressions. For instance we performed it when $\alpha = 1/2, A_1 = 0.6$, leading to $h_{c1} \approx 0.46$. This is in good agreement with the Monte Carlo data which gives $h_{c1} \approx 0.47 \pm 0.01$ (dotted curve in Fig.III.3 ). It can be understood from the previous discussion that $h_Y$ is always a lower boundary of the critical field:

$$h_{c1} \geq 1 + \alpha - 3{A_1}^2, \ \Delta < 0. \tag{III.29}$$

If we increase $A_1$ while keeping $\alpha$ fixed, $h_Y$ eventually becomes negative (as it is the case for $A_1 = 0.8$, dash-dotted blue curve in Fig. III.3) and we can generally not conclude using this small unit cell configuration. We should keep in mind that the regime where $A_1$ becomes large is not well described by our initial Hamiltonian since in that case one should include the effects of the lattice also in the next-nearest neighbor interactions.

### 3.2.2 Critical field $h_{c2}$ to exit from the plateau phase

We shall now focus on the state observed in the high-field region to find the corresponding upper critical field $h_{c2}$ above which the plateau disappears. By comparing $h_{c1}$ to $h_{c2}$, we should be able to conclude on the existence of the 1/3 magnetization plateau.
In the upper critical region, the situation is far more under control. The system can be seen to be well described by a 3-spins coplanar "canted" configuration with two degrees of freedom (see Fig. III.4). The energy of such a configuration is given by

$$E_{\text{canted}}(\theta_1, \theta_2) = (1+\alpha)\,(1 - 2U(\theta_1, \theta_2)) - \frac{A_1^2}{2}\left(1 + 2U(\theta_1, \theta_2)^2\right) - h(2\cos\theta_1 - \cos\theta_2) \tag{III.30}$$

where $U(\theta_1, \theta_2) = \sin\theta_1 \sin\theta_2 + \cos\theta_1 \cos\theta_2$.
The configuration $UUD$, which corresponds to $\theta_1 = \theta_2 = 0$, is always a critical point of the function $E_{\text{canted}}(\theta_1, \theta_2)$. A closer look at the second order derivatives with respect to $\theta_1$ and $\theta_2$ shows

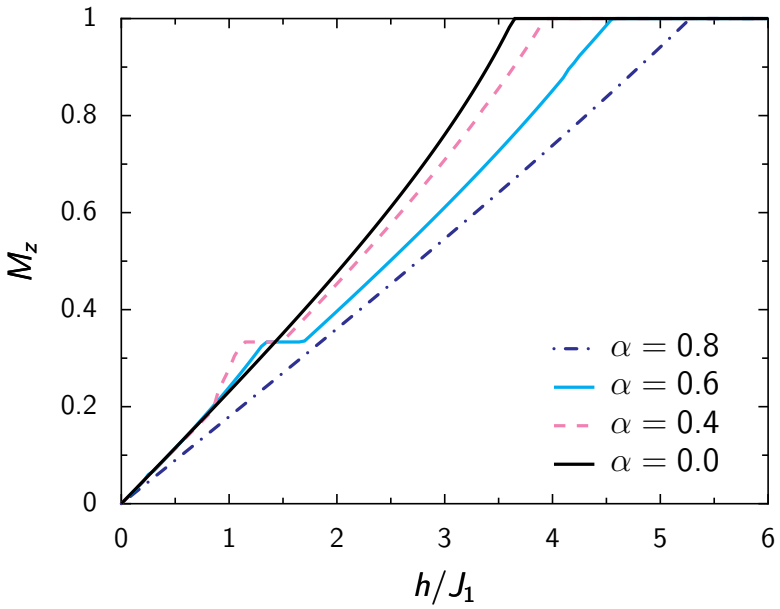


Figure III.5: *Magnetization curves $M(h)$ for $N = 30$ spins with $A_1 = 0.3$ and $\alpha = 0.0, 0.4, 0.6, 0.8$. Periodic boundary conditions are applied on the chain. The system is gradually cooled to $T \approx 0$ over $3 \times 10^6$ Monte Carlo sweeps.*

that it is a local minimum only for $0 \leq h \leq 1 + \alpha + {A_1}^2$. The other critical points satisfy the following set of equations

$$Y = 2X \tag{III.31}$$

$$h = \left(1 + \alpha + A_1^2\left(2X^2 + \sqrt{1-X^2}\sqrt{1-4X^2}\sigma_1\sigma_2\right)\right)\left(2\sqrt{1-X^2} - \sqrt{1-4X^2}\sigma_1\sigma_2\right) \tag{III.32}$$

where

$$\sin\theta_1 = X, \cos\theta_1 = \sigma_1\sqrt{\left(1-X^2\right)} \tag{III.33}$$

$$\sin\theta_2 = Y, \cos\theta_2 = \sigma_2\sqrt{\left(1-Y^2\right)} \tag{III.34}$$

The quantities $\sigma_1, \sigma_2 = \pm 1$ account for all the possible signs of both cosines. We see from Eq. III.31 that there is a strong constraint on $(\theta_1, \theta_2)$ verified regardless of the values of the couplings. At $h = 1 + \alpha + {A_1}^2$, Eq. III.32 admits only one solution which turns out to be $UUD$. For larger value of $h$, $UUD$ can no longer be a critical point, which implies

$$h_{c2} = 1 + \alpha + {A_1}^2, \tag{III.35}$$

corresponding to the exit of the plateau in the high-field region.

### 3.2.3 Domain of existence of the plateau

From this discussion it can be concluded that whenever our assumptions are correct, there is a plateau at $M_z = 1/3$ of length $\Delta h_{1/3} = 4A_1^2$ starting at $h_{c1}$. This result has been checked to be consistent with the Monte Carlo computations and the analytical value of $h_{c2}$ matches the

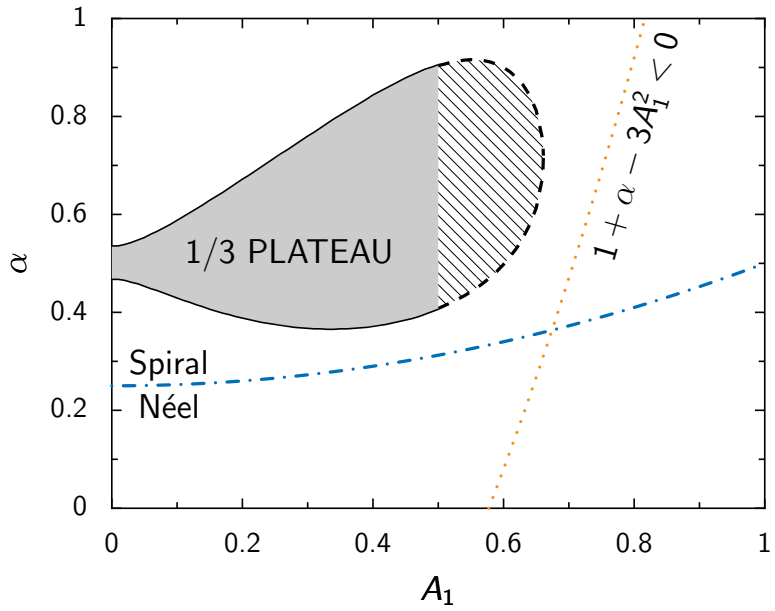


Figure III.6: *Qualitative* $(A_1, \alpha)$ *phase diagram. The filled area between the two full curves corresponds to the region of the parameters space where the* $M_z = 1/3$ *plateau is observed. The hatched region between the two dashed curves is the region of the parameter space for which our approach is no longer observed to be fully valid. Also represented the limit between Néel and Spiral ground states at* $h = 0$ *(blue dash-dotted line) and the region where* $1 + \alpha - 3A_1^2 < 0$ *(dotted orange line).*

value estimated from all the curves in Fig. III.3. There is one more question we need to address: for which set of parameters $(A_1, \alpha)$ can we observe this plateau?
Under the previous assumptions regarding the states observed in the low and high-field regions, we can conclude it exists *for any* $A_1 > 0$. Yet the system can not be described in such a manner for all values of $\alpha$ and $A_1$. Working at a fixed lattice coupling $A_1 = 0.3$, we were able to obtain some magnetization curves varying the frustration $\alpha$. Some of those curves are plotted in Fig. III.5, which clearly shows that there is *only a narrow region* in $\alpha$ where the plateau is observed. A precise answer to the previous question is rather challenging, and we shall first try to discuss this point in a more qualitative manner before adopting a more precise strategy.

At $M_z = 1/3$, we can of course expect to see a lot of different configurations, depending on the values of the couplings. However, the Monte Carlo simulations suggest that the plateau always corresponds to the $UUD$ configuration. This state is perfectly collinear, minimizing the quartic contribution to the effective Hamiltonian Eq. III.22. For instance, it can be seen numerically that for $\alpha = 1/2$ with no coupling to the lattice, the system reaches $1/3$ magnetization in the $UUD$ configuration. Even a small positive value of $A_1$ will then stabilize the $UUD$ state enough for it to be stable when the field is slightly increased. On the opposite, if one antiferromagnetic coupling dominates the other, the system will be in a different state at $M_z = 1/3$. In the extreme case where $\alpha \approx 0$ for instance, the system will favor Néel order in the $xy$ plane, each spin having the same $z$-axis projection $S_z = 1/3$. This layout already trades off some collinearity in favor of

magnetic field alignment. There is no surprise that this trade-off will be further enhanced as the magnetic field is increased, so that no plateau should be observed.

A more accurate way to tackle this issue is to start from the $h = 0$ spiral ground state and ponder over the state adopted by the system when the magnetic field increases. We have already performed part of this task earlier, suggesting that the system slowly moves to a "Y" configuration, whose out of plane components make it a "precursor" of the $UUD$ configuration. Another plausible solution is that the spins, while keeping their spiral structure in the $xy$-plane, all acquire the same $S_z$ projection. In this case, the $n^{\text{th}}$ spin reads

$$\mathbf{S_n} = \left(\sqrt{1-z^2}\cos(n\theta), \sqrt{1-z^2}\sin(n\theta), z\right), \tag{III.36}$$

with $\cos\theta = 1/(A_1^2 - 4\alpha)$. The energy per site,

$$E_{\text{sz}}(z) = z^2 + \left(1-z^2\right)\cos\theta + \alpha\left(z^2 + \left(1-z^2\right)\cos 2\theta\right) - \frac{A_1^2}{2}\left(z^2 + \left(1-z^2\right)\cos\theta\right)^2 - hz, \tag{III.37}$$

can be minimized with respect to $z$ to find the lowest energy configuration at a given magnetic field. Our idea is to perform this minimization at $h = h_{c1}$, and to see if the corresponding configuration is of lower energy than $UUD$ at the same field. If so, the system will not enter the plateau at $h_{c1}$, and of course as mentioned the previous paragraph no plateau should be observed.
For a fixed value of $A_1$, we can determine the range in $\alpha$ leading to $UUD$ at $h_{c1}$. The roots of the polynomial equation are evaluated numerically, from which we sketch the phase diagram represented in Fig. III.6. This approach only makes sense when we have a precise value for $h_{c1}$, which we saw is the case if $A_1$ is not too large ($A_1 \lesssim 0.5$ from the Monte Carlo data). We notice that the diagram is in agreement with the situation depicted in Fig. III.5, as well as the one in Fig. III.3 when $A_1$ is not too large. The most remarkable feature is that for an arbitrary small yet strictly positive $A_1$, one can find a value of $\alpha$ for which the plateau phase is observed.

The effect of temperature on the magnetization plateau is potentially important as an *Order by Disorder* effect [10, 112] could further stabilize the plateau. We calculated the fluctuation matrix (see Section 2.2) up to second order in spin deviations, but no full branch of soft modes was obtained. We investigated the effect of thermal fluctuations by performing Monte Carlo simulations at different temperatures, without annealing the system. A sample is given in Fig. III.7, and in general we observed no remarkable features. The increasing thermal fluctuations quickly destroy the plateau. We should also mention that we observed no strong finite size effects in the numerical simulations, which is why we were always able to work on systems with less than a hundred spins.

### 3.2.4 Deformation of the lattice in the plateau phase

We conclude this section by focusing on the lattice deformations so as to get more insight on the structure of the lattice deformation inside the plateau phase.
For that matter, we modified our Monte Carlo algorithm to take into account the lattice degrees

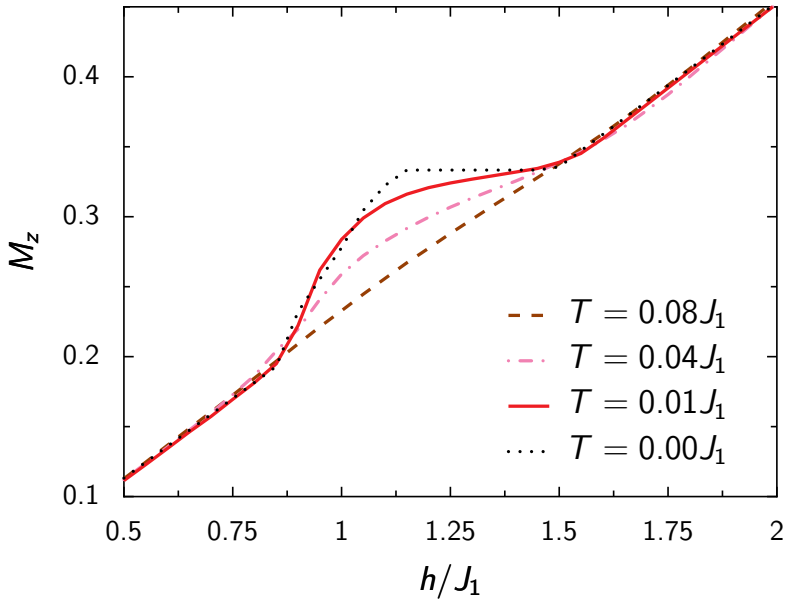


Figure III.7: *Magnetization curves $M(h)$ for $N = 30$ spins with $A_1 = 0.3$ and $\alpha = 0.4$ around $M_z = 1/3$ for different temperatures $T = 0, 0.04, 0.08$ in units of $J_1$. Averages are computed on $2^{22}$ sweeps through the lattice after an initial $2^{18}$ sweeps of thermalization. Increasing the temperature quickly destroys the plateau observed at $M_z = 1/3$.*

of freedom as well. Starting from the Hamiltonian Eq. III.18, we used the Metropolis algorithm for both the spin positions and orientations, applying periodic boundary conditions on the chain. We studied the normalized histograms of the displacements $\delta_i$ at finite temperature. We fixed $\alpha = 0.4$ and $A_1 = 0.3$, the same values used in Fig. III.7 to allow a direct comparison between the two figures, and selected the magnetic field so that the system is at $M_z \approx 1/3$. Besides the value of $A_1 = \tilde{A}_1/\sqrt{K}$, we need to give $K$, the spring constant in III.18, a sensible value. We took $K = 10^3 J_1$, large enough to make sure the displacements remain small. This corresponds to $\tilde{A}_1 \approx 9.5$. We mention that both $K$ and $A_1$ are of the same order of magnitude as the one for a more complex two dimensional material such as $SrCu_2(BO_3)_2$ [136] and that they can be considered at least as "realistic" for copper germanate or lithium vanadate [137]. The results are given in Fig. III.8.

We see that the lattice deformations are not uniform and that their histogram presents two peaks at $T = 0.01 J_1$. They are centered around a negative and positive value of the displacement $\delta_i$. This suggests that the underlying deformation consists of $UDU$ trimers (Up-Down-Up) on the chain. Let us introduce $\delta_+$ the displacement between two consecutive trimers and $\delta_-$ the displacement between the down spin and its two nearest neighbors inside the trimer. The energy of this unit cell is given by:

$$E = 3K\delta_-^2 + 4J_1\tilde{A}_1\delta_- - J_1 + J_2 - H, \tag{III.38}$$

where the periodic boundary conditions imply $\delta_+ = -2\delta_-$. Minimizing the energy, the defor-

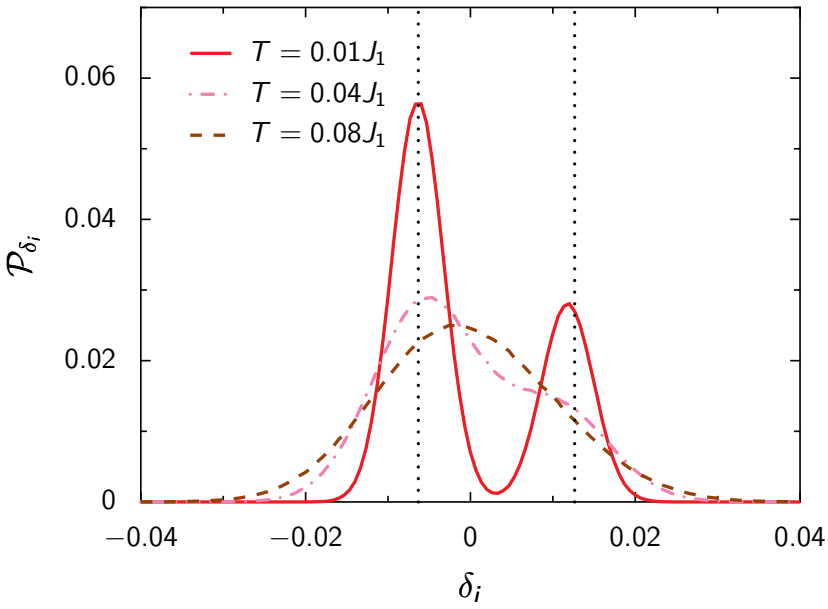


Figure III.8: *Normalized lattice displacement histograms for* $N = 30$ *spins with* $\alpha = 0.5$, $A_1 = 0.4$ *(*$K = 10^3 J_1$*) and* $h = 1.5$ *at different temperatures.* 300 *points were used in the interval* $[-0.1, 0.1]$. *The two dotted vertical lines correspond to the* $T = 0$ *limit calculated in the text. The data was obtained using a direct classical Monte Carlo for the Hamiltonian.*

mation should become

$$\delta_+ = -2\delta_- = \frac{4\tilde{A}_1 J_1}{3K} \tag{III.39}$$

at $T = 0K$. Going back to Fig. III.8, at $T = 0.01J_1$ the distribution clearly exhibits two peaks and we can see that they are almost centered around $\delta_+$ and $\delta_-$ respectively. The ratio between the height of the two peaks is about 2, a consequence of the fact there are twice as many up spins than down spins in the $UUD$ state. Those results seem to validate the trimer scenario at low temperature. When the temperature increases to $T = 0.04J_1$, the peaks start to overlap, betraying the gradual destruction of the plateau already seen in Fig. III.8. Finally at $T = 0.08J_1$, we end up with a single peaked, almost gaussian, distribution: the plateau eventually disappeared. We end up by stating that expectation value of the displacement is always zero as the periodic boundary conditions applied ensure the length of the chain remains fixed throughout the simulation.

## 3.3 Transition to saturation

The study of the upper critical magnetic field yields another interesting result: we can get a precise picture of how the system eventually reaches saturation.
This result can be foreseen using classical Monte Carlo, which shows that the canted state describes the system quite well even for $h > h_{c2}$. A close look at Fig. III.3 shows that two

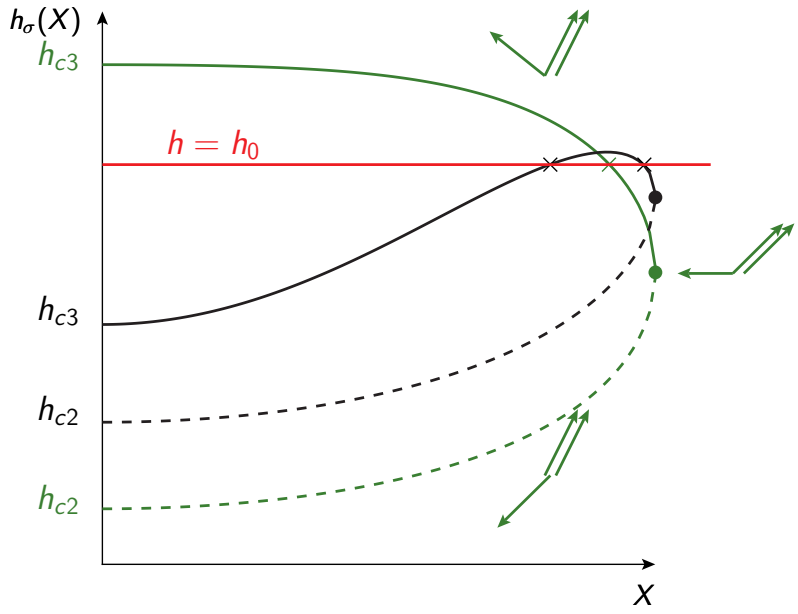


Figure III.9: *"Low magnetization" (dashed line) and "high magnetization" (plain line) curves as a functions of* $X = \sin\theta_1$ *for* $\alpha = 0.5$, $A_1 = 0.5$ *(green) and* $\alpha = 0.5$, $A_1 = 0.8$ *(black). The typical shape of the minima's unit cell along the green curves are depicted in the different magnetic field regions. The intersections (crosses) with the line* $h = h_0$ *(red) gives the competing critical point at this magnetic field. The colored dots correspond to the minimal configuration with one spin in the* $xy$*-plane.*

different behaviors of the magnetization between $h_{c2}$ and the saturation value are observed. For different values of spin-phonon coupling, the system can undergo a *first or second order transition* to reach saturation. We are going to demonstrate that this result can be derived from energetic considerations on the canted state.

From Eq. III.30, we see that the saturated state, reached for $\theta_1 = 0$ and $\theta_2 = \pi$, minimizes the energy for a magnetic field greater than:

$$h_{c3} = 3(1 + \alpha - {A_1}^2) \tag{III.40}$$

This imposes a lower boundary on the saturation field $h_U$. We assume that the couplings $A_1$ and $\alpha$ are such that $h_{c2} < h_{c3}$, a situation where the previous discussion on the existence of the 1/3 magnetization plateau still holds. To be consistent with the state of system for $h > h_{c2}$, we set $\sigma_1 = 1$ and let $\sigma_2 = -\sigma$ take the values $\pm 1$ so as to be able to move from $UUD$ to saturation continuously. At a given magnetic field, one can obtain the corresponding critical configurations by finding the roots of Eq. III.32. This task reduces to the study of the two functions $h_\sigma$:

$$h_\sigma(X) = \left(1 + \alpha + A_1^2\left(2X^2 - \sqrt{1-X^2}\sqrt{1-4X^2}\sigma\right)\right)\left(2\sqrt{1-X^2} + \sqrt{1-4X^2}\sigma\right). \tag{III.41}$$

Their roots can be determined graphically for a fixed field $h_0$ as they are the values of $X$ for which the line $h = h_0$ intersects $h_\sigma(X)$. The "low magnetization" function $h_-$ will give us solutions with one spin still pointing down, whereas the "high magnetization" function $h_+$ will give

us states where all the spins have a positive $S_z$ component.
Fig. III.9 is a plot of both functions for two sets of values $\alpha$, $A_1$. In both cases, the curves for $h_+$ and $h_-$ join at:

$$h_{c4} = \sqrt{3}(1 + \alpha + A_1/2) \tag{III.42}$$

This point is represented with filled colored dots in Fig. III.9 (where the plain and dashed lines join). For this value of the magnetic field, the root of $h_\sigma$ corresponds to a configuration in which one of the three spins lies precisely in the $xy$-plane. Two possible behaviors are observed. For instance when $\alpha = A_1 = 0.5$ (green curves in Fig. III.9), we see that for a fixed magnetic field $h \in [h_{c2}, hc3]$ there is only one critical point of the energy, which can be shown to be a minimum. We are able to follow easily the state of system as the magnetic field increases. The two up spins first slightly tilt to let the down spin reach the $xy$-plane and then they all progressively align along the $z$-axis while still satisfying Eq. III.31. The three-spins unit cell configuration smoothly goes from $UUD$ to saturation.

For $A_1 = 0.8$ (black curves in Fig. III.9), the "high magnetization" function $h_+$ (plain line) presents a maximum. In this case, three states are potentially competing for $h$ between $h_{c3}$ and its maximum value: the saturated state and the two roots of $h_+$. We ought to compare their energies to conclude, but it is not surprising that the outcome can be a first order transition to saturation. We numerically solved the analytical equations involved to get the magnetization curve from the exit of the plateau to saturation for $A_1 = 0.8$. The saturation field we obtain is $h_U \approx 3.17063$, for which the system jumps from $M_z \approx 0.58434$ to saturation. The comparison between this minimization and the Monte Carlo data is given in Fig. III.10 and shows the excellent agreement achieved.

A more in-depth study of the $h_\sigma$ functions' extrema allows to work out the range in $(\alpha, A_1)$ for which the transition to saturation is of first or of second order.
A second order transition, which are related to the existence of a non trivial maximum in $h_+$, occur only if:

$$1 \leq (1 + \alpha) / A_1^2 \leq \frac{11}{2} \tag{III.43}$$

which in agreement with our numerical observations.

Finally, it can be pointed out from Eq. III.41 that for $X = 1/\sqrt{5}$ the function $h_+$ does no longer depend on the coupling $A_1$. If this state is reached, it will be the minimum of the canted configuration energy for a magnetic field:

$$h_\times = \frac{5}{\sqrt{5}}(1 + \alpha). \tag{III.44}$$

At this field the magnetization is $M_z = M_\times = 5/(3\sqrt{5})$. This explains why for our selection of parameters, all the curves except one in Fig. III.3 cross at a field whose estimate, given in Section 3.2, coincides with $h_\times$. Regardless the value of $A_1$, if the system is not saturated at $h_\times$ then its magnetization will always be $M_\times$.

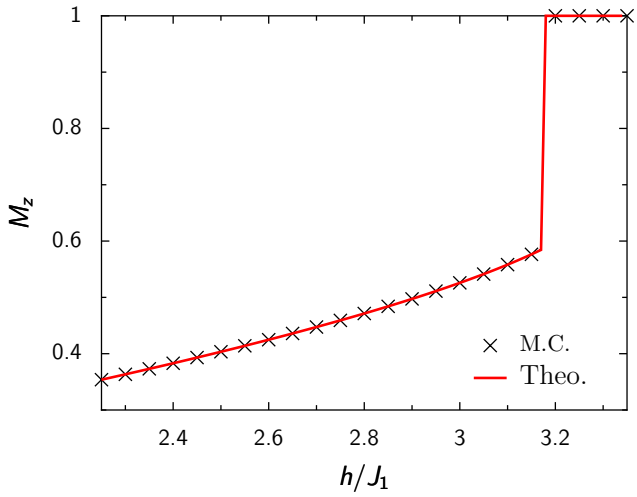


Figure III.10: *Upper region of the magnetization curve for* $\alpha = 0.5$ *and* $A_1 = 0.8$ *at* $T = 0$. *The full line represents the results obtained using the analytical minimization of the "canted" state energy, crosses the data obtained by Monte Carlo.*

## 3.4 Summary and Conclusion

The effects of lattice deformations at the classical level in a frustrated spin system has been illustrated working on a simple $J_1 - J_2$ classical spin chain coupled to adiabatic phonons.
Using both analytical and numerical (Monte Carlo) methods, we provided an overall picture of the magnetization properties for a large set of the parameters $\alpha, A_1$ introduced in our model. We have found that a plateau at $M_z = 1/3$ is present in certain region of the parameters space, while no other plateaux are observed. We found conditions on the existence of these plateaux:

- Frustration is a necessary ingredient, as the plateaux can only arise when the zero field ground state is a spiral.
- The coupling to lattice deformations, is such that for an arbitrary small yet strictly positive $A_1$, one can find a value of $\alpha$ for which the plateau phase is beheld. Further increasing $A_1$ will broaden the region in the parameter space for which the plateau occurs, until the effective coupling is no longer mild enough for our analytical approach to be valid, even if a numerical approach is still achievable.

It should be emphasized that the stabilization mechanism is purely energy driven and triggered by the quartic interaction induced by the lattice coupling in the effective Hamiltonian Eq. III.22. The underlying lattice deformation shows the chain is made of "$UDU$" trimers inside the plateau phase.
We also analyzed the transition to saturation and obtained a condition on the parameters of the Hamiltonian which allows us to determine whether this transition is of first or second order.
The absence of plateaux at $M_z = 0$ and $M_z = 1/2$ in the classical model as compared to the quantum case can be understood by analyzing the ground state structure of the plateaux in the quantum case. It is only for $M_z = 1/3$ that one observes a classical type of spin configuration, of the $UUD$ type, while in the other cases a quantum state is apparent.

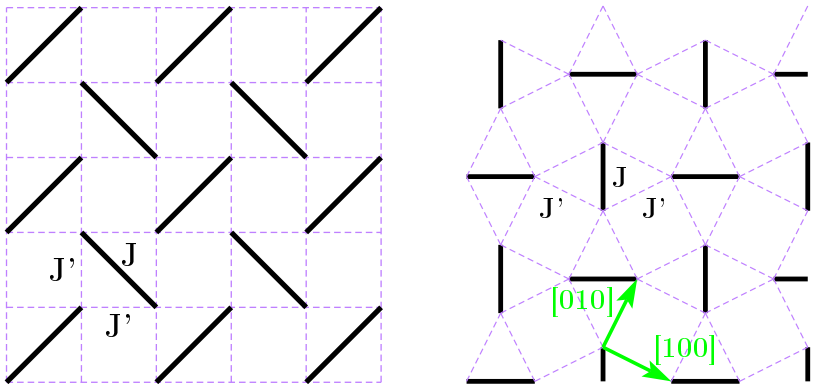


Figure III.11: *Left panel: The Shastry-Sutherland lattice. Right panel: The topologically identical structure realized in the* (001) *plane of* $SrCu_2(BO_3)_2$ *and rare-earth tetraborides.* $J'$ *bonds are the magnetic couplings along the edges of the squares (clear dashed lines) and* $J$ *(black bold lines) the diagonal dimers couplings.*

# 4 Classical Heisenberg spins on the Shastry-Sutherland lattice

This section reviews the work done on the magnetization process of the Shastry-Sutherland lattice with classical Heisenberg spins [6, 7].
The Shastry-Sutherland lattice was considered more than twenty years ago as an interesting example of a frustrated quantum spin system with an exact orthogonal dimer singlet ground state [136, 138]. This model was later found to present extremely interesting physical properties such as a very rich phase diagram as the ratio between the magnetic couplings varies and plateaux in its magnetization curve.
This lattice was originally studied by Shastry and Sutherland as a toy model, however a first experimental realization was obtained in the beginning of the nineties by Smith and Keszler [139] with the $SrCu_2(BO_3)_2$ compound. Today other chemical compounds, such as the rare-earth tetraborides, are known to present plans of atoms that realize a lattice topologically equivalent to the Shastry-Sutherland lattice.

The Shastry-Sutherland lattice can be described as a square lattice with $J'$ antiferromagnetic couplings between nearest neighbors and additional $J$ antiferromagnetic couplings between next nearest neighbors in one square over two (see Fig. III.11 left panel). However it has been experimentally observed that in chemical compounds the $J$ diagonal couplings are often stronger or almost equal with the $J'$ couplings. Therefore the plans of atoms do not exactly realize the lattice showed in Fig. III.11 but a topologically equivalent lattice in which the frustrated squares are distorted into rhombi (see Fig. III.11 right panel). The diagonal $J$ couplings order as orthogonal dimers whose length is shorter that the edges couplings $J'$. [3]

The Hamiltonian of the Shastry-Sutherland lattice under an external magnetic field $h$ applied

[3] Therefore one cannot talk about nearest or next nearest neighbors in the Shastry-Sutherland lattice without specifying which configuration of the lattice is considered.

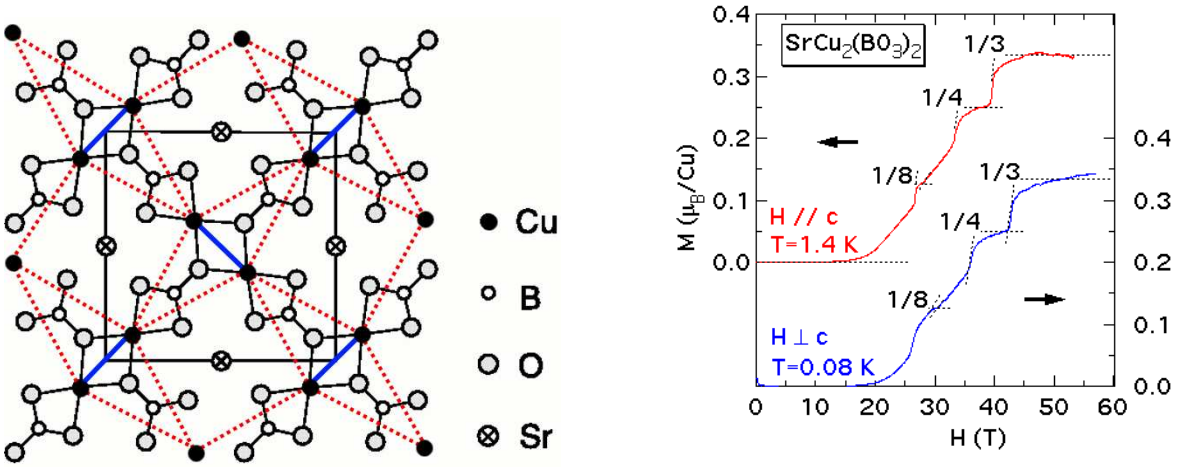


Figure III.12: *Left panel: Schematic view of the layers of $CuBO_3$ and Sr layers in the $SrCu_2(BO_3)_2$ compound. The Shastry-Sutherland lattice (plain $J$ dimer bonds and dashed $J'$ bonds) has been depicted on top to show how it is realized by Cu atoms (figure based on Kodama* et al. *[141]). Right panel: Experimental magnetization curve of $SrCu_2(BO_3)_2$ (figure from Onizuka* et al. *[142]).*

along the $z-$axis is given by:

$$\mathscr{H} = J' \sum_{edges}^{N} \hat{s_i}.\hat{s_j} + J \sum_{diagonal}^{N} \hat{s_i}.\hat{s_j} - h \sum_{i}^{N} \hat{s_i}^z \tag{III.45}$$

## 4.1 A brief summary of the quantum Shastry-Sutherland lattice

The quantum Shastry-Sutherland lattice has been widely studied both theoretically and experimentally [14].
As the ratio $J'/J$ varies, it presents a rich phase diagram with quantum phase transitions between the gaped dimer singlet ground state ($J'/J < 0.68$) that was originally discussed by Shastry and Sutherland [136], a plaquette resonating valence bond state ($J'/J < 0.86$) and a gapless magnetic state [140].

The first experimental realization of the Shastry-Sutherland lattice, the $SrCu_2(BO_3)_2$ compound [139], crystallizes in the tetragonal structure and it has a layer structure of $Cu(BO_3)$ planes separated by magnetically inert Sr atoms (see Fig. III.12 left panel). The $Cu^{2+}$ ions carry a spin $S = 1/2$ and are located on a lattice topologically equivalent to the Shastry-Sutherland lattice in which dimer $J$ bonds have stronger magnetic couplings than $J'$ bonds ($J'/J \approx 0.65$).
The magnetic susceptibility of $SrCu_2(BO_3)_2$ exhibits a Curie-Weiss behavior at high temperatures ($T \sim 20$ K), followed by an abrupt decrease and zero spin susceptibility at $T = 0$ which are characteristics for spin gap system. Theoretical and experimental activities have revealed that $SrCu_2(BO_3)_2$ is actually located in the vicinity of an antiferromagnetic state and a resonating valence bond plaquette singlet state. Its realizes the exact dimer singlets ground state [136, 143].

Ueda and Miyahara showed that this is maintained even if interlayer couplings are added [144]. The application of a magnetic field creates polarized triplets on the dimer bonds. The orthogonality of the dimer ground state leads to a particular behavior for the elementary excitations: triplets excitations are almost localized [145]. The finite gap in the magnetic excitations was estimated by different methods (magnetic susceptibility, nuclear magnetic resonance, nuclear quadrupole resonance and electron spin resonance) and it was found to be $\Delta \approx 35$ K [143, 146–148].
Since the hopping of the triplet is extremely restricted they can easily form regular lattices for various rational of the saturated magnetization $M/M_{sat}$ (see Fig. III.13). At $M/M_{sat} = 1/8$, $1/4$, $1/3$ and $1/2$, the triplets form superstructures and magnetization plateaux appear [149] (see Fig III.12 left panel and Fig III.13). The $M/M_{sat} = 1/2$ and $1/8$ present respectively a square and a rhomboid cells while the $M/M_{sat} = 1/3$ and $1/4$ have a magnetic superstructure of stripe. The $SrCu_2(BO_3)_2$ compound is known as the first example of a system in which the appearance of magnetization plateaux is accompanied by a lowering of the translational symmetry (excepted for the $M/M_{sat} = 1/2$ plateau) [150]. In particular nuclear magnetic resonance experiments reported 16 different Cu sites in the $M/M_{sat} = 1/8$ plateau [141, 151] (see Fig. III.13 right panel).
Momoi and Totsuka derived a Hamiltonian up to third order in $J'/J$ and reproduced the $M/M_{sat} = 1/2$ and $1/3$ plateaux [150, 152] (see phase diagram in Fig. III.13 left panel). They explained these plateaux with insulator-supersolid transitions. However their analysis could not reproduce the $M/M_{sat} = 1/4$ and $1/8$ plateaux.
From an experimental point of view, due to accessible magnetic fields, magnetization plateaux were only observed for $M/M_{sat} = 1/8$, $1/4$ and $1/3$ in high-magnetic fields experiments [142, 143, 153] (Fig. III.12 right panel).
Recently Sebastian *et al.* [154] reported additional magnetization plateaux at $M/M_{sat} = 1/9$, $1/7$, $1/6$, $1/5$ and $2/15$. Although presence of those new plateaux is still debated [155], recent studies reproduced them [156**?** ].

Apart of $SrCu_2(BO_3)_2$, very few compounds are currently known to realize the Shastry-Sutherland lattice. One can cite:

- **$Nd_2BaZnO_5$**: this compound crystallizes in the tetragonal space group $I4/mcm$. The existence of an antiferromagnetic ordered phase was confirmed by the study of the magnetization at different temperatures. The $Nd^{3+}$ ions present large total momenta and form a Shastry-Sutherland lattice with magnetic couplings evaluated $J'/J \approx 1$ [153].

- **$Yb_2Pt_2Pb$**: this compound was recently synthesized by Kim *et al.* [157] who showed that its strong magnetic frustration arises from the underlying Shastry-Sutherland lattice. This compound also crystallizes in the tetragonal structure and presents a layered magnetic structure. Below 2.07 K, $Yb_2Pt_2Pb$ orders antiferromagnetically. Magnetization measurements at low temperatures showed a strong magnetic anisotropy which indicates that the magnetic moments of the Yb ions are confined to planes. In each plane the moments lie on isosceles triangles which can be mapped onto the Shastry-Sutherland lattice. The structure of $Yb_2Pt_2Pb$ can be described as layers of Yb ions localized on the Shastry-Sutherland lattice separated by layers of platinum and lead. Two different types

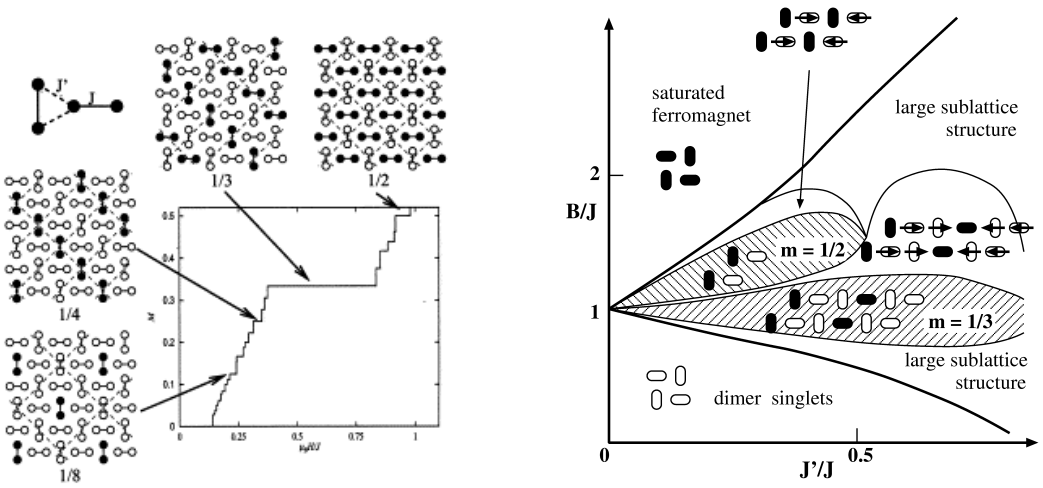


Figure III.13: *Left panel: Structures in the magnetization plateaux of $SrCu_2(BO_3)_2$. The full circles correspond to the triplet excitations and the empty circles to the singlets. Figure from Miyahara and Ueda [149]. Right panel: Phase diagram of $SrCu_2(BO_3)_2$ as a function of the ratio $J'/J$ and the magnetic field at $T = 0$. Figure from Momoi and Totsuka [152]*

of Yb layers were identified.

- The rare-earth tetraborides compounds $RB_4$ also realize the Shastry-Sutherland lattice and some of them exhibit plateaux in their magnetization curves. This will be discussed in detail in the next section.

## 4.2 Experimental motivation for the classical Shastry-Sutherland lattice

Recently rare-earth tetraborides $RB_4$ have been attracting new interest on the Shastry-Sutherland lattice. $RB_4$ crystallize in the tetragonal structure with space group $P4/mbm$. R ions are placed on a sublattice in the (001) plane which consists of R-R dimers that are alternatively orthogonal along the [110] axis. This sublattice is topologically equivalent to the SSL (see Fig. III.11 right panel). The bond length between the nearest neighbors and next nearest neighbors rare-earth atoms is very close. Hence one can expect the edges magnetic couplings $J'$ to be close from the diagonal couplings $J$ and the frustration to be very strong.
Recent experiments showed that a couple of rare-earth tetraborides present magnetization plateaux for various rational values of the saturated magnetization. Those compounds present large total angular momenta $J > 1$ (see Fig. III.14), which justifies the relevance of a *classical* model.

Fig.III.14 briefly summarizes experimental data on the $RB_4$ compounds that have been found to exhibit plateaux in their magnetization curves. More details and references are given in the

| **$RB_4$** | **Total moment $\mathscr{J}$** | **Structure at h = 0** | **Magnetization plateaux (h//z)** |
|---|---|---|---|
| $GdB_4$ | | $J'/J \ll 1$, spiral. | no plateau |
| $TbB_4$ | 6 | Magnetization process suggests an helicoidal structure ($J'/J < 1$). | 9 jumps in the magnetization curve. Plateaux identified at $M/M_{sat} = 1/4, 1/3$ and $1/2$ |
| $DyB_4$ | 15/2 | | $M/M_{sat} = 1/2$ |
| $ErB_4$ | 15/2 | Thought to be a collinear spiral with $J'/J < 1$. | $M/M_{sat} = 1/2$ |
| $TmB_4$ | 6 | Neél ordered: one can expects $J'/J \geq 1$. | $M/M_{sat} = 1/2$ and $M/M_{sat} = 1/8$ (only in the descending field process). $M/M_{sat} = 1/7$ and $1/9$ recently reported. |

Figure III.14: *Brief summary of the recent experimental data on magnetization plateaux in $RB_4$.*

text below.

- **$TbB_4$**: This compound is described as a classical system due to its large total angular momenta $\mathscr{J} = 6$. Two antiferromagnetic transitions occur at $T_{N1} = 44$ K and $T_{N2} = 24$. Neutron scattering indicates that between $T_{N1}$ and $T_{N2}$ the moments are confined in the $(x, y)$ plane with a strong anisotropy along the dimers axis ([110]) [158]. At $T_{N1}$ a structural transition takes place and the moments rotates in the $(x, y)$ plane. Yoshii *et al.* [19] studied $TbB_4$ below $T_{N1}$ in high magnetic fields up to 54 T. In such $(x, y)$ systems, under $h//z$, one could expect a linear magnetization process with moments raising as the field increases. However, under a magnetic field applied according to the $z-$axis, the magnetization curve curve presents a nine-step-field-induced jumps (see Fig. III.15, right panel) and magnetization plateaux are observed at $M/M_{sat} = 1/4, 1/3$ and $1/2$. On the other hand the magnetization curve present one jump at $h = 6$ T for $h//x$ and at $h = 12$ T for $h$ along the dimers axis [110].
  The magnetic structure of $TbB_4$ under no magnetic field is not known yet. However the similarities between its magnetization process with $h//x$ and the one of a helimagnetic system suggests that $J'/J < 1$ (spiral configuration).

- **$DyB_4$**: has a large total momentum $\mathscr{J} = 15/2$. Watakuni *et al.* [159] studied the frustration of the orbital degrees of freedom of the $4f$ electrons and called it the first example of geometrically quadrupolar (orbital) frustrated system. $DyB_4$ undergoes phase transitions at $T_1 = 20.3$ K and $T_2 = 12.7$ K which are characterized by the ordering of the $z$ and $x, y$ components of the magnetic moments [159].
  Watanuki *et al.* recently reported the presence of a $M/M_{sat} = 1/2$ magnetization plateau for $h//z$ at $T < T_1$[160].

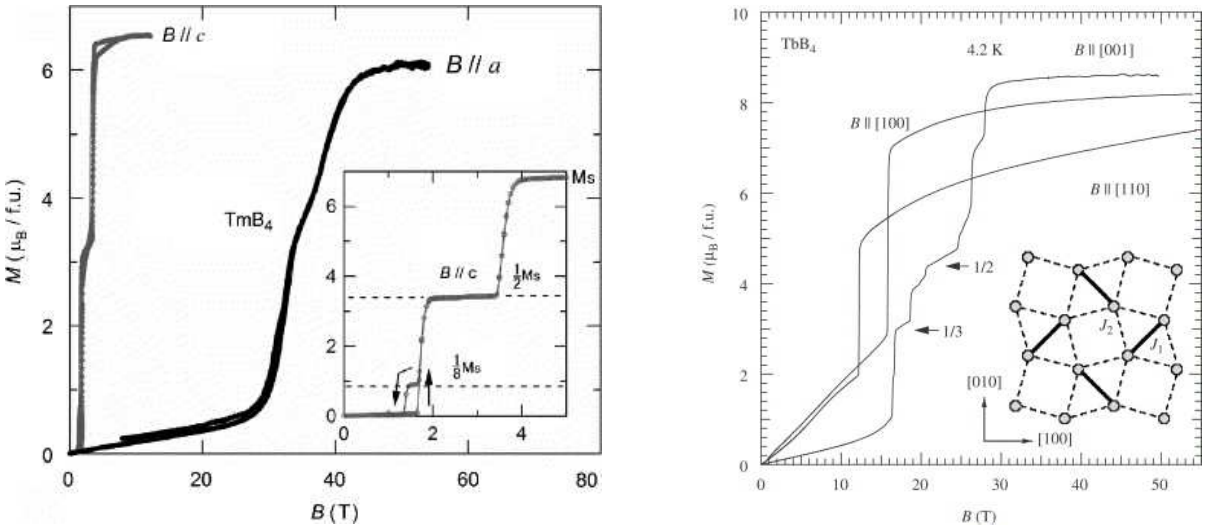


Figure III.15: *Left panel: Magnetization of $TmB_4$ for $h//z$ ($z-$axis ≡ **c**) and $h$ in the $(x,y)$ plane ($x-$ or $y-$axis ≡ **a**) at 1.3 K. Inset is the low-field data for $h//z$ at 2 K. Figure from Iga* et al. *[16]. Right panel: Magnetization of $TbB_4$ at at 4.2 K ($< T_{N1}$) along the directions:* [100] *($x-$ or $z-$ axis), [1 1 0] (along the dimers axis) and [0 0 1] ($z-$axis). Inset: Tb atoms (circles) on the Shastry-Sutherland in the* (001) *plane. Figure from Yoshii* et al. *[19].*

- **$ErB_4$**: Magnetization and neutron measurements revealed that $ErB_4$ orders antiferromagnetically below $T = 15.4K$ [21]. It presents highly anisotropic magnetic susceptibility which is much larger along the $z-$axis than in the $(x,y)$ plane. $ErB_4$ exhibits successive metamagnetic transitions with a plateau at 1/2 of the saturated magnetization for both $h//z$ and $h//x$. Moreover a first-order transition due to strong multipole interactions takes place for $h//x$ [22]. Mishimura *et al.* mention that the 1/2 plateau with $h//z$ could be understood as a competition of the Zeeman energy with the frustration due to the Shastry-Sutherland lattice with $J'/J < 1$. Since $ErB_4$ has a total momentum $\mathscr{J} = 15/2$ a classical approach is relevant and the configuration in zero field may be a collinear spiral.

- **$TmB_4$**: $TmB^{3+}$ ions have a total moment $\mathscr{J} = 6$ which allows a classical treatment. According to Siemensmeyer *et al.* [17] at low temperature ($T < 9.8$ K) the zero field structure is Neél ordered with a strong Ising type anisotropy (moments aligned according to the $z-$axis). The ratio of the magnetic couplings is expected to be $J'/J \approx 1$. High field measurements up to 54 T showed that $TmB_4$ presents an extremely anisotropic behavior. For $h//x$ and $h$ along the dimers axes saturation takes place at 30 T and the system exhibits magnetization plateaux $M/M_{sat} = 1/2$. One the other hand for $h//z$ the system reaches saturation at 4 T and the magnetization plateaux at $M/M_{sat} = 1/2$ remain. At $M/M_{sat} = 1/2$ the Tm moments seem to present a strong Ising type single-ion anisotropy leading to a collinear structure along the $z-$axis in which three out of four spins point in the field direction ($UUUD$ configuration) [15]. An additional plateau appears at

$M/M_{sat} = 1/8$ only in the descending field process [15, 16]. Those plateau are destroyed by a temperature $T > 8$ K (see magnetization curve in Fig. III.15, left panel). Recently additional plateaux at $M/M_{sat} = 1/9$ and $1/7$ were reported for $h//z$ arising from a stripe structure [17, 18].

On the other hand $GdB_4$ does not present plateaux of jumps in its magnetization curve [161]. Its magnetic coupling constants were evaluated as $J'/J \ll 1$ which suggests a spiral structure at $h = 0$.

To conclude, the recent discovery of chemical compounds that present planes of atoms with large total momenta localized on a lattice topologically equivalent to the Shastry-Sutherland lattice motivates a study through a *classical* approach. The existence of those magnetization plateaux at various rational values of$M/M_{sat}$ within a classical model is still not understood yet.
Inami *et al.* [158] proposed a model for the $M/M_{sat} = 1/2$ plateau in $TmB_4$. They included anisotropy in the $(x, y)$ plane and suggested that the exited states can be described by Ising spins. This model reproduces the $M/M_{sat} = 1/2$ plateau in the limit of infinite anisotropy by allowing moments perpendicular to the field axis ($z-$axis). In this model the structure in the plateau is not the collinear $UUUD$ structure that is indicated by neutron scattering in some $RB_4$.

## 4.3 Spin configuration and magnetization process at zero temperature

We studied the Shastry-Sutherland lattice in the classical limit in order to understand the appearance of the $M/M_{sat} = 1/3$ plateaux. At zero temperature, the magnetization process of the Shastry-Sutherland lattice present similarities with the classical triangular lattice.
We performed preliminaries Monte Carlo simulations in which magnetization curves exhibit pseudo-plateaux at $M/M_{sat} = 1/3$ for non zero temperature. In order to understand the presence of these pseudo-plateaux, we carried out an analytical study by means of classical spin-waves (see Section 2.1 ) and showed that thermal fluctuations select of a particular collinear configuration which allows the pseudo-plateaux to exist. The spectrum of the thermal fluctuations matrix allows a comparison with other frustrated systems. By means of Monte Carlo simulations we obtained the phase diagram of the classical Shastry-Sutherland lattice as a function of magnetic field and temperature. We started from the particular ratio of the magnetic coupling $J'/J = 1/2$ and discussed how the phase diagram is modified away from this ratio.

### 4.3.1 The Model

We study classical Heisenberg spins on the Shastry-Sutherland lattice. Heisenberg spins are represented by simple vectors $\mathbf{S_i} = \|\mathbf{S_i}\|\big(\cos\theta_i \sin\phi_i, \sin\theta_i \sin\phi_i, \cos\phi_i\big)$ with $\|\mathbf{S_i}\| = 1$. The magnetic field is applied along the $z-$axis, $\mathbf{h} = h\mathbf{e}_z$. This corresponds to $\mathbf{h}//[001]$ in the experiments carried out on $RB_4$.
The sums are taken over nearest neighbors pairs according to the edges of the squares with

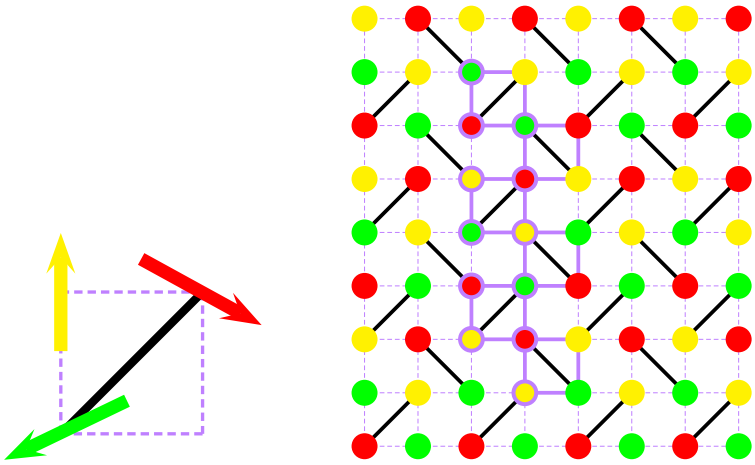

Figure III.16: *Spin configuration of the Shastry-Sutherland lattice for the ratio $J'/J = 1/2$. The 3 sublattices, $\mathbf{S_A}$, $\mathbf{S_B}$, and $\mathbf{S_C}$, are represented by red, yellow and green circles. The 12 spin unit cell is depicted in bold lines.*

magnetic coupling $J'$ and over the diagonals with diagonal couplings $J$. The Hamiltonian Eq. III.45 is rewritten with classical spins as:

$$\mathscr{H} = \frac{J'}{J} \sum_{\text{edges}}^{N} \mathbf{S_i} \cdot \mathbf{S_j} + \sum_{\text{diagonal}}^{N} \mathbf{S_i} \cdot \mathbf{S_j} - \frac{h}{J} \sum_{i}^{N} S_i^z . \tag{III.46}$$

Under no magnetic field, Shastry and Sutherland showed that the lowest energy configuration is coplanar [136]. It is Néel ordered for $J'/J \geq 1$ else it is a spiral state with an angle $\varphi = \pi \pm \arccos\left(\frac{J'}{J}\right)$ between nearest-neighbor spins. The two possible optimum values for $\varphi$ give a discrete chiral degeneracy to each triangle. The choice of the angles $\varphi$ in two neighboring triangles determines the direction of the helix. Four helices are possible which creates a supplementary four-fold discrete degeneracy in addition to the continuous one [136].

In Section 2.2, the Hamiltonian for the Kagomé lattice was rewritten as a sum on triangles. For particular ratio of the magnetic couplings, the Hamiltonian of a frustrated system can sometimes be rewritten as a sum on elementary plaquettes. For instance it is the case for the frustrated square lattice with $J_{edges}/J_{diagonal} = 2$ [162] or for the checkerboard lattice with $J_{edges}/J_{diagonal} = 1$ [163]. In the Shastry-Sutherland lattice these plaquettes are triangles which share edges along the diagonal dimer bonds and otherwise corners. When the diagonal couplings are twice as big as the edge couplings (i.e. $J'/J = 1/2$) the Hamiltonian Eq. III.46 can be written as a sum over triangles up to a constant term:

$$\mathscr{H}_\Delta = \frac{1}{J} \sum_{\Delta}^{N_\Delta} \left( \frac{J'}{2} \mathbf{S}_\Delta^2 - \frac{h}{3} \mathbf{S}_\Delta \right) , \ (J'/J = 1/2) , \tag{III.47}$$

where $\mathbf{S}_\Delta = \sum_{i \in \Delta} \mathbf{S_i}$ is the total spin of one triangle and $N_\Delta$ is the number of triangles ($N_\Delta = N$). The classical ground state at zero temperature and in the absence of a magnetic field is a coplanar configuration with an angle $\varphi = \pm 2\pi/3$ between two nearest-neighbor spins. There are

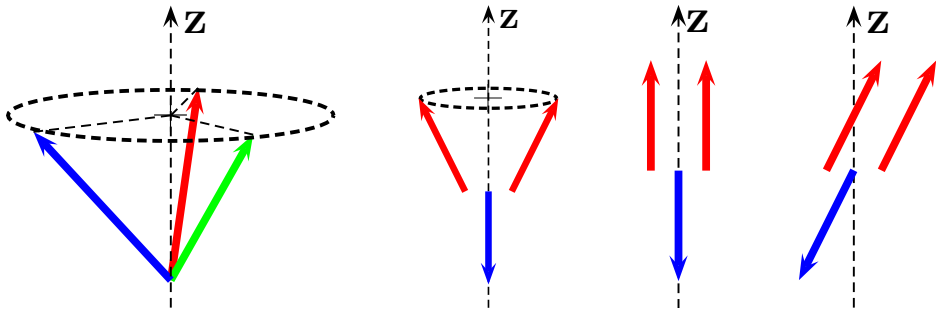


Figure III.17: *Spin configurations in a triangle: the umbrella (stable at $T = 0$), from low to high magnetic field: "Y -state", $UUD$ state and canted state*

three possible spin orientations $\mathbf{S_A}$, $\mathbf{S_B}$, and $\mathbf{S_C}$ and the unit cell contains 12 sublattices (see Fig. III.16 left panel). Minimizing the energy on a single triangle, one obtains the constraint:

$$\mathbf{S}_\Delta = \frac{\mathbf{h}}{3J'} \ , \ (J'/J = 1/2) \, . \tag{III.48}$$

The classical ground state is obtained when this constraint is satisfied in every triangle. The saturation field $h_{sat}$ is determined by the condition $S^z_\Delta = 3$ which gives $h_{sat} = 9J'$. At this value all the spins are aligned with the $z-$axis ("$UUU$ state"). We focus on the field range $0 \leq h \leq h_{sat}$. According to the classical constraint Eq. III.48 the classical ground state has only the typical global rotation as a degeneracy.

Let us have a closer look at the particular value $M/M_{\text{sat}} = 1/3$. The magnetic field to apply is:

$$h_{1/3} = 3J' \ , \ (J'/J = 1/2) \, . \tag{III.49}$$

Stable configurations at $h = h_{1/3}$ must verify $\mathbf{S}_\Delta = \mathbf{e}_z$. Very different spin configurations satisfy this requirement: the "umbrella configuration" and the "Up-Up-Down" state (see Fig. III.17). In the umbrella configuration the three kinds of spins raise as the field increases and they always have the same projection on the $z-$axis (at $M/M_{\text{sat}} = 1/3$, $S^z_A = S^z_B = S^z_C = 1/3$). In this case, the picture of the classical ground state with three kinds of spin orientations remains until saturation (see Fig. III.16 left panel). On the other hand the "Up-Up-Down" state ($UUD$ state) is a collinear state in which each triangle contains two spins Up and one spin Down (see left panel of Fig. III.19). As discussed in Section 1, this classical ground state is required in order to have a classical plateau at $M/M_{\text{sat}} = 1/3$ [111].
One can easily show that at zero temperature and $M/M_{\text{sat}} = 1/3$, both configurations, umbrella and $UUD$, have the same classical energy. Since energetic considerations do not favor the $UUD$ state its existence is restricted to the field value $h_{1/3}$. Hence no magnetization plateau can appear at zero temperature.

Minimizing the energy on triangles naturally leads to a comparison with the classical triangular lattice, with magnetic coupling $J_\Delta$ between nearest neighbors. This lattice was the subject of many theoretical studies [23, 24, 164]. Kawamura and Miyashita [24] studied classical Heisenberg spins on the triangular lattice in the presence of a magnetic field along the $z-$axis. They

obtained classical constraints that are strictly equivalent to Eq. III.48 for the Shastry-Sutherland lattice. Minimizing the energy of a single triangle they showed that the classical ground state is completely specified by the conditions:

$$\begin{aligned} \|\mathbf{S_A}\| = \|\mathbf{S_B}\| = \|\mathbf{S_C}\| &= 1\,, \\ \mathbf{S_A} + \mathbf{S_B} + \mathbf{S_C} &= \frac{\mathbf{h}}{3J_\Delta}\,,\ (h < h_{\text{sat}})\,. \end{aligned} \tag{III.50}$$

These constraints give information on the magnetization process of the classical triangular and Shastry-Sutherland lattices at zero temperature. Under the application of the magnetic field, the global symmetry of the Hamiltonian, $O(3)$, is reduced to $U(1)$. In other terms, at zero temperature and under a magnetic field, the 120° structure raises in the umbrella configuration that closes as the field increases and reaches the $UUU$ configuration at saturation.

## 4.4 Effects of thermal fluctuations

For non-zero temperature the scenario of the magnetization process is completely different. In the case of the triangular lattice with classical Heisenberg spins, Kawamura [23] showed that the non-trivial degeneracy no longer persists. Even in the low-temperature limit, the most favorable spin configuration is determined not only by its energy but also by the density of states just above the ground state. This entropic selection is responsible for the appearance of new phases. We expect the same scenario to take place in the Shastry-Sutherland lattice and in this section we treat in details how thermal fluctuations affect the magnetization process. But first let us review how thermal fluctuations affect other two-dimensional classical spin systems.

### 4.4.1 Thermal fluctuations in a couple of two-dimensional classical spins systems

The Kagomé lattice with classical Heisenberg spins was discussed without an applied magnetic field in Section 2.2 as an example of a system presenting *Order by Disorder* . This system presents one full branch of soft modes which favor coplanar spin configurations. Zhitomirsky [25] showed that *Order by Disorder* also takes place under an applied magnetic field. As $h \to h_{1/3}$, the system reaches the $UUD$ state. This configuration has zero modes and is therefore selected by thermal fluctuations. As a consequence a pseudo-plateau is observed at $M/M_{sat} = 1/3$. A phase diagram was obtained as a function of magnetic field and temperature showing the region of existence of those pseudo-plateaux.
Cabra *et al.* [165] added to that model anisotropy along the $z-$axis. They showed that it extends the $UUD$ region for energetic (and not entropic) reasons and the soft modes are removed. On the other hand quantum fluctuations seem to stabilize the 1/3 plateau.

However a full branch of soft modes is not a necessary condition in order to have entropic selection. In this section we review the effect of thermal fluctuations on the classical triangular and frustrated square lattices. The details of the calculations are given in App. B.

- **Triangular lattice:** The triangular lattice with classical spins exhibits a magnetization pseudo-plateau at $M/M_{sat} = 1/3$ at non-zero temperature. Kawamura and Miyashita [24]

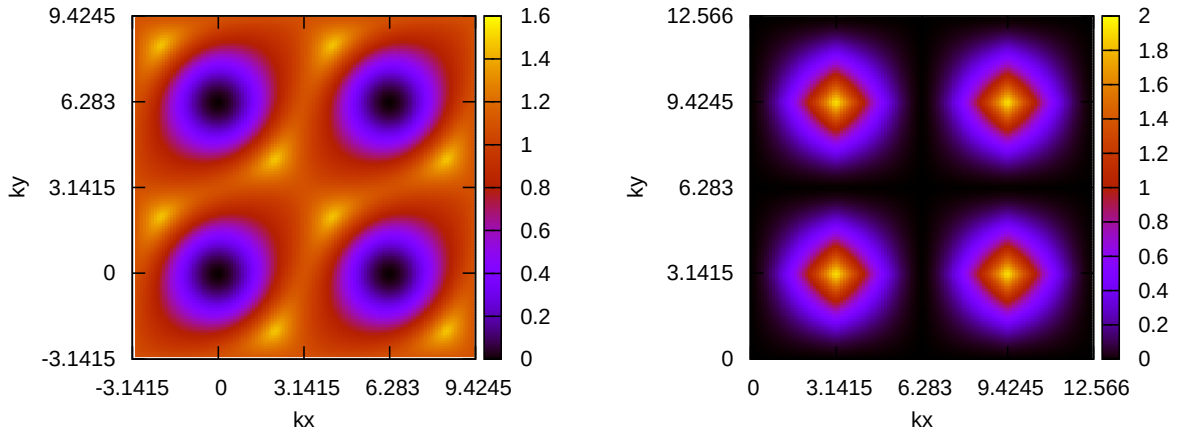


Figure III.18: *Spectra of fluctuation matrices in Fourier space* $(k_x, k_y)$ *over a couple of Brillouin zones. The darkest zones correspond to the cancellation of the eigenvalues. Left panel: "soft points" above the* $UUD$ *state in the triangular lattice with Heisenberg spins. Left panel: Lines of soft modes above the* $UUUD$ *state in the frustrated square lattice with Heisenberg spins.*

showed that at zero temperature, under an applied magnetic field the spins raise in the umbrella configuration. Using Monte Carlo simulations they obtained a phase diagram as a function of the applied magnetic field and temperature. At non zero temperature, below and until $h_{1/3}$, the spins lie in the collinear $UUD$ state. This phase is sandwiched between a $Y$ configuration (see Fig. III.17) in the low field region and the canted state (see Fig. III.17) in the high field region, before saturation. The matrix of thermal fluctuations up to second order is given in App. B. One can find a set of points in Fourier space that cancel the determinant. Hence this system only has *punctual soft modes*. The spectrum of the thermal fluctuations matrix obtained by exact diagonalization in the Fourier space is presented in Fig. III.18 (left panel). The dark spot corresponds to the "soft point". In this system, the $UUD$ state is favored by thermal fluctuations even though it only has "soft points".

Classical spins on the triangular lattice were also the subject of many studies with the plane rotator model ($XY$ model) with in-plane magnetic field [166–168]. Kawamura [23] performed classical spin-waves and showed that in this model as well the collinear $UUD$ is selected.

Quantum fluctuations on the $XY$ model on the triangular lattice were considered by Chubukov and Golosov [167] and it also confirms the selection if the $UUD$ state. However the main difference in the phase diagram is that the $UUD$ state survives even at zero temperature. Experimental confirmation of this phase diagram was given by Tsujii *et al.* [169] with the compound $Cs_2CuBr_4$.

- **Frustrated square lattice:** The frustrated square lattice with classical Heisenberg spins

and for the particular ratio $J_{edges}/J_{diagonal} = 2$ exhibits a magnetization plateau at $M/M_{sat} = 1/2$ [162]. At $M/M_{sat} = 1/2$ the system lies in a collinear configuration in which each square contains three spins Up and and spin Down ($UUUD$ configuration). Lines of Up spins ($UUU\ldots UUU$) alternate with lines of Up and Down spins ($UDU\ldots DUD$). The matrix of the thermal fluctuations up to second order is detailed in App. B. This system does not have any full branch of soft modes but one can find *lines* of soft modes defined by relations between $k_x$ and $k_y$ so that the determinant of the matrix cancels. The spectrum of the thermal fluctuations matrix obtained by exact diagonalization is presented in Fig. III.18 (right panel). These soft modes correspond to a continuous rotation of the spins of the Up-Down lines which costs no energy in the harmonic approximation.
On the other hand quantum fluctuations in this system also seem to favor collinear states. The magnon spectrum of the $\mathbf{q} = \mathbf{0}$ $UUUD$ configuration is gaped and quantum fluctuations allow the appearance of a real magnetization plateau at $M/M_{sat} = 1/2$.

### 4.4.2 Thermal fluctuations in the Shastry-Sutherland lattice

The Monte Carlo simulations reported in the forthcoming Section 4.5 indicate that, at finite temperature, the $UUD$ state is the favored configuration for a magnetic field range below and until $h = h_{1/3}$. This is possible if thermal fluctuations raise the entropy of the $UUD$ state relatively to adjacent states. Kawamura and Miyashita [23, 24] showed that in the case of the triangular lattice non-zero temperature lifts the degeneracy of the classical ground state in the presence of a magnetic field. Also on the Shastry-Sutherland lattice only a discrete degeneracy due to the possible chiralities of the triangles remains.

Following the same steps as described in Section 2.1 for the Kagomé lattice, we calculated the spectrum of the $UUD$ state in the quadratic approximation in thermal fluctuations by applying small deviations on the spin coordinates from the collinear $UUD$ state [120]. At zero temperature the 12 sublattices of the unit cell presented in Fig. III.19 (left panel) are collinear with the $z-$axis. Under non-zero temperature their new coordinates are expressed in their own frame as:

$$\mathbf{S_i}(\mathbf{r}_i) = \left(\epsilon_i^x(\mathbf{r}_i), \epsilon_i^y(\mathbf{r}_i), 1 - \alpha_i(\mathbf{r}_i)\right), \tag{III.51}$$

where $\alpha_i = 1/2\left((\epsilon_i^x)^2 + (\epsilon_i^y)^2\right)$ is verifying the condition $\|\mathbf{S_i}\| = 1$ up to quadratic order.
Following Ref. [11] the Hamiltonian is expanded in spin deviations from the $UUD$ state:

$$\mathscr{H} = E_{UUD} + \sum_{n\geq 2} \mathscr{H}_n, \tag{III.52}$$

where $E_{UUD}$ is the classical energy and $\mathscr{H}_n \sim \mathscr{O}(\epsilon^n)$. Up to second order in those fluctuations the Hamiltonian becomes, in Fourier space:

$$\mathscr{H}_2 = \sum_{\mathbf{k}, v=x,y} \mathscr{V}_v^t(-\mathbf{k}) \mathscr{M} \mathscr{V}_v(\mathbf{k}). \tag{III.53}$$

Fluctuations are applied on the 12 sublattices of the unit cell and the vectors $\mathscr{V}_v^t(-\mathbf{k})$ $(v = x, y)$ read:

$$\mathscr{V}_v^t(-\mathbf{k}) = \left(\tilde{\epsilon}_1^v(-\mathbf{k}), \ldots, \tilde{\epsilon}_{12}^v(-\mathbf{k})\right) \tag{III.54}$$

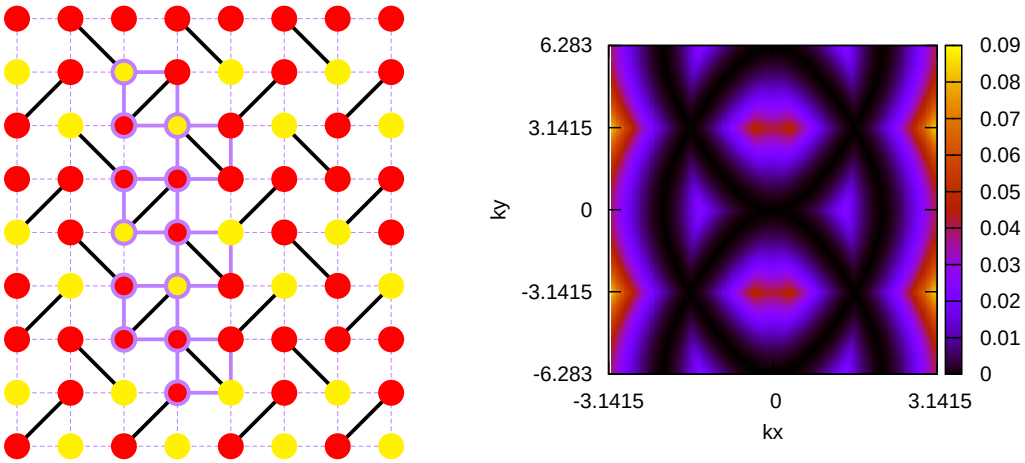


Figure III.19: *Left panel: Spin texture of the Shastry-Sutherland lattice in the UUD state at* $M/M_{sat} = 1/3$. *Each triangle contains two spins Up (red) and one spin down (yellow) The 12 spin unit cell is depicted in bold lines. Right panel: Spectrum of the fluctuation matrix above the UUD state in Fourier space* $(k_x, k_y)$ *obtained by exact diagonalization. In the darkest regions, the black lines represent the lines of soft modes whose analytical expressions are given in the text.*

$\mathscr{M}$ is a $12 \times 12$ matrix which exact expression is given in App. B. Fluctuations act exactly the same way on the $x$- and $y$-components and as a consequence the matrices are the same for fluctuations in the $x$- and $y$-directions. Eigenvalues should be determined by solving an order 12 polynomial which cannot be done analytically. However, we can determine the soft modes from the zeros of the determinant which reads:

$$\det(\mathscr{M}) \propto \left(-2 + 3\cos k_x - 3\cos 2k_x + \cos 3k_x + \cos k_y\right)^2 \tag{III.55}$$

This result shows that we have lines of soft modes, but no full branch.

We further performed numerical diagonalization of $\mathscr{M}$ at each point in the Fourier space $(k_x, k_y)$. For each point the smallest eigenvalue was selected in order to obtain a picture of the ground state. Fig. III.19 shows the picture obtained over a couple of Brillouin zones. The darkest regions correspond to the lowest points and we indeed observe *lines* of soft modes corresponding to a cancellation of the quadratic energy. The height of the barriers between those lines is $\Delta E \approx = 0.1$ meaning that low-temperature behavior is expected to appear only for $T \lesssim 0.1$. The analytical expression of the lines of soft modes can be found by finding relations between $k_x$ and $k_y$ so that the determinant Eq. III.55 vanishes:

$$k_x = \pm \arccos\left(\frac{1}{2} - \frac{(1 \pm i\sqrt{3})(1 - u(k_y))}{4u(k_y)}\right), \tag{III.56}$$

where $u(k_y) = (\sqrt{\cos^2 k_y - 1} - \cos k_y)^{-1/3}$.

Champion and Holdsworth [170] considered the pyrochlore lattice with a planar constraint. They obtained planes in reciprocal space in which at least one eigenvalue cancels. Using the counting arguments developed by Chalker *et al.* [11], they showed that the expression of the specific heat per spin should be:

$$\frac{C_h}{Nk_BT} = \frac{1}{2} - C.\frac{1}{L} \tag{III.57}$$

where $L$ is the system size ($N = L^2$) and $C$ is a constant related with the number of soft modes. Then they computed with Monte Carlo the specific heat at very low temperature ($T/J = 0.0001$) for various system size $L$. They obtained a straight line when plotting $1/2 - C_h/Nk_BT$ as a function of $1/L$, meaning that the *Order by Disorder* scenario was correct.

Following the calculations performed by Champion and Holdsworth in the pyrochlore lattice, the specific heat $C_h$ per spin of the Shastry-Sutherland lattice is given by:

$$\frac{C_h}{Nk_BT} = 1 - \gamma\frac{1}{L}, \tag{III.58}$$

where $\gamma$ is a constant related with the number of lines of soft modes.
The manifold of soft modes for the Shastry-Sutherland lattice with magnetic couplings verifying $J'/J = 1/2$ scales like $L$ in a $L^2$ Fourier space. Eq. III.58 clearly shows that the drop in the specific heat, or in other terms the effect of the soft modes, will disappear in the thermodynamic limit. The lines of soft modes are reminiscent of the $\mathbf{q} = \mathbf{0}$ $UUUD$ state in the frustrated square lattice [162]. However, the precise mechanism is somewhat different in the Shastry-Sutherland lattice since here the soft modes do not correspond to continuous deformations of the ground state. Nevertheless, the $UUD$ state is still selected for entropic reasons, like in the triangular lattice [23, 24]: the soft modes simply result in a free energy which is lower for the $UUD$ state than for non-collinear phases. The triangular lattice with classical Heisenberg spins does not have full branches of soft modes either, but the manifold of soft modes consists of points in Fourier space. Still, the triangular lattice exhibits pseudo-plateaux at finite temperature.

## 4.5 Monte Carlo simulations on the Shastry-Sutherland lattice

We performed Monte Carlo simulations using a standard single-spin flip Metropolis algorithm [108]. As a small refinement, we propose changes of the spin projection along and perpendicular to the field direction independently. Pseudo random numbers were generated by the Mersenne-Twister random number generator [171]. We studied square samples ($L_x = L_y = L = \sqrt{N}$) with periodic boundary conditions. Their sizes are chosen so as to be commensurate with the 12 sublattice unit cell represented in Fig. III.19 (left panel): $L = 6, 12, 18, 24$, and 30. In the simulations the diagonal coupling $J$ is set to 1. Monte Carlo simulations computed in particular the magnetization, the susceptibility $\chi = dM/dh$ and the specific heat $C_h$. All physical quantities are normalized per spin. After reaching thermal equilibrium, data was collected with up to $\sim 10^7$ Monte Carlo steps per point depending on the size and temperature considered. Error bars are determined from independent Monte Carlo runs (the

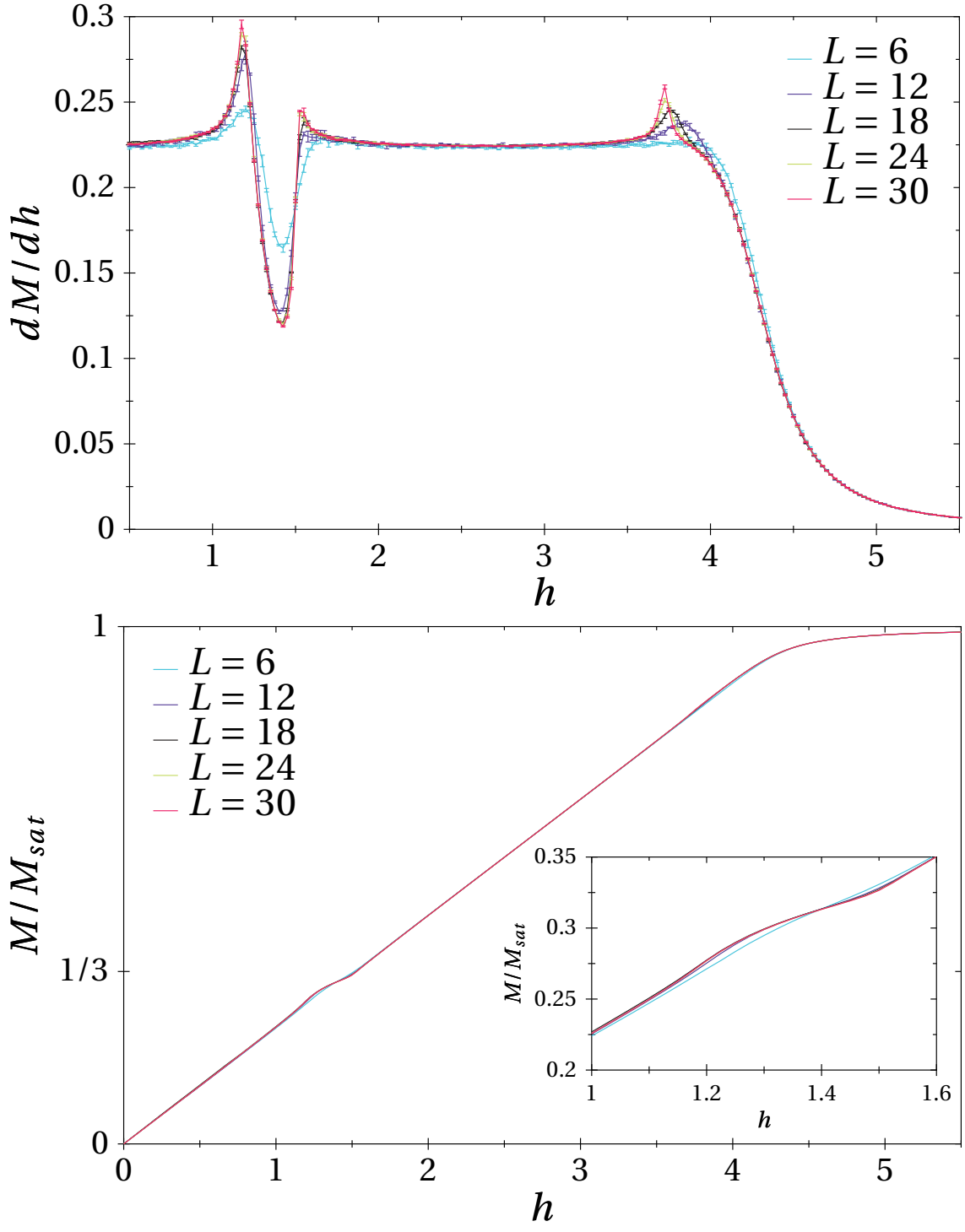


Figure III.20: *Susceptibility (upper panel) and magnetization (lower panel) as a function of the magnetic field of the Shastry-Sutherland lattice for various system sizes ($J'/J = 1/2$ and T=0.02). The inset shows a zoom on the magnetization pseudo-plateaux.*

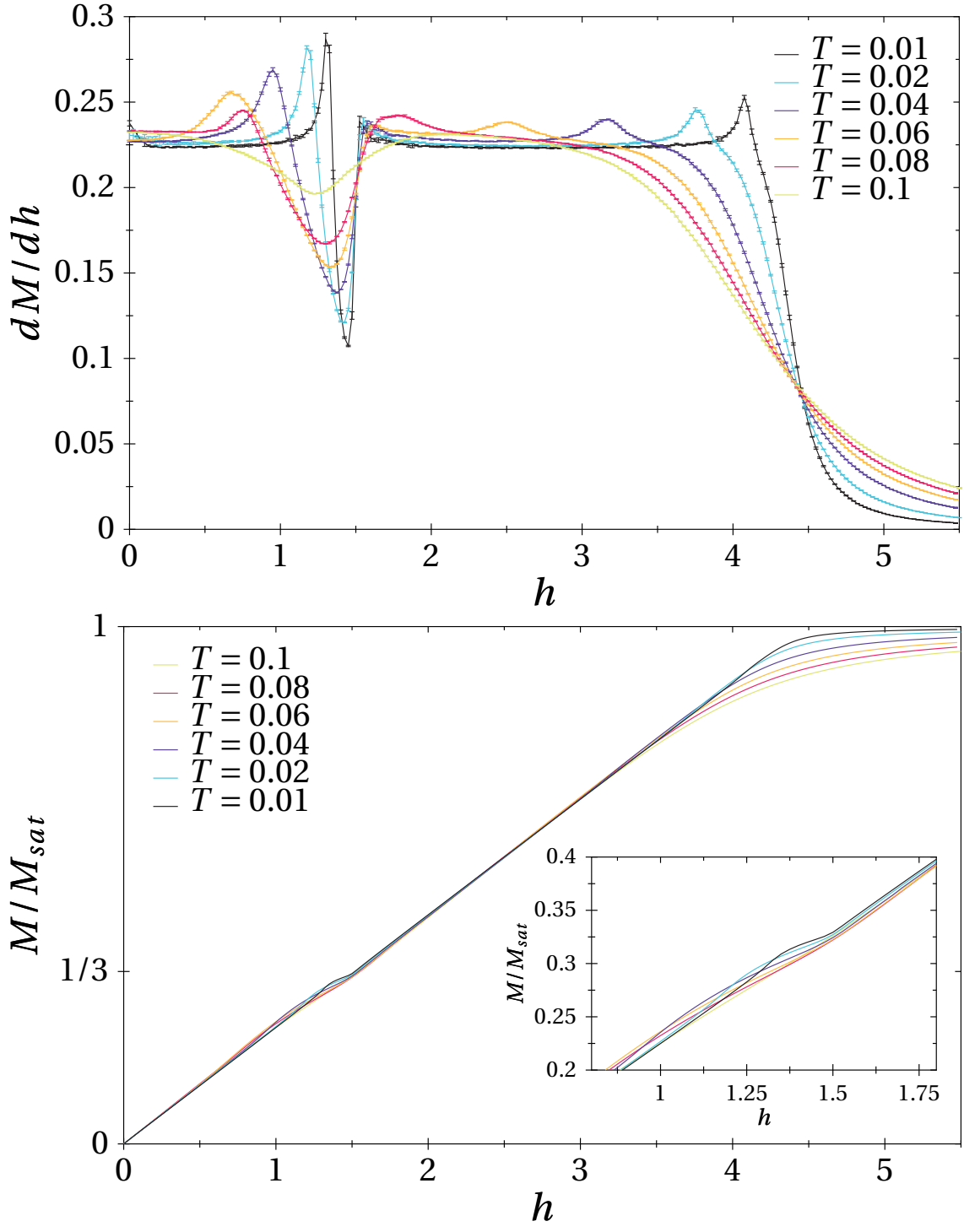


Figure III.21: *Susceptibility (upper panel) and magnetization (lower panel) as a function of the magnetic field of the Shastry-Sutherland lattice at different temperatures ($J'/J = 1/2$ and $L = 18$). The inset gives a zoom on the magnetization pseudo-plateaux.*

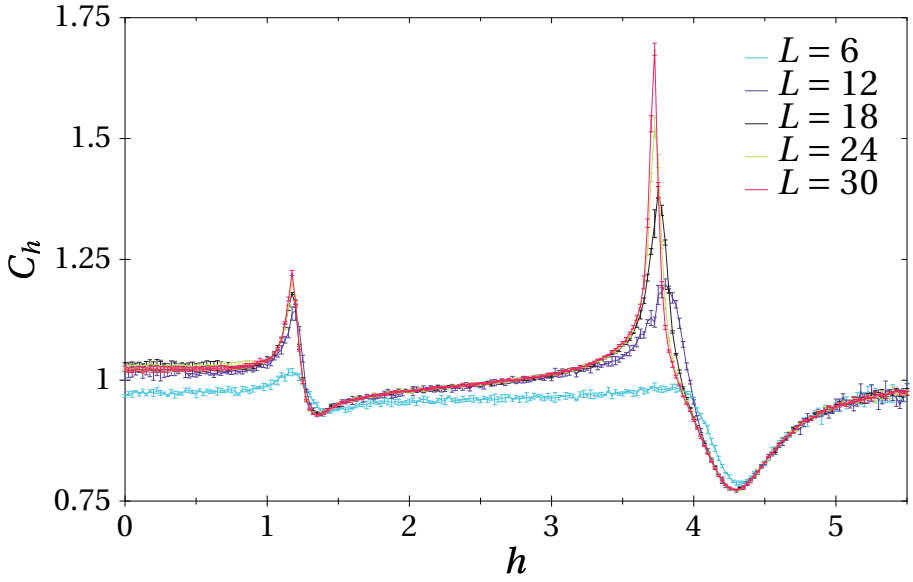


Figure III.22: *Specific heat of the Shastry-Sutherland lattice with* $J'/J = 1/2$ *at* $T = 0.02$ *and for various system sizes.*

average number of simulations per point is five).

Fig. III.20 shows the susceptibility and the magnetization as a function of the system size at $J'/J = 1/2$ for $T = 0.02$. A pseudo-plateau is observed in the magnetization curve at $M/M_{\text{sat}} = 1/3$ (see inset in the magnetization curve). Following the previous analytical discussion this means that the $UUD$ configuration is thermally selected at this temperature. Its existence in no longer strictly limited to one single point at $h = h_{1/3}$, but it exists for a range of magnetic field values below and until $h_{1/3}$. The width of those pseudo-plateaux increases with system size. Moreover the peaks in the susceptibility become sharper and higher as the system size increases. This indicates the presence of phase transitions to the $UUD$ state.

The stability of the susceptibility peak positions and height for $L \geq 18$ show that $L = 18$ captures reasonably well the behavior of the plateau region in the thermodynamic limit. Fig. III.21 shows the effect of the temperature on the susceptibility and magnetization for a $L = 18$ system. The magnetization curve should tend to a straight line as the temperature decreases. This is confirmed by the Monte Carlo simulations: at very low temperature (see $T = 0.01$ in Fig. III.21) the pseudo-plateau is extremely small. The susceptibility presents two very sharp peaks around $h_{1/3}$. As the temperature increases the pseudo-plateau becomes broader, which confirms the entropic selection of the $UUD$ state in the plateau phase. Finally higher temperature (see $T = 0.1$ in Fig. III.21) destroys it. The peaks in the susceptibility curve become rounded and then completely disappear.

The specific heat $C_h$ (Fig. III.22) exhibits a first peak attributed to the transition from the collinear $UUD$ state to a low magnetic field state that will be detailed in Section 4.6. Monte

Carlo simulations on system sizes $L = 6 - 42$ showed that the height of this peak scales with increasing system size as $\sim L^{\alpha/\nu}$ with $\alpha/\nu \ll 1$ which suggests a continuous phase transition.

## 4.6 Phase diagram for $J'/J = 1/2$

Next we discuss the domain of existence of the $UUD$ collinear phase in the $(h, T)$ plane. Up to 5 Monte Carlo simulations per point were performed on a $L = 12$ ($N = 144$) system which gives a good qualitative picture of the position and nature of the phases. Both temperature and magnetic field scans were performed. The boundaries of the phases are determined by the positions of the peaks in the susceptibility $\chi$. Fig. III.24 shows this schematic phase diagram in the plane $(h, T)$. Numbers are attributed to the susceptibility peaks from low to high magnetic field in magnetic field scans (curves with circles) and from low to high temperature in temperature scans (curves with triangles).

We simulated by means of Monte Carlo the spin texture for $L = 18$ systems in order to obtain a qualitative picture of the spin configuration in the phases below and above the $UUD$ phase (see $UUD$ in Fig. III.23, left panel). Like in the classical triangular lattice the magnetization process at finite temperature is very different from the one at zero temperature. The phase in the low-field region is the "$Y$ configuration" (see Fig. III.17). In this configuration each triangle contains two spins above the $(x, y)$ plane while the last one is pointing down and is almost collinear with the $z-$axis. This state is characterized by a single angle between the two spins pointing in the positive $z-$direction. The $Y$ configuration breaks the rotational symmetry around the $z-$axis and as a consequence of the Mermin-Wagner theorem [172] cannot be long-range ordered for $T > 0$. The spins above the $(x, y)$ plane are at most quasi-long-range-ordered with correlation functions that decay algebraically. On the other hand one can expect long-range order on the remaining down spin sublattices.

Then in a magnetic field range below and until $h_{1/3}$ the collinear $UUD$ state is the lowest energy configuration. As the temperature goes to zero, the width of this phase converges to a single point at exactly $h = h_{1/3} = 3/2$ which is in complete agreement with the analytical prediction. This phase does not break the $U(1)$ symmetry and hence true long-range order is realized.

In the high-field region the ground state is the "canted state" (see Fig. III.17). In this state the spins down are raising as the magnetic field increases while the spins up are no longer collinear with the $z-$axis. This state is characterized by two angles: one between the $z-$axis and the two spins above the $(x, y)$ plane and one between the $z-$axis and the single spin below the $(x, y)$ plane. As in the $Y$ phase, at most quasi-long-range order is expected at finite temperature.

In the higher field region the system reaches saturation and all spins are pointing up collinearly with the $z-$axis ($UUU$ state). The zero-temperature limit of the saturation field is $h_{\text{sat}} = 9/2$, as derived in Section 4.3. At higher temperature the system enters the disordered paramagnetic phase. The highest temperature were the $UUD$ state still exists $T^*$ is estimated

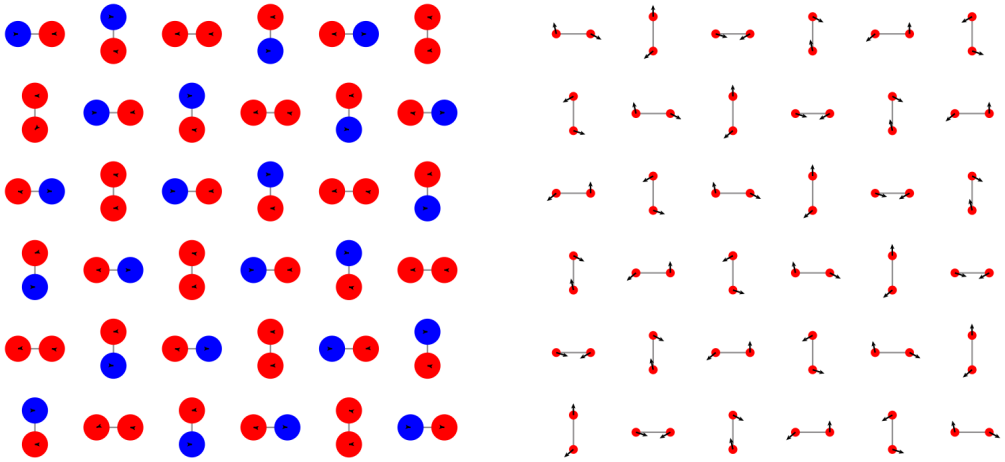

Figure III.23: *Spin texture at $M/M_{sat} = 1/3$ given by Monte Carlo. The Shastry-Sutherland lattice is viewed in the $(x, y)$ plane. The arrows denote the projection of the spins in this plane, whereas the circles represent their $z-$component (red for $S^z > 0$, blue otherwise and radius proportional to $|S^z|$). Left panel: UUD configuration for $J'/J = 1/2$. Right panel: $J'/J = 0.4$, umbrella with $S^z = 1/3$ for all spins.*

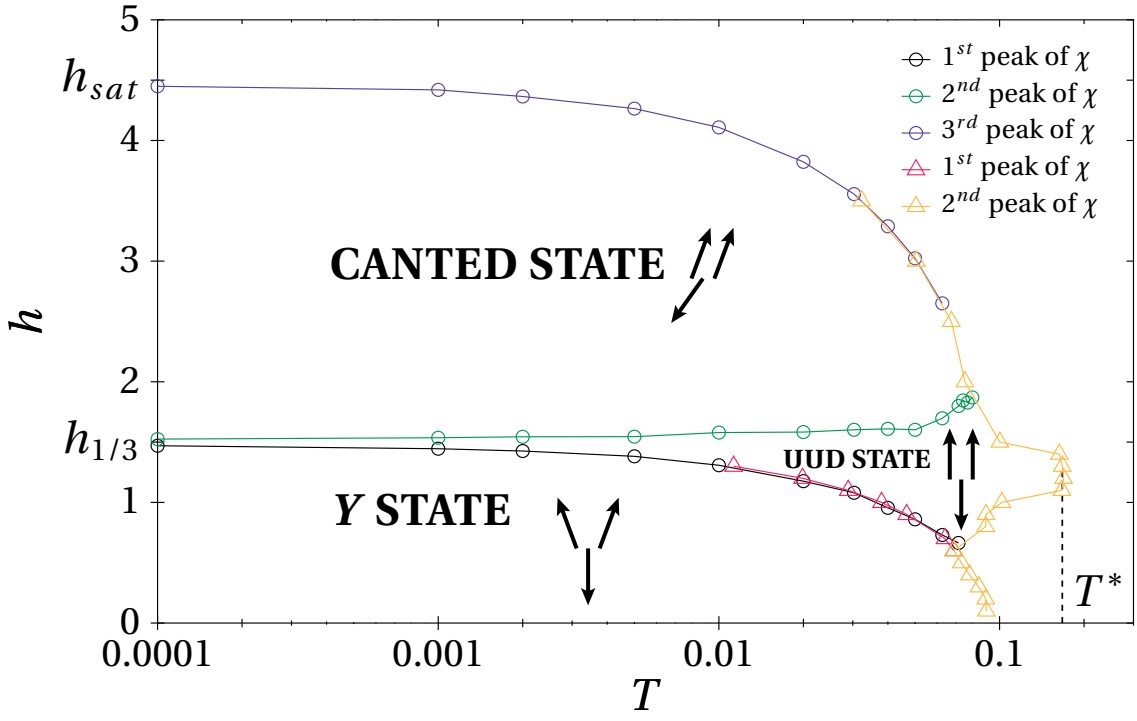


Figure III.24: *Phase diagram of the classical Shastry-Sutherland lattice for the ratio of the magnetic couplings $J'/J = 1/2$.*

as $T^* \approx 0.17$. Note that the classical spin-wave spectrum contains energy barriers between lines of soft modes of the same order of magnitude. Hence this temperature agrees with the range of temperatures in which we expected the low-temperature behavior to appear.

The phase diagram of the Shastry-Sutherland lattice with the particular coupling ratio $J'/J = 1/2$ presents similarities with the one of the classical triangular [24] and Kagomé [25] lattices. Watarai *et al.* [173] suggested that in the classical triangular lattice with Heisenberg spins these transitions could be of the second order. The scaling of the specific heat shown in Fig. III.22 is in agreement with a continuous transition. We propose that a Berezinskiĭ-Kosterlitz-Thouless transition [174–176] takes place as the system enters the $UUD$ phase. Following what was obtained in the case the triangular lattice, the transition from the collinear $UUD$ state to the disordered phase should belong to the universality class of the three-state Potts model [177, 178].

## 4.7 Study of ratios $J'/J = 1/2 \pm \epsilon$

In this section we consider now a small deviation $\epsilon$ from the ratio $J'/J = 1/2$. In the following discussion we use Monte Carlo results for $J'/J = 0.4$ (i.e. $\epsilon = -0.1$). We observed that qualitatively similar behavior also appears for the other sign of $\epsilon$.
We performed Monte Carlo simulations on systems sizes $L = 6, 12, 18, 24$, and 30. Data were collected with up to $10^7$ Monte Carlo steps per point. Figure III.25 shows the susceptibility and the magnetization as a function of the magnetic field at the same temperature as in Fig. III.20 for the ratio $J'/J = 1/2$. The susceptibility still presents two peaks around $M/M_{\text{sat}} = 1/3$ and a pseudo-plateau is observed in the magnetization curve. Therefore one can expect $UUD$ to be the selected configuration at $T = 0.02$ even for ratios $J'/J = 1/2 + \epsilon$. According to the position of the peaks of the susceptibility, the width of the pseudo-plateau increases as the system size increases.

Following exactly the same calculations as the ones presented in Section 4.4.2 for $J'/J = 1/2$, we applied thermal fluctuations on top of the $UUD$ state for the ratio $J'/J = 0.4$. We found that $UUD$ is no longer the favored configuration in the quadratic approximation for the spin deviations. In other words, the collinear $UUD$ state is no longer selected at "very low temperatures" for $J'/J \neq 1/2$. We used Monte Carlo simulations in order to obtain a picture of the spin configuration in the temperature range $T < 0.001$. It turns out that the favored configuration is an umbrella that is closing until saturation as the magnetic field increases (see Fig. III.23, right panel). At "higher temperature" ($T \geq 0.01$) we observed that for $h \approx h_{1/3}$ the system enters the $UUD$ phase. This "high temperature" regime is not analytically accessible with lowest-order thermal fluctuations.

We performed magnetic field and temperature scans in order to determine the region in which the $UUD$ state survives. Figure III.26 shows a schematic phase diagram for the Shastry-Sutherland lattice at $J'/J = 1/2 + \epsilon = 0.4$ in the $(h, T)$ plane.
Five separate simulations per point were performed on $L = 12$ systems. Monte Carlo data were collected up to $10^7$ Monte Carlo steps per point. Temperature (circles) and field (triangles)

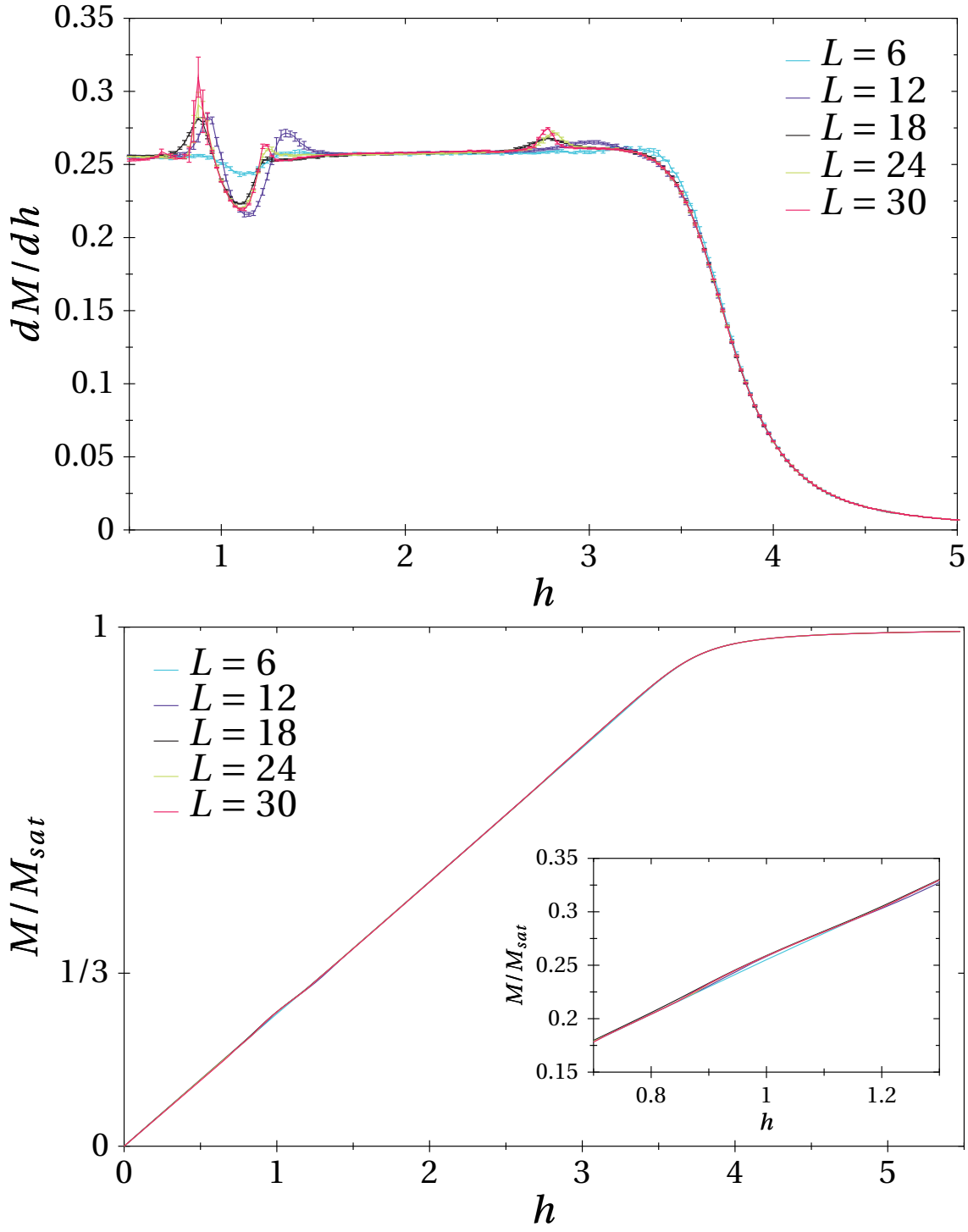


Figure III.25: *Susceptibility (upper panel) and magnetization (lower panel) as a function of the magnetic field of the Shastry-Sutherland lattice for various system sizes ($J'/J = 0.4$ and T=0.02). The inset gives a zoom on the magnetization pseudo-plateaux.*

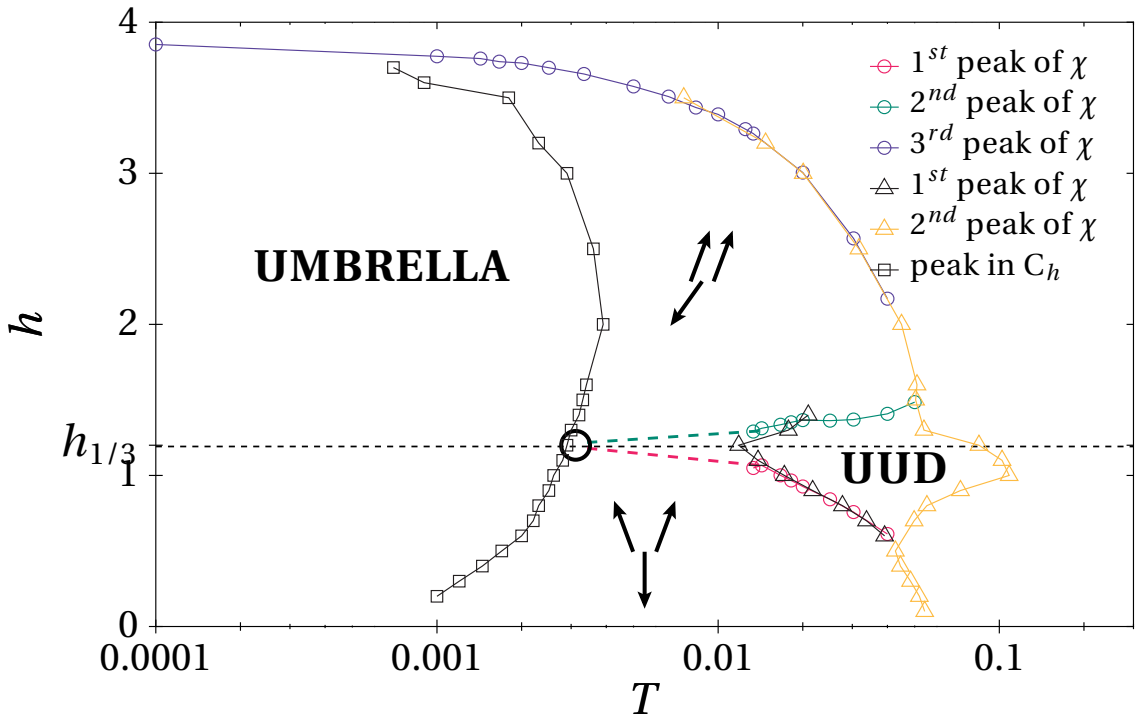


Figure III.26: *Phase diagram of the classical Shastry-Sutherland lattice for the ratio of the magnetic couplings* $J'/J = 1/2 \pm \epsilon$.

scans were performed with the same ordering of the susceptibility peaks as in Section 4.6. As one expects from the analytical arguments, the resulting phase diagram differs from the case $J'/J = 1/2$. In the lowest temperature region, the system undergoes the same kind of magnetization process as at zero temperature: the coplanar spiral becomes an umbrella configuration as the magnetic field increases. The angle between two nearest-neighbor spins is $\pi \pm \arccos(1/2+\epsilon)$. Hence, the spiral at zero temperature is not exactly commensurate with a 12 spin unit cell. However, as the temperature increases the spin positions fluctuate and a 12 sublattice unit cell is recovered in average on the spin positions. Hence we suggest that the transition from the umbrella to the phases with 12 sublattices (black square in Fig. III.26) is an incommensurate-commensurate phase transition.

At higher temperature we recover the three phases that were obtained for $J'/J = 1/2$ in different magnetic field regions. In the low-field region we still obtain the "$Y$ configuration" and in the high-field region, before saturation, the "canted state". The long-range-ordered $UUD$ collinear state still survives in a small region between the two aforementioned phases. For $T < 0.01$ the $UUD$ phase is expected to become narrower as the temperature decreases (dashed bold lines). A precise determination how the four phases merge (black circle) is beyond the scope of this work.

## 4.8 Influence of lattice distortions on the Shastry-Sutherland lattice

In the previous section we discussed the presence of magnetization pseudo-plateaux in the Shastry-Sutherland lattice at $M/M_{sat} = 1/3$. We showed that since they are due to the entropic selection of the collinear $UUD$ state they no longer exist at zero temperature. Following the study done on the $J_1 - J_2$ frustrated classical spin chain (see Sec. 3), we started to study the influence of lattice distortions on the Shastry-Sutherland lattice with classical Heisenberg spins. The aim is to determine if lattice distortions can induce a magnetization plateau at $M/M_{sat} = 1/3$ even at zero temperature by stabilizing the $UUD$ state.

A model for the quantum Shastry-Sutherland lattice with lattice distortions was previously considered by Miyahara *et al.* [179]. They studied the effect of adiabatic phonons on the $S = 1/2$ dimer model by means of self-consistent Lanczos diagonalization of small clusters. They showed that spin-lattice coupling can stabilize particular spin textures in the plateaux at $M/M_{sat} = 1/2, 1/3, 1/4$ and $1/8$ plateau of $SrCu_2(BO_3)_2$. In particular they recovered in the $1/8$ plateau the spins patterns previously suggested by the hard-core boson approach [180] and that is in agreement with the NMR experimental results [141].
Once the lattice distortions are added, the Shastry-Sutherland lattice depicted in the left panel of Fig. III.11 is no longer equivalent to the one in the right panel. In order to stick with the real compound $SrCu_2(BO_3)_2$ Miyahara *et al.* focused on the latter. Their Hamiltonian is the following:

$$\begin{aligned} \mathcal{H}_{qSSL} &= \sum_{dimers} \left\{ J(d_{ij})\hat{s_i}.\hat{s_j} + \frac{K}{2}\left(\frac{\|\delta\mathbf{r}_i - \delta\mathbf{r}_j\|}{d^0_{ij}}\right)^2 \right\} \\ &+ \sum_{NNN} \left\{ J'(d_{ij})\hat{s_i}.\hat{s_j} + \frac{K'}{2}\left(\frac{\|\delta\mathbf{r}_i - \delta\mathbf{r}_j\|}{d^0_{ij}}\right)^2 \right\} \end{aligned} \tag{III.59}$$

where $\hat{s_i}$ is the spin$-1/2$ operator at the site $i$, $K$ and $K'$ are elastic constants. $d^0_{ij} = \|\mathbf{r}^0_i - \mathbf{r}^0_j\|$ is the equilibrium distance between the copper sites $i$ and $j$ with coordinates $\mathbf{r}^0_i$ and $\mathbf{r}^0_j$. $d_{ij}$ is the relative distance between sites $i$ and $j$: $d_{ij} = \|\mathbf{r}^0_i + \delta\mathbf{r}_i - \mathbf{r}^0_j - \delta\mathbf{r}_j\|$. $\delta d_{ij} = d_{ij} - d^0_{ij}$ is the displacement of the sites. It is assumed to be small enough (i.e. $\delta d_{ij} \approx (\mathbf{r}^0_i - \mathbf{r}^0_j)(\delta\mathbf{r}_i - \delta\mathbf{r}_j)$) so that the antiferromagnetic couplings $J(d_{ij})$ and $J'(d_{ij})$ can be linearized:

$$J(d_{ij}) = J\big(\frac{d_{ij}}{d^0_{ij}}\big)^{\alpha} \approx J\big(1 - \alpha\frac{\delta d_{ij}}{d^0_{ij}}\big) \tag{III.60}$$

We performed preliminary Monte Carlo simulations on the Shastry-Sutherland lattice with classical Heisenberg spins and lattice distortions, using Eq. III.59 as an ansatz. We conserved $J'/J = 1/2$ since we know that, for this ratio, a pseudo-plateau exists at $M/M_{sat} = 1/3$ for non zero temperature. In order to stick with the results of Miyahara *et al.* for the quantum case, we used $\alpha' = 1.75\alpha$ and $K = K' = 1000$. Figure III.27 shows a result of a simulation for $\alpha = 10$ (red curve) and for the undistorted system (black curve). On the one hand, the temperature is low enough so that the case without phonons presents no plateau ($T \sim 10^{-8} J$). This means that it is low enough so as to capture the behavior in the zero temperature limit. On the other hand, the

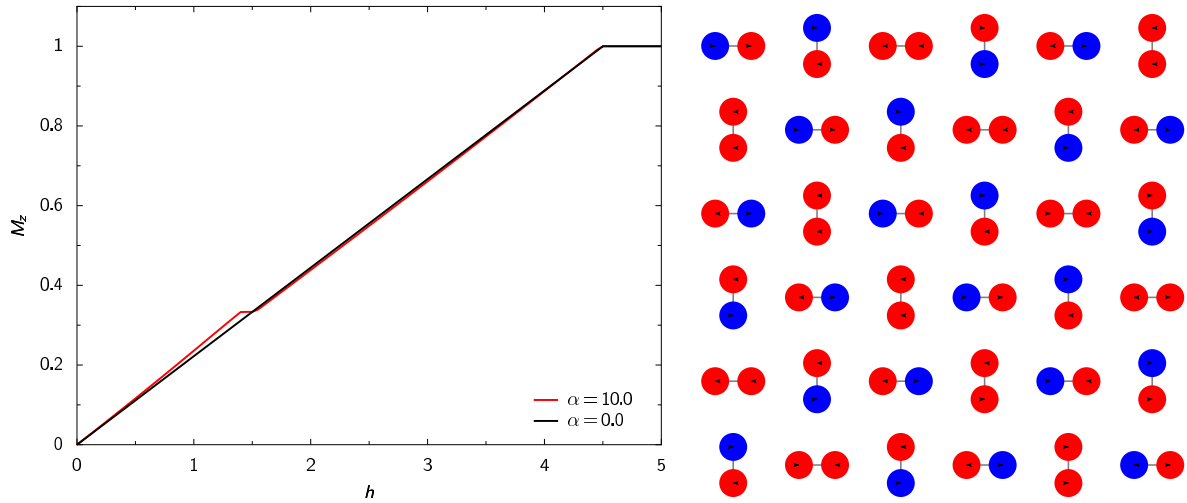


Figure III.27: *Left panel: Magnetization curve of the Shastry-Sutherland lattice* ($J'/J = 1/2$) *with (red) and without (black) lattice distortions* ($\alpha' = 1.75\alpha$, $K = K' = 1000$, $T \sim 0$). *Right panel: Monte Carlo simulation of the spin texture in the* $M/M_{sat} = 1/3$ *plateau. It show that the* $UUD$ *configuration survives for* $T \to 0$ *(Up spins in red, Down in blue). Monte Carlo simulations by F. Stauffer.*

red curve exhibits a plateau at $M/M_{sat} = 1/3$. Moreover, snapshots of the spin texture in the plateau were performed on 72 spins systems (commensurate with the 12 spins unit cell) and it clearly appear that the spins configuration is the $UUD$ state (see Fig. III.27, right panel).
To summarize, Monte Carlo simulations indicate that lattice distortions stabilize the collinear $UUD$ state even in the limit $T \to 0$. A real plateau at $M/M_{sat} = 1/3$ is observed and it is much wider than what was observed at non zero-temperature in the undistorted case.

Following the work done analytically on the $J_1 - J_2$ chain, let us rewrite the Hamiltonian with *classical* Heisenberg spins taking into account the previous approximations. The Hamiltonian of the Shastry-Sutherland lattice with classical spins, coupled with lattice distortions and under an applied magnetic field reads:

$$\begin{aligned} \mathcal{H}_{cSSL} &= \frac{K}{2}\sum_{dimers}\delta_{ij} + \frac{K'}{2}\sum_{NNN}\delta_{ij} \\ &+ J\sum_{dimers}(1-\alpha\delta_{ij})\mathbf{S_i}.\mathbf{S_j} + J'\sum_{NNN}(1-\alpha'\delta_{ij})\mathbf{S_i}.\mathbf{S_j} - h\sum_i S_i^z \end{aligned} \tag{III.61}$$

In this two-dimensional lattice, distortions are coupled and cannot be integrated as in the $J_1-J_2$ chain. In order to obtain a simpler model, we made a couple of assumptions on the deformations of the lattice:

- Deformations are applied on the $J$ bonds only and as a consequence, $J'$ bonds also are distorted.

- $J'$ bonds are the edges of isosceles triangles. Using experimental results as an input we

consider that those triangles remain isosceles after applying the deformations. As a consequence, the $J$ bonds can elongate but not rotate.

Even under these approximations, to many degrees of freedom were left in the Hamiltonian and an analytical treatments such as in the $J_1 - J_2$ chain is not possible.

However these approximations give informations on the stability of the spin structure in the $M/M_{sat} = 1/3$ plateau. We consider the $UUD$ spins structure of Fig.III.27, left panel. Due to antiferromagnetic couplings, the lattice distortions should tend to increase the Up-Up bonds' length and the decrease Up-Down's. We consider three kinds of deformations: $\delta_1$ and $\delta_3$ on Up-Up $J$ bonds [4] and $\delta_2$ on Up-Down $J$ bonds.
The classical energy for this deformed $UUD$ state can be calculated:

$$\begin{aligned} E &= E_0 + 2\delta_1^2[2K + K'(\lambda_b^2 + \lambda_s^2 + (\lambda_s + \lambda_b)^2)] + 4A\delta_1(J + J'\lambda_s) \\ &\quad + 4\delta_2^2[K + K'(\lambda_b^2 + \lambda_s^2)] + 4A\delta_2(-J + 2J'\lambda_b) \\ &\quad + 2\delta_3^2[2K + K'(\lambda_b^2 + \lambda_s^2 + (\lambda_s + \lambda_b)^2)] + 4A\delta_3(J + J'\lambda_s) \\ &\quad + 8K'\lambda_b\lambda_s\delta_2(\delta_1 + \delta_3) \\ &= E_0 + \beta_1\delta_1^2 + \beta_2\delta_1 + \beta_3\delta_2^2 + \beta_4\delta_2 + \beta_5\delta_3^2 + \beta_6\delta_3 + \beta_7\delta_2(\delta_1 + \delta_3) \end{aligned} \tag{III.62}$$

Here $E_0$ stands for the energy of the undistorted $UUD$ state. $\lambda_b$ and $\lambda_s$ are constants that depend on the values of the base and edges of the triangles. This energy can be minimized for the distortions $\delta_i$:

$$\delta_1 = \delta_3 = \delta^+ = \frac{-2\beta_6\beta_7\beta_2 - \beta_7^2\beta_1 + 4\beta_6\beta_5\beta_1 + \beta_7^2\beta_3}{2(\beta_6\beta_7^2 - 4\beta_6\beta_5\beta_4 + \beta_7^2\beta_4)} \tag{III.63}$$

$$\delta_2 = \delta^- = \frac{\beta_1\beta_6\beta_7 - 2\beta_4\beta_6\beta_2 + \beta_3\beta_7\beta_4}{-\beta_6\beta_7^2 + 4\beta_6\beta_5\beta_4 - \beta_7^2\beta_4} \tag{III.64}$$

The energy is minimized for non-zero lattice distortions meaning that we have a Peierls distortion. Therefore, even under strong hypothesis on the lattice deformations, analytical prediction also agrees with a stabilization of the $UUD$ configuration due to lattice distortions.

To conclude, the Shastry-Sutherland lattice coupled to adiabatic phonons may exhibits very interesting properties also in the case of classical Heisenberg spins. Monte Carlo simulations indicate that at $M/M_{sat} = 1/3$ a real plateau appears, even for $T \to 0$. Under strong approximations on the deformations of the lattice, one can show that a Peierls distortions exists in the $UUD$ state.

Recently Wang and Vishwanath [181, 182] considered the effect of spin-lattice coupling on the triangular and Kagomé lattices with classical Heisenberg spins. They argue that the "bond model" for phonons as used by Penc *et al.* [12] that consider independent bonds displacements may be oversimplified for those two-dimensional lattices. In state, they used the model of

[4] Of course we expect $\delta_1$ and $\delta_3$ to be equal. This is verified since they play the same role in the expression of the energy.

Bergman *et al.* [183] which takes into account the bonds correlation. They showed that even moderate couplings can act as a mechanism to stabilize collinear states and predicted the appearance of magnetization plateaux at various rational values of the saturated magnetization. The Bergman model for adiabatic phonons may hence be a good lead to pursue the analytical study of the Shastry-Sutherland lattice.

# 5 Classical spin systems: conclusion and outlook

In this chapter we reviewed the work done on two classical spin systems: the frustrated $J_1 - J_2$ chain coupled with lattice distortions and the Shastry-Sutherland lattice.
Before presenting the work done, we first evoked the nature of the spin configurations in the magnetization plateaux of classical spin systems, which should be *collinear* configurations. In the particular case of a 1/3 magnetization plateau, the configuration is the $UUD$ state. We also discussed the effect of thermal fluctuations on frustrated classical spin systems, which can partially lift the large degeneracy of those systems. This effect is called *Order by Disorder* and can stabilize a particular state for entropic reasons.

We studied the frustrated $J_1 - J_2$ chain with classical Heisenberg spins coupled to lattice distortions and found magnetization plateaux at 1/3 of the saturation magnetization. The same study was previously carried on in the quantum case with $S = 1/2$ spins and other plateaux were observed at $M/M_{sat} = 0$ and 1/2. However the study of the ground state structures in the plateau phases revealed that the only classical plateau is the one at 1/3 of the magnetization, which explains why is the only one to survive in the classical limit.
Both analytical and numerical (Monte Carlo) methods were used to establish a phase diagram, in the plane magnetic coupling ratio $\alpha$ versus spin-lattice coupling $A_1$, showing the domain of existence of these plateaux. We obtained an analytical expression of the critical magnetic field values at the entrance and exit of the plateau, as well as conditions so that the plateaux exist. Moreover, we investigated the nature of the lattice deformation in the plateau phase which was found to be $UDU$ trimers.
We furthermore determined the nature of the phase transition to the saturated state $UUU$ which can be either first or second order depending on the values of $\alpha$ and $A_1$.

We then moved to a two-dimensional case and studied the magnetization process of the Shastry-Sutherland lattice in the classical limit. We found a pseudo-plateau at 1/3 of the saturated magnetization at non-zero temperature which corresponds to a collinear $UUD$ state. We investigated the *Order by Disorder* scenario and found that the spectrum of spin waves above this state has lines of soft modes, like the $\mathbf{q} = \mathbf{0}$ $UUUD$ state on the frustrated square lattice. However, in contrast to the frustrated square lattice, the $M/M_{\text{sat}} = 1/3$ ground state of the Shastry-Sutherland lattice has no local continuous degeneracies. Therefore, the selection mechanism of the $UUD$ state in the Shastry-Sutherland lattice is more similar to the triangular lattice.
Furthermore, we performed Monte Carlo simulations and obtained a phase diagram in the

$(h, T)$ plane for the particular magnetic coupling ratio $J'/J = 1/2$. It was found to be similar with the one for the triangular and Kagomé lattices with classical spins and it presents two quasi-long-range-ordered phase below and above the long-ranged-ordered $UUD$ phase. We also showed that the pseudo-plateau survives for a small variation $\epsilon$ of the magnetic coupling ratio around $J'/J = 1/2$. The phase diagram was found to present a new incommensurate umbrella phase in the low-temperature region, at least for $J'/J = 0.4$.

Furthermore, we performed preliminary Monte Carlo simulations that indicate that spin-lattice coupling can stabilize the $UUD$ state in the $T \to 0$ limit and create real magnetization plateaux. Calculations with a very simplified model for distortions show a Peierls instability. This model could be improved using correlated distortions, which were already shown to lead to magnetization plateaux in the triangular and Kagomé lattices.

In the future, it would also be interesting to include magnetic anisotropies in the Shastry-Sutherland lattice which are expected to be important for the rare-earth tetraborides. It may be interesting to note that also the magnetization curve of the Ising model on the Shastry-Sutherland lattice exhibits exactly one plateau with $M/M_{\text{sat}} = 1/3$ [184, 185].

# Chapter IV

# Hubbard chain coupled with adiabatic phonons

In this chapter we study one-dimensional quantum systems in the low-energy limit and we focus on systems with no magnetic field applied.
We first review the low energy effective theory of the Hubbard model without lattice coupling. The low energy limit is obtained by linearizing the dispersion relation in the vicinity of the Fermi points. We bosonize the effective Hamiltonian and show that, even in the interacting case, the spin and charge sectors are decoupled.
We then discuss the particular case of quarter-filled systems in presence of lattice distortions. Two kinds of lattice distortions are considered: the Holstein lattice coupling that modifies the chemical potential and the Peierls lattice coupling that modulates the bond lengths. Without phonons, both the spin and charge sectors are gapless at quarter-filling. We show that this is no longer true once the system is coupled with lattice distortions. We discuss the appearance of different charge-density-wave phases as the repulsion increases and compare them with previously obtained numerical results.

## 1 Low energy effective field theory of the Hubbard chain

In this section, we derive a low energy effective theory from the Hubbard model that was discussed in Chapter II, Sec. 1.2:

$$\mathscr{H} = -t\sum_{j,\sigma}(c^{+}_{j,\sigma}c_{j+1,\sigma} + h.c.) + U\sum_{j} n_{j,\uparrow}n_{j,\downarrow} + \mu\sum_{j,\sigma} n_{j,\sigma} \tag{IV.1}$$

Where $j$ is the site index ($i = 1 \dots N$), the spin values are $\sigma = \uparrow, \downarrow$ and $t$ is the hopping constant which will be used as an energy scale ($t \equiv 1$). $\mu$ is the chemical potential that fixes the number of electrons $N_e$. $U$ is the on-site interaction. We only consider repulsive interaction $U > 0$.
Since we are dealing with fermions, we will have to consider two degrees of freedom: spin ($S = 1/2$) and charge. However, this case is technically not much more difficult than the $XXZ$ spin chain which only has the spin degree of freedom.
In the $XXZ$ spin chain, a supplementary step is required: the spin operators are first mapped into *spinless* fermionic operators through the Jordan-Wigner transformations (see for example Ref. [3]). The collective excitations are therefore charge-density-waves. The Dirac spinless fermions are rewritten through the bosonization procedure in terms of compactified

bosons that have the $U(1)$ symmetry. Since $U(1)$ is an abelian group, this bosonization is called *abelian bosonization*. More details on the bosonization technique can be found in Ref. [3, 26, 27, 46, 118, 186].
In the Hubbard chain, we consider fermions and we will have too branches of excitations: the charge-density-wave discussed above and a spin-density-wave that describes "chargeless" particles with a spin $S = 1/2$. The charge sector exhibits the $U(1)$ symmetry while the spin sector has a $SU(2)$ symmetry. After the bosonization process, this model is described by one boson for each sector. Since the resulting spin and charge bosons both have $U(1)$ symmetry, the $SU(2)$ symmetry is somehow hidden [1].

## 1.1 Free fermions

Let us first focus on the gas of free fermions on a one-dimensional lattice, described by a tight-binding Hamiltonian with a chemical potential:

$$\mathscr{H}_{\mathrm{t}-\mu} = -t\sum_{j,\sigma}(c^{+}_{j,\sigma}c_{j+1,\sigma} + h.c.) + \mu\sum_{j,\sigma} n_{j,\sigma} \tag{IV.2}$$

The Fourier transform of the free Hamiltonian is given by:

$$\begin{aligned}
\mathscr{H}_{\mathrm{t}} &= \frac{1}{2\pi}\sum_{\sigma}\int_{-k_F}^{k_F} dk\varepsilon(k)c^{+}_{\sigma}(k)c_{\sigma}(k) && \text{(IV.3)}\\
\varepsilon(k) &= 2t\cos(ka) && \text{(IV.4)}\\
c_{\sigma}(k) &= \frac{1}{\sqrt{N}}\sum_{j=1}^{N} c_{\sigma,j}e^{iajk} && \text{(IV.5)}\\
\left\{c_{\sigma}(k), c^{+}_{\sigma'}(k')\right\} &= 2\pi\delta_{\sigma,\sigma'}\delta(k-k') && \text{(IV.6)}
\end{aligned}$$

where $c^{+}_{\sigma}(k)$ (resp. $c_{\sigma}(k)$) creates (resp. annihilates) a fermion with spin $\sigma$ and wave vector $k$.

We are interested in the low-energy limit, or in other terms, what happens in the vicinity of the Fermi points $\pm k_F$. The low-energy excitations create electrons above the Fermi points and holes below. One replaces the band curvature of the dispersion relation by a linear spectrum. In order to keep only the momenta close to $|k_F|$, we later introduce a cut-off. This procedure defines a left and a right sector respectively in the vicinity of $-k_F$ and $+k_F$. A picture of the linearization of the dispersion relation is given in Fig. IV.1.

Under an external magnetic field, the Fermi vector is $k_F = n\pi/2(1+M)$, where $M$ is the normalized magnetization per spin and $n = N_e/N$, the filling of the system. The magnetic field acts on the $\uparrow$ and $\downarrow$ spin populations similarly with a chemical potential on the charges. We are interested in systems with no magnetic field and the Fermi wave vector only depends on the filling. The $\uparrow$ and $\downarrow$ spin populations have the same Fermi vector:

$$k_{F_\uparrow} = k_{F,\downarrow} = k_F = n\frac{\pi}{2} \quad \text{(no magnetic field)} \tag{IV.7}$$

[1] In case the spin sector symmetry needs to be treated more carefully, another method would be considering one boson and a Wess-Zumino-Witten model. This method is called *non-abelian bosonization*. It is not only restricted to the $SU(2)$ group and also allows considering $S > 1/2$.

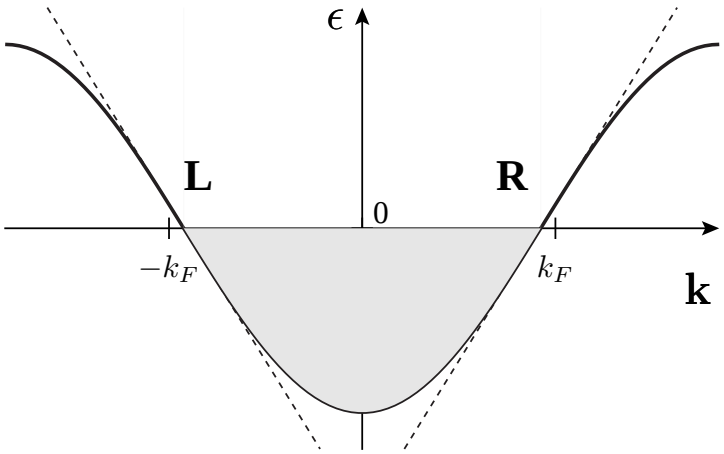


Figure IV.1: *Dispersion relation for the free fermion (bold line) and linearization in the vicinity of the Fermi points (dashed line). The left and right sectors correspond to the $-k_F$ and $+k_F$ Fermi points. The gray area corresponds to the energy levels filled at zero temperature. For simplicity only one band with spin $\sigma$ ($\sigma = \uparrow, \downarrow$) is represented.*

The chemical potential at zero temperature is equal to the Fermi energy:

$$\mu = \varepsilon(k_F) = 2t\cos(k_F a) \tag{IV.8}$$

In order to describe the excitations, let us define the $a(k)$ and $b(k)$ annihilation's operators that respectively annihilate electrons and holes around the "left Fermi point" $-k_F$ ($k<0$) and around the "right Fermi point" $k_F$ ($k>0$):

$$\begin{array}{rclcrcl} a_\sigma(-k) & = & c_\sigma(-k_F-k)\,, & & a_\sigma(k) & = & c_\sigma(k_F+k) \\ b_\sigma(-k) & = & c^+_\sigma(k-k_F)\,, & & b_\sigma(k) & = & c^+_\sigma(k_F-k) \end{array} \tag{IV.9}$$

We will restrict the integration to momenta around the Fermi points by adding an ultraviolet cutoff $\Lambda$ that depends on the lattice spacing $a$ ($\Lambda \ll k_F$ i.e. $\Lambda \ll n\pi/2a$):

$$|k \pm k_F| \leq \Lambda \tag{IV.10}$$

We define the Fermi velocity $v_F$ [2]:

$$\left.\frac{\partial\varepsilon(k)}{\partial k}\right|_{k=k_F} = 2ta\sin(ak_F) = v_F \tag{IV.11}$$

We now move to the continuum limit and define the left and right chiral fields corresponding to the $+k_F$ and $-k_F$ Fermi points in terms of the electron and hole operators [3]:

$$\psi_{L,\sigma}(x,t) = \frac{1}{\sqrt{2\pi}}\int_{-\infty}^{0} dk\left[e^{-ik(t+x)}a_\sigma(k) + e^{ik(t+x)}b^+_\sigma(k)\right] \tag{IV.12}$$

$$\psi_{R,\sigma}(x,t) = \frac{1}{\sqrt{2\pi}}\int_{0}^{\infty} dk\left[e^{ik(t-x)}a_\sigma(k) + e^{-ik(t-x)}b^+_\sigma(k)\right] \tag{IV.13}$$

[2] Since the Fermi vectors for $\uparrow$ and $\downarrow$ spins are equal (no magnetic field), the Fermi velocity does not depend on $\sigma$ and can be pulled out of the sums.

[3] We use the notation of Affleck [118].

We consider systems in $1+1$ dimension. However we are only interested in the spatial dependence with coordinates $x = j \cdot a$, where $a$ is the lattice spacing and $j$ a discrete position index. We see later that calculations are much easier if we take the time dependence into account, at least implicitly, by introducing complex variables.

The chiral fermionic fields satisfy the anti-commutation relations (at equal time):

$$\begin{aligned} \left\{\psi_{v,\sigma}(x), \psi^{+}_{u,\sigma'}(x')\right\} &= 0 \text{ if } u \neq v \text{ or } \sigma \neq \sigma' \text{ , } (u, v = R, L \text{ and } \sigma, \sigma' = \uparrow, \downarrow) \\ \left\{\psi_{v,\sigma}(x), \psi^{+}_{u,\sigma'}(x')\right\} &= \delta(x - x') \text{ if } u = v \text{ and } \sigma = \sigma' \end{aligned} \tag{IV.14}$$

The fermionic annihilation operator (and field in the continuum limit) can be rewritten in terms of the left and right chiral fields:

$$\lim_{a \to 0} \frac{c_{\sigma,j}}{\sqrt{a}} = \psi_\sigma(x) = e^{ik_{F,\sigma}x}\psi_{\sigma,L}(x) + e^{-ik_{F,\sigma}x}\psi_{\sigma,R}(x) + \dots \tag{IV.15}$$

The dots stand for higher order terms that are needed to reproduce the Bethe ansatz result for the correlation functions.

Calculations are detailed in App. C. In particular we see that the chemical potential term cancels part of the free term. In the continuum limit, we can rewrite the non-interacting Hamiltonian Eq. IV.2 in terms of fermionic fields as:

$$\mathscr{H}_{\mathrm{t}-\mu} = i v_F \sum_\sigma \int dx \left[\psi^{+}_{R,\sigma}(x)\partial_x \psi_{R,\sigma}(x) - \psi^{+}_{L,\sigma}(x)\partial_x \psi_{L,\sigma}(x)\right] \tag{IV.16}$$

Note that this Hamiltonian is actually an effective Hamiltonian due to the integration around the Fermi points. We obtain in both $\uparrow$ and $\downarrow$ sector a Dirac Hamiltonian. The chiral fields play the role of the components of the Dirac spinor and the Fermi velocity corresponds to the light velocity.

## 1.2 Interacting fermions

Let us now consider the on-site interaction term:

$$\mathscr{H}_{\mathrm{U}} = U \sum_j n_{\uparrow,j} n_{\downarrow,j} \tag{IV.17}$$

### 1.2.1 Low energy limit

We show (see details in App. C) that in the continuum limit this terms is rewritten as:

$$\mathscr{H}_{\mathrm{U}} = a^2 U \int dx (J_{R,\uparrow} + J_{L,\uparrow})(J_{L,\downarrow} + J_{R,\downarrow}) \tag{IV.18}$$

$$+ a^2 U \int dx \left(e^{i2xk_+}\psi^{+}_{R,\uparrow}\psi_{L,\uparrow}\psi^{+}_{R,\downarrow}\psi_{L,\downarrow} + h.c.\right) \tag{IV.19}$$

$$+ a^2 U \int dx \left(e^{i2xk_-}\psi^{+}_{R,\uparrow}\psi_{L,\uparrow}\psi^{+}_{L,\downarrow}\psi_{R,\downarrow} + h.c.\right) \tag{IV.20}$$

where we defined the following quantities:

$$k_+ = k_{F,\uparrow} + k_{F,\downarrow}\ ,\ k_+ = 2k_F \text{ at h=0} \tag{IV.21}$$

$$k_- = k_{F,\uparrow} - k_{F,\downarrow}\ ,\ k_- = 0 \text{ at h=0} \tag{IV.22}$$

The terms $J_{\sigma,r}$ ($r = L, R$) are the left and right currents. These are fluctuations of the left and right densities:

$$J_{\sigma,r}(x) \equiv \psi^+_{\sigma,r}\psi_{\sigma,r}(x) \tag{IV.23}$$

The terms $\propto e^{i4xk_F}$ are incommensurate and will disappear in the large scale physics, unless $k_F = \pi/2$, which corresponds to half-filling. We come back to this point later. The interacting part of the Hamiltonian becomes:

$$\mathscr{H}_{\text{U}} = a^2 U \int dx \Big[ (J_{R,\uparrow} + J_{L,\uparrow})(J_{L,\downarrow} + J_{R,\downarrow}) + \left(\psi^+_{R,\uparrow}\psi_{L,\uparrow}\psi^+_{L,\downarrow}\psi_{R,\downarrow} + h.c.\right) \Big] \tag{IV.24}$$

We will see next that the second term leads to a cosine interaction in the spin sector which is hence described by a sine-Gordon model. However this interaction is marginally irrelevant and the spin sector remains gapless.

### 1.2.2 The umklapp scattering

At half-filling ($n = 1$), the terms $\propto e^{i4xk_F}$ are commensurate. They correspond to the scattering of particles from one side of the Fermi surface to the other (i.e. two left electrons become right, or vice-versa). This scattering process is called *umklapp*:

$$\mathscr{H}_{\text{umklapp}} = a^2 U \int dx \left(e^{i4xk_F}\psi^+_{R,\uparrow}\psi_{L,\uparrow}\psi^+_{R,\downarrow}\psi_{L,\downarrow} + h.c.\right) \tag{IV.25}$$

We see later that the umklapp leads to a cosine term and the charge sector is described by a sine-Gordon model. This time, the interaction term is relevant. Hence the umklapp opens a gap in the charge sector at half-filling. The system becomes a *Mott insulator*.

### 1.2.3 The g-ology approach

Another approach for treating the interaction consists in splitting it in various scattering processes. The method is called *g-ology* due to the labeling $g_i$ of the couplings' strengths in front of each term. In the present work we will not use this method, however we later compare our results for the Hubbard model coupled with lattice distortions with results obtained previously with the g-ology approach. More details on g-ology can be found in Ref. [3, 27, 187].
The Hamiltonian of interaction Eq. IV.17 can be split in four scattering processes restricted to the vicinity of the Fermi points. These four processes are represented in Fig. IV.2.

- The $g_1$ backscattering couples fermions on one side of the Fermi surface with fermions of the other side. Fermions exchange side after the interaction but keep their spins. This term corresponds to Eq. IV.20

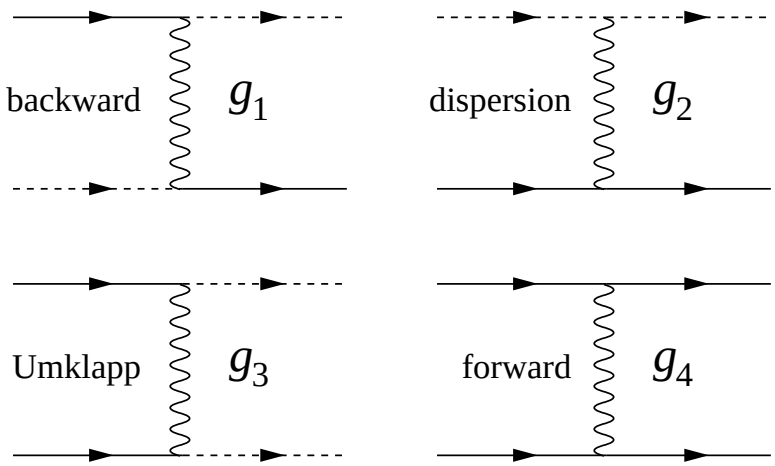


Figure IV.2: *The low-energy sector of the interaction can be decomposed in four scattering processes. Right moving (resp. left moving) electrons are represented in continuous (resp. dashed) lines. Figure from Sénéchal [27].*

- The $g_2$ dispersion scattering also couples fermions on one side of the Fermi surface with fermions of the other side. However, in this case each species stays on the same side after the interaction.
- The $g_3$ scattering corresponds to the umklapp scattering and takes place only at half-filling (Eq. IV.19).
- The $g_4$ forward scattering couples fermions of the same side.

Now that we have obtained an effective Hamiltonian in terms of fermionic fields, we will rewrite it with bosonic fields thanks to the bosonization rules.

# 2 Bosonization

In this section we present the bosonization technique and apply it to the Hubbard chain. The technical details of the bosonization calculations are presented in Appendix C. We show that part of this interaction contributes to the Luttinger liquid and the remaining part creates cosine terms whose relevance is discussed later. We rewrite the Hamiltonian in terms of spin and charge sectors, which are decoupled as long as non magnetic field is applied.

## 2.1 Bosonization rules

The chiral fermionic fields Eq. IV.15 are rewritten as a function of the chiral bosonic fields $\phi_{R,\sigma}$ and $\phi_{L,\sigma}$ according to the bosonic rules [3, 26, 27, 46, 118, 186]:

$$\psi_{R,\sigma}(x) = \eta_{R,\sigma}\frac{1}{\sqrt{2\pi a}} :e^{i\sqrt{4\pi}\phi_{R,\sigma}}: \tag{IV.26}$$

$$\psi_{L,\sigma}(x) = \eta_{L,\sigma}\frac{1}{\sqrt{2\pi a}} :e^{-i\sqrt{4\pi}\phi_{L,\sigma}}: \tag{IV.27}$$

Let us also define the bosonic field $\phi_\sigma$ and its dual field $\theta_\sigma$:

$$\phi_\sigma = \phi_{R,\sigma} + \phi_{L,\sigma} \tag{IV.28}$$
$$\theta_\sigma = \phi_{R,\sigma} - \phi_{L,\sigma} \tag{IV.29}$$

The factors $\eta_{\sigma,r}$ ($r = R, L$) are called *Klein factors*. They obey a Clifford algebra and insure the anti-commutation relations of the fermionic fields rewritten in terms of bosonic fields. Since we have four species of bosons ($\{\uparrow L, \uparrow R, \downarrow L, \downarrow R\}$), we need four species of Klein factors and the minimal dimension of the Clifford algebra is 4. The representation that is used is detailed in App. C. The Klein factors act on a Hilbert space that differs from the space generated by the bosonic modes. Therefore once the product of Klein factor is diagonalized, we simply have to pick one eigenstate and replace the product of Klein value by the corresponding eigenvalue ($\pm 1$, see App. C). This is somehow equivalent with doing a gauge choice.

The notation $:e^{i\alpha\phi}:$ for the vertex operator $e^{i\alpha\phi}$ stands for *normal ordering*. It consists in putting all creation operators to the left of annihilation operators while performing a mode expansion. The products of fermionic fields become, after bosonization, products of normal ordered vertex operators. If the bosonic fields have different degrees or freedom (i.e. $\sigma \neq \sigma'$ or $r \neq r'$) these products are simple exponential products.
Otherwise, due to normal ordering, one has to take into account the value of the boson correlator:

$$:e^{i\alpha\phi_{\sigma,r}(z)}::e^{i\beta\phi_{\sigma,r}(w)}:= |z-w|^{\frac{\alpha\beta}{4\pi}}:e^{i\left(\alpha\phi_{\sigma,r}(z)+\beta\phi_{\sigma,r}(w)\right)}: \tag{IV.30}$$

Normal ordered products defined "at the same point" are calculated by the point-splitting method:

$$:\psi^+_{\sigma,r}(z)\psi_{\sigma,r}(z):=\lim_{\epsilon\to 0}\left[\psi^+_{\sigma,r}(z+\epsilon)\psi_{\sigma,r}(z)-\langle\psi^+_{\sigma,r}(z+\epsilon)\psi_{\sigma,r}(z)\rangle\right] \tag{IV.31}$$

Using this limit, on can show (see App. C) that the left and right currents defined in Eq. IV.23 read:

$$J_{\sigma,L}(z) = \frac{i}{\sqrt{\pi}}\partial_{\bar{z}}\phi_{\sigma,L}(\bar{z}) \tag{IV.32}$$
$$J_{\sigma,R}(\bar{z}) = -\frac{i}{\sqrt{\pi}}\partial_{z}\phi_{\sigma,R}(z) \tag{IV.33}$$
$$\tag{IV.34}$$

The left and right currents are actually the conserved currents through a translation of the lattice spacing $a$, $\phi_\sigma(x) \to \phi_\sigma(x+a)$ in the action of the free scalar boson.

## 2.2 Bosonization of the Hubbard chain

Let us now come back to the low-energy effective Hamiltonian define by Eq. IV.16 and Eq. IV.24 and apply the bosonization rules on it. We also study the umklapp term Eq. IV.25. We then rewrite it in terms of charge and spin bosons and discuss the appearance of gaps in each sector, which is found to depend on the filling.

### 2.2.1 Bosonization of interacting Hubbard model

Using the bosonization rules and point-splitting (details in App. C), the free Hamiltonian Eq. IV.16 reads:

$$\mathscr{H}_{\mathrm{t}-\mu} = \frac{v_F}{2} \sum_{\sigma=\uparrow,\downarrow} \int dx \Big( (\partial_x \phi_\sigma)^2 + (\partial_x \theta_\sigma)^2 \Big) \tag{IV.35}$$

We obtain a free boson Hamiltonian in both ↑ and ↓ sectors. Since no magnetic field is applied, the "light velocity" (Fermi velocity) is the same in each sector.

The interaction is bosonized as:

$$\mathscr{H}_{\mathrm{U}} = -\frac{aU}{\pi} \int dx \partial_x \theta_\uparrow \partial_x \theta_\downarrow + \frac{U}{2\pi^2} \int dx \cos\left(\sqrt{4\pi}(\phi_\downarrow - \phi_\uparrow)\right) \tag{IV.36}$$

The umklapp term present only at half-filling is:

$$\mathscr{H}_{\mathrm{umklapp}} = \frac{U}{2\pi^2} \int dx \cos\left(\sqrt{4\pi}(\phi_\downarrow + \phi_\uparrow)\right) \tag{IV.37}$$

Instead of continuing with ↑ and ↓ bosons, we will now rewrite the bosonized Hubbard model in a more meaningful base: in terms of spin and charge bosons.

### 2.2.2 Spin and charge sectors in the Hubbard Hamiltonian

The ↑ and ↓ bosons and the spin and charge bosons are related through the *dressed-charge matrix Z*. Its matrix elements are determined by a set of coupled integral equations that were calculated by Frahm and Korepin [37, 38, 47] starting from the Bethe ansatz solution of the Hubbard model [48]. The dressed charge matrix is:

$$Z = \begin{pmatrix} Z_{cc} & Z_{cs} \\ Z_{sc} & Z_{ss} \end{pmatrix} \tag{IV.38}$$

The coefficients $Z_{ij}$ depend on the repulsion $U$, on filling $n$ of the system (i.e. on the chemical potential) and on the magnetic field $h$.
The dressed charge matrix relates the spins and charge boson to the ↑ and ↓ bosons as:

$$\begin{pmatrix} \phi_c \\ \phi_s \end{pmatrix} = \frac{1}{detZ} \begin{pmatrix} Z_{ss} & Z_{ss} - Z_{cs} \\ Z_{sc} & Z_{sc} - Z_{cc} \end{pmatrix} \begin{pmatrix} \phi_\uparrow \\ \phi_\downarrow \end{pmatrix} \tag{IV.39}$$

And the spin and charge dual bosons are given by:

$$\begin{pmatrix} \theta_c \\ \theta_s \end{pmatrix} = \begin{pmatrix} Z_{cc} - Z_{sc} & Z_{sc} \\ Z_{ss} - Z_{cs} & -Z_{ss} \end{pmatrix} \begin{pmatrix} \theta_\uparrow \\ \theta_\downarrow \end{pmatrix} \tag{IV.40}$$

However we are interested in systems with no magnetic field applied. In this case, the expression of the dressed charge matrix becomes simpler. Below half-filling (i.e. $n \leq 1$) and for all value of $U$, the dressed-charge matrix is:

$$Z_{h=0} = \begin{pmatrix} \xi & 0 \\ \xi/2 & 1/\sqrt{2} \end{pmatrix} \tag{IV.41}$$

Frahm and Korepin gave a numerical solution of the evolution of the coefficient $\xi$ for a density $0 < n < 1$ using the Bethe ansatz integral equations. Figure 1 in Ref. [37] shows the lines of constant $\xi(\mathbf{k})$ in the density $n$ versus repulsion $n$ plane. The exact value is known exactly for limit cases:

$$\lim_{U\to 0} \xi = \sqrt{2} \tag{IV.42}$$

$$\lim_{U\to \infty} \xi = 1 \tag{IV.43}$$

Hence, with no magnetic field the charge and spin bosons $\phi_c$ and $\phi_s$ read:

$$\phi_c = \frac{1}{\xi}\Big(\phi_\uparrow + \phi_\downarrow\Big) \tag{IV.44}$$

$$\phi_s = \frac{1}{\sqrt{2}}\Big(\phi_\uparrow - \phi_\downarrow\Big) \tag{IV.45}$$

Let us rewrite the Hamiltonian for $h = 0$. The spin and charge sectors are separated:

$$\mathscr{H} = \mathscr{H}_\mathrm{s} + \mathscr{H}_\mathrm{c} \tag{IV.46}$$

We will just give a general idea on how to proceed, and do not detail the value of the coupling constants. In the forthcoming calculations we do not use a perturbative treatment of the Hubbard chain but the solution from the Bethe ansatz.

The free part of the Hamiltonian becomes:

$$\mathscr{H}_\mathrm{free} = \frac{v_F}{2}\sum_{\sigma=\uparrow,\downarrow}\int dx\Big((\partial_x\phi_\sigma)^2 + (\partial_x\theta_\sigma)^2\Big) \tag{IV.47}$$

The charge sector is corresponds to a Luttinger Hamiltonian with a Luttinger parameter $K_c = \xi^2/2$ which is used to renormalize the spin boson and its dual. The bosonized form is:

$$\mathscr{H}_\mathrm{c} = \frac{v_c}{2}\int dx\big[(\partial_x\phi_s)^2 + (\partial_x\theta_s)^2\big] \tag{IV.48}$$

The situation is different at half-filling. The model is expected to become an insulator for large repulsion $U$, since any excitation is will cost $U$. At half-filling the umklapp adds a cosine interaction:

$$\mathscr{H}_\mathrm{umklapp} = \frac{U}{2a\pi^2}\int dx\cos(2k_+x - \xi\sqrt{4\pi}\phi_c) \tag{IV.49}$$

and the charge sector is described by a sine-Gordon model.

One can perform the same treatment in the spin sector (with $K_s = 1$). However, part of the interaction (the backscattering in g-ology language $g_1 \equiv g_s$) remains in an extra cosine term. Hence the spin sector is described by a sine-Gordon model:

$$\mathscr{H}_\mathrm{s} = \frac{v_s}{2}\int dx\big[(\partial_x\phi_s)^2 + (\partial_x\theta_s)^2\big] + g_s\int dx\cos\big(\sqrt{2\pi}\phi_s\big) \tag{IV.50}$$

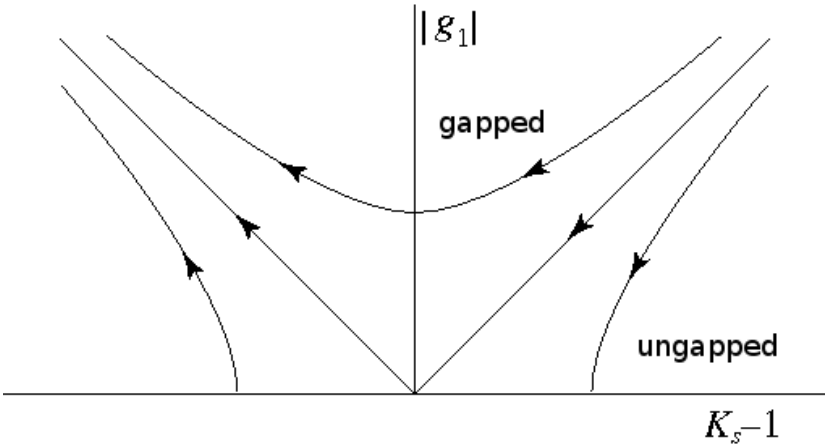


Figure IV.3: *Renormalization group flow of the sine-Gordon model in the spin sector ($g_1 = g_s$). Figure from Sénéchal [27].*

The spin sector and the charge sector at half-filling are described by a sine-Gordon model in which the first term corresponds to a Luttinger liquid, while the cosine interaction tends to minimize the energy for a given value of the bosonic filed. According to the relative values of the Luttinger parameter $K$ and of the couplings $g$, the system will lie in one of these two possible configurations. This transition is studied by the *renormalization group analysis*. We will just give a qualitative explanation to justify that in our case the Hubbard chain with no lattice distortion is described by a Luttinger liquid. The renormalization group flow of the sine-Gordon model can be found in many textbooks such as Ref. [27, 188]. Figure IV.3 shows the renormalization group flow of the sine-Gordon model.

The Luttinger liquid is a fixed point theory and in the spin sector and in the charge sector at half-filling (umklapp), a cosine interaction defines a sine-Gordon model (gapped region in Fig. IV.3). These interactions will be kept only if they grow algebraically under renormalization. Such perturbations are called *relevant*. If it decreases it is called irrelevant and is not taken into account (ungaped region in Fig. IV.3). If it evolves logarithmically it is called marginal (separatrix in Fig. IV.3) and logarithmic corrections sometimes need to be taken into account in the calculations of correlations functions. It two dimension (1 + 1 in our case) a relevant operator has a scaling dimension $\Delta < 2$, a marginal operator $\Delta = 2$ and an irrelevant operator $\Delta > 2$.

Due to the $SU(2)$ symmetry of the spin sector, unless a magnetic field is applied, the Luttinger parameter is $K_s = 1$. This interaction is marginal and the spin sector remains gapless. One can apply the same treatment to the umklapp term at half-filling.

In the following, we will be working at quarter-filling in order to describe the Bechgaard and Fabre salts. Hence the charge sector is gapless. Moreover, since we do not apply any magnetic field, the spin sector is also gapless. Therefore the bosonized Hubbard Hamiltonian we are

using is:

$$\mathscr{H} = \sum_{j=s,c} \frac{v_j}{2} \int dx \Big[ (\partial_x \phi_j)^2 + (\partial_x \theta_j)^2 \Big] \tag{IV.51}$$

In the next section, after reviewing the experimental motivation for the quarter-filled chain, we will add lattice distortions which open gaps and couple the spin and charge sectors.

# 3 Charge ordering in molecular conductors

Organic conductors such as for the Bechgaard salts $(TMTSF)_2X$, the Fabre salts $(TMTTF)_2X$ (see Sec. 3.2), the BEDT-TTF and more recently the $(EDO\text{-}TTF)_2X$ [189] (Fig. IV.4) can be described with low-dimensional models such as chain, ladders and trellis. These compounds exhibit very rich phase diagrams and the *charge ordering* phenomenon has been widely studied since it plays a key role in their physical properties, such as metal-insulator transitions. The main issue in the study of these compounds is to determine the nature of the charge ordering in the insulating phases and this has been the subject of a considerable numerous amount of experimental and theoretical works. Many experimental techniques such as X-ray scattering, NMR experiments, Muon Spin Rotations ($\mu$sr) measurements, magnetic susceptibility and and angle-dependent magnetoresistance oscillations agree on the fact that the TM family of compounds exhibits phases with a $4k_F$ instability in addition to the usual $2k_F$ Peierls instability. Since these systems are quarter-filled, the Fermi wave vector is $k_F = \pi/4$ (under no magnetic field). Therefore a $4k_F$ distortion corresponds to a *dimerization* and a $2k_F$ one to a *tetramerization*.

In the study of the charge ordering, one has to consider that on the one hand, there is a periodic modulation of the inter site distance which is called *Bond Order Wave* (BOW) and on the other hand the charge density adapts itself to this distortion. The resulting modulation of the intra site charge density is called *Charge Density Wave* (CDW). Experimental results indicate that both CDW and BOW can have $2k_F$ and $4k_F$ periodicity. Moreover, charge-transfer solids also exhibit broken symmetry phase with spin ordering such as *Spin Density Wave* (SDW) and *spin-Peierls* (SP) states.

As explained in Section 3.2, changing the nature of the counter ion is equivalent with varying the repulsion. Hence the different phases observed experimentally in organic conductors should appear in a phase diagram as a function of the repulsion. Hirsch and Scalapino [190–192] showed in the eighties that the $4k_F$ and $2k_F$ CDW do not coexist and thereafter quarter-filled Hubbard chain coupled with adiabatic phonons have been the subject of an increasing numbers of work. Various techniques both numerical and analytical were used such as: exact diagonalization [29, 30], Density Matrix Renormalization Group (DMRG) [33], mean-field [193] g-ology and renormalization group analysis [33, 34, 189, 194, 195]. The quarter-filled extended $t-J$ model was also investigated by Bissola *et al.* [196]. A all-comprehensive presentation of the rich physics of the charge transfer solids is far beyond the scope of this manuscript and for a review on on both theoretical and experimental aspect of charge ordering in molecular conductors one can refer to Ref. [197] and references therein.

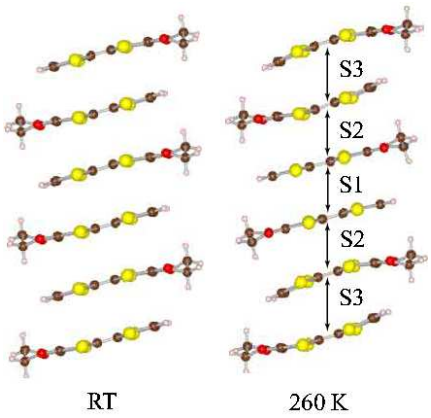


Figure IV.4: *Crystal structure of the (EDO-TTF)$_2$PF$_6$ compound at room temperature (left) and at 260 K (right). At room temperature there is a very weak almost uniform dimerization along the stacking axis while at 260 K there is a strong variation among the overlap integral ($S_1$, $S_2$ and $S_3$). Figure from Tsuchiizu and Suzumura [189].*

In Section 3.2 we recalled that many organic compounds can be described as stacks of flat molecules. The particularity of the TM Bechgaard and Fabre salts is to exhibit as small dimerization in the stacking. This suggests that lattice distortion may play a major role in the apparition of the charge ordering.
The opening of gaps due to inter sites phonons were studied by Rice [198, 199] and later Su, Schrieffer and Heeger developed the SSH model to describe soliton excitations in quasi-one dimensional conducting polymers such as polyacetylene $(CH)_n$ [200–202]. Ung *et al.* [203] considered both inter site phonons and intra molecular vibration in quarter and third-filled Hubbard chains and showed that both types of interactions can cooperate.
Let us now see more precisely what are these types of distortions:

- **The Holstein coupling** corresponds to electron-molecular vibrations and modifies the chemical potential on the sites [4]. We also refer to it as on-site coupling. The Hubbard-Holstein Hamiltonian in the adiabatic limit for the phonons reads:

$$\mathscr{H}_{\text{Holstein}} = \frac{K^H}{2}\sum_j \delta_j^2 - t\sum_{j,\sigma}(c^+_{j,\sigma}c_{j+1,\sigma} + h.c.) + U\sum_j n_{j,\uparrow}n_{j,\downarrow} + tA^H\sum_{j,\sigma}\delta_j n_{j,\sigma} \quad \text{(IV.52)}$$

  We will discuss the effect of the Holstein coupling in the $NaV_2O_5$ quarter-filled compound [29]. As represented in Figure IV.5, its trellis lattice can be described as a two-legs ladders coupled by zig-zag chains.

- **The Peierls coupling** corresponds to modulation of the inter sites bonds. It acts on the nearest-neighbors couplings. The Hubbard-Peierls Hamiltonian in the adiabatic limit for phonons reads:

$$\mathscr{H}_{\text{Peierls}} = \frac{K^P}{2}\sum_j \delta_j^2 - t\sum_{j,\sigma}(1 - A^P\delta_j)(c^+_{j,\sigma}c_{j+1,\sigma} + h.c.) + U\sum_j n_{j,\uparrow}n_{j,\downarrow} + \mu\sum_{j,\sigma} n_{j,\sigma} \quad \text{(IV.53)}$$

[4] We absorb the chemical potential in the definition of the Holstein fermion-lattice coupling $(\mu - A) \to A$.

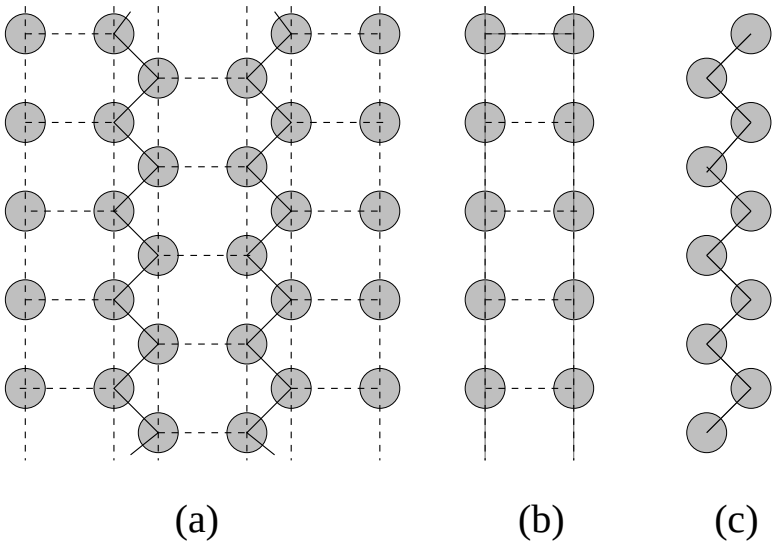


Figure IV.5: *The structure of the quarter-filled $NaV_2O_5$ compound is a trellis lattice (a) which can be decomposed as a ladder (b) and a zig-zag chain (c). Our bosonization study focus on the latter. Figure from Poilblanc and Riera [29].*

In the following we will study the Peierls couplings in relation with the Bechgaard and Fabre TM salts.

We study the quarter-filled Hubbard model ($n = 1/2$) coupled with adiabatic phonons. Holstein and Peierls couplings will be considered separately. Moreover, since the nearest-neighbor repulsion $V$ ($V > 0$) was found to play a major role in organic charge-transfer molecular conductors we should consider an *extended* Hubbard model.
Our goal is to reproduce the phase diagrams as a function of elastic coupling and on-site repulsion that were obtained by Poilblanc and Riera both for the Hubbard-Holstein chain Eq. IV.52 [29] and for the Hubbard-Peierls chain Eq. IV.53 [30].
In the next sections we first review the numerical results, then present the analytical results obtained by means of g-ology and renormalization group analysis and finally we detail our method and compare our results with the previous ones.

# 4 Review of the numerical results to reproduce with bosonization

As mentioned above, many studies were carried out with various numerical methods (Exact diagonalization, DMRG, mean-field). We chose to focus on the phase diagrams that were obtained by Poilblanc and Riera for the quarter-filled Hubbard-Peierls [30] and Hubbard-Holstein Hamiltonians [29]. In this section we do a quick review of the phases they obtained before starting the bosonization analysis to reproduce them.
This work was performed by exact diagonalization and self-consistent procedure. The lowest energy equilibrium lattice configuration is obtained self-consistently without making any as-

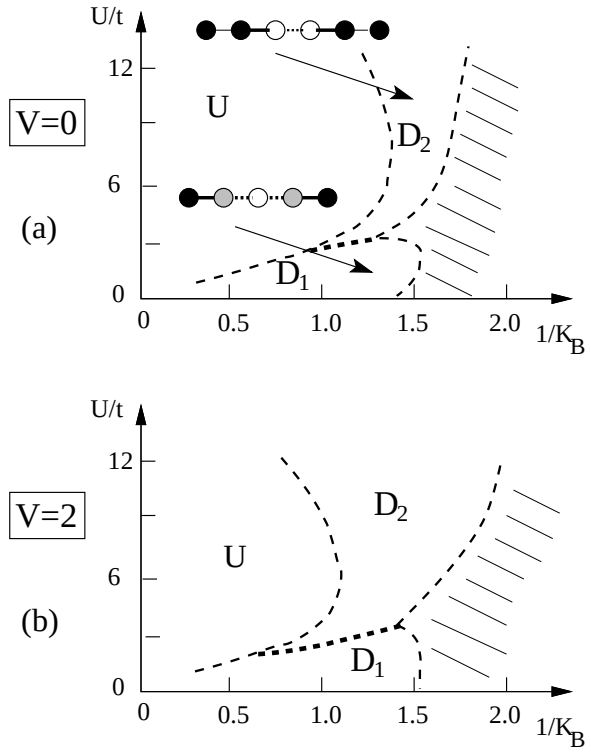


Figure IV.6: *Phase diagram for the Hubbard-Peierls chain. Details on the $D_1$ and $D_2$ insulating phases are given in the text. Hashed regions are unphysical. Figure from Poilblanc and Riera [30].*

sumption on the broken symmetry ground state. The total energy functional $E\big(\{\delta_i\}\big)$ is minimized with respect to the sets of distortions $\{\delta_i\}$ by solving non-linear coupled equations with a regular iterative procedure:

$$K^u\{\delta_i^u\} + t\langle c^+_{\sigma,i}c_{\sigma,i+1} + h.c.\rangle = 0 \tag{IV.54}$$

Here $u = H, P$ for Holstein or Peierls distortions and $\langle\ldots\rangle$ is the ground state mean value obtained by exact diagonalization using the Lanczos algorithm of Hamiltonians Eq. IV.53 for Peierls coupling (and Eq. IV.52 for Holstein) on cyclic $L-$site rings.

## 4.1 Peierls distortions

In this section, we present the insulating phases obtained by Poilblanc and Riera in Ref. [30]. The Peierls-Hubbard Hamiltonian Eq. IV.53 was studied with a general distortion given by:

$$\frac{\Delta n_i}{\bar{n}} = \rho_{4k_F}\cos(2\pi\frac{r_i}{2a}) + \rho_{2k_F}\cos(2\pi\frac{r_i}{4a} + \Phi_{2k_F}) \tag{IV.55}$$

where $\Delta n_i = \langle n_i\rangle - \bar{n}$.
The quarter-filled Hubbard chain coupled with Peierls distortions exhibits coexisting CDW and

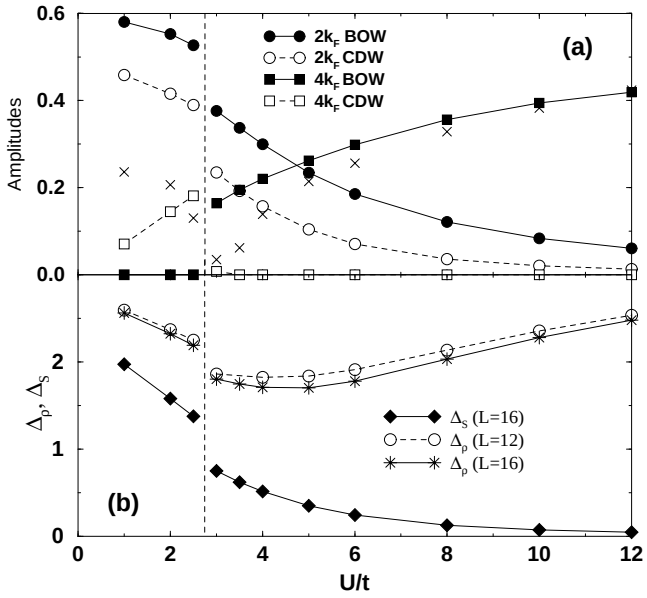


Figure IV.7: *Upper panel: amplitudes of the CDW (open symbols) $\rho_{2k_F}$ and $\rho_{4k_F}$ and of the BOW (filled symbols) $\delta_2$ and $\delta_4$ components versus $U/t$ for $1/K = 1.25$ and $V = 2$, computed on a 16-site ring. Note that, although identical symbols have been used, the $2k_F$ orders are in fact different, i.e. have different phases $\Phi_{2k_F}$ and $\Phi^B_{2k_F}$ in the $D_1$ and $D_2$ phases. The crosses indicate the energy difference (in absolute value) between the states with these two patterns. Lower panel: charge ($\Delta_c$) and spin ($\Delta_s$) gaps in unit of $t$ versus $U/t$ computed on $12-$ and $16-$site rings ($\Delta_s$ on $L = 12$ and $L = 16$ are indistinguishable). Figure from Poilblanc and Riera [30].*

BOW. The BOW is given by:

$$\delta^B(x) = cte + \delta^B_{2k_F}\cos(\frac{\pi}{2}x + \varphi^B_{2k_F}) + \delta^B_{4k_F}\cos(\pi x) \tag{IV.56}$$

Figure IV.6 shows the phase diagrams that were obtained as a function of the repulsion $U$ versus the elastic constant $K^P$ without next-nearest-neighbor repulsion ($V = 0$, upper panel) and with $V = 2$ (lower panel). Two insulating phases with coexisting CDW and BOW are obtained:

1. Weak repulsion region, $U < 3$: the **"$\mathbf{D_1}$ Phase"**.
   The BOW has a $2k_F$ modulation with a phase $\varphi^B_{2k_F} = \pi/4$:

   $$\delta^B(x) \sim \delta^B_{2k_F}\cos(\frac{\pi}{2}x + \pi/4) \tag{IV.57}$$

   The CDW has weaker amplitude and it is the combination of site centered $2k_F$ modulation with a $4k_F$ modulation:

   $$\rho(x) \sim A_{2k_F}\cos(\frac{\pi}{2}x) + A_{4k_F}\cos(\pi x) \tag{IV.58}$$

   The relative amplitudes of the CDW harmonics are $A_{4k_F} \ll A_{2k_F}$. Therefore, CDW is *tetramerized.*

2. Large repulsion region: the **"$D_2$ Phase"**.
   This time the BOW is a combination of a $2k_F$ with a $4k_F$ harmonics with equivalent amplitudes.

$$\delta^B(x) \sim \delta^B_{2k_F}\cos(\frac{\pi}{2}x) + \delta^B_{4k_F}\cos(\pi x) \tag{IV.59}$$

   One every two bonds of the dimerized state becomes weaker so that electrons become weakly bound in singlet pairs on next-nearest-neighbor bond. The "$D2$ phase" is a realization of the spin-Peierls phase.
   The CDW is a single $2k_F$ harmonic with a phase:

$$\rho(x) \sim A_{2k_F}\cos(\frac{\pi}{2}x + \pi/4) \tag{IV.60}$$

   Hence, again the CDW is tetramerized.

The amplitude of the CDW and BOW are represented in Fig. IV.7, upper panel. The left side corresponds to the $D_1$ phase, the right side to the $D_2$ phase. Furthermore, the boundary between the $D1$ and $D2$ phases is a first order transition.

The lower panel of Figure IV.7 shows the evolution of the spin and charge gaps $\Delta_s$ and $\Delta_c$:

- The spin gap $\Delta_s$ follows the magnitude of the $2k_F$ CDW-BOW. In the large repulsion region ($D_2$ phase), the systems behaves like a $S = 1/2$ antiferromagnet (the electrons are localized on strong bonds) and $\Delta_s$ is expected to vanish in this limit. In $D_1$ electrons are strongly localized in pairs on two adjacent strong bonds (i.e. on 3 sites) so that $\Delta_s \sim t$.
- The charge gap $\Delta_c$ has a minimum in the large repulsion $D_2$ phase in the region corresponding to the crossover from dominant $2k_F$ to $4k_F$ BOW-CDW.
- Both spin and charge gaps $\Delta_s$ and $\Delta_c$ are discontinuous at the first order transition between $D_1$ and $D_2$.

## 4.2 Holstein distortions

In this section, we present the insulating phases obtained by Poilblanc and Riera in Ref. [29] on the Holstein-Hubbard Hamiltonian. The charge density is given by:

$$\rho(x) = cte + A_{2k_F}\cos(\frac{\pi}{2}x + \varphi_{2k_F}) + A_{4k_F}\cos(\pi x + \varphi_{4k_F}) \tag{IV.61}$$

Figure IV.8 shows the phase diagrams that were obtained as a function of the repulsion $U$ versus the elastic constant $K^P$ without next-nearest-neighbor repulsion ($V = 0$, upper panel) and with $V = 0.5$ (lower panel). Three insulating phases are obtained:

1. Weak repulsion region: the **"$P_1$ Phase"**.
   The CDW has a single $2k_F$ harmonic centered on the sites:

$$\rho(x) \sim A_{2k_F}\cos(\frac{\pi}{2}x) \tag{IV.62}$$

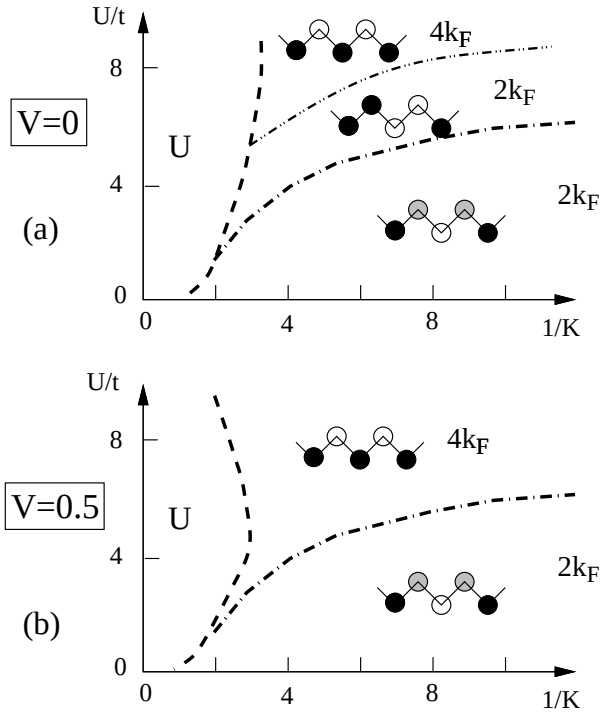


Figure IV.8: *Phase diagram for the Hubbard-Holstein chain. Upper panel, from weak to large repulsion $U$: the $2k_F$ site-centered $P_1$ phase, $2k_F$ bond-centered $P_1$ phase and the $4k_F$ site-centered $P_3$ phase. Figure from Poilblanc and Riera [29].*

2. Intermediate repulsion, $4 \leq U \leq 8$: the **"$P_2$ Phase"**.
   The CDW still has $2k_F$ harmonic. However the density is centered on the bonds and has a $\pi/4$ phase:

$$\rho(x) \sim A_{2k_F} \cos(\frac{\pi}{2}x + \pi/4) \tag{IV.63}$$

3. Large repulsion: the **"$P_3$ Phase"**.
   In this region, the CDW is dimerized and the density is centered on the sites:

$$\rho(x) \sim A_{4k_F} \cos(\pi x) \tag{IV.64}$$

The lower panel of Figure IV.8 shows th effect of a small nearest-neighbors repulsion ($V = 0.5$). The $P_2$ phase disappear and the dimerized $P_4$ phase is stabilized.
No information about the spin gap is given. However, the $P_3$ dimerized $4k_F$ phase is expected to be anti-ferromagnetic and the $2k_F$ phases should have a gap (at least the $P_2$ phase with the $\pi/4$ phase) [204].

In this section we have reviewed the phases that we should recover analytically. In the next section we will derive a bosonized Hamiltonian both for the Holstein-Hubbard and Peierls-Hubbard models.

# 5 Bosonization of the Hubbard chain coupled to lattice distortions

In this section we present the work carried out with the bosonization technique on the quarter-filled Hubbard chain coupled with Holstein and Peierls lattice distortions. We first introduce bosonization rules with more harmonics and derive the Hamiltonian. An analytical study was previously carried out on these systems by means of g-ology. We will first present our results and then show that we actually recover a Hamiltonian similar with the one obtained by the g-ology.

## 5.1 Bosonization rules with more Harmonics

Using the Bethe-ansatz and conformal field theory, Frahm and Korepin [37, 38] calculated the correlation function of the Hubbard chain for all fillings, for all interaction $U$ and under an external magnetic field. The correlation function are given by:

$$\langle\phi(x,t)\phi(0,0)\rangle \sim \sum_{D_c,D_s} \frac{a(D_c,D_s)e^{-2iD_c k_{F,\uparrow}x}e^{-2i(D_c+D_s)k_{F,\downarrow}x}}{(x-u_c t)^{2\Delta_c^+}(x+u_c t)^{2\Delta_c^-}(x-u_s t)^{2\Delta_s^+}(x+u_s t)^{2\Delta_s^-}} \tag{IV.65}$$

The Hubbard model was known to belong to the class of universality of the Luttinger model. However the relationships between the parameters of the models were only known in the weak coupling limit where they could be calculated by the g-ology. Penc and Sólyom [205] later used the exact expression of th correlation functions to find the mapping between the Hubbard and the Luttinger models for arbitrary repulsion $U$, filling $n$ and under a magnetic field.

Cabra *et al.* [35, 36] used the expression of these correlation functions to add more harmonics in the bosonization rules Eq. IV.27 by comparing the critical exponents of the terms in the sum of Eq. IV.65. This result was used in Ref. [35, 36] in order to study a p-merized Hubbard chain. We will use these bosonization rules in order to have all the commensurate terms of the Hamiltonian with lattice distortions. These rules are defined by:

$$\begin{aligned}
\psi_\downarrow(x) &= r_1 e^{-ik_{F,\downarrow}x}\psi_{R,\downarrow}(x) \\
&+ r_2 e^{-i(k_+ + k_{F,\uparrow})x}\psi_{R,\downarrow}(x)\psi^+_{L,\uparrow}(x)\psi_{R,\uparrow}(x) \\
&+ r_3 e^{i(k_- + k_{F,\uparrow})x}\psi_{R,\downarrow}(x)\psi^+_{R,\uparrow}(x)\psi_{L,\uparrow}(x) + \dots \\
&+ l_1 e^{ik_{F,\downarrow}x}\psi_{L,\downarrow}(x) \\
&+ l_2 e^{i(k_+ + k_{F,\uparrow})x}\psi_{L,\downarrow}(x)\psi^+_{R,\uparrow}(x)\psi_{L,\uparrow}(x) \\
&+ l_3 e^{-i(k_- + k_{F,\uparrow})x}\psi_{L,\downarrow}(x)\psi^+_{L,\uparrow}(x)\psi_{R,\uparrow}(x) + \dots
\end{aligned} \tag{IV.66}$$

The dots stand for higher order harmonic that lead to irrelevant terms. $\psi\uparrow$ is obtained by converting $\downarrow$ into $\uparrow$ in the previous expression. More details are given in App. C and in particular we explain how to take care of the Klein factors products.

We consider the quarter-filled Hubbard chain coupled to lattice distortions. The general Hamiltonian for Holstein or Peierls coupling of is given by:

$$\mathscr{H} = -t\sum_{j,\sigma}(c^{+}_{j,\sigma}c_{j+1,\sigma}+h.c.)+U\sum_{j}n_{j,\uparrow}n_{j,\downarrow}+\frac{K}{2}\sum_{j}\delta_i^2+tA\sum_{j,\sigma}\delta_j(c^{+}_{j,\sigma}c_{j+m,\sigma}+h.c.)+V\sum_{j}n_jn_{j+1} \tag{IV.67}$$

The parameter $m$ fixes the kind of adiabatic phonons we consider. It takes the value $m=0$ for Holstein (on-site) phonons, $m=1$ for Peierls phonons. The lattice spacing fixed to $a=1$.
In further calculations, in order to reduce the number of parameters use $t$ as the energy scale and define the parameters:

$$\delta \rightarrow (K/t)^{1/2}\delta \tag{IV.68}$$
$$A \rightarrow (t/K)^{1/2}A \tag{IV.69}$$
$$U \rightarrow U/t \tag{IV.70}$$

In the continuum limit, and taking into account the bosonized Hubbard chain Eq. IV.51, this Hamiltonian reads:

$$\mathscr{H} = \mathscr{H}_0+\mathscr{H}_{\text{elas}}+\mathscr{H}_{\text{int}}+\mathscr{H}_V \tag{IV.71}$$
$$\mathscr{H}_0 = \sum_{j=s,c}\frac{v_j}{2}\int dx\Big[(\partial_x\phi_j)^2+(\partial_x\theta_j)^2\Big] \tag{IV.72}$$
$$\mathscr{H}_{\text{elas}} = \frac{K}{2}\int dx\delta(x)^2 \tag{IV.73}$$
$$\mathscr{H}_{\text{int}} = tA\int dx\delta(x)\mathscr{O}_m(x) \tag{IV.74}$$
$$\mathscr{H}_V = V\int dx\mathscr{O}_0(x)\mathscr{O}_0(x+1) \tag{IV.75}$$

Here we defined the bosonized operator:

$$\mathscr{O}_m(x) = \psi^{+}_{\uparrow}(x+m)\psi_{\uparrow}(x)+\psi^{+}_{\downarrow}(x+m)\psi_{\downarrow}(x)+h.c. \tag{IV.76}$$

The details of the calculations are given in App. C. Using the bosonization rules Eq. IV.66, one obtains the bosonized operator at quarter-filling ($k_F=\pi/4$):

$$\begin{aligned}\mathscr{O}_m(x) &= -\lambda_{11}\sin\big(\frac{\pi}{2}x+\frac{\pi}{4}m-\xi\sqrt{\pi}\phi_c\big)\cos(\sqrt{2\pi}\phi_s)\\ &\quad -\lambda_{12}\cos\big(\pi x+\frac{\pi}{2}m-2\xi\sqrt{\pi}\phi_c\big)\end{aligned} \tag{IV.77}$$

Here we defined:

- $\lambda_{11}=8r_1l_1\mathbf{1}\otimes\sigma_3$
- $\lambda_{12}=8(r_1l_2+r_2l_1)\cos\big(\frac{\pi}{4}m\big)\mathbf{1}\otimes\sigma_3$

- Dependence on the repulsion $U$ of the constants $r_i$ and $l_i$: in the $U = 0$ limit we should recover that all coefficients $r_i$ and $l_i$ should be zero excepted $r_1 = l_1 = 1/\sqrt{2\pi a}$ = constant. We also know that at lowest order, the coefficients $r_2$ and $l_2$ are linear in $U$. For higher values of $U$ the behaviors of these coefficients is not known.

Eq. IV.77 clearly shows that:

- Coupling with the lattice (both Holstein and Peierls mechanisms) couples the spin and charge degrees of freedom. This term as a coupling constant $\propto r_1 l_1$. From the dependence in $U$ explained above, this term should be dominating in the weak coupling region. Once coupled with a suitable harmonic, this term will favor a $2k_F$ CDW (i.e. a tetramerized pattern).
- The product of the two first harmonics of the bosonization rules opens a charge gap. This term is $\propto U(A+B\cdot U)$ ($A$ and $B$ are constants) and it is expected to dominate in the region of higher repulsion.
  Once coupled with the lattice distortion, this term will favor a $4k_F$ CDW (i.e. a dimerization).

The generic lattice distortion that adapts to the relevant terms so as to make them commensurate is:

$$\delta(x) = \delta_2 \cos(2k_F x + \beta_2) + \delta_4 \cos(4k_F x) \tag{IV.78}$$

$$= \delta_2 \cos(\frac{\pi}{2} x + \beta_2) + \delta_4 (-1)^x \tag{IV.79}$$

The elastic energy reads:

$$\mathscr{H}_{\text{elas}} = \frac{N}{2}\left(\frac{1}{2}\delta_2^2 + \delta_4^2\right) \tag{IV.80}$$

Let us now study separately what we obtain for the Holstein and Peierls couplings and compare it with the numerical results.

## 5.2 Results for the Holstein case

The bosonized Holstein operator becomes commensurate by multiplying with the lattice distortion:

$$\delta(x)\mathscr{O}_0(x) = \frac{\delta_2 \lambda_{11}}{2} \sin(\xi\sqrt{\pi}\phi_c + \beta_2)\cos(\sqrt{2\pi}\phi_s) - \delta_4 \lambda_{12} \cos(2\xi\sqrt{\pi}\phi_c) \tag{IV.81}$$

Hence the Holstein-Hubbard Hamiltonian is:

$$\begin{aligned}
\mathscr{H} &= \mathscr{H}_0 \\
&+ \frac{N}{2}\left(\frac{1}{2}\delta_2^2 + \delta_4^2\right) \\
&+ A\frac{\delta_2 \lambda_{11}}{2} \int dx \sin(\xi\sqrt{\pi}\phi_c + \beta_2)\cos(\sqrt{2\pi}\phi_s) \\
&- A\delta_4 \lambda_{12} \int dx \cos(2\xi\sqrt{\pi}\phi_c) \\
&+ V\frac{\lambda_{12}^2}{2} \int dx \cos(4\xi\sqrt{\pi}\phi_c)
\end{aligned} \tag{IV.82}$$

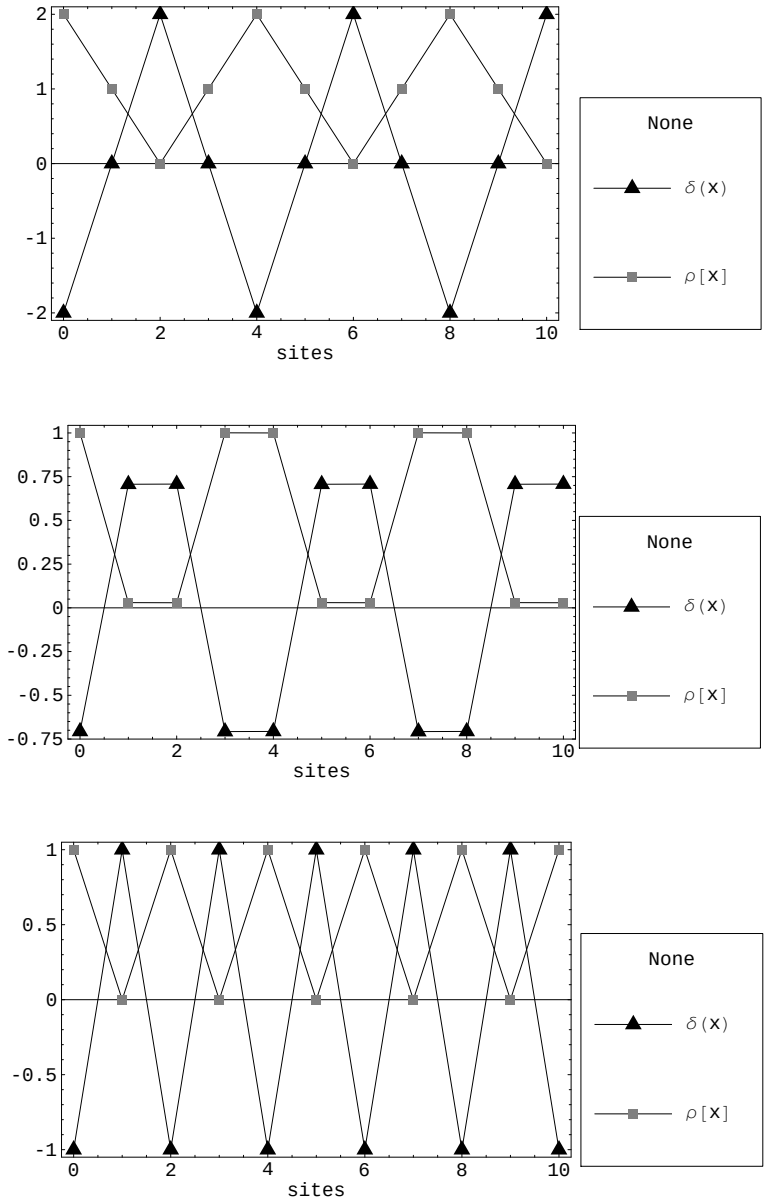


Figure IV.9: *CDW ($\rho$, squares) and BOW ($\delta$, triangles) in the quarter-filled Holstein-Hubbard model. The $x-$axis stands for the sites indices $j$. Upper panel: weak repulsion limit, tetramerized on-site centered "$P_1$ phase". Center panel: tetramerized bond-centered "$P_2$ phase". Lower panel: larger repulsion, dimerized "$P_3$ phase".*

Within the semi-classical approximation, the energy per site depends on five parameters: $\delta_2$, $\delta_4$, $\phi_c$, $\phi_s$ and $\beta$. We obtain different degenerated configurations [5]. It is important to keep in mind that we are using an ansatz on the dependence on $U$ of the coefficients $r_i$ and $l_i$ that is valid only in the weak coupling region $U/t \ll 1$. Therefore, a quantitative study of the energies and especially of the crossings is meaningless since we do not know the behavior of the energies as a function of $U$. We will simply give a *qualitative* picture of what happens.
We recover three insulating phases, as $U$ increases in our ansatz we have:

- A $\delta_4 = 0$, $\delta_2 \neq 0$ and $\beta_2 = 0$ phase, i.e. a tetramerized site-centered phase. Its CDW and BOW are represented in the upper panel of Fig. IV.10. The CDW pattern has to be compared with the CDW depicted in the $P_1$ phase of Fig. IV.8. The gray (resp. black, empty) circles correspond to our zero (resp. +2, −2) line.

- A $\delta_4 \neq 0$, $\delta_2 \neq 0$ and $\beta_2 = \pi/4$ phase. We have $\delta_4 < \delta_2$ and we obtain a tetramerized bond-centered phase with the same $\pi/4$ phase as in the numerical results. The CDW and BOW are represented in the center panel of Fig. IV.10. The CDW pattern ($\bullet\bullet oo$) is similar with the one of the $P_2$ phase of Fig. IV.8.

- Finally we obtain a $\delta_4 \neq 0$, $\delta_2 = 0$ and $\beta_2 = 0$ phase that is dimerized. The CDW and BOW are represented in the lower panel of Fig. IV.10. It matches with the CDW pattern of the $P_3$ phase of Fig. IV.8.

To conclude, we *qualitatively* recover the three phases of the quarter-filled Holstein-Hubbard of Ref. [29] and the CDW patterns are in agreement.

However the behavior with next-nearest-neighbor repulsion $V$ is still problematic. Indeed we expect the energy of the $P_2$ phase to increase since it consists in two consecutive occupied sites followed by two consecutive unoccupied sites. And as observed in Fig. IV.8 this phase actually disappeared for $V = 0.5$ (lower panel). Also the energy of the $P_3$ phase should not be affected by adding the repulsion $V$ and the energy of the $P_1$ phase should increase. Our bosonized next-nearest-neighbor repulsion term does not work in this scenario and for example tends to lower the energy of the $P_2$ phase, which is not possible. We are not able to explain this discrepancy so far.

## 5.3 Results for the Peierls case

The bosonized Peierls operator becomes commensurate by multiplying with the lattice distortion:

$$\delta(x)\mathcal{O}_1(x) = -\frac{\delta_2\lambda_{11}}{2}\sin(\frac{\pi}{4} - \xi\sqrt{\pi}\phi_c - \beta_2)\cos(\sqrt{2\pi}\phi_s) - \frac{\delta_4\lambda_{12}\sqrt{2}}{2}\sin(2\xi\sqrt{\pi}\phi_c) \quad \text{(IV.83)}$$

[5] We will not mention the solutions corresponding to the undistorted case $\delta_2 = \delta_4 = 0$.

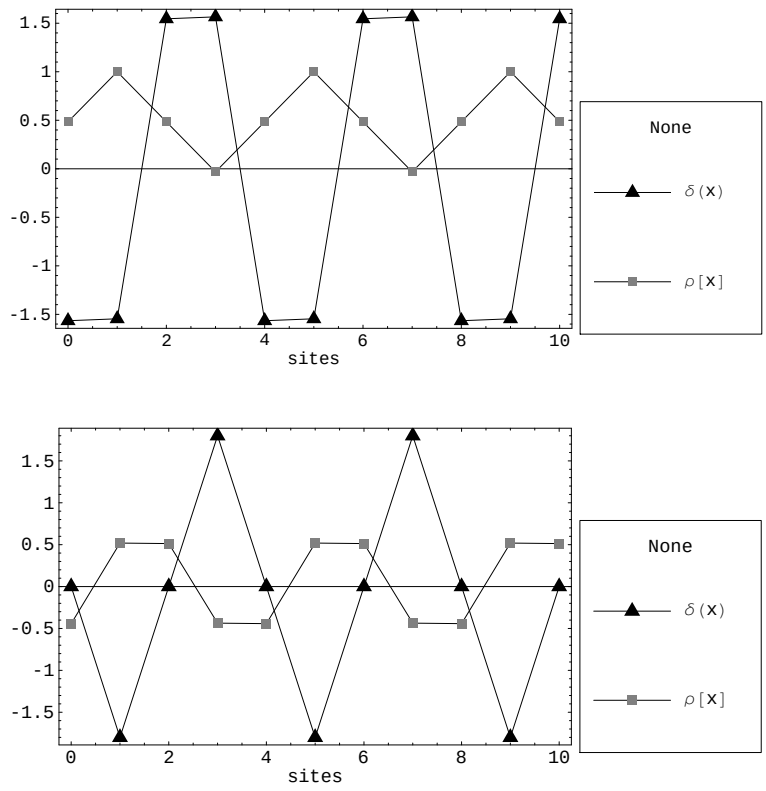


Figure IV.10: *CDW ($\rho$, squares) and BOW ($\delta$, triangles) in the quarter-filled Peierls-Hubbard model. The $x-$axis stands for the sites indices $j$. Upper panel: weak repulsion limit, "$D_1$ phase". Lower panel: larger repulsion, "$D_2$ phase".*

The quarter-filled Peierls-Hubbard Hamiltonian is:

$$\begin{aligned}\mathscr{H} &= \mathscr{H}_0 \\ &+ \frac{N}{2}\left(\frac{1}{2}\delta_2^2+\delta_4^2\right) \\ &- A\frac{\delta_2\lambda_{11}}{2}\int dx \sin(\frac{\pi}{4}-\xi\sqrt{\pi}\phi_c-\beta_2)\cos(\sqrt{2\pi}\phi_s) \\ &- A\delta_4\lambda_{12}\frac{\sqrt{2}}{2}\int dx \sin(2\xi\sqrt{\pi}\phi_c) \\ &+ V\frac{\lambda_{12}^2}{2}\int dx \cos(4\xi\sqrt{\pi}\phi_c) \end{aligned} \tag{IV.84}$$

We proceed like previously in the Holstein case and obtain again three phases. However, the dimerized ($\delta_2 = 0$) phase has higher energy and hence the ground state is always tetramerized. We obtain:

- A $2k_F$ BOW ($\delta_4 = 0$). The BOW and CDW are represented in the upper panel of Fig. IV.10: the BOW has a $\bullet\bullet oo$ pattern and the CDW a $A-B-\bar{A}-B$ pattern ($B$ corresponds to the 0.5 line). Both are in agreement with Ref. [30].

- A tetramerized BOW two harmonics $\delta_2 \neq 0$ and $\delta_4 \neq 0$. The BOW and CDW are represented in the lower panel of Fig. IV.10. They are in agreement with Ref. [30]

To conclude, the Peierls coupling also give qualitative results that are in agreement with the phase diagram presented in Ref. [30]. In the next section we compare our result on the Peierls-Hubbard quarter-filled chain with the results obtained with the bosonization.

# 6 Comparison with the g-ology results

Let us do a short review of the analytical results that were obtained by the g-ology. Kuwabara *et al.* [33] studied the Hubbard-Peierls chain at quarter-filling using the higher order perturbations that were calculated by Yoshioka *et al.* [34] in the quarter-filled extended Hubbard chain.

$$\mathscr{H} = \mathscr{H}_{elas} + \mathscr{H}_\rho + \mathscr{H}_\sigma + \mathscr{H}_{1/4} + \mathscr{H}_d + \mathscr{H}_t \tag{IV.85}$$

where

$$\begin{aligned}
\mathscr{H}_{elas} &= \frac{K}{2}\sum_i u_i^2 \\
\mathscr{H}_\rho &= \frac{v_\rho}{4\pi}\int dx\Big[\frac{1}{K_\rho}(\partial_x\phi_\rho)^2 + K_\rho(\partial_x\theta_\rho)^2\Big] \\
\mathscr{H}_\sigma &= \frac{v_\sigma}{4\pi}\int dx\Big[\frac{1}{K_\sigma}(\partial_x\phi_\sigma)^2 + K_\sigma(\partial_x\theta_\sigma)^2\Big] \\
\mathscr{H}_{1/4} &= g_{1/4}\int dx\cos(4\phi_\rho) \\
\mathscr{H}_d &= -g_d u_d\int dx\sin(2\phi_\rho) \\
\mathscr{H}_t &= -g_t u_t\int dx\cos(\phi_\rho - \chi_t - \pi/4)\cos(\phi_\sigma)
\end{aligned} \tag{IV.86}$$

- $\mathscr{H}_\sigma$ and $\mathscr{H}_\rho$ describe the Tomonaga-Luttinger liquid with parameters $K_\sigma$ and $K_\rho$ and Fermi velocities $v_\rho$ and $v_\sigma$. The $SU(2)$ symmetry of the undistorted limit ($u_i = 0$) requires $K_\sigma = 1$.

- $\mathscr{H}_{1/4}$ is the quarter-filled umklapp scattering. It favors a charge-ordered state coexisting with a spin-Peierls tetramerization (see the schematic ground-state (b) in Fig. IV.11). Kuwabara *et al.* consider it favors the appearance of a new phase in the large repulsion on-site and between nearest-neighbors $U$ an $V$ region, that we will refer a the "$D_2'$ phase". They also mention that this phase is very sensitive to the cluster size. According to Ref. [33] the size effects are negligible in the $L = 36$ systems used for the DMRG study. This "$D_2'$ phase" was not obtained by exact diagonalization by Poilblanc and Riera on $L$-site rings with $L$ up to 16. According to Fig. IV.7, under strong repulsion the BOW should tend to a dimerization. Indeed the amplitudes of the $2k_F$ harmonic becomes smaller than the one of the $4k_F$ for $U > 5$ (at $V = 2$). Either the nearest neighbor repulsion $V$ is not strong

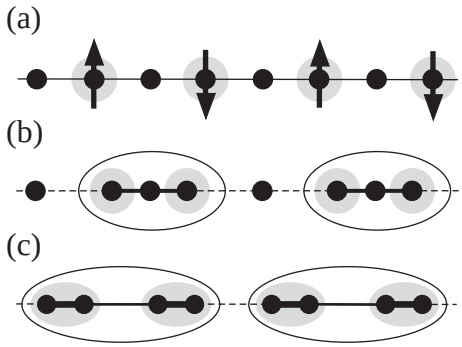


Figure IV.11: *Schematic ground states obtained by the g-ology: the arrow represent the ordered spins, the gray area the density localization, the ellipses the spin-single formation and the BOW is represented by the thickness of the bonds. (a) Charge ordering and Neél ordering, not obtained in one-dimensional models. (b) Charge-ordering and spin-Peierls lattice distortion ("$D_2'$ phase") and (c) Mott insulating state and spin-Peierls lattice distortion ("$D_2$ phase"). Note that the grey areas indicate that the density is bond-centered, but since the two-sites of the strong bonds are not equivalent the do not have the same density. Figure from Kuwabara* et al. *[33].*

enough (the "$D_2'$ phase" is expected for $V > 4$), or size effects prevent its appearance. However we shall not focus on this phase since bosonization cannot give precise answers for strong nearest-neighbor repulsion.

- $\mathscr{H}_d$ is the half-filled umklapp scattering. It favors a dimer Mott insulating state with a spin-Peierls dimerization (see the schematic ground-state (c) in Fig. IV.11). This state corresponds to the "$D_2$ phase" described by Poilblanc and Riera (see Fig. IV.6).

- The term $\mathscr{H}_t$ is derived from the kinetic energy in presence of the lattice tetramerization $u_t$. This term was firstly neglected by Yoshioka *et al.* [34] in their renormalization group calculations. According to Kuwabara *et al.* [33], in the low $U$ and $V$ region, his term produces the $2k_F$ state due to Peierls instability and fixes: $\phi_\rho = \pi/4$, $\phi_\sigma = 0$ and $\chi_t = 0$ (i.e. a tetramerized CDW centered on the sites). This is in agreement with Poilblanc and Riera's results and this corresponds to the "$D_1$ phase".

The indices $d$ stands for dimerization and $t$ for tetramerization. The generic lattice distortion is the same with our model:

$$u_i = u_d \cos(\pi x_i) + u_t \cos(x_i \pi/2 + \chi_t) \tag{IV.87}$$

The coupling constants were computed perturbatively by Yoshioka *et al.* [34] from the weak coupling regime:

$$g_{1/4} \propto \frac{U^2(U-4V)}{t^2} \tag{IV.88}$$

$$g_d \propto U - \frac{AU(U-2V)}{t} \text{ where } A \text{ in a constant} \tag{IV.89}$$

$$g_t \propto t \tag{IV.90}$$

From those couplings' expressions one clearly see that, for small on-site repulsion $U$ and between nearest-neighbors $V$, the tetramerizing term $\propto g_t$ is leading. For larger $U$ and $V$ this coupling between the spin and charge sectors can be neglected in comparison with the couplings that increase with the repulsion. Hence there is a competition between $\mathscr{H}_{1/4}$ and $\mathscr{H}_d$. Kuwabara *et al.* [33] then explained that to compare the relative stability of these states, the above bosonization is not appropriate. Indeed, on the one hand the coupling constants are obtained perturbatively from the weak coupling regime and of the other hand the treatment of the three non-linear terms together with the lattice degree of freedom may become problematic. Finally they continued the study numerically by means of DMRG. We will not detail their study but compare our results with the g-ology:

- Our Hamiltonian for the Peierls case is very similar with the one obtained with the g-ology.
- Phase diagram: Our situation is similar and we cannot obtain more information than the g-ology from our bosonized Hamiltonian. Even though the bosonization rules we are using are much stronger in the sense that they do not require to stay in the weak coupling limit, we do not know the analytical expression of the coefficients $r_i$ and $l_i$ as a function of the repulsion $U$. In the weak repulsion limit ($U/t \ll 1$), we recover coupling constants that are in the line with the ones obtained by the g-ology. Hence we cannot study *quantitatively* the positions of the energy crossings and establish a phase diagram to compare with the results of Poilblanc and Riera [29, 30].
- Phases of the operators: the spin operators obtained by the g-ology in the interaction term does not have the same phases with our bosonized operators (i.e. cosine instead of sine). So far we do no explain this discrepancy.

# 7 Quarter-filled Hubbard model: conclusion and outlook

The one-dimensional Hubbard model at the commensurate quarter-filling ($n = 1/2$) is a good model for describing the organics charge-transfer salts like the Bechgaard and the Fabre salts. These systems exhibit very rich phase diagrams, including various types of charge-density-waves.
The quarter-filled Hubbard chain coupled with Holstein or Peierls distortions has been widely studied by means of various numerical methods such as exact diagonalization and DMRG. In the weak repulsion limit (i.e. $U/t \ll 1$), the g-ology gives a qualitative prediction of the appearance of the different phases.

We obtained, by means of bosonization with supplementary harmonics, a Hamiltonian similar with the one obtained by the g-ology. We recover *qualitatively* the tetramerized and dimerized phases that were previously obtained. However our method is not capable to give more information than the g-ology, or in other terms, we cannot determine *quantitatively* the crossings between the different phases. Indeed we are using bosonization rules based on a comparison with the critical exponents of the correlation functions that were calculated by Frahm and Korepin [37, 38] from the Bethe ansatz solution. Hence the terms we are adding can

be used for any repulsion $U$. However, establishing a precise phase diagram as a function of the repulsion $U$ implies knowing the analytical expression of the coefficients that appear in front of our bosonization harmonics as a function of the repulsion $U$. Calculating these functions implies coming back to the Bethe ansatz solution which is far beyond the scope of this project. To conclude, our approach can be seen as an alternative to the g-ology method but it cannot give a quantitative description of the phase transitions for $U/t \gg 1$.

To continue, we will study both types of lattice distortions simultaneously and study the interplay between Holstein and Peierls phonons. This study was partly done [31, 32, 206]. We will add a magnetic field as a new ingredient. We expect magnetization plateaux to arise such as in the frustrated spin chain coupled with lattice distortions [13].

# Chapter V

# Conclusion and outlook

Low dimensional systems coupled with phonons can exhibit very interesting behaviors such as charge-density waves, bond-order waves and magnetization plateaux at rational value of the saturation magnetization. We studied the influence of phonons in the adiabatic limit on a couple of classical and quantum spin systems in one and two dimensions.

After introducing the basic knowledges for the study of low-dimensional strongly correlated systems in a Chapter II, we first studied in Sec. 3 of Chapter III the frustrated classical spin chain with competing interactions between nearest and next-to-nearest neighbors coupled with adiabatic phonons. The motivation is twofold: on the one hand, magnetization plateaux were shown to arise at 1/2 of the saturation magnetization in the pyrochlore lattice with classical spins coupled with adiabatic phonons [12]. And on the other hand, adiabatic phonons were previously found to be a mechanism for the appearance of magnetization plateaux in the $S = 1/2$ frustrated spin chain [13]. We showed that the 1/3 plateau, which exhibits a classical structure in the quantum case can survive in the frustrated *classical* spin chain. The spin configuration in the plateau phase is the collinear 'Up-Up-Down' configuration, which is deformed in 'Up-Down-Up' trimers due to the spin-lattice coupling.
We carried out a study analytically and numerically by means of Monte Carlo simulations. We showed that frustration is a necessary ingredient for the appearance of a magnetization plateau while the lattice coupling widens its domain of existence. The latter was determined as a function of the spin-lattice coupling and the magnetic coupling ratio, which characterizes the frustration. We obtained the analytical values of the critical fields at the entrance and exit of the plateau and hence determined the width of the plateau. Furthermore we showed that the nature of the phase transition to saturation can be either of the first or of the second order depending of the values of the the magnetic coupling ratios and of the spin-lattice coupling.

In Sec. 4 of Chapter III, we continued the study of classical spin systems with the two-dimensional Shastry-Sutherland lattice. The quantum version of this lattice has been the subject of many experimental and theoretical work in relation with the $SrCu_2(BO_3)_2$ compound [14]. Recently the observation of plateaux in the magnetization curves of rare-earth tetraborides $RB_4$ motivated a study of the classical version of this lattice, due to the large total momenta of those compounds.
We showed that for non-zero temperature the magnetization curve of the Shastry-Sutherland lattice exhibits pseudo-plateaux at 1/3 of the saturation magnetization. We carried out a study

by means of classical spin-waves and Monte Carlo simulations and established a phase diagram in the plane magnetic field versus temperature a the particular ratio of the magnetic couplings. The latter is very similar with the phase diagrams of the triangular [24] and Kagomé lattices [25] with classical spins, in which the collinear 'Up-Up-Down' state is sandwiched between two quasi-long-range-ordered phases. In these lattices, the existence of the pseudo-plateaux is due to the entropic selection of the 'Up-Up-Down' state relatively to adjacent states. In the Kagomé lattice, a full branch of soft modes in the spectrum of the spin deviations on top of the 'Up-Up-Down' state (*Order by Disorder* effect) stabilizes a 1/3 pseudo-plateau, while in the triangular lattice, the spectrum only exhibits a couple of soft points. We found that the Shastry-Sutherland lattice presents *lines* of soft modes, like the $\mathbf{q} = \mathbf{0}$ 'Up-Up-Up-Down' state on the frustrated square lattice [162]. However, the classical ground state of the Shastry-Sutherland lattice in the pseudo-plateau has no local continuous degeneracies, which makes the selection mechanism of the 'Up-Up-Down' state in the Shastry-Sutherland lattice is more similar to the triangular lattice.
We furthermore studied the behavior of the pseudo-plateaux away from the particular ratio of magnetic couplings and showed that a pseudo-plateau phase still exists. However, its domain of existence is restricted to higher temperature since the spin configuration in the low temperature region is an incommensurate spiral.
Finally, we started investigating the Shastry-Sutherland lattice in the presence of adiabatic phonons and found that a 1/3 plateau arises at zero temperature. Using a very simple model for the lattice distortions, we found a Peierls distortion. The model could be improved by using correlated distortions, as previously done in the triangular and Kagomé lattices [181].

The last chapter, Chapter IV, of this thesis is dedicated to the study of a quantum system coupled with adiabatic phonons. We studied the quarter-filled Hubbard chain in the presence of Holstein phonons, which modulate the chemical potentials of the sites, and Peierls phonons, which act on the bonds. This system has been previously widely studied as a model for the organic charge-transfer salts like the Bechgaard and Fabre salts. Numerical studies predicted a very rich phase diagram including tetramerized and dimerized phases [29, 30]. The low repulsion region was also studied with the g-ology method and renormalization group analysis [33, 34].
In order to take into account all commensurate relevant terms, we used bosonization rules including more harmonics [36]. These rules were previously constructed from the analysis of the critical exponents of the correlation functions of the Hubbard model obtained from the Bethe ansatz solution [37, 38, 205]. We obtained an effective bosonic Hamiltonian that is in the line with the results of g-ology. The fermion-lattice coupling couples the spin and charge sectors, which become gapped. The ground state is a charge-density wave whose periodicity depends on the strength of the repulsion.
Our method allows to recover *qualitatively* the sequence of charge-density wave phases that were obtained numerically [29, 30] but the lack of information on the dependence in repulsion does not allow a quantitative study away from the weak repulsion limit. Hence this method is an alternative to the g-ology but it does not bring more information.
However it is a good start to continue the study of the interplay between Holstein and Peierls

phonons and also add an applied magnetic field. The latter is expected to lead to plateaux at rational values of the magnetization like in the frustrated $S = 1/2$ spin chain [13].

# Appendices

# Appendix A

# Convention for the notation

The notations that were used in the whole manuscript are explained here. In general, bold letters in mathematical fonts indicate vectors. Then we used:

| | | |
|---|---|---|
| $A$ | : | Spin-lattice coupling constant |
| $\alpha$ | : | Chap. II: Index for an energy band |
| $\alpha$ | : | Chap. III: Ratio of the magnetic couplings ($\alpha = J_1/J_2$) |
| $\beta$ | : | $\beta = 1/k_B T$, where $k_B$ is the Boltzmann constant |
| $c_{j,\sigma}$ | : | Annihilation operator, annihilates a fermion on site $j$ with spin $\sigma$ |
| $c^+_{j,\sigma}$ | : | Creation operator, creates a fermion on site $j$ with spin $\sigma$ |
| $\delta_j$ | : | Displacement of the site $j$ |
| $\delta_{ij}$ | : | Elongation ($\delta_{ij}$>0)/contraction ($\delta_{ij}$<0) of the bond between the sites $i$ and $j$ |
| $\delta_2$ | : | Amplitude of the $2_{K_F}$ harmonic of the generic lattice distortion |
| $\delta_4$ | : | Amplitude of the $4_{K_F}$ harmonic of the generic lattice distortion |
| $\delta^H_j$ | : | Lattice distortions on site $j$ for the Holstein coupling |
| $\delta^P_j$ | : | Lattice distortions on site $j$ for the Peierls coupling |
| $\epsilon(\mathbf{k})$ | : | Energy of a free particle with momentum $\mathbf{k}$ |
| $E(\mathbf{k})$ | : | Energy of an interacting particle with momentum $\mathbf{k}$ |
| $\phi_\sigma$ | : | Bosonic field with spin $\sigma$ |
| $\phi_{\sigma,L}$ | : | Chiral bosonic field for left movers with spin $\sigma$ |
| $\phi_{\sigma,R}$ | : | Chiral bosonic field for right movers with spin $\sigma$ |
| $\phi_c$ | : | Boson for the charge degree of freedom |
| $\phi_s$ | : | Boson for the spin degree of freedom |
| $\varphi_{\mathbf{k},\alpha}$ | : | Bloch function in the band $\alpha$ and with wave wavevector $\mathbf{k}$ |
| $\varphi_{\mathbf{r}_j,\alpha}$ | : | Wannier function in the band $\alpha$ and around site $j$ |
| $\mathscr{FBZ}$ | : | First Brillouin Zone |

| | | |
|---|---|---|
| $k$ | : | Scalar $k$. If in one dimension, $k = k_x$ |
| $k_F$ | : | Fermi wavevector, $k_F = n\pi/2(1-M)$ |
| $\mathbf{k}$ | : | Wavevector $k$ with coordinates $k_x$, $k_y$ and $k_z$ if in three dimensions |
| $K$ | : | Spring constant |
| $K^H$ | : | Spring constant for the Holstein coupling |
| $K^P$ | : | Spring constant for the Peierls coupling |
| $\mu$ | : | Chemical potential |
| $M$ | : | Magnetization |
| $M_{sat}$ | : | Saturation magnetization |
| $n$ | : | Filling of the system: $n = N_e/N$ $(0 \leq n \leq 2)$ |
| $N$ | : | Number of lattice sites |
| $N_e$ | : | Number of electrons in the lattice |
| $n_{\sigma,j}$ | : | Density operator: $n_{j,\sigma} = c^+_{j,\sigma} c_{j,\sigma}$ |
| $\psi_\sigma$ | : | Fermionic field with spin $\sigma$ |
| $\psi_{\sigma,L}$ | : | Chiral fermionic field for left movers with spin $\sigma$ |
| $\psi_{\sigma,R}$ | : | Chiral fermionic field for right movers with spin $\sigma$ |
| $\sigma$ | : | Spin index. We consider electrons, thus: $\sigma = \uparrow, \downarrow$ |
| $S$ | : | Norm of a spin, ex: $S = 1/2$ |
| $\mathbf{S_j}$ | : | Classical spin (vector) on site $j$ |
| $S_j$ | : | Norm of the classical spin $\mathbf{S_j}$ (then set to 1) |
| $\hat{s}_j$ | : | Spin operator on site $j$ |
| $t$ | : | Hopping integral. We take $t_{ij} = t$ ($i$, $j$ are NN in the tight-binding approximation) |
| $U$ | : | On-site repulsion ($U > 0$) |
| $V$ | : | Repulsion between nearest-neighbor sites ($V > 0$) |
| $Z$ | : | Amplitude of the discontinuity in the particule distribution of a Fermi liquid (Sec 2.1) |
| $\mathcal{Z}$ | : | Partition function |

# Appendix B

# Thermal fluctuations matrices of a couple of two-dimensional systems

In this appendix we give the thermal fluctuations matrices of a couple of two-dimensional lattices with classical Heisenberg spins that are discussed in Sec. 4.4. We consider the triangular lattice, the frustrated square lattice and the Shastry-Sutherland lattice. In all these systems thermal fluctuations act the same way on the $x-$ and $y-$ components. Hence the matrices $\mathscr{M}$ are the same for fluctuations in the $x-$ and $y-$ directions.

## 1 Classical Heisenberg spins on the triangular lattice

We consider the triangular lattice with $J$ magnetic couplings. For non-zero temperature and at $M/M_{sat} = 1/3$ the system is in the $UUD$ state in which each triangle contains two spins Up and one spin Down [24]. One has to consider 3 sublattices. The magnetic field to apply is $h = h_{1/3} = J$.
The matrix of thermal fluctuations up to $2^{nd}$ order on top of the $UUD$ state is:

$$\mathscr{M}_{UUD,\Delta} = \begin{pmatrix} -3J-\frac{h}{2} & -\frac{J}{2}\left(1+e^{-i(-k_x+k_y)}+e^{ik_x}\right) & -\frac{J}{2}\left(1+e^{-i(-k_x+k_y)}+e^{-ik_y}\right) \\ -\frac{J}{2}\left(1+e^{i(-k_x+k_y)}+e^{-ik_x}\right) & \frac{h}{2} & \frac{J}{2}\left(1+e^{-ik_y}+e^{-ik_x}\right) \\ -\frac{J}{2}\left(1+e^{i(-k_x+k_y)}+e^{ik_y}\right) & \frac{J}{2}\left(1+e^{ik_y}+e^{ik_x}\right) & \frac{h}{2} \end{pmatrix}$$

## 2 Classical Heisenberg spins on the frustrated square lattice

We consider the square lattice with $J$ edge couplings and additional diagonal couplings $J'$. We focus on th ratio $J' = J/2$ [162]. At $M/M_{sat} = 1/2$ the system lies in the colinear $UUUD$ state. Line of Up spins ($\uparrow\uparrow \ldots \uparrow\uparrow\uparrow$) alternate with lines of Upand Down spins ($\uparrow\downarrow \ldots \downarrow\uparrow\downarrow$). The unit cell contains 4 spins. The magnetic field is $h = h_{1/2} = 4J$.

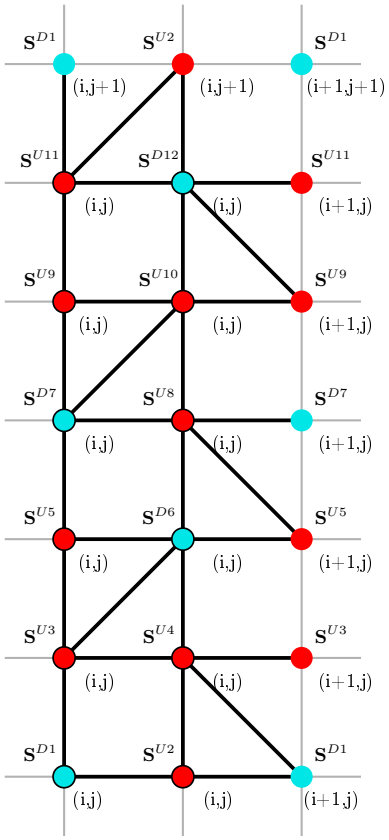


Figure B.1: *Unit cell of the Shastry-Sutherland lattice at $M = 1/3$ (black lines). It contains 12 spins labelled $(i, j)$: Up in red, Down in blue, circles with a black line for the spins belonging to the cell.*

The matrix of thermal fluctuations up to $2^{nd}$ order on top of the $UUUD$ state is:

$$\mathscr{M}_{UUUD} = \begin{pmatrix} 2J+2J'-\frac{h}{2} & -\frac{J}{2}(1+e^{-ik_y}) & -\frac{J'}{2}(1+e^{ik_x}+e^{-ik_y}+e^{i(k_x-k_y)}) & -\frac{J}{2}(1+e^{ik_x}) \\ -\frac{J}{2}(1+e^{ik_y}) & -2J'+\frac{h}{2} & \frac{J}{2}(1+e^{ik_x}) & \frac{J'}{2}(1+e^{i(k_x+k_y)}+e^{ik_y}+e^{ik_x}) \\ -\frac{J'}{2}(1+e^{-ik_x}+e^{ik_y}+e^{i(-k_x+k_y)}) & \frac{J}{2}(1+e^{-ik_x}) & -2J+2J'+\frac{h}{2} & \frac{J}{2}(1+e^{ik_y}) \\ -\frac{J}{2}(1+e^{-ik_x}) & \frac{J'}{2}(1+e^{-i(k_x+k_y)}+e^{-ik_y}+e^{-ik_x}) & \frac{J}{2}(1+e^{-ik_y}) & -2J'+\frac{h}{2} \end{pmatrix}$$

# 3 Classical Heisenberg spins on the Shastry-Sutherland lattice

We consider the Shastry-Sutherland lattice with $J'$ edge couplings and $J$ diagonal couplings. We focus on the ratio $J'/J = 1/2$. For non-zero temperature and at $M/M_{sat} = 1/3$ the system lies in the $UUD$ state. The magnetic field is $h = h_{1/3} = 3J'$. We have to consider the 12 sublattices depicted in Fig. B.1.

The matrix of thermal fluctuations up to $2^{nd}$ order on top of the $UUD$ state is:

$$\mathscr{M}_{UUD,SSL} = \begin{pmatrix}
3J' - \frac{h}{2} & -\frac{J'}{2}(1+e^{-ik_x}) & -\frac{J'}{2} & -J'e^{-ik_x} & 0 & 0 & 0 & 0 & 0 & 0 & -\frac{J'}{2}e^{-ik_y} & 0 \\
-\frac{J'}{2}(1+e^{ik_x}) & \frac{h}{2} & 0 & \frac{J'}{2} & 0 & 0 & 0 & 0 & 0 & 0 & J'e^{-ik_y} & -\frac{J'}{2}e^{-ik_y} \\
-\frac{J'}{2} & 0 & \frac{h}{2} & \frac{J'}{2}(1+e^{-ik_x}) & \frac{J'}{2} & -J' & 0 & 0 & 0 & 0 & 0 & 0 \\
-J'e^{ik_x} & \frac{J'}{2} & \frac{J'}{2}(1+e^{ik_x}) & \frac{h}{2} & 0 & -\frac{J'}{2} & 0 & 0 & 0 & 0 & 0 & 0 \\
0 & 0 & \frac{J'}{2} & 0 & \frac{h}{2} & -\frac{J'}{2}(1+e^{-ik_x}) & -\frac{J'}{2} & J'e^{-ik_x} & 0 & 0 & 0 & 0 \\
0 & 0 & -J' & -\frac{J'}{2} & -\frac{J'}{2}(1+e^{ik_x}) & 3J' - \frac{h}{2} & 0 & -\frac{J'}{2} & 0 & 0 & 0 & 0 \\
0 & 0 & 0 & 0 & -\frac{J'}{2} & 0 & 3J' - \frac{h}{2} & -\frac{J'}{2}(1+e^{-ik_x}) & -\frac{J'}{2} & -J' & 0 & 0 \\
0 & 0 & 0 & 0 & J'e^{ik_x} & -\frac{J'}{2} & -\frac{J'}{2}(1+e^{ik_x}) & \frac{h}{2} & 0 & \frac{J'}{2} & 0 & 0 \\
0 & 0 & 0 & 0 & 0 & 0 & -\frac{J'}{2} & 0 & \frac{h}{2} & \frac{J'}{2}(1+e^{-ik_x}) & \frac{J'}{2} & -J'e^{-ik_x} \\
0 & 0 & 0 & 0 & 0 & 0 & -J' & \frac{J'}{2} & \frac{J'}{2}(1+e^{ik_x}) & \frac{h}{2} & 0 & -\frac{J'}{2} \\
-\frac{J'}{2}e^{ik_y} & J'e^{ik_y} & 0 & 0 & 0 & 0 & 0 & 0 & \frac{J'}{2} & 0 & \frac{h}{2} & -\frac{J'}{2}(1+e^{-ik_x}) \\
0 & -\frac{J'}{2}e^{ik_y} & 0 & 0 & 0 & 0 & 0 & 0 & -J'e^{ik_x} & -\frac{J'}{2} & -\frac{J'}{2}(1+e^{ik_x}) & 3J' - \frac{h}{2}
\end{pmatrix}$$

# Appendix C

# Bosonization

This appendix gives more details on the computations of the bosonized operators from Chapter IV. The conventions used for the signs in the expression of the fermionic fields change from one textbook to another. We use the bosonization rules used in Ref. [26, 118].
In the first section we rewrite the Hubbard Hamiltonian in the continuum limit, in term of fermionic fields. The second section is dedicated to the bosonization of the Hubbard Hamiltonian. Finally, in the third section, we add the lattice coupling terms, which requires a bosonization with more harmonics [35–38, 205].

## 1 Low energy effective field theory of the Hubbard model

We are considering the Hubbard Hamiltonian:

$$\mathscr{H} = -t\sum_{\sigma,j}(c^{+}_{\sigma,j}c_{\sigma,j+1} + h.c.) + U\sum_{j} n_{\uparrow,j}n_{\downarrow,j} + \mu\sum_{\sigma,j} n_{\sigma,j} \tag{C.1}$$

The ground state of the free part is obtained by filling all the single particles states in the interval $[-k_F, k_F]$. Since the low-lying excitations are constructed by taking into account the modes with wavevectors close to the Fermi points $\pm k_F$, we will decompose the fermionic field in left $(-k_F)$ and right $(k_F)$ components.

### 1.1 Continuum limit of Fermi operators

We consider fermionic fields with spin $\sigma$ ($\sigma = \uparrow, \downarrow$) in $1+1$ dimension that correspond to the continuum limit of the discret fermionic creation/annihilation operators:

$$\lim_{a\to 0}\frac{c_{\sigma,j}}{\sqrt{a}} = \psi_\sigma(x) = e^{ik_{F,\sigma}x}\psi_{\sigma,L}(x) + e^{-ik_{F,\sigma}x}\psi_{\sigma,R}(x) + \dots \tag{C.2}$$

The dots stand for higher order terms that are needed to reproduce the Bethe ansatz result for the correlation functions. We will introduce more terms when we include the lattice coupling.

As discussed in Chapter IV, one can write the mode expansion of the left and right fermionic

fields in terms of the electrons and holes operators $a(k)$ and $b(k)$ around the Fermi point:

$$\psi_{L,\sigma} = \frac{1}{\sqrt{2\pi}}\int_{-\infty}^{0} dk\left[e^{-ik(t+x)}a_\sigma(k) + e^{-ik(t+x)}b_\sigma^+(k)\right] \tag{C.3}$$

$$\psi_{R,\sigma} = \frac{1}{\sqrt{2\pi}}\int_{0}^{\infty} dk\left[e^{ik(t-x)}a_\sigma(k) + e^{-ik(t-x)}b_\sigma^+(k)\right] \tag{C.4}$$

We are interested in $t = 0$ [1] and the fields only depend on a space variable $x = m \cdot a$, where $m \in \mathbb{Z}$ and $a$ is the lattice spacing ($a > 1/\Lambda$, $\Lambda$ is the cutoff discussed in Chapter IV).

Let us rewrite the products of creation/annihilation operators from the hopping term in terms of fields:

$$\begin{aligned}\frac{1}{a}c_{\sigma,j}^+ c_{\sigma,j+1} &= \psi_\sigma^+(x)\psi_\sigma(x+a)\\ &= e^{ik_{F,\sigma}a}J_{\sigma,L}(x) + e^{-ik_{F,\sigma}a}J_{\sigma,R}(x)\\ &\quad + ae^{ik_{F,\sigma}a}\psi_{\sigma,L}^+(x)\partial_x\psi_{\sigma,L}(x) + ae^{-ik_{F,\sigma}a}\psi_{\sigma,R}^+(x)\partial_x\psi_{\sigma,R}(x)\\ &\quad + e^{-ik_{F,\sigma}(2x+a)}\psi_{\sigma,L}^+(x)\psi_{\sigma,R}(x) + e^{ik_{F,\sigma}(2x+a)}\psi_{\sigma,R}^+(x)\psi_{\sigma,L}(x)\\ &\quad + ae^{ik_{F,\sigma}(2x+a)}\psi_{\sigma,R}^+(x)\partial_x\psi_{\sigma,L}(x) + ae^{-ik_{F,\sigma}(2x+a)}\psi_{\sigma,L}^+(x)\partial_x\psi_{\sigma,R}(x)\end{aligned} \tag{C.5}$$

The left and right currents $J_{\sigma,r}$ ($r = L, R$) are fluctuations of the densities of the chiral fields:

$$J_{\sigma,r}(x) = \psi_{\sigma,r}^+(x)\psi_{\sigma,r}(x) \tag{C.6}$$

The number operators in the continuum limit reads:

$$\begin{aligned}\frac{1}{a}n_{\sigma,j} &= \psi_\sigma^+(x)\psi_\sigma(x)\\ &= J_{\sigma,L}(x) + J_{\sigma,R}(x) + e^{-i2k_{F,\sigma}x}\psi_{\sigma,L}^+(x)\psi_{\sigma,R}(x) + e^{i2k_{F,\sigma}x}\psi_{\sigma,R}^+(x)\psi_{\sigma,L}(x)\end{aligned} \tag{C.7}$$

## 1.2 Wave vectors

Under an applied magnetic field, the fermions from the $\uparrow$ and $\downarrow$ bands do not have the same Fermi wave-vectors and one can define:

$$\begin{aligned}k_+ &= k_{F,\uparrow} + k_{F,\downarrow} = \pi n\\ k_- &= k_{F,\uparrow} - k_{F,\downarrow} = \pi\langle M\rangle\end{aligned} \tag{C.8}$$

Where $n$ is the density $n = N_e/N$, and $\langle M\rangle$ the magnetization.
We will focus on systems with no magnetic field applied. The wave vectors simply become:

$$k_{F,\uparrow} = k_{F,\downarrow} = k_F = n\frac{\pi}{2} \tag{C.9}$$

$$k_- = 0 \tag{C.10}$$

$$k_+ = n\pi \tag{C.11}$$

[1] We come back to this point later by introducing complex coordinates.

## 1.3 Non-interacting model ($U = 0$)

We first focus on the gas of free fermions on a one-dimensional lattice with $N$ sites with a chemical potential $\mu$ that fixes the number of electrons $N_e$.

$$\mathscr{H}_{t\mu} = -t\sum_{\sigma,j}(c^+_{\sigma,}c_{\sigma,j+1} + h.c.) + \mu\sum_{\sigma,j} n_{\sigma,j} \tag{C.12}$$

In the following results, the terms that are oscillating are directly thrown away since they are incommensurate and will disappear in thet large scale physics.

The Hamiltonian in continuum limit reads:

$$\begin{aligned}\mathscr{H}_{t\mu} &= -t\sum_{\sigma}\int dx\Big[e^{ik_{F,\sigma}a}J_{\sigma,L}(x) + e^{-ik_{F,\sigma}a}J_{\sigma,R}(x) \\ &\quad + a\big(e^{ik_{F,\sigma}a}\psi^+_{\sigma,L}(x)\partial_x\psi_{\sigma,L}(x) + e^{-ik_{F,\sigma}a}\psi^+_{\sigma,R}(x)\partial_x\psi_{\sigma,R}(x)\big) + h.c.\Big] \\ &\quad + \mu\sum_{\sigma}\int dx\big[J_{\sigma,L}(x) + J_{\sigma,R}(x)\big]\end{aligned} \tag{C.13}$$

The chemical potential at zero temperature is equal to the Fermi energy:

$$\mu = 2t\cos(k_F a) \tag{C.14}$$

Therefore while summing the free fermions term with the chemical potential term, the currents $J_r$ cancel and we get:

$$\mathscr{H}_{t\mu} = -ta\sum_{\sigma}\int dx\big[e^{ik_{F,\sigma}a}\psi^+_{\sigma,L}(x)\partial_x\psi_{\sigma,L}(x) + e^{-ik_{F,\sigma}a}\psi^+_{\sigma,R}(x)\partial_x\psi_{\sigma,R}(x) + h.c.\big] \tag{C.15}$$

After integration we obtain in each spin sectors a massless Dirac Hamiltonian:

$$\mathscr{H}_{t\mu} = iv_F\sum_{\sigma}\int dx\big[\psi^+_{\sigma,R}(x)\partial_x\psi_{\sigma,R}(x) - \psi^+_{\sigma,L}(x)\partial_x\psi_{\sigma,L}(x)\big] \tag{C.16}$$

The Fermi velocity $v_F$ plays the role of the velocity of light [2]:

$$\frac{\partial\varepsilon(k)}{\partial k}\Big|_{k=k_F} = 2ta\sin(ak_F) = v_F \tag{C.17}$$

## 1.4 With interaction ($U \neq 0$)

Let us now consider the interaction term:

$$\mathscr{H}_{\mathrm{U}} = U\sum_j n_{\uparrow,j}n_{\downarrow,j} \tag{C.18}$$

[2] One notes that if a magnetic field was applied we would have different Fermi velocities $v_{F,\uparrow}$ and $v_{F,\downarrow}$ in each spin sector.

We use the expression of the number operators Eq. C.7 in order to rewrite the four fermions products in terms of fermionic fields. After removing oscillatory terms we have:

$$\begin{aligned}\mathscr{H}_{\mathrm{U}} &= aU\int dx\Big[(J_{R,\uparrow}+J_{L,\uparrow})(J_{L,\downarrow}+J_{R,\downarrow})\\ &+ \left(e^{i2xk_+}\psi^+_{R,\uparrow}\psi_{L,\uparrow}\psi^+_{R,\downarrow}\psi_{L,\downarrow}+h.c.\right)+\left(e^{i2xk_-}\psi^+_{R,\uparrow}\psi_{L,\uparrow}\psi^+_{L,\downarrow}\psi_{R,\downarrow}+h.c.\right)\Big]\\ &= aU\int dx\Big[(J_{R,\uparrow}+J_{L,\uparrow})(J_{L,\downarrow}+J_{R,\downarrow})\\ &+ \left(e^{i4xk_F}\psi^+_{R,\uparrow}\psi_{L,\uparrow}\psi^+_{R,\downarrow}\psi_{L,\downarrow}+h.c.\right)+\left(\psi^+_{R,\uparrow}\psi_{L,\uparrow}\psi^+_{L,\downarrow}\psi_{R,\downarrow}+h.c.\right)\Big] \qquad \text{(C.19)}\end{aligned}$$

As long as the system is not half-filled (i.e. $n \neq 1$), the terms $\propto e^{i4xk_F}$ are oscillating and can be removed. The Hamiltonian becomes:

$$\mathscr{H}_{\mathrm{U}} = aU\int dx\Big[(J_{R,\uparrow}+J_{L,\uparrow})(J_{L,\downarrow}+J_{R,\downarrow})+\left(\psi^+_{R,\uparrow}\psi_{L,\uparrow}\psi^+_{L,\downarrow}\psi_{R,\downarrow}+h.c.\right)\Big] \qquad \text{(C.20)}$$

As detailed next, the spin sector is described by a sine-Gordon model. However the intercation term is marginally irrelevant and the spin sector remains gapless.

At half-filling ($n = 1$), the terms $\propto e^{i4xk_F}$ are commensurate. They correspond to the scattering of particles from one side of the Fermi surface to the other (i.e. two left electrons become right, or vice-versa). This scattering process is called *umklapp*:

$$\mathscr{H}_{\mathrm{umklapp}} = aU\int dx\left(e^{i4xk_F}\psi^+_{R,\uparrow}\psi_{L,\uparrow}\psi^+_{R,\downarrow}\psi_{L,\downarrow}+h.c.\right) \qquad \text{(C.21)}$$

After the bosonization a relevant interaction term remains in the charge sector due to the umklapp and a charge gap appears at half-filling (Mott insulator).

# 2 Bosonization

## 2.1 Complex coordinates

We consider fields in $1+1$ dimension with the complex coordinates:

$$\begin{aligned} z &= t+ix\\ \bar{z} &= t-ix \end{aligned} \qquad \text{(C.22)}$$

The bosonic field $\phi_\sigma$ and its dual $\theta_\sigma$ are defined in terms of chiral left and right bosonic fields that are respectively analytic and anti-analytic functions:

$$\phi_\sigma(x,t) = \phi_\sigma(z,\bar{z}) = \phi_{\sigma,R}(z)+\phi_{\sigma,L}(\bar{z}) \qquad \text{(C.23)}$$

$$\theta_\sigma(x,t) = \theta_\sigma(z,\bar{z}) = \phi_{\sigma,R}(z)-\phi_{\sigma,L}(\bar{z}) \qquad \text{(C.24)}$$

The derivatives with respect to $z$ and $\bar{z}$ are :

$$\partial_z = \frac{1}{2}(\partial_t - i\partial_x) \qquad \text{(C.25)}$$

$$\partial_{\bar{z}} = \frac{1}{2}(\partial_t + i\partial_x) \qquad \text{(C.26)}$$

Using Eq. C.24, C.25 and C.26 we have:

$$\partial_z \phi_\sigma(z,\bar{z}) = \partial_z \phi_{\sigma,R}(z) \tag{C.27}$$
$$\partial_{\bar{z}} \phi_\sigma(z,\bar{z}) = \partial_{\bar{z}} \phi_{\sigma,L}(\bar{z}) \tag{C.28}$$

## 2.2 Bosonization dictionnary

The left and right components of the fermionic fields $\psi_{\sigma,R}$ and $\psi_{\sigma,L}$ are given as a function of the left and right bosonic fields $\phi_{\sigma,R}$ and $\phi_{\sigma,L}$ :

$$\psi_{\sigma,R}(z) = \frac{1}{\sqrt{2\pi a}} \eta_{\sigma,R} : e^{i\sqrt{4\pi}\phi_{\sigma,R}(z)} : \tag{C.29}$$
$$\psi_{\sigma,L}(\bar{z}) = \frac{1}{\sqrt{2\pi a}} \eta_{\sigma,L} : e^{-i\sqrt{4\pi}\phi_{\sigma,L}(\bar{z})} : \tag{C.30}$$

The operators $e^{i\alpha\phi_{\sigma,r}}$ are called *vertex operators*.
The notation $: e^{i\alpha\phi_{\sigma,r}} :$ stands for normal ordering. It consists in putting all annihilation operators on the right of the creation operators in the expansion of the vertex operator. This prescription allows to have a zero average value.
$\eta_{\sigma,r}$ $(r = L,R)$ are the *Klein factors* that guaranty the anti-commutation of the bosonized fermionic fields. We detail how to treat them in Section 2.3.

### 2.2.1 Correlation functions of bosonic fields

Let us remind the value of the correlators that are useful for the forthcoming calculations.
Chiral left and right bosons:

$$\langle \phi_{\sigma,L}(\bar{z})\phi_{\sigma,L}(\bar{w})\rangle = -\frac{1}{4\pi}\ln(\bar{z}-\bar{w}) \tag{C.31}$$
$$\langle \phi_{\sigma,R}(z)\phi_{\sigma,R}(w)\rangle = -\frac{1}{4\pi}\ln(z-w) \tag{C.32}$$

Free bosonic field:

$$\langle \phi_\sigma(z,\bar{z})\phi_\sigma(w,\bar{w})\rangle = -\frac{1}{2\pi}\ln|z-w| \tag{C.33}$$

### 2.2.2 Normal ordered products of vertex operators

The products of fermionic fields become, after bosonization, products of vertex operators. If the bosonic fields have different degrees or freedom (i.e. $\sigma \neq \sigma'$ or $r \neq r'$) these products are simple exponential products.
Otherwise, due to normal ordering, one has to take into account the value of the boson correlator:

$$: e^{i\alpha\phi_{\sigma,r}(z)} :: e^{i\beta\phi_{\sigma,r}(w)} : = : e^{i\left(\alpha\phi_{\sigma,r}(z)+\beta\phi_{\sigma,r}(w)\right)} : e^{-\alpha\beta\langle\phi_{\sigma,r}(z)\phi_{\sigma,r}(w)\rangle} \tag{C.34}$$
$$\langle \phi_{\sigma,r}(z)\phi_{\sigma',r'}(w)\rangle = -\frac{1}{4\pi}\delta_{\sigma,\sigma'}\delta_{r,r'}\ln(z-w) \tag{C.35}$$

We are working with field operators $\mathcal{O}(z,\bar{z})$ that belong to a conformal field theory. Such operators scale as:

$$\mathcal{O}(\alpha z,\bar{\alpha}\bar{z}) = \alpha^{-h}\bar{\alpha}^{-\bar{h}}\mathcal{O}(z,\bar{z}) \tag{C.36}$$

$$\Delta = h+\bar{h} \tag{C.37}$$

$$s = h-\bar{h} \tag{C.38}$$

$h$ and $\bar{h}$ are the left and right conformal dimensions. We will discuss later how important it is to know the value of the operators dimensions.
If we apply to the operator $\mathcal{O}(z,\bar{z})$ a dilation (i.e. $\alpha=\bar{\alpha}$), it scales as the sum of the left and right dimensions, which is called the *ordinary scaling dimension* of the operator $\Delta$:

$$\mathcal{O}(\alpha z,\alpha\bar{z}) = \alpha^{-\Delta}\mathcal{O}(z,\bar{z}) \tag{C.39}$$

If we apply a rotation (i.e. $\alpha = e^{i\theta}$ and $\bar{\alpha}=e^{-i\theta}$), the operator scales as the difference of the right and left dimensions, which is called the *conformal spin* of th operator, $s$:

$$\mathcal{O}(e^{i\theta}z, e^{-i\theta}\bar{z}) = e^{is\theta}\mathcal{O}(z,\bar{z}) \tag{C.40}$$

The value of the conformal dimensions can be obtained by calculating the two-points correlation function of an operator:

$$\langle\mathcal{O}(z,\bar{z})\mathcal{O}(w,\bar{w})\rangle = \frac{1}{(z-w)^{2h}}\frac{1}{(\bar{z}-\bar{w})^{2\bar{h}}} \tag{C.41}$$

Since the vertex operators are scaling fields, one can compute their conformal dimension from the exponents of the bosons Green function:

$$\langle :e^{i\beta\phi_\sigma(z,\bar{z})}:\big(:e^{i\beta\phi_\sigma(w,\bar{w})}:\big)^\dagger\rangle = e^{-\beta^2/(4\pi)\ln|z-w|^2}$$

$$= |z-w|^{-\beta^2/(2\pi)} \tag{C.42}$$

$$= \frac{1}{|z-w|^{2h+2\bar{h}}} \tag{C.43}$$

After identification, the dimensions of the chiral bosonic fields are:

| | | $h$ | $\bar{h}$ | $\Delta$ |
|---|---|---|---|---|
| Right-moving boson | $\phi_{\sigma,R}(z)$ | $\beta^2/8\pi$ | 0 | $\beta^2/8\pi$ |
| Left-moving boson | $\phi_{\sigma,L}(\bar{z})$ | 0 | $\beta^2/8\pi$ | $\beta^2/8\pi$ |
| Free boson | $\phi_\sigma(z,\bar{z})$ | $\beta^2/8\pi$ | $\beta^2/8\pi$ | $\beta^2/4\pi$ |

### 2.2.3 Bosonization of the currents

In order to calculate the currents $J_{\sigma,r}$, the normal ordering is achieved by using *point-splitting*:

$$J_{\sigma,r}(z) =: \psi^+_{\sigma,r}(z)\psi_{\sigma,r}(z) := \lim_{\epsilon\to 0}\left[\psi^+_{\sigma,r}(z+\epsilon)\psi_{\sigma,r}(z) - \langle\psi^+_{\sigma,r}(z+\epsilon)\psi_{\sigma,r}(z)\rangle\right] \tag{C.44}$$

For example, the right current is:

$$\begin{aligned} J_{\sigma,R}(z) &= \frac{\eta^{+}_{\sigma,R}\eta_{\sigma,R}}{2\pi a}\lim_{\epsilon\to 0}\Big( :e^{-i\sqrt{4\pi}\phi_{\sigma,R}(z+\epsilon)}::e^{i\sqrt{4\pi}\phi_{\sigma,R}(z)}: -\langle e^{i\sqrt{4\pi}\phi_{\sigma,R}(z+\epsilon)}e^{i\sqrt{4\pi}\phi_{\sigma,R}(z)}\rangle\Big) \\ &= \frac{1}{2\pi a}\lim_{\epsilon\to 0}\Big( :e^{-i\sqrt{4\pi}\left(\phi_{\sigma,R}(z+\epsilon)-\phi_{\sigma,R}(z)\right)}: e^{4\pi\langle\phi_{\sigma,R}(z+\epsilon)\phi_{\sigma,R}(z)\rangle} - \langle e^{i\sqrt{4\pi}\phi_{\sigma,R}(z+\epsilon)}e^{i\sqrt{4\pi}\phi_{\sigma,R}(z)}\rangle\Big) \\ &= \frac{1}{2\pi a}\lim_{\epsilon\to 0}\Big( :e^{-i\sqrt{4\pi}\left(\epsilon\partial_z\phi_{\sigma,R}+\mathcal{O}(\epsilon^2)\right)}: e^{-\frac{4\pi}{4\pi}\ln\epsilon} - \epsilon^{\frac{-4\pi}{4\pi}}\Big) \\ &= \frac{1}{2\pi a}\lim_{\epsilon\to 0}\Big(\frac{1}{\epsilon}\big(1-i\sqrt{4\pi}\left(\epsilon\partial_z\phi_{\sigma,R}+\mathcal{O}(\epsilon^2)\right)\big)-\frac{1}{\epsilon}\Big) \\ &= -\frac{i}{\sqrt{\pi}}\partial_z\phi_{\sigma,R}(z) \end{aligned} \tag{C.45}$$

Similarly, the left currents reads:

$$J_{\sigma,L}(\bar{z}) = \frac{i}{\sqrt{\pi}}\partial_{\bar{z}}\phi_{\sigma,L}(\bar{z}) \tag{C.46}$$

The left and right currents are actually the conserved currents through a translation of the lattice spacing $a$, $\phi_\sigma(x)\to\phi_\sigma(x+a)$ in the action of the free scalar boson.

The free part of the Hamiltonian (Eq. C.16) is also bosonized using the point-splitting:

$$\begin{aligned} :\psi^{+}_{\sigma,R}(z)\partial_x\psi_{\sigma,R}(z): &= \lim_{\epsilon\to 0}\left[\psi^{+}_{\sigma,R}(z+\epsilon)\partial_z\psi_{\sigma,R}(z) - \langle\psi^{+}_{\sigma,R}(z+\epsilon)\partial_z\psi_{\sigma,R}(z)\rangle\right] \\ &\propto \left(\partial_z\phi_{\sigma,R}\right)^2 \end{aligned} \tag{C.47}$$

Similarity, one obtains:

$$:\psi^{+}_{\sigma,L}(\bar{z})\partial_x\psi_{\sigma,L}(\bar{z}):\propto \left(\partial_x\phi_L\right)^2 \tag{C.48}$$

## 2.3 Klein factors

In order to preserve the anti-commutation relations of the bosonized fermionic fields, one adds in front of the vertex operators *Klein factors*. We need four species of Klein factors since we have four species of fermions. Klein factors present the following properties:

- Klein factors are real: $\eta^{*}_{\sigma,r}=\eta_{\sigma,r}$.
- Klein factors obey a Clifford algebra:

$$\left\{\eta_{\sigma,r},\eta_{\sigma',r'}\right\} = 2\delta_{\sigma,\sigma'}\delta_{r,r'} \tag{C.49}$$

As a consequence, we have (for simplicity, let us call $\{i,j,k,l\}=\{\uparrow R,\uparrow L,\downarrow R,\downarrow L\}$):

$$\eta_i\eta_j = -\eta_j\eta_i \tag{C.50}$$

$$\eta^{*}_i\eta_i = 1 \tag{C.51}$$

- Klein factor act on a Hilbert space that differs from the boson Hilbert space. The idea is to diagonalize the Klein factors products, select one eigenstate and work in it. The products of Klein factor hence simply become a constant. For example, the products of four Klein factors the appear in the interaction terms have two possible eigenvalues: $\pm 1$. One has to make sure to select the same Klein eigenstate in each term and then simply replace it by $\pm 1$.

- Representation: Since the minimal dimension of the Klein factors Clifford algebra is four like Dirac matrices in $3+1$ dimensions, one can use a representation in terms of tensor products of Pauli matrices $\sigma_i$. Let us use the same representation of the Clifford algebra as Sénéchal [27]:

$$\sigma_1 = \begin{pmatrix} 0 & 1 \\ 1 & 0 \end{pmatrix}, \sigma_2 = \begin{pmatrix} 0 & -i \\ i & 0 \end{pmatrix}, \sigma_3 = \begin{pmatrix} 1 & 0 \\ 0 & -1 \end{pmatrix} \tag{C.52}$$

$$\eta_{R,\uparrow} = \sigma_1 \otimes \sigma_1 = \begin{pmatrix} 0 & \sigma_1 \\ \sigma_1 & 0 \end{pmatrix} = \begin{pmatrix} 0 & 0 & 0 & 1 \\ 0 & 0 & 1 & 0 \\ 0 & 1 & 0 & 0 \\ 1 & 0 & 0 & 0 \end{pmatrix} \tag{C.53}$$

$$\eta_{L,\uparrow} = \sigma_2 \otimes \sigma_1 = i \begin{pmatrix} 0 & -\sigma_1 \\ \sigma_1 & 0 \end{pmatrix} = i \begin{pmatrix} 0 & 0 & 0 & -1 \\ 0 & 0 & -1 & 0 \\ 0 & 1 & 0 & 0 \\ 1 & 0 & 0 & 0 \end{pmatrix} \tag{C.54}$$

$$\eta_{R,\downarrow} = \sigma_3 \otimes \sigma_1 = \begin{pmatrix} \sigma_1 & 0 \\ 0 & -\sigma_1 \end{pmatrix} = \begin{pmatrix} 0 & 1 & 0 & 0 \\ 1 & 0 & 0 & 0 \\ 0 & 0 & 0 & -1 \\ 0 & 0 & -1 & 0 \end{pmatrix} \tag{C.55}$$

$$\eta_{L,\downarrow} = \mathbb{1} \otimes \sigma_2 = \begin{pmatrix} \sigma_2 & 0 \\ 0 & \sigma_2 \end{pmatrix} = i \begin{pmatrix} 0 & -1 & 0 & 0 \\ 1 & 0 & 0 & 0 \\ 0 & 0 & 0 & -1 \\ 0 & 0 & 1 & 0 \end{pmatrix} \tag{C.56}$$

## 2.4 Charge and spin sectors

So far we gave bosonization rules terms of $\uparrow$ and $\downarrow$ bosons. Before rewriting the Hamiltonian, let us define a more meaningful base, in terms of charge and spin bosons. For this we use the expression of the dressed charge matrix proposed by Frahm and Korepin [37, 38].

### 2.4.1 The dressed charge matrix

The dressed charge matrix $Z$ is given by:

$$Z = \begin{pmatrix} Z_{cc} & Z_{cs} \\ Z_{sc} & Z_{ss} \end{pmatrix} \tag{C.57}$$

The coefficients are function of the repulsion $U$, the filling $n$ and eventually the magnetic field: $Z_{ij} = Z_{ij}(U, n, h)$.

The spins and charge boson are related to the $\uparrow$ and $\downarrow$ bosons as:

$$\begin{pmatrix} \phi_c \\ \phi_s \end{pmatrix} = \frac{1}{detZ} \begin{pmatrix} Z_{ss} & Z_{ss} - Z_{cs} \\ Z_{sc} & Z_{sc} - Z_{cc} \end{pmatrix} \begin{pmatrix} \phi_\uparrow \\ \phi_\downarrow \end{pmatrix} \tag{C.58}$$

The same with the dual bosons:

$$\begin{pmatrix} \theta_c \\ \theta_s \end{pmatrix} = \begin{pmatrix} Z_{cc} - Z_{sc} & Z_{sc} \\ Z_{ss} - Z_{cs} & -Z_{ss} \end{pmatrix} \begin{pmatrix} \theta_\uparrow \\ \theta_\downarrow \end{pmatrix} \tag{C.59}$$

Let us focus on systems with no magnetic field applied. The dressed charge matrix is simpler:

$$Z_{h=0} = \begin{pmatrix} \xi & 0 \\ \xi/2 & 1/\sqrt{2} \end{pmatrix} \tag{C.60}$$

The coefficients only depends on the repulsion and filling: $\xi = \xi(U, n)$.

The spin and charge bosons and their duals are defined as:

$$\phi_c = \frac{1}{\xi}(\phi_\uparrow + \phi_\downarrow) \ , \ \theta_c = \frac{\xi}{2}(\theta_\downarrow + \theta_\uparrow) \tag{C.61}$$

$$\phi_s = \frac{1}{\sqrt{2}}(\phi_\uparrow - \phi_\downarrow) \ , \ \theta_s = \frac{1}{\sqrt{2}}(\theta_\uparrow - \theta_\downarrow) \tag{C.62}$$

These bosonic fields need to obey the symmetries of the charge and spin sectors. In the spin sector, the $SU(2)$ symmetry imposes:

$$\phi_s = \phi_s + m2\pi R_s \ , \ m \in \mathbb{Z} \ , \ R_s = 1/\sqrt{2\pi} \tag{C.63}$$

Where $R_s$ is the compactification radius of the spin sector. Since we consider systems with no magnetic field we have a Luttinger parameter $K_s = 1$ in the spins sector.
The charge sector is more complicated since it depends on the dressed charge matrix coefficient $\xi(U, n)$. The Luttinger parameter is $K_c = \xi^2/2$ and the compactification radius $R_c = \sqrt{\pi}/|\xi|$.

### 2.4.2 Hamiltonian in term of spin and charge boson

Let us rewrite the bosonized Hamiltonian in term of the spins and charge bosons. We just give a general form and do not detail the calculations nor the values of the coupling constant since we will actually use the exact solution from the Bethe ansazt[37, 38, 205].

Using the expressions of the bosonized currents, the free Hamiltonian Eq.IV.35 can be rewritten:

$$\mathscr{H}_{\text{free}} = \frac{v_F}{4} \sum_{j=s,c} \int \left( (\partial_x \phi_j)^2 + (\partial_x \theta_j)^2 \right) \tag{C.64}$$

Including the interaction, one rewrites the charge sector as:

$$\mathscr{H}_c = \frac{v_F}{2}\int dx\Big[\frac{\xi^2}{2}(\partial_x\phi_c)^2 + \frac{2}{\xi^2}(1-\frac{aU}{v\pi})(\partial_x\theta_c)^2\Big] \tag{C.65}$$

This is then simplified by defining rescaled fields:

$$\begin{aligned}
\mathscr{H}_c &= \frac{v_c}{2}\int dx\big[(\partial_x\tilde{\phi}_c)^2 + (\partial_x\tilde{\theta}_c)^2\big] && \text{(C.66)}\\
\tilde{\phi}_c &= \sqrt{K_c}\phi_c && \text{(C.67)}\\
\tilde{\theta}_c &= \sqrt{\frac{1}{K_c}}\theta_c && \text{(C.68)}\\
K_c &= \frac{2}{\xi^2}\big(1-\frac{aU}{\pi v_F}\big)^{1/2} && \text{(C.69)}\\
v_c &= v_F\frac{\xi^2}{2}K_c && \text{(C.70)}
\end{aligned}$$

where $K_c$ is the Luttinger parameter and $v_c$ the velocity of the charge sector. Note that this perturbative solution gives a different value of $K_c$ than the value obtained from the exact solution $K_c = \xi^2/2$.

One can perform the same treatent in the spin sector:

$$\begin{aligned}
\mathscr{H}_s &= \frac{v_s}{2}\int dx\big[\frac{1}{K_s}(\partial_x\phi_s)^2 + K_s(\partial_x\theta_s)^2\big] + g_s\int dx\cos\Big(\sqrt{8\pi}\phi_s\Big) && \text{(C.71)}\\
K_s &= 1 && \text{(C.72)}\\
& && \text{(C.73)}
\end{aligned}$$

The spin sector a described by a sine-Gordon model. However the cosine term in not relevant. As a consequence, as long as no magnetic field is applied, the spin sector remains gapless and is simply described by a free boson.

The charge sector is gapless excepted at half-filling where the umklapp adds a cosine term:

$$\mathscr{H}_{\text{umklapp}} = g_c\int dx\cos\big(\xi\sqrt{4\pi}\phi_c\big) \tag{C.74}$$

The charge sector is gapless as long as the filling differs from one-half. At one half, it corresponds to a sine-Gordon model with a relevant cosine term.

One also notes that the velocities in the different sectors, $v_s$ and $v_c$, are not the same.

# 3 Fermion-lattice interaction: bosonization with more harmonics

We focus on quarter-filled systems ($n = 1/2$) that are good models for quasi-one-dimensional organic conductors. Adiabatic phonons couple the fermions to the lattice. We consider two

kinds of phonons: Holstein on-site phonons that act as a modulation of the chemical potential and Peierls phonons that modulate the bonds lengths. The lattice coupling induce new relevant terms that we will recover using bosonization rules with more harmonics.

## 3.1 New bosonic expansion of the fermionic fields

We use the bosonization rules that were used by Cabra *et al.* [36]. This rules were built from the expression of the correlations functions of the Hubbard model [37, 38]. It consists in including subleading terms to the expression of the bosonized fermionic fields Eq. C.29 and C.30. The bosonized fermions operators are given by:

$$\begin{aligned}
\psi_\downarrow(x) &= r_1 e^{-ik_{F,\downarrow}x}\psi_{R,\downarrow}(x) \\
&+ r_2 e^{-i(k_+ + k_{F,\uparrow})x}\psi_{R,\downarrow}(x)\psi^+_{L,\uparrow}(x)\psi_{R,\uparrow}(x) \\
&+ r_3 e^{i(k_- + k_{F,\uparrow})x}\psi_{R,\downarrow}(x)\psi^+_{R,\uparrow}(x)\psi_{L,\uparrow}(x) + \dots \\
&+ l_1 e^{ik_{F,\downarrow}x}\psi_{L,\downarrow}(x) \\
&+ l_2 e^{i(k_+ + k_{F,\uparrow})x}\psi_{L,\downarrow}(x)\psi^+_{R,\uparrow}(x)\psi_{L,\uparrow}(x) \\
&+ l_3 e^{-i(k_- + k_{F,\uparrow})x}\psi_{L,\downarrow}(x)\psi^+_{L,\uparrow}(x)\psi_{R,\uparrow}(x) + \dots
\end{aligned} \tag{C.75}$$

Using:

$$\begin{aligned}
\psi_{R,\sigma}(x) &= \eta_{R,\sigma} e^{i\sqrt{4\pi}\phi_{R,\sigma}(x)} \\
\psi_{L,\sigma}(x) &= \eta_{L,\sigma} e^{-i\sqrt{4\pi}\phi_{L,\sigma}(x)}
\end{aligned} \tag{C.76}$$

it becomes:

$$\begin{aligned}
\psi_\downarrow(x) &= e^{-ik_{F,\downarrow}x} e^{i\sqrt{4\pi}\phi_{\downarrow,R}(x)} \big( r_1\eta_{R,\downarrow} + r_2\eta_{R,\downarrow}\eta_{L,\uparrow}\eta_{R,\uparrow} e^{-i2k_{F,\uparrow}x} e^{i\sqrt{4\pi}\phi_\uparrow(x)} \\
&+ r_3\eta_{R,\downarrow}\eta_{R,\uparrow}\eta_{L,\uparrow} e^{i2k_{F,\uparrow}x} e^{-i\sqrt{4\pi}\phi_\uparrow(x)} + \dots \big) \\
&\quad e^{ik_{F,\downarrow}x} e^{-i\sqrt{4\pi}\phi_{\downarrow,L}(x)} \big( l_1\eta_{L,\downarrow} + l_2\eta_{L,\downarrow}\eta_{R,\uparrow}\eta_{L,\uparrow} e^{i2k_{F,\uparrow}x} e^{-i\sqrt{4\pi}\phi_\uparrow(x)} \\
&+ l_3\eta_{L,\downarrow}\eta_{L,\uparrow}\eta_{R,\uparrow} e^{-i2k_{F,\uparrow}x} e^{i\sqrt{4\pi}\phi_\uparrow(x)} + \dots \big)
\end{aligned} \tag{C.77}$$

The dots stand for higher order harmonic that lead to irrelevant terms. $\psi\uparrow$ is obtained by converting $\downarrow$ into $\uparrow$ in the previous expression.

The constant $r_i$ and $l_i$ are unknown numerical constants which were not studied explicitly from the Bethe ansatz results [37, 38, 205]. At lowest order, $r_i$ and $l_i$ ($i = 2, 3$) are linear in $U$, and only $r_1 = l_1 = 1/\sqrt{2\pi a}$ remains, which is in agreement with the bosonization with one harmonic described in the previous section.

### 3.1.1 Terms $r_1 l_1$

Let us detail the calculation of the first term, that corresponds to the product of the first harmonics together. We call $b$ the product of Klein factors in front, here $b = \mathbb{1} \otimes \sigma_3$:

$$\begin{aligned}
\{\psi_\downarrow^+(x+m)\psi_\downarrow(x)\}_{r_1 l_1} &= ibr_1 l_1 \big[ e^{i(k_{F,\downarrow}(2x+m))} e^{-i\sqrt{4\pi}\phi_{R,\downarrow}(x+m)} e^{-i\sqrt{4\pi}\phi_{L,\downarrow}(x)} \\
&\quad - e^{-ik_{F,\downarrow}(2x+m)} e^{i\sqrt{4\pi}\phi_{L,\downarrow}(x+m)} e^{i\sqrt{4\pi}\phi_{R,\downarrow}(x)} \big] \\
&= ibr_1 l_1 \big[ e^{i(k_{F,\downarrow}(2x+m))} e^{-i[\sqrt{4\pi}\phi_\downarrow + m\sqrt{4\pi}\partial_z \phi_{R,\downarrow}]} - e^{-ik_{F,\downarrow}(2x+m)} e^{i[\sqrt{4\pi}\phi_\downarrow + m\sqrt{4\pi}\partial_{\bar{z}}\phi_{L,\downarrow}]} \big] \\
&= ibr_1 l_1 \big[ e^{i(k_{F,\downarrow}(2x+m))} e^{-i\sqrt{4\pi}\phi_\downarrow}(1+...) - e^{-ik_{F,\downarrow}(2x+m)} e^{i\sqrt{4\pi}\phi_\downarrow}(1+...) \big] \\
&\sim -2br_1 l_1 \sin\big(k_{F,\downarrow}(2x+m) - \sqrt{4\pi}\phi_\downarrow\big)
\end{aligned}$$

$$\begin{aligned}
\{\psi_\downarrow^+(x)\psi_\downarrow(x+m)\}_{r_1 l_1} &= ibr_1 l_1 \big[ e^{ik_{F,\downarrow}(2x+m)} e^{-i\sqrt{4\pi}\phi_{R,\downarrow}(x)} e^{-i\sqrt{4\pi}\phi_{L,\downarrow}(x+m)} \\
&\quad - e^{-ik_{F,\downarrow}(2x+m)} e^{i\sqrt{4\pi}\phi_{L,\downarrow}(x)} e^{i\sqrt{4\pi}\phi_{R,\downarrow}(x+m)} \big] \\
&\sim ibr_1 l_1 \big[ e^{ik_{F,\downarrow}(2x+m)} e^{-i\sqrt{4\pi}\phi_\downarrow} - e^{-ik_{F,\downarrow}(2x+m)} e^{i\sqrt{4\pi}\phi_\downarrow} \big] \\
&= -2br_1 l_1 \sin\big(k_{F,\downarrow}(2x+m) - \sqrt{4\pi}\phi_\downarrow\big)
\end{aligned}$$

Adding the complex conjugates we get:

$$\begin{aligned}
\{\psi_\downarrow^+(x+m)\psi_\downarrow(x) + h.c.\}_{r_1 l_1} &= -4br_1 l_1 \sin\big(k_{F,\downarrow}(2x+m) - \sqrt{4\pi}\phi_\downarrow\big) \\
\{\psi_\uparrow^+(x+m)\psi_\uparrow(x) + h.c.\}_{r_1 l_1} &= -4br_1 l_1 \sin\big(k_{F,\uparrow}(2x+m) - \sqrt{4\pi}\phi_\uparrow\big)
\end{aligned}$$

We finally obtain in term of $\uparrow$ and $\downarrow$ bosons:

$$\begin{aligned}
\mathcal{O}_{m,r_1 l_1}(x) &= \{\psi_\downarrow^+(x+m)\psi_\downarrow(x) + \psi_\uparrow^+(x+m)\psi_\uparrow(x) + h.c.\}_{r_1 l_1} \\
&= -8br_1 l_1 \sin\big(k_+(x+\frac{m}{2}) - \sqrt{\pi}[\phi_\uparrow + \phi_\downarrow]\big)\cos\big(k_-(x+\frac{m}{2}) - \sqrt{\pi}[\phi_\uparrow - \phi_\downarrow]\big) \quad \text{(C.78)}
\end{aligned}$$

Since no magnetic field is applied, $k_- = 0$ and we obtain in term of spin and charge boson:

$$\mathcal{O}_{m,r_1 l_1}(x) = -8br_1 l_1 \sin\big(k_F(2x+m) - \xi\sqrt{\pi}\phi_c\big)\cos\big(\sqrt{2\pi}\phi_s\big) \quad \text{(C.79)}$$

### 3.1.2 Terms $r_1 l_2 + r_2 l_1$

Let us detail the calculation of the second term, that corresponds to the product of the first with the second harmonics. Again, we call $b$ the product of Klein factors in front, here $b = \mathbb{1} \otimes \sigma_3$:

$$\begin{aligned}
\{\psi_\downarrow^+(x+m)\psi_\downarrow(x)\}_{r_1 l_2 + r_2 l_1} &= ibr_1 l_2 \big[ e^{i(2k_+ x + k_{F,\downarrow} m)} e^{-i\sqrt{4\pi}\phi_{R,\downarrow}(x+m)} e^{-i\sqrt{4\pi}\phi_{L,\downarrow}(x)} e^{-i\sqrt{4\pi}\phi_\uparrow(x)} \\
&\quad - e^{-i(k_+(2x+m)+k_{F,\uparrow} m)} e^{i\sqrt{4\pi}\phi_{L,\downarrow}(x+m)} e^{i\sqrt{4\pi}\phi_\uparrow(x+m)} e^{i\sqrt{4\pi}\phi_{R,\downarrow}(x)} \big] \\
&\quad + ibr_2 l_1 \big[ e^{i(k_+(2x+m)+k_{F,\uparrow} m)} e^{-i\sqrt{4\pi}\phi_{R,\downarrow}(x+m)} e^{-i\sqrt{4\pi}\phi_\uparrow(x+m)} e^{-i\sqrt{4\pi}\phi_{L,\downarrow}(x)} \\
&\quad - e^{-i(2k_+ x + k_{F,\downarrow} m)} e^{i\sqrt{4\pi}\phi_{L,\downarrow}(x+m)} e^{i\sqrt{4\pi}\phi_{R,\downarrow}(x)} e^{i\sqrt{4\pi}\phi_\uparrow(x)} \big] \\
&= ibr_1 l_2 \big[ e^{i(2k_+ x + k_{F,\downarrow} m)} e^{-i\sqrt{4\pi}[\phi_\downarrow + \phi_\uparrow + m\partial_z \phi_{R,\downarrow}]} \\
&\quad - e^{-i(k_+(2x+m)+k_{F,\uparrow} m)} e^{i\sqrt{4\pi}[\phi_\downarrow + \phi_\uparrow + m\partial_{\bar z}\phi_{L,\downarrow} + m\partial_z \phi_{R,\uparrow} + m\partial_{\bar z}\phi_{L,\uparrow}]} \big] \\
&\quad + ibr_2 l_1 \big[ e^{i(k_+(2x+m)+k_{F,\uparrow} m)} e^{-i\sqrt{4\pi}[\phi_\downarrow + \phi_\uparrow + m\partial_z \phi_{R,\downarrow} + m\partial_{\bar z}\phi_{L,\uparrow} + m\partial_z \phi_{R,\uparrow}]} \\
&\quad - e^{-i(2k_+ x + k_{F,\downarrow} m)} e^{i\sqrt{4\pi}[\phi_\downarrow + \phi_\uparrow + m\partial_{\bar z}\phi_{L,\downarrow}]} \big] \\
&= ibr_1 l_2 \big[ e^{i(2k_+ x + k_{F,\downarrow} m)} e^{-i\sqrt{4\pi}[\phi_\downarrow + \phi_\uparrow]} - e^{-i(k_+(2x+m)+k_{F,\uparrow} m)} e^{i\sqrt{4\pi}[\phi_\downarrow + \phi_\uparrow]} \big] \\
&\quad + ibr_2 l_1 \big[ e^{i(k_+(2x+m)+k_{F,\uparrow} m)} e^{-i\sqrt{4\pi}[\phi_\downarrow + \phi_\uparrow]} - e^{-i(2k_+ x + k_{F,\downarrow} m)} e^{i\sqrt{4\pi}[\phi_\downarrow + \phi_\uparrow]} \big] \\
\{\psi_\downarrow^+(x)\psi_\downarrow(x+m)\}_{r_1 l_2 + r_2 l_1} &= ibr_1 l_2 \big[ e^{i(k_+(2x+m)+k_{F,\uparrow} m)} e^{-i\sqrt{4\pi}\phi_{R,\downarrow}(x)} e^{-i\sqrt{4\pi}\phi_{L,\downarrow}(x+m)} e^{-i\sqrt{4\pi}\phi_\uparrow(x+m)} \\
&\quad - e^{-i(2k_+ x + k_{F,\downarrow} m)} e^{i\sqrt{4\pi}\phi_{L,\downarrow}(x)} e^{i\sqrt{4\pi}\phi_\uparrow(x)} e^{i\sqrt{4\pi}\phi_{R,\downarrow}(x+m)} \big] \\
&\quad + ibr_2 l_1 \big[ e^{i(2k_+ x + k_{F,\downarrow} m)} e^{-i\sqrt{4\pi}\phi_{R,\downarrow}(x)} e^{-i\sqrt{4\pi}\phi_\uparrow(x)} e^{-i\sqrt{4\pi}\phi_{L,\downarrow}(x+m)} \\
&\quad - e^{-i(k_+(2x+m)+k_{F,\uparrow} m)} e^{i\sqrt{4\pi}\phi_{L,\downarrow}(x)} e^{i\sqrt{4\pi}\phi_{R,\downarrow}(x+m)} e^{i\sqrt{4\pi}\phi_\uparrow(x+m)} \big] \\
&= ibr_1 l_2 \big[ e^{i(k_+(2x+m)+k_{F,\uparrow} m)} e^{-i\sqrt{4\pi}[\phi_\downarrow + \phi_\uparrow]} - e^{-i(2k_+ x + k_{F,\downarrow} m)} e^{i\sqrt{4\pi}[\phi_\downarrow + \phi_\uparrow]} \big] \\
&\quad + ibr_2 l_1 \big[ e^{i(2k_+ x + k_{F,\downarrow} m)} e^{-i\sqrt{4\pi}[\phi_\downarrow + \phi_\uparrow]} - e^{-i(k_+(2x+m)+k_{F,\uparrow} m)} e^{i\sqrt{4\pi}[\phi_\downarrow + \phi_\uparrow]} \big]
\end{aligned}$$

Adding the complex conjugates:

$$\begin{aligned}
\{\psi_\downarrow^+(x+m)\psi_\downarrow(x) + h.c.\}_{r_1 l_2 + r_2 l_1} &= -2b(r_1 l_2 + r_2 l_1) \Big[ \sin\big(2k_+ x + m k_{F,\downarrow} - \sqrt{4\pi}[\phi_\downarrow + \phi_\uparrow]\big) \\
&\quad + \sin\big(k_+(2x+m) + m k_{F,\uparrow} - \sqrt{4\pi}[\phi_\downarrow + \phi_\uparrow]\big) \Big] \\
\{\psi_\uparrow^+(x+m)\psi_\uparrow(x) + h.c.\}_{r_1 l_2 + r_2 l_1} &= -2b(r_1 l_2 + r_2 l_1) \Big[ \sin\big(2k_+ x + m k_{F,\uparrow} - \sqrt{4\pi}[\phi_\downarrow + \phi_\uparrow]\big) \\
&\quad + \sin\big(k_+(2x+m) + m k_{F,\downarrow} - \sqrt{4\pi}[\phi_\downarrow + \phi_\uparrow]\big) \Big]
\end{aligned}$$

We finally obtain in term of $\uparrow$ and $\downarrow$ bosons:

$$\mathcal{O}_{m,(r_1 l_2 + r_2 l_1)}(x) = -8b(r_1 l_2 + r_2 l_1) \cos\big(\frac{m}{2} k_-\big) \cos\big(\frac{m}{2} k_+\big) \sin\big(k_+(2x+m) - 2\sqrt{\pi}[\phi_\downarrow + \phi_\uparrow]\big) \quad \text{(C.80)}$$

Since no magnetic field is applied, $k_- = 0$ and we obtain in term of spin and charge boson:

$$\mathcal{O}_{m,(r_1 l_2 + r_2 l_1)}(x) = -8b(r_1 l_2 + r_2 l_1) \cos\big(m k_F\big) \sin\big(2k_F(2x+m) - 2\xi\sqrt{\pi}\phi_c\big) \quad \text{(C.81)}$$

### 3.1.3 Terms $r_1 l_3 + r_3 l_1$

The products of the first with the third harmonics may be marginal and hence needs to be calculated. This term is found to be:

$$\mathcal{O}_{m,(r_1 l_3 + l_1 r_3)}(x) \propto (r_1 l_3 + l_1 r_3) \sin\left(\frac{m}{2} k_-\right) \sin\left(\frac{m}{2} k_+\right) \sin\left(k_-(2x+m) - 2\sqrt{\pi}[\phi_\uparrow - \phi_\downarrow]\right) \quad \text{(C.82)}$$

This term is proportional to $\sin(k_0) = 0$. Therefore, as long as no magnetic field is applied, this term cancels. Otherwise it is marginally irrelevant.

## 3.2 Fermion-lattice coupling term

We are interested in quarter-filled systems ($n = 1/2$) whose Fermi wavevector is $k_F = \pi/4$ (no magnetic field applied). The fermion-lattice operator is the sum of the terms Eq. C.79 and C.81. We use a parameter $m$ that takes the values $m = 0$ for Holstein couplings and $m = 1$ for Peierls couplings. It reads:

$$\mathcal{O}_m^{1/2}(x) = -\lambda_{11} \sin\left(\frac{\pi}{2} \cdot x + m \cdot \frac{\pi}{4} - \xi\sqrt{\pi}\phi_c\right) \cos\left(\sqrt{2\pi}\phi_s\right) - \lambda_{12} \sin\left(\pi \cdot x + m \cdot \frac{\pi}{2} - 2\xi\sqrt{\pi}\phi_c\right) \quad \text{(C.83)}$$

Where

$$\lambda_{11} = 8 r_1 l_1 \cdot \mathbb{1} \otimes \sigma_3 \quad \text{(C.84)}$$

$$\lambda_{12} = 8(r_1 l_2 + r_2 l_1) \cdot \cos\left(m\frac{\pi}{4}\right) \cdot \mathbb{1} \otimes \sigma_3 \quad \text{(C.85)}$$

The Klein factor products for these two terms are given by $\mathbb{1} \otimes \sigma_3$. We are sure to work in the same eigenstate for both terms and we are free to pick one eigenvalue between $\pm 1$ so as to replace the product.

The scaling dimensions of these two terms depend on the dressed charge matrix coefficient $\xi$. The value of $\xi$ as a function of the repulsion and filling was studied by Frahm and Korepin [37, 38]:

$$\begin{array}{ccccccc} U = \infty & & & & & & U = 0 \\ 1 & \leq & & \xi(U,n) & & \leq & \sqrt{2} \\ 3/4 & \leq & \Delta_{11} & = & \xi^2/4 + 1/2 & \leq & 1 \\ 1 & \leq & \Delta_{12} & = & \xi^2 & \leq & 2 \end{array} \quad \text{(C.86)}$$

Note that $\Delta_{11} < \Delta_{12}$ is equivalent to $\xi < \sqrt{2/3}$, which is never reached. Though the first term is always more relevant.

Under a magnetic field, one should also take into account a radiatively generated term coming from the normal-ordered product of the $\lambda_{11}$ and $\lambda_{12}$ terms. However for vanishing magnetic field, this term becomes $\sim \lambda_3 \cos\left(2\sqrt{2\pi}\phi_s\right)$. Its dimension is $\Delta_{\lambda_3} = 2$ for all fillings. This term is marginally irrelevant [36] and will not be treated.

The lattice distortion is such that is avoid these two relevant terms to be cancelled by fluctuations. Therefore it exhibits two harmonics, one in $2k_F$ and one in $4k_F$:

$$\begin{aligned}\delta(x) &= \delta_2\cos(2k_Fx+\beta_2)+\delta_4\cos(4k_Fx)\\ &= \delta_2\cos(\frac{\pi}{2}x+\beta_2)+\delta_4(-1)^x\end{aligned} \tag{C.87}$$

The elastic energy that corresponds to this distortion is:

$$\mathscr{H}_{\text{elas}} = \frac{K}{2}\int dx\big(\delta(x)\big)^2 = \frac{NK}{2}\big(\frac{1}{2}\delta_2^2+\delta_4^2\big) \tag{C.88}$$

To simplify the notation, we perform the following changes [3]:

$$\phi_s \equiv \sqrt{2\pi}\phi_s \tag{C.89}$$

$$\phi_c \equiv \sqrt{\pi}\xi\phi_c \tag{C.90}$$

For Holstein on-site ($m=0$) lattice coupling, we obtain:

$$\mathscr{O}_0^{1/2}\delta(x) = \frac{\delta_2\lambda_{11}}{2}\int dx\sin(\phi_c+\beta_2)\cos(\phi_s)-\delta_4\lambda_{12}\int dx\cos(2\phi_c) \tag{C.91}$$

For Peierls ($m=1$) lattice coupling, we obtain:

$$\mathscr{O}_1^{1/2}\delta(x) = -\frac{\delta_2\lambda_{11}}{2}\int dx\sin(\frac{\pi}{4}-\phi_c-\beta_2)\cos(\phi_s)-\frac{\delta_4\lambda_{12}\sqrt{2}}{2}\int dx\cos(2\phi_c) \tag{C.92}$$

These operators are used in Chapter IV. One can see that the effect of lattice distortions is to couple the spin and charge sector, even with no magnetic field applied.

[3] This is equivalent with changing the spin and charge compactification radii.

# Publications


[1] *Influence of lattice distortions in classical spin systems*
D. C. Cabra, M. Moliner and F. Stauffer
Phys. Rev. B **74**, 014428 (2006)
arXiv:cond-mat/0603514.

[2] *Magnetization plateaux in the classical Shastry-Sutherland lattice*
M. Moliner, D. C. Cabra, A. Honecker, M. Moliner, P. Pujol and F. Stauffer
J. Phys.: Conf. Ser. **145**, 012053 (2009)
Proceedings of the "Highly Frustrated Magnetism 2008 Conference" (HFM2008)

[3] *Magnetization Process of the Classical Heisenberg Model on the Shastry-Sutherland Lattice*
M. Moliner, D. C. Cabra, A. Honecker, M. Moliner, P. Pujol and F. Stauffer
arXiv:0809.5249
To appear in Phys. Rev. B. (2009)

[4] *Effect of lattice distortions on the Hubbard chain at quarter-fillling*
M. Moliner and H. D. Rosales
*in preparation*

# Bibliography


[1] J. G. Bednorz and K. A. Müller, Z. Phys. B **64**, 189 (1986).

[2] E. Dagotto, Rev. Mod. Phys. **66**, 763 (1994).

[3] T. Giamarchi, *Quantum Physics in One Dimension* (Oxford Science Publications, 2004).

[4] H. J. Schulz, *Fermi liquids and non-Fermi liquids*, in *Mesoscopic quantum physics*, edited by E. Akkermans, G. Montambaux, J. Pichard, and J. Zinn-Justin, Proceedings of Les Houches Summer School LXI, p. 533, Elsevier, Amsterdam, (1995).

[5] D. C. Cabra, M. Moliner, and F. Stauffer, Phys. Rev. B **74**, 014428 (2006).

[6] M. Moliner, D. C. Cabra, A. Honecker, P. Pujol, and F. Stauffer, submitted to Phys. Rev. B (2008), preprint: Cond-Mat 0809.5249.

[7] M. Moliner, D. C. Cabra, A. Honecker, P. Pujol, and F. Stauffer, J. Phys.: Conf. Ser. **145**, 012053 (2009), Proceedings of the "Highly Frustrated Magnetism 2008 Conference" (HFM2008).

[8] M. Moliner and H. D. Rosales, in preparation (2009).

[9] H. T. Diep, H. Giacomini, O. Nagai, T. Horiguchi, S. Miyashita, B. Delamotte, D. Mouhanna, M.Tissier, D. Loison, G. Misguish, C. Lhuillier, P. Lecheminant, S. T. Bramwell, M. J. P. Gingras, P. C. W. Holdsworth, B. D. Gaulin, J. S. Gardner, N. Kawashima, and H. Rieger, *Frustrated Spin Systems* (World-Scientific, 2004).

[10] E. F. Shender and P. C. W. Holdsworth, Order by Disorder and Topology in Frustrated Magnetic Systems, in *Fluctuations and Order*, edited by M. Millonas, chap. 16, p. 299, Springer (Berlin), 1995.

[11] J. T. Chalker, P. C. W. Holdsworth, and E. F. Shender, Phys. Rev. Lett. **68**, 855 (1992).

[12] K. Penc, N. Shannon, and . Shiba, Phys. Rev. Lett. **93**, 197203 (2004).

[13] T. Vekua, D. C. Cabra, A. Dobry, C. Gazza, and D. Poilblanc, Phys. Rev. Lett **96**, 117205 (2006), cond-mat/0511368.

[14] S. Miyahara and K. Ueda, J. Phys.: Condens. Matter **15**, R327 (2003).

[15] S. Yoshii, T. Yamamoto, M. Hagiwara, A. Shigekawa, S. Michimura, F. Iga, T. Takabatake, and K. Kindo, J. Phys.: Conf. Series **51**, 59 (2006).

[16] F. Iga, A. Shigekawa, Y. Hasegawa, S. Michimura, T. Takabatake, S. Yoshii, T. Yamamoto, M. Hagiwara, and K. Kindo, J. Magn. and Magn. Mat. **310**, e443 (2007).

[17] K. Siemensmeyer, E. Wulf, H. J. Mikeska, K. Flachbart, S. Gabáni, S. Mat'as, P. Priputen, A. Evdokimova, and N. Shitsevalova, Phys. Rev. Lett. **101**, 177201 (2008), arXiv:0712.1537v2.

[18] S. Gabáni, S. Mat'aš, P. Priputen, K. Flachbart, K. Siemensmeyer, E. Wulf, A. Evdokimova, and N. Shitsevalova, Acta Phys. Pol. **113**, 227 (2008), Proceedings of the $13^{th}$ Czech and Slovak Conference on Magnetism.

[19] S. Yoshii, T. Yamamoto, M. Hagiwara, T. Takeuchi, A. Shigekawa, S. Michimura, F. Iga, T. Takabatake, and K. Kindo, J. Magn. and Magn. Mat. **310**, 1282 (2007).

[20] S. Yoshii, T. Yamamoto, M. H. andS. Michimura, A. Shigekawa, F. Iga, T. Takabatake, and K. Kindo, Phys. Rev. Lett. **101**, 087202 (2008).

[21] S. Michimura, A. Shigekawa, F. Iga, M. Sera, T. Takabatake, K. Ohoyama, and Y. Okabe, Physica B **378-380**, 596 (2006).

[22] S. Michimura, A. Shigekawa, F. Iga, M. Sera, T. Takabatake, A. Kikkawa, Y. Tanaka, and K. Katsumata, Journal of Magnetism and Magnetic Materials **310**, e446 (2007).

[23] H. Kawamura, J. Phys. Soc. Jap. **53**, 2452 (1984).

[24] H. Kawamura and S. Miyashita, J. Phys. Soc. Jap. **54**, 4530 (1985).

[25] M. E. Zhitomirsky, Phys. Rev. Lett. **88**, 057204 (2002).

[26] D. C. Cabra and P. Pujol, Field Theoretical Methods in Quantum Magnetism, in *Quantum Magnetism*, edited by U. Schollwöck, J. Richter, D. Farnell, and R. Bishop, Lecture Notes in Physics Vol. 645, chap. 6, p. 253, Springer-Verlag Berlin Heidelberg, 2004.

[27] D. Sénéchal, An Introduction to Bosonization, in *Theoretical Methods for Strongly Correlated Electrons*, edited by A.-M. T. D. Sénéchal and C. Bourbonnais, chap. 4, p. 139, Springer-Verlag, Heidelberg, 2003.

[28] C. Bourbonnais and D. Jérôme, *Advances in Synthetic Metals, Twenty years of Progress in Science and Technology*, chap. The normal phase of quasi-one-dimensional organic superconductors, pp. 206–301, (Elsevier, New York, 1999).

[29] D. Poilblanc and J. Riera, Phys. Rev. B **59**, 2667 (1999).

[30] D. Poilblanc and J. Riera, Phys. Rev. B **62**, 16243(R) (2000).

[31] R. T. Clay, S. Mazumbar, and D. K. Campbell, Phys. Rev. B **67**, 115121 (2003).

[32] S. Mazumdar, S. Ramasesha, R. T. Clay, and D. K. Campbell, Phys. Rev Lett. **82**, 1522.

[33] M. Kuwabara, H. Seo, and M. Ogata, J. Phys. Soc. Jap. **72**, 225 (2003).

[34] H. Yoshioka, M. Tsuchiizu, and Y. Suzumura, J. Phys. Soc. Jap. **69**, 651 (2000).

[35] D. C. Cabra, A. De Martino, A. Honecker, P. Pujol, and P. Simon, Phys. Lett. A **268**, 418 (2000).

[36] D. C. Cabra, A. De Martino, A. Honecker, P. Pujol, and P. Simon, Phys. Rev. B **63**, 094406 (2001).

[37] H. Frahm and V. E. Korepin, Phys. Rev. B **42**, 10553 (1990).

[38] H. Frahm and V. E. Korepin, Phys. Rev. B **43**, 5653 (1991).

[39] C. Kittel, *Introduction to Solid State Physics*, 6 ed. (J. Wiley, New York, 1986).

[40] N. W. Ashcroft and N. D. Mermin, *Solid State Physics* (Thomson Learning, 1976).

[41] A. Auerbach, *Interacting Electrons and Quantum Magnetism*, 1st ed. (Springer-Verlag (New York), 1994).

[42] P. W. Anderson, *The Theory of Supeconductivity in the High-$T_C$ Cuprates* (Princeton Series in Physics, 1997).

[43] J. Hubbard, Proc. Roy. Soc. A **276**, 238 (1963).

[44] J. Hubbard, Proc. Roy. Soc. A **277**, 237 (1963).

[45] J. Hubbard, Proc. Roy. Soc. A **281**, 401 (1964).

[46] E. Fradkin, *Field Theories of Condensed Matter Systems*Frontiers in Physics (Addison-Wesley, 1991).

[47] F. H. L. Essler, H. Frahm, F. Göhmann, A. Klümper, and V. E. Korepin, *The One-Dimensional Hubbard Model* (Cambridge University Press, 2005).

[48] E. Lieb and F. Wu, Phys. Rev. Lett. **20**, 1445 (1968).

[49] H. A. Bethe, Z. Phys. **71**, 205 (1931).

[50] R. E. Peierls, *Quantum Theory of Solids*, chap. 5, p. 109, (Oxford University Press, 1955).

[51] A. M. Tsvelik, *Quantum Field Theory in Condensed Matter Physics (2nd Ed.)* (Cambridge University Press, 2003).

[52] T. Giamarchi, Chem. Rev. **104**, 5037 (2004).

[53] D. Pines and P. Nozieres, *Theory of Quantum Liquids* (Westview Press, 1999).

[54] L. D. Landau, Sov. Phys. JETP **5**, 101 (1957).

[55] L. D. Landau, Sov. Phys. JETP **3**, 920 (1957).

[56] L. D. Landau, Sov. Phys. JETP **8**, 70 (1958).

[57] J. Voit, Reports on Progress in Physics **58**, 977 (1995).

[58] S. Tomonaga, Prog. Theor. Phys **5**, 544 (1950).

[59] J. M. Luttinger, J. Math. Phys. **4**, 1154 (1963).

[60] A. Schilling, M. Cantoni, J. D. Guo, and H. R. Ott, Nature **363**, 56 (1993).

[61] P. W. Anderson, Phys. Rev. B **42**, 2624 (1990).

[62] Z.-X. Shen, D. S. Dessau, B. O. Wells, D. M. King, W. E. Spicer, A. J. Arko, D. Marshall, L. W. Lombardo, A. Kapitulnik, P. Dickinson, S. Doniach, J. DiCarlo, T. Loeser, and C. H. Park, Phys. Rev. Lett. **70**, 1553 (1993).

[63] F. C. Zhang and T. M. Rice, Phys. Rev. B **37**, 3759 (1988).

[64] R. Simon, Physics Today **44**, 64 (1991).

[65] K. Bechgaard, C. Jacobsen, K. Mortensen, H. J. Pedersen, and N. Thorup, Solid St. Commun **33**, 1119 (1980).

[66] K. Bechgaard and D. Jérôme, Phys. Scr. **39**, 37 (1991).

[67] C. Bourbonnais and L. Caron, Europhys. Lett. **5**, 209 (1988).

[68] S. Iijima, Nature **354**, 56 (1991).

[69] S. Iijima and T. Ichihashi, Nature **363**, 603 (1993).

[70] D. S. Bethune, C. H. Kiang, M. S. deVries, G. Gorman, R. Savoy, J. Vazquez, and R. Beyers, Nature **363**, 605 (1993).

[71] M. W. Bockrath, *Carbon Nanotubes: Electrons in One Dimension*, PhD thesis, University of California, Berkeley, (1999).

[72] S. Tarucha, T. Honda, and T. Saku, Solid State Commun **94**, 413 (1995).

[73] A. Y. et al., Phys. Rev. Lett. **77**, 4612 (1996).

[74] M. Bockrath, D. H. Cobden, J. Lu, A. G. Rinzler, E. S. Richard, L. Balents, and P. L. McEuen, Nature **397**, 601 (1999).

[75] R. Egger and A. Gogolin., Phys. Rev. Lett. **79**, 5082 (1997).

[76] C. Kane and L. B. M. P. A. Fisher., Phys. Rev. Lett. **79**, 5086 (1997).

[77] M. Bockrath, M. Cobden, D. H. M. Euen, P. L. Chopra, N. G. Zettl, A. Thess, and R. E.

Smalley, Science **275**, 1922 (1997).

[78] S. J. Tans, M. H. Devoret, H. J. Dai, A. Thess, R. E. Smalley, L. J.Geerligs, and C. Dekker, Nature **386**, 474 (1997).

[79] H. Rauf, T. Pichler, M. Knufer, J. Fink, and H. Kataura, Phys. Rev. Lett **93**, 096805 (2004).

[80] G. H. Wannier, Phys. Rev. **79**, 357 (1950).

[81] J. Villian, J. Phys. C **10**, 1717 (1977).

[82] G. Toulouse, Commun. Phys. **2**, 115 (1977).

[83] P. W. Anderson, Mater. Res. Bull. **8**, 153 (1973).

[84] S. Wessel and M. Troyer, Phys. Rev. Lett. **95**, 127205 (2005).

[85] D. Heidarian and K. Damle, Phys. Rev. Lett. **95**, 127206 (2005).

[86] R. G. Melko, A. Paramekanti, A. A. Burkov, A. Vishwanath, D. N. Sheng, and L. Balents, Phys. Rev. Lett. **95**, 127207 (2005).

[87] J.-D. Picon, A. F. Albuquerque, K. P. Schmidt, N. Laflorencie, M. Troyer, and F. Mila, Phys. Rev. B **78**, 184418 (2008).

[88] M. J. Harris, S. T. Bramwell, D. F. McMorrow, T.Zeiske, and K. W. Godfrey, Phys. Rev. Lett. **79**, 2554 (1997).

[89] A. P. Ramirez, A. Hayashi, R. J. Cava, R. B. Siddharthan, and S. Shastry, Nature **399**, 333 (1999).

[90] S. T. Bramwell, M. J. P., and Gingras, Science **294**, 1495 (2001).

[91] C. Castelnovo, R. Moessner, and S. L. Sondhi, Nature **45**, 42 (2008).

[92] L. D. C. Jaubert, J. T. Chalker, P. C. W. Holdsworth, and R. Moessner, Phys. Rev. Lett. **100**, 067207 (2008).

[93] R. Moessner, Can. J. Phys. **79**, 1283 (2001).

[94] J. Richter, J. Schulenburg, and A. Honecker, Quantum Magnetism in Two Dimensions: From Semi-classical Néel Order to Magnetic Disorder, in *Quantum Magnetism, Lecture Notes in Physics* Vol. 645, chap. 2, p. 85, Springer, 2004.

[95] G. Misguich and C. Lhuillier, *Frustrated Spin Systems*, chap. Two-dimensional quantum antiferromagnets, p. 229, (World-Scientific, 2004).

[96] G. Misguich and C. Lhuillier, *Frustrated Quantum Magnets*, in *Lecture notes of the Cargese summer school on "Trends in high magnetic field science"*, (2001).

[97] A. P. Ramirez, Annu. Rev. Mater. Sci. **24**, 453 (1994).

[98] P. Schiffer and A. P. Ramirez, Comments Cond. Mat. Phys. **18**, 21 (1996).

[99] T. Kaplan, Phys. Rev. **116**, 888 (1959).

[100] J. Villain, Phys. Chem. Solids. **11**, 303 (1959).

[101] A. Yoshimori, J. Phys. Soc. Jpn. **14**, 807 (1959).

[102] J. T. Chalker, *Highly Frustrated Magnetism*, chap. Geometrically frustrated antiferromagnets, thermal and dynamical fluctuations, (, 2007), Lecture notes for Trieste Summer School, August 2007 and book to appear.

[103] M. J. Harris, S. T. Bramwell, D. F. McMorrow, T. Zeiske, and K. W. Godfrey, Phys. Rev. Lett. **79**, 2554 (1997).

[104] A. P. Ramirez, A. Hayashi, R. J. Cava, R. Siddharthan, and B. S. Shastry, Nature **399**, 333

(1999).

[105] *Proceedings of the International Conference on Highly Frustrated Magnetism HFM2008, Journal of Physics: Conference Series (to appear in 2009)*, 2009.

[106] N. Metropolis, A. W. Rosenbluth, M. N. Rosenbluth, A. H. Teller, and E. Teller, J. Chem. Phys **43**, 1145 (1993).

[107] K. Binder and D. W. Hermann, *Monte Carlo Simulation in Statistical Physics, an Introduction, , 3 rd Ed.*Solid-State Sciences (Springer, 1997).

[108] D. P. Landau and K. Binder, *A Guide to Monte Carlo Simulations in Statistical Physics, 2Nd Ed.* (Cambridge University Press, 2005).

[109] J. M. Thijssen, *Computational Physics* (Cambrige University Press, 1999).

[110] R. J. Glauber, J. Math. Phys. **4**, 294 (1963).

[111] K. Hida and I. Affleck, J. Phys. Soc. Jpn. **74**, 1849 (2005).

[112] J. Villain, R. Bidaux, J. Carton, and R. Conte, J. Physique (Paris) **41**, 1263 (1980).

[113] E. F. Shender, Soviet Physics JETP **56**, 178 (1982).

[114] A. B. Harris, C. Kallin, and A. J. Berlinsky, Phys. Rev. B **45**, 2899 (1992).

[115] I. Ritchey, P. Chandra, and P. Coleman, Phys. Rev. B **47**, 15342 (1993).

[116] R. Moessner and J. T. Chalker, Phys. Rev. Lett. **80**, 2929 (1998).

[117] R. Moessner and J. T. Chalker, Phys. Rev. B **58**, 12049 (1998).

[118] I. Affleck, *Field Theory Methods and Quantum Critical Phenomena*, in *Fields, Strings and Critical Phenomena*, edited by E. Brézin and J. Zinn-Justin, Proceedings of Les Houches Summer School XLIX, Amsterdam, Elsevier Science Publishers, (1988).

[119] J. N. Reimers and A. J. Berlinsky, Phys. Rev. B **48**, 9539 (1993).

[120] E. F. Shender and P. C. W. Holdsworth, J. Phys. Cond. Mat. **7**, 3295 (1995).

[121] S. R. White, Phys. Rev. Lett. **69**, 2863 (1992).

[122] U. Schollwöck, Rev. Mod. Phys. **77**, 259 (2005).

[123] I. Peschel, K. Hallberg, X. Wang, and M. Kaulke, *Density Matrix Renormalization: a New Numerical Method*, Lecture Notes in Physics No. 528 (Springer, N.Y., 1999).

[124] O. Tchernyshyov, R. Moessner, and S. L. Sondhi, Phys. Rev. Lett. **88**, 067203 (2002).

[125] K. Hida, J. Phys. Soc. Jpn. **63**, 2359 (1994).

[126] K. Okamoto, Solid State Commun. **98**, 245 (1996).

[127] J. P. Boucher and L. Regnault, J. Phys. I (Paris) **6**, 1939 (1996).

[128] M. Isobe and Y. Ueda, J. Phys. Soc. Jpn. **65**, 3142 (1996).

[129] N. Fujiwara, H. Yasuoka, M. Isobe, , and Y. Ueda, Phys. Rev. B **55**, R11945 (1997).

[130] J. Rieira and A. Dobry, Phys. Rev. B **51**, 16098 (1995).

[131] M. F. Thorpe and M. Blume, Phys. Rev. B **5**, 1961 (1972).

[132] M. Blume, P. Heller, and N. Lurie, Phys. Rev. B **11**, 4483 (1975).

[133] J. Stephenson, J. Math. Phys. **17**, 1645 (1976).

[134] A. Oguchi and Y. Tsushida, Prog. Theor. Phys. **56**, 1976 (1977).

[135] C. Kittel, Phys. Rev. **120**, 335 (1960).

[136] B. S. Shastry and B. Sutherland, Physica B and C **108**, 1069 (1981).

[137] F. Becca, F. Mila, and D. Poilblanc, Phys. Rev. Lett. **91**, 067202 (2003).

[138] B. Sutherland and B. S. Shastry, Journal of Statistical Physics **33**, 477 (1983).

[139] R. W. Smith and D. A. Keszler, J. Solid State Chem. **93**, 430 (1991).

[140] A. Koga and N. Kawakami, Phys. Rev. Lett. **84**, 4461 (2000).

[141] K. Kodama, M. Takigawa, M. Horvatic, C. Berthier, H. Kageyama, Y. Ueda, S. Miyahara, F. Becca, and F. Mila, Science **298**, 395 (2002).

[142] K. Onizuka, H. Kageyama, Y. Narumi, K. Kindo, Y. Ueda, and T. Goto, J. Phys. Soc. Jap. **69**, 1016 (2000).

[143] H. Kageyama, K. Yoshimura, R. Stern, N. Mushnikov, K. Onizuka, M. Kato, K. Kosuge, C. Slichter, T. Goto, and Y. Ueda, Phys. Rev. Lett. **82**, 3168 (1999).

[144] K. Ueda and S. Miyahara, J. Phys.: Condens. Matter **11**, L175 (1999).

[145] S. Miyahara and K. Ueda, Phys. Rev. Lett. **82**, 3701 (1999).

[146] H. Nojiri, H. Kageyama, K. Onizuka, Y. Ueda, and M. Motokawa, J. Phys. Soc. **68**, 2906 (1999).

[147] H. Kageyama, K. Onizuka, T. Yamauchi, Y. Ueda, S. Hane, H. Mitamura, T. Goto, K. Yoshimura, and K. Kosuge, J. Phys. Soc. Jpn. **68**, 1821 (1999).

[148] H. Kageyama, M. Nishi, N. Aso, K. Onizuka, T. Yosihama, K. Nukui, K. Kodama, K. Kakurai, and Y. Ueda, Phys. Rev. Lett. **84**, 5876 (2000).

[149] S. Miyahara and K. Ueda, Physica B **281**, 661 (2000).

[150] T. Momoi and K. Totsuka, Phys. Rev. B **61**, 3231 (2000).

[151] M. Takigawa, K. Kodamaa, M. HorvatiImage, Berthier, H. Kageyamaa, Y. Uedaa, S. Miyahara, F. Beccad, and F. Mila, Physica B: Condensed Matter **346**, 27 (l 2004).

[152] T. Momoi and K. Totsuka, Phys. Rev. B **62**, 15067 (2000).

[153] H. Kageyama, Y. Ueda, Y. Narumi, K. Kindo, M. Kosaka, and Y. Uwatoko, Prog. Theor. Phys. Sup. **145**, 17 (2002).

[154] S. E. Sebastian, N. Harrison, P. Sengupta, C. D. Batista, S. Francoual, E. Palm, T. Murphy, N. Marcano, H. A. Dabkowska, and B. D. Gaulin, PNAS **105**, 20157 (2008), preprint arXiv:0707.2075v2.

[155] F. Levy, I. Sheikin, C. Berthier, M. Horvatić, M. Takigawa, H. Kageyama, T. Waki, and Y. Ueda, Europhysics Letters (EPL) **81**, 67004 (2008).

[156] A. Abendschein and S. Capponi, (2008), preprint arXiv:0807.1071 v1.

[157] M. S. Kim, M. C. Bennett, and M. C. Aronson, Phys. Rev. B **77**, 144425 (2008).

[158] T. Inami, K. Ohwada, Y. H. Matsuda, Z. W. Ouyang, H. Nojiri, D. Okuyama, T. Matsumura, and Y. Murakami, (2007).

[159] R. Watanuki, G. Sato, K. Suzuki, M. Ishihara, T. Yanagisawa, Y. Nemoto, and T. Gotto, J. Phys. Soc. Jpn. **74**, 2169 (2005).

[160] R. Watanuki, G. Sato, K. Suzuki, M. Ishihara, T. Yanagisawa, Y. Nemoto, and T. Gotto, Physica B: Condensed Matter **378-380**, 594 (2006).

[161] A. Kikkawa, K. Katsumata, Y. Narumi, K. S. andT. Kukui andT. Sugaya, F. I. K. Kindo, and S. Michimura, Journal of the Physical Society of Japan **76**, 024711 (2007).

[162] M. E. Zhitomirsky, A. Honecker, and O. A. Petrenko, Phys. Rev. Lett. **85**, 3269 (2000).

[163] B. Canals and M. E. Zhitomirsky, J. Phys: Condens. Matter **16**, S759 (2004).

[164] D. H. Lee, J. D. Joannopoulos, J. W. Negele, and D. P. Landau, Phys. Rev. Lett. **52**, 433 (1984).
[165] D. Cabra, M. Grynberg, P. Holdsworth, and P. Pujol, Phys. Rev. B **65**, 094418 (2002).
[166] S. E. Korshunov, J. Phys. C: Solid State Phys **19**, 5927 (1986).
[167] A. V. Chubukov and D. I. Golosov, J. Phys.: Cond. Matt. **3**, 69 (1991).
[168] S. E. Korshunov, Phys. Uspekhi **49**, 225 (2006).
[169] H. Tsujii, C. R. Rotundu, T. Ono, H. Tanaka, B. Andraka, K. Ingersent, and Y. Takano, Phys. Rev. B **76**, 060406(R) (2007).
[170] J. M. D. Champion and P. C. W. Holdsworth, J. Phys. Cond. Mat. **16**, S665 (2004).
[171] M. Matsumoto and T. Nishimura, ACM Trans. Model. Comput. Simul. **8**, 3 (1998).
[172] N. D. Mermin and H. Wagner, Phys. Rev. Lett. **17**, 1133 (1966).
[173] S. Watarai, S. Miyashita, and H. Shiba, J. Phys. Soc. Jpn. **70**, 532 (2001).
[174] V. L. Berezinskiĭ, Soviet Physics JETP **32**, 493 (1971).
[175] J. M. Kosterlitz, J. Phys. C: Solid State Phys. **7**, 1046 (1974).
[176] J. M. Kosterlitz and D. J. Thouless, J. Phys. C **6**, 1181 (1973).
[177] R. B. Potts, Proc. Camb. Phil. Soc. **48**, 106 (1952).
[178] F. Y. Wu, Rev. Mod. Phys. **54**, 235 (1982).
[179] S. Miyahara, F. Becca, and F. Mila, Phys. Rev. B **68**, 024401 (2003).
[180] S. Miyahara and K. Ueda, Phys. Rev. B **61**, 3417 (2000).
[181] F. Wang and A. Vishwanath, Phys. Rev. Lett. **100**, 077201 (2008).
[182] F. Wang, A. Vishwanath, and Y. B. Kim, Phys. Rev. B **76**, 094421 (2007).
[183] D. L. Bergman, R. Shindou, G. A. Fiete, and L. Balents, Phys. Rev. B **74**, 134409 (2006).
[184] Z. Y. Meng and S. Wessel, Phys. Rev. B **78**, 224416 (2008), preprint arXiv:0808.3104v1.
[185] M. C. Chang and M. F. Yang, (2008), arXiv:0812.0402v1.
[186] A. O. Gogolin, A. A. Nersesyan, and A. M. Tsvelik, *Bosonization and Strongly Correlated Systems* (Cambridge University Press, 1999).
[187] J. Sóloym, Advances in Physics **28**, 201 (1979).
[188] J. Cardy, *Scaling and Renormalization in Statistical Physics*, Cambridge Lecture Notes in Physics No. 5 (Cambridge University Press, 1996).
[189] M. Tsuchiizu and Y. Suzumura, Phys. Rev. B **77**, 195128 (2008).
[190] J. E. Hirsch and D. J. Scalapino, Phys. Rev. Lett. **50**, 1168 (1983).
[191] J. E. Hirsch and D. J. Scalapino, Phys. Rev. B **27**, 7169 (1983).
[192] J. E. Hirsch and D. J. Scalapino, Phys. Rev. B **29**, 5554 (1984).
[193] Y. Omori, M. Tsuchiizu, and Y. Suzumura, J. Phys. Soc. Jap. **76**, 114709 (2007).
[194] M. Tsuchiizu, H. Yoshioka, and Y. Suzumura, Physica B **284-288**, 1547 (2000).
[195] M. Sugiura and Y. Suzumura, J. Phys. Soc. Jpn **72**, 1458 (2003).
[196] S. Bissola and A. Parola, Phys. Rev. B **73**, 195108 (2006).
[197] H. Seo, J.Merino, H. Yoshioka, and M. Ogata, J. Phys. Soc. Jap. **75**, 051009 (2006).
[198] M. J. Rice, Phys. Rev. Lett. **37**, 36 (1976), see also erratum Phys. Rev. Lett. 37, 390 - 390 (1976).
[199] M. J. Rice and Y. N. Gartstein, J. Phys. Cond. Mat. **15**, 4617 (2005).

[200] W. P. Su, J. R. Schrieffer, and A. J. Heeger, Phys. Rev. Lett. **42**, 1698 (1979).
[201] W. P. Su, J. R. Schrieffer, and A. J. Heeger, Phys. Rev. B **22**, 2099 (1980).
[202] A. J. Heeger, S. Kivelson, J. R. Schrieffer, and W. P. Su, Rev. Mod. Phys. **60**, 781 (1988).
[203] K. C. Ung, S. Mazumbar, and D. K. Campbell, Sol. State Comm. **85**, 917 (1993).
[204] *Private conversation with D. Poilblanc.*
[205] Penc and Sóloym, Phys. Rev. B **47**, 6273 (1991).
[206] K. C. Ung, S. Mazumbar, and D. Toussaint, Phys. Rev. Lett. **74**, 2603 (1994).

# ABSTRACT

This thesis deals with the effects of phonons, in the adiabatic limit, on low-dimensional strongly-correlated systems. In a first part, we focus on spin systems in the classical limit (large $S$). We study the frustrated $J_1 - J_2$ chain coupled with lattice distortions and under an applied magnetic field. By means of analytical and numerical (Monte-Carlo) methods, we show that, for a wide range of the spin-lattice coupling, a magnetization plateau at 1/3 of the saturated magnetization is stabilized. We then study the two-dimensional frustrated Shastry-Sutherland lattice. A magnetization pseudo-plateau is found at 1/3 of the saturated magnetization for non-zero temperature. Classical spin-waves and Monte-Carlo simulations show that this pseudo-plateau is due to the entropic selection of a particular collinear configuration through the *Order by Disorder* effect. By means of Monte-Carlo simulations, we obtain a phase diagram in the plane magnetic field versus temperature. The second part is dedicated to the quarter-filled Hubbard chain. Both Holstein (on-site) and Peierls distortions are considered. We derive a bosonic Hamiltonian in the low-energy limit by means of the bosonization technique. We include more harmonics in the bosonic expansion of the fermionic fields and show that the lattice coupling couples the spin and charge degrees of freedom. We qualitatively recover tetramerized and dimerized phases that were obtained in previous numerical works.


Keywords: Low-dimensional strongly correlated systems, frustrated systems, adabatic phonons, *Order by Disorder* , Hubbard model, bosonization, organic conductors.


---


# RÉSUMÉ

Cette thèse porte sur l'effet de phonons, dans la limite adiabatique, sur des systèmes de basse dimensionalité fortement corrélés. Dans une première partie, nous considérons uniquement des systèmes de spins classiques (limite grand $S$). Nous étudions la chaîne de spins frustrés $J_1 - J_2$ couplée avec des distorsions du réseau et en présence d'un champ magnétique. Par des méthodes analytiques et numériques (Monte-Carlo), nous montrons que pour une large gamme de couplage spin-réseau un plateau d'aimantation est stabilisé à 1/3 de l'aimantation de saturation. Nous étudions ensuite un réseau frustré à deux dimensions, le réseau de Shastry-Sutherland. Nous trouvons un pseudo-plateau d'aimantation à 1/3 de l'aimantation de saturation à température non-nulle. Nous montrons, via des ondes de spins classiques et des simulations Monte-Carlo, que ce pseudo-plateau est dû à une sélection entropique d'une configuration colinéaire à travers l'effet d'*Ordre par le Désordre*. Nous obtenons par des simulations Monte-Carlo un diagramme de phase en fonction de la température et du champ appliqué. La seconde partie passe en revue le travail effectué sur la chaîne de Hubbard quart-remplie. Nous considérons des distorsions de Holstein (sur site) et de Peierls. Nous dérivons un Hamiltonien bosonique dans la limite basse énergie en incluant davantage d'harmoniques aux champs fermioniques et montrons que le couplage avec le réseau couple les degrés de liberté de charge et de spin. Nous retrouvons qualitativement les phases tétra et dimérisées qui ont été obtenues dans des travaux numériques antérieurs.


Mots-clés : Systèmes de basse dimensionalité fortement corrélés, systèmes frustrés, phonons adiabatiques, *Ordre par le Désordre*, modèle de Hubbard, bosonisation, conducteurs organiques.